

# BANDSTRUCTURE CALCULATION OF THE ELECTRON MOMENTUM DISTRIBUTIONS IN VANADIUM AND VANADIUM DEUTERIDE

by

KRISHNA GANDHI, K. R.

TH  
PHY 119781D  
K 8976  
PhD

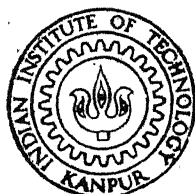
PHY

1978

D

GANDHI

BAN



DEPARTMENT OF PHYSICS

INDIAN INSTITUTE OF TECHNOLOGY KANPUR

AUGUST, 1978

# **BANDSTRUCTURE CALCULATION OF THE ELECTRON MOMENTUM DISTRIBUTIONS IN VANADIUM AND VANADIUM DEUTERIDE**

**A Thesis Submitted  
In Partial Fulfilment of the Requirements  
for the Degree of  
DOCTOR OF PHILOSOPHY**

**by  
KRISHNA GANDHI, K. R.**

15482

**to the**

**DEPARTMENT OF PHYSICS  
INDIAN INSTITUTE OF TECHNOLOGY KANPUR  
AUGUST, 1978**


L.I.T. 1000000  
**CENTRAL**  
**App. No. 58471**

10 MAY 1979

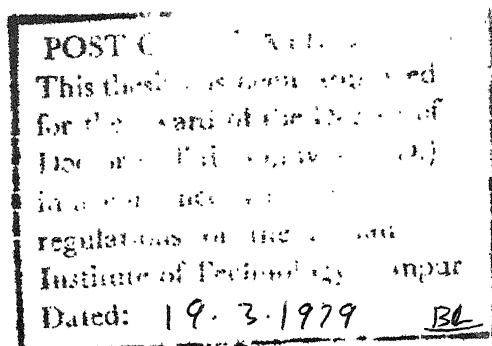
PHY-1978-D-GAN-BAN

## CERTIFICATE

This is to certify that the work presented in this thesis entitled 'Bandstructure Calculation of Electron Momentum Distributions in Vanadium and Vanadium Deuteride' by Krishna Gandhi, K.R. has been done under my supervision and it has not been submitted elsewhere for a degree or diploma.

  
R. M. Singru  
Department of Physics  
Indian Institute of Technology  
Kanpur, India

August 1978





## ACKNOWLEDGEMENTS

I am grateful to Professor R. M. Singru for suggesting the problem and for giving me his patient and continued guidance throughout the work.

I am thankful to Dr. P. E. Mijnaerends for providing the computer programs for this work as well as for communicating to us his results prior to publication.

I thank Professor T. V. Ramakrishnan for his valuable comments and for his help especially when Professor R. M. Singru was on leave.

Thanks are due to Dr. D. G. Kanhere for the stimulating discussions and help in the computer work, to Dr. Anil Seth for valuable suggestions and to Dr. Sushma Tiwari (nee Bhatnagar) for allowing me to use her computer program.

It is a pleasure to thank all those whose association I had the fortune to enjoy while working in the 'Nuclear Lab'.

I thank my wife and all my friends who in one way or another helped and encouraged me to complete this work.

Thanks are due to Mr. N. Ahmad for the neat typing, to Mr. B. B. Srivastava for the drawings and to Mr. Lalloo Singh for cyclostyling the typewritten sheets.

A part of this work was done under a special project of the Special Commission on Electron Charge, Spin and Momentum Density instituted by the International Union of Crystallography. I acknowledge with thanks all the relevant communications from Professor V. Smith in this connection.

KRISHNA GANDHI, K.R.

## CONTENTS

	<u>Page</u>
LIST OF TABLES	vii
LIST OF FIGURES	ix
SYNOPSIS	xiv
 CHAPTER 1 INTRODUCTION	 1
1.1 Introduction	1
1.2 Photon Compton Scattering	2
1.3 Some Other Experimental Methods for the Determination of EMD	11
1.4 Theoretical Calculation of the Electron Momentum Density	24
1.5 Comparison Between Theory and Experiment	33
1.6 Motivation Behind the Present Work	34
References	39
 CHAPTER 2 REVIEW OF BANDSTRUCTURE AND FERMI SURFACE STUDIES OF VANADIUM	 42
2.1 Introduction	42
2.2 Survey of the Bandstructure Calculations for Vanadium	49
2.3 Survey of the Fermi Surface Studies of Vanadium	58
2.4 Survey of the Compton Profile Studies of Vanadium	62
References	66
 CHAPTER 3 THE APPROXIMATE CALCULATION OF ELECTRON BANDSTRUCTURE AND MOMENTUM DENSITY	 69
3.1 Introduction	69
3.2 Hubbard's Fast Approximate Scheme	71
3.3 Calculation of Electron Wavefunctions and Momentum Density	77
3.4 Computational Details	79
References	93

	<u>Page</u>
CHAPTER 4 ELECTRON MOMENTUM DISTRIBUTION IN VANADIUM: RESULTS AND DISCUSSION	95
4.1 Introduction	95
4.2 Energy Bands and Bandwidths	98
4.3 Fermi Surface of Vanadium	108
4.4 Electron Momentum Distribution in Vanadium	114
Summary	157
References	162
CHAPTER 5 DIRECTIONAL COMPTON PROFILES AND THEIR ANISOTROPIES FOR VANADIUM	164
5.1 Introduction	164
5.2 Method of Calculation	166
5.3 Results and Discussion	168
References	189
CHAPTER 6 COMPTON PROFILES OF VANADIUM DEUTERIDE	190
6.1 Introduction	190
6.2 Method of Calculation	192
6.3 Results and Discussion	199
Summary	211
References	213
VITAE	xvii

<u>Table No.</u>		<u>Page</u>
4.5	Specification of the components of the $12p^+$ directions	139
5.1	Comparison of the spherically averaged Compton profile (present calculations) and the experimental polycrystalline values	173

## LIST OF FIGURES

<u>Fig. No.</u>		<u>Page</u>
1.1	Photon Compton scattering by a stationary electron	3
1.2	Schematic diagram of the Compton profile	5
1.3	Basic process of photon Compton scattering	5
1.4	Schematic diagram of the experimental set-up for photon Compton profile measurements	9
1.5	Schematic diagram of the experimental set-up for ACPAR measurements	12
1.6	Schematic diagram of the experimental set-up for electron Compton scattering	16
1.7	(e,2e) Scattering	20
1.8	Fermi distribution at $T = 0^{\circ}\text{K}$ of (a) free electron gas (b) interacting electron gas	26
1.9	Reciprocity of the radial charge density distribution and momentum density distribution for the different electronic orbitals of argon	26
1.10	The EMD in p-space, $\rho(p)$ , obtained from the EMD in the first BZ, $\rho(k)$ , through Unklapp processes for different positions of the Fermi level (one dimensional case)	31
2.1	Hybridisation of the s and d bands for a fcc transition metal	48
2.2	General features of the FS of vanadium: (a) second band octahedral hole surface (b) third band hole sheets	59

<u>Fig. No.</u>		<u>Page</u>
2.3	Fermi surface of vanadium group metals predicted by Mattheiss [12] from (a) calculations on tungsten (b) calculations on iron by Wood [14]	60
3.1	The 1/48th part of the first BZ for a bcc metal	91
3.2	The $\vec{k}$ points in the (100) and (110) planes involved in the calculations of EMD	92
4.1	The energy bands of vanadium along the principal symmetry axes (case V1)	99
4.2	The energy bands of vanadium along the principal symmetry axes (case V1)	100
4.3	The energy bands of vanadium along the principal symmetry axes (case V2)	101
4.4	The energy bands of vanadium along the principal symmetry axes (Case V2)	102
4.5	The energy bands of vanadium along the principal symmetry axes (case V3)	103
4.6	The energy bands of vanadium along the principal symmetry axes (case V3)	104
4.7	The density of states histogram for vanadium (case V1)	109
4.8	The cross-section of the FS of vanadium in the (100) and (110) planes (case V1)	110
4.9	The cross-section of the FS of vanadium in the (100) and (110) planes (case V2)	111
4.10	The cross-section of the FS of vanadium in the (100) and (110) planes (case V3)	112
4.11	The EMD along the $\langle 100 \rangle$ direction for vanadium (case V1)	119

<u>Fig. No.</u>		<u>Page</u>
4.12	The EMD along the $\langle 100 \rangle$ direction for vanadium (case V2)	120
4.13	The EMD along the $\langle 100 \rangle$ direction for vanadium (case V3)	121
4.14	The $\vec{p}$ -directions $\Gamma A$ near the $\langle 100 \rangle$ direction and $\Gamma B$ near the $\langle 110 \rangle$ direction	123
4.15	The EMD along the direction $\Gamma A$	124
4.16	The EMD along the $\langle 110 \rangle$ direction (case V1)	126
4.17	The EMD along the $\langle 110 \rangle$ direction (case V2)	127
4.18	The EMD along the $\langle 110 \rangle$ direction (case V3)	128
4.19	The EMD along the $\langle 110 \rangle$ direction for Fermi level dipping below the $\Sigma_1$ band (case V1)	130
4.20	The EMD along the direction $\Gamma B$ .	132
4.21	The EMD along the $\langle 111 \rangle$ direction (case V1)	134
4.22	The EMD along the $\langle 111 \rangle$ direction (case V2)	135
4.23	The EMD along the $\langle 111 \rangle$ direction (case V3)	136
4.24	The 12 $\vec{p}$ directions in the (100) and (110) planes along which EMD was calculated	138
4.25	The EMD along direction 2	140
4.26	The EMD along direction 3	141
4.27	The EMD along direction 4	142
4.28	The EMD along direction 5	143
4.29	The EMD along direction 7	144
4.30	The EMD along direction 8	145
4.31	The EMD along direction 9	146
4.32	The EMD along direction 10	147



Fig. No.

4.33	The EMD along direction 12	148
4.34	The total electron momentum isodense curves in the (100) and (110) planes (case V1)	150
4.35	The total electron momentum isodense curves in the (100) and (110) planes (case V2)	151
4.36	The electron momentum isodense curves in the (100) and (110) planes due to the lowest energy band (case V1); see text.	153
4.37	The electron momentum isodense curves in the (100) and (110) planes due to the second lowest energy band (case V1); see text	154
4.38	The electron momentum isodense curves in the (100) and (110) planes due to the third lowest energy band (case V1); see text	155
5.1	The spherically averaged Compton profile $g_0(p)$ and the spherically averaged EMD, $\rho_0(p)$ (case V1)	169
5.2	The Kubic harmonic components $g_4(p)$ and $g_6(p)$ of the Compton profiles (case V1)	170
5.3	The Kubic harmonic components $\rho_4(p)$ and $\rho_6(p)$ of the EMD (case V1)	171
5.4	The spherically averaged Compton profile for the band electrons: comparison between theory and experiment	174
5.5	The theoretical Compton profiles [present work] along the $\langle 100 \rangle$ , $\langle 110 \rangle$ and $\langle 111 \rangle$ directions	177
5.6	The schematic diagram of the FS topology showing the various symmetry planes [10]	179
5.7	The directional Compton profiles calculated by Wakoh et al. [11]	182

<u>Fig. No.</u>		<u>Page</u>
5.8	The Compton profile anisotropies (a) measured by Terasaki et al. [13] (b) calculated by Weiss [14]	183
5.9	The theoretical Compton profile anisotropy $J_{110}-J_{100}$	184
5.10	The theoretical Compton profile anisotropy $J_{111}-J_{100}$	185
5.11	The theoretical Compton profile anisotropy $J_{111}-J_{110}$	186
6.1	The theoretical (SPM and MPM) and the experimental difference curves for the spherically averaged Compton profiles from $VD_{0.72}$	200
6.2	The theoretical Compton profiles for V and $VD_{0.72}$ (SEM) along the $\langle 100 \rangle$ direction	202
6.3	The difference curves $\Delta J_{100}$ (SPM and MPM) for $VD_{0.72}$ (see text)	203
6.4	The difference curves $\Delta J_{110}$ (SPM and MPM) for $VD_{0.72}$ (see text)	206
6.5	The difference curves $\Delta J_{111}$ (SPM and MPM) for $VD_{0.72}$ (see text)	207
6.6	The theoretical Compton profile anisotropy curve $J_{110}-J_{100}$ (SPM and MPM) for $VD_{0.72}$	208
6.7	The theoretical Compton profile anisotropy curve $J_{100}-J_{111}$ (SPM and MPM) for $VD_{0.72}$	209
6.8	The theoretical Compton profile anisotropy curve $J_{110}-J_{111}$ (SPM and MPM) for $VD_{0.72}$	210

## SYNOPSIS

### BAND STRUCTURE CALCULATION OF ELECTRON MOMENTUM DISTRIBUTIONS IN VANADIUM AND VANADIUM DEUTERIDE

By

KRISHNA GANDHI, K. R.  
Department of Physics  
Indian Institute of Technology  
Kanpur 208 016, India

May 1978

Recently the experimental determination of the electron momentum distributions (EMD) by the measurement of photon Compton scattering has become an important tool to study the electronic structure of solids. In order to make a detailed comparison between theory and experiment it is necessary to perform a band-structure calculation of the EMD. This is particularly important for the transition metals because of their interesting band-structure. The bandstructure and Fermi surface of vanadium (which has partially filled 3d bands) are known to be sensitive to the choice of crystal potential, outer electron configuration and exchange parameter. In the present work we have calculated the bandstructure and EMD (for photon Compton scattering) in vanadium for three different crystal potentials using the Hubbard-Mijnarends method. The results for the EMD are analyzed in terms of the bandstructure and Fermi surface topology. Directional Compton profiles (and their anisotropies) are calculated from the

EMD obtained. The results are extended to calculate the directional Compton profiles for the vanadium deuteride in the framework of rigid band protonic model.

In Chapter 1 a general introduction to the subject of EMD is provided. The four important experimental methods to determine the EMD, that is, photon Compton scattering, positron annihilation, electron Compton scattering and  $(e, 2e)$  scattering are briefly described and compared with each other. A brief introduction to the theoretical calculation of the EMD in metals is given. At the end the motivation behind the present work is explained.

A review of the bandstructure and Fermi surface studies for vanadium reported in the literature is given in Chapter 2. Dependence of these properties on the electron configuration and exchange parameter used in the crystal potential of vanadium is discussed.

Chapter 3 provides a brief summary of Hubbard's fast approximate scheme used by us to calculate the bandstructure of vanadium. The extension of this method by Mijnaerends to calculate the EMD is also outlined. Necessary formulas and numerical parameters used by us are also presented.

The results obtained by us for the bandstructure, Fermi surface and EMD of vanadium for the three crystal potentials are presented in Chapter 4. The results for the EMD are

discussed in terms of the bandstructure, Fermi surface and the group theoretical selection rule. The results for the EMD along twelve  $\vec{p}$  directions as well as the constant EMD contours in the (100) and (110) planes are given. Possible ways of comparing theoretical and experimental EMD are suggested.

In Chapter 5 the results of the calculation of the directional Compton profiles  $J_{hkl}(p_z)$  and their anisotropies are described. These results are also analyzed in terms of the bandstructure and Fermi surface of vanadium.

In Chapter 6 the results for the EMD in pure vanadium are extended to obtain the EMD and the directional Compton profiles in vanadium deuterides. These calculations were made in terms of a protonic model in which the dissolved deuterium is assumed to donate its electrons to the host metal. These results are explained in terms of the bandstructure of vanadium. A possible test to examine the electronic structure (and validity of the protonic model) of the transition metal hydrides is suggested.

## Chapter 1

### INTRODUCTION

#### 1.1 Introduction

In recent years there has been considerable interest in the theoretical calculation and experimental determination of the momentum distributions of electrons in atoms, molecules and solids. At present there are four important experimental techniques for the determination of the electron momentum densities (EMD) and these are photon Compton scattering, positron annihilation, electron Compton scattering and (e,2e) electron scattering. These experimental techniques provide an indirect or direct information about the EMD,  $\rho(\vec{p})$ , which is defined as

$$\rho(\vec{p}) = |\chi(\vec{p})|^2 \quad (1.1)$$

where  $\chi(\vec{p})$  is the electron wavefunction in the momentum space. Usually the momentum wavefunction is obtained from the position space wavefunction  $\psi(\vec{r})$  through the well-known Dirac transformation

$$\chi(\vec{p}) = \int \psi(\vec{r}) \exp(-i\vec{p} \cdot \vec{r}) d\vec{r} \quad (1.2)$$

The determination of the EMD, therefore, provides a test of the electron wavefunctions in atoms, molecules, metals and other solids and hence is of great interest. In the next section we shall discuss the technique of photon Compton scattering since the results of the present work can be directly verified by this technique. In §1.3 a brief outline of the other experimental methods to determine EMD will be given. The theoretical methods for the calculation of the EMD would be briefly reviewed in §1.4. Methods to compare experiment and theory are discussed in §1.5 while the motivation behind the present calculation would be discussed in §1.6.

## 1.2 Photon Compton Scattering

Although it was known as early as in the 1930's that photon Compton scattering can provide information about the EMD,  $\rho(\vec{p})$ , this technique lay neglected until 1965 when new experimental as well as theoretical developments led to a revival of research interest in this field. The interesting history of the development of photon Compton scattering technique is given by Cooper [1,2].

Photon Compton scattering is a name given to the inelastic scattering of a photon by an electron. In the case of a photon (wavelength  $\lambda_1$ ) incident on a stationary, unbound electron the wavelength shift ( $\Delta\lambda$ ) after Compton scattering

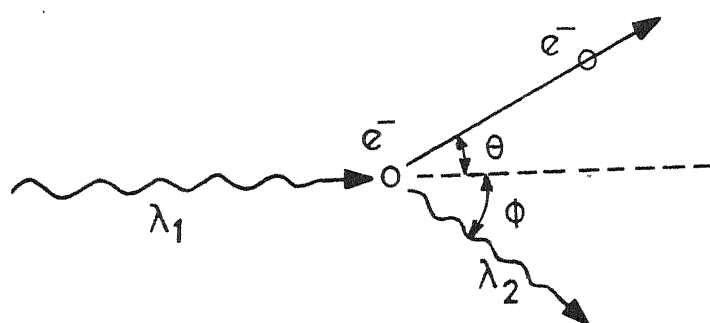


Fig. 1.1 : Photon Compton scattering in elastic collision.



through an angle  $\phi$  (Fig. 1.1) is given by,

$$\Delta\lambda = \frac{2h}{mc} \sin^2 \phi/2 \quad (1.3)$$

In a real solid the scattering electron is neither stationary (it has actually a finite linear momentum governed by the EMD) nor is it unbound. As long as the energy transferred to the recoil electron is large compared to the binding energy of the electron, the effect of the finite nature of  $\vec{p}$  (the electron momentum) is to modify Eq. (1.3) [1] as

$$\Delta\lambda = \frac{2h}{mc} \sin^2 \phi/2 - \left( \frac{2\lambda_1}{mc} \sin \phi/2 \right) p_z \quad (1.4)$$

where  $p_z$  is the projection of  $\vec{p}$  on the scattering vector (taken to be along the z-axis). Examination of Eq. (1.4) shows that the intensity distribution  $I(\lambda)$  of the Compton scattered line observed at an angle  $\phi$  will show a wavelength broadening instead of the monochromatic line as suggested by Eq. (1.3). The broadened lineshape  $I(\lambda)$  versus  $\lambda$  (Fig. 1.2) is usually termed as the Compton profile and the amount of broadening of a Compton profile is determined by the  $p_z$ -component through the EMD [3,4].

The usefulness of the experimental Compton profiles for the determination of the EMD rests basically on the validity of the so-called 'impulse approximation (IA)' [3]. The central assumption in the IA is that the electron-photon

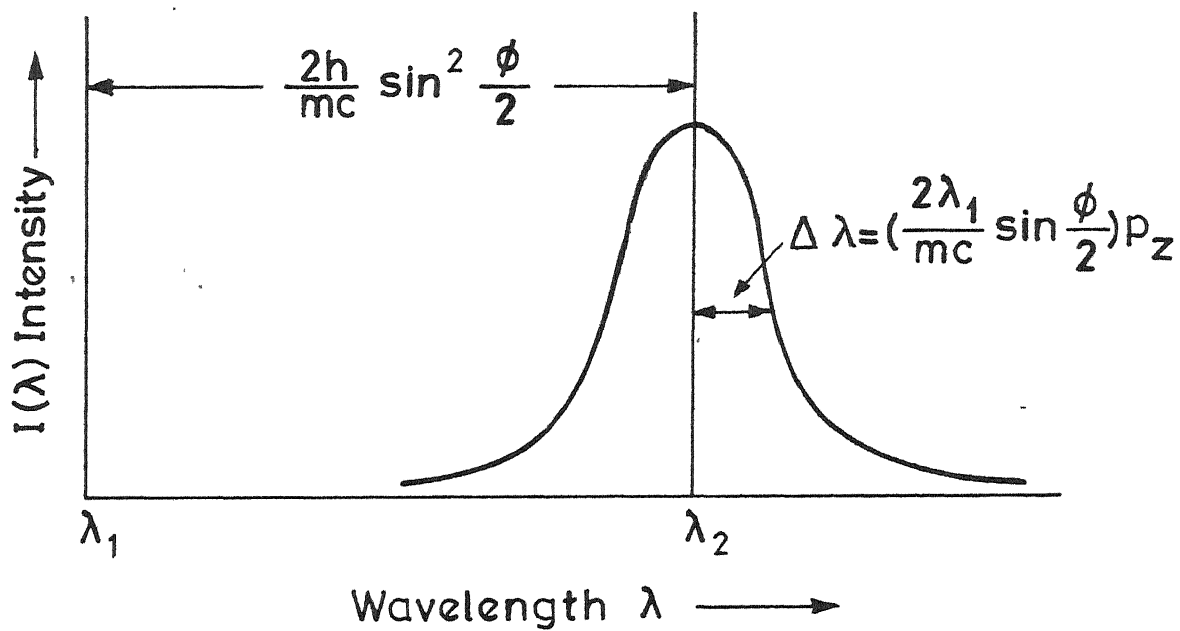


Fig. 1.2 : Calculated profile of the Compton profile.

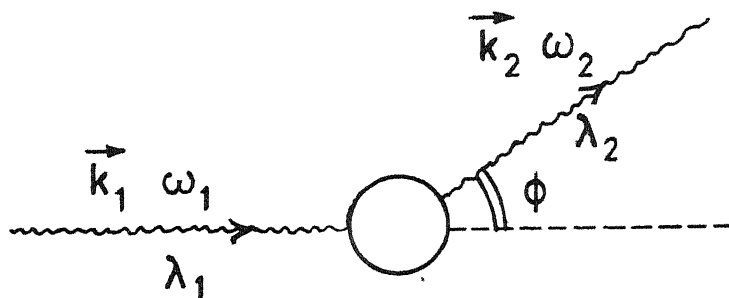


Fig. 1.3 : Basic process of photon Compton scattering.

interaction time (involved in the Compton scattering) is short and the electron receives enough energy to get excited into the continuum. This enables us to use a plane-wave description for the final state of the electron. It has been shown by Platzman and Tzoar [5] that the IA is valid for free electrons while Eisenberger and Platzman [6] demonstrated that it is also valid for the bound electrons provided that the electron's recoil energy ( $E_R$ ) is much greater than its binding energy ( $|E_B|$ ).

The cross section for Compton scattering (in the framework of the IA and using  $\hbar = c = 1$ ) is given by

$$\frac{d\sigma}{d\omega d\Omega} = \left| \frac{d\sigma}{d\Omega} \right|_{Th} \frac{\omega_2}{\omega_1} \int \rho(\vec{p}) \delta\left(\omega - \frac{k^2}{2m} - \frac{\vec{k} \cdot \vec{p}}{m}\right) d\vec{p} \quad (1.5)$$

where  $\left| \frac{d\sigma}{d\Omega} \right|_{Th}$  is the elastic or Thomson cross section while  $\vec{k}_1, \omega_1$  ( $\vec{k}_2, \omega_2$ ) denote the momentum and energy of the incident (scattered) photons (Fig. 1.3), and  $\vec{k} = \vec{k}_1 - \vec{k}_2, \omega = \omega_1 - \omega_2$ . The cross section is thus related to the Compton profile

$$J_{\vec{k}}(q)$$

$$J_{\vec{k}}(q) = \int \rho(\vec{p}) \delta\left(q - \frac{\vec{p} \cdot \vec{k}}{|\vec{k}|}\right) d\vec{p} \quad (1.6)$$

through the relation

$$\frac{d\sigma}{d\omega d\Omega} = \left| \frac{d\sigma}{d\Omega} \right|_{Th} \frac{\omega_2}{\omega_1} \cdot \frac{m}{|\vec{k}|} J_{\vec{k}}(q) \quad (1.7)$$

where

$$q = \frac{m\omega}{|\vec{k}|} - \frac{1}{2} |\vec{k}| \quad (1.8)$$

and the quantity  $q$  is thus a measure of the electron momentum in the direction of momentum transfer. If the  $z$ -axis is chosen along  $\vec{k}$ , the scattering vector, the expression for the Compton profile (CP) can be written as

$$J_{\vec{k}}(q) = \iint_{-\infty}^{+\infty} [\rho(\vec{p})]_{p_z=q} dp_x dp_y \quad (1.9)$$

It is observed from Eq. (1.5) that the frequency of the scattered photon is shifted by the momentum transfer term ( $k^2/2m$ ) as well as by the Doppler shift term ( $\vec{k} \cdot \vec{p}/m$ ). The CP is thus obtained as a double integral [Eq. (1.9)] of the EMD,  $\rho(\vec{p})$ , in the momentum space. The relationship between the CP and the EMD assumes a simple form [Eq. (1.9)] in the framework of the IA and hence it is important to know the conditions under which the IA is valid. Investigation of this problem [6,7] has shown that the corrections to the IA are of the order of  $(E_B/E_R)^2$  where  $E_B$  is the binding energy and  $E_R$  the recoil energy of the electron. These considerations show that for vanadium (the metal studied in the present work) the IA is expected to be valid if gamma rays of energy  $E_\gamma = 60$  keV (e.g. from  $^{241}\text{Am}$ ) or higher are used. We have, therefore, performed the present calculations (Chapters 5 and 6) within the framework of IA. We shall now give a brief description of the experimental method.

The basic idea in the experimental measurement of a CP is to measure the energy spectrum of the photons Compton scattered at a fixed angle  $\phi \sim 170^\circ$  (Fig. 1.1). Until recently X-rays (e.g. the 17.4 keV radiation of the Mo- $K_\alpha$  X-rays or the 22.2 keV radiation from the Ag- $K_\alpha$  X-rays) were used as the primary incident radiation. The details of the X-ray Compton spectrometer are described by Cooper [1]. The use of X-rays, however, involved the following serious disadvantages:

(i) The X-ray sources emitted radiation which has a doublet (i.e.  $K_{\alpha I} - \alpha_{II}$ ) structure riding on a continuous bremsstrahlung radiation. The primary incident radiation is thus not monochromatic. (ii) The wavelength analysis of the scattered radiation is usually done by employing a  $\theta_B:2\theta_B$  Bragg diffraction measurement and this involves a slow point-by-point scan. This amounted to long counting periods typically of the order of several weeks. (iii) At the X-ray energies (typically  $< 20$  keV) the photoelectric absorption cross section is higher than the Compton scattering cross section and the useful (signal) counting rate is reduced. Secondly the validity of the IA which goes as  $(E_B/E_R)^2$  becomes poor with X-rays if a scatterer with high  $Z$  is used. This restriction limited the use of X-rays to those elements which have  $Z \leq 20$ .

These difficulties were considerably minimised when nuclear gamma rays were introduced as the primary incident radiation to study Compton profiles. Felsteiner et al. [8]

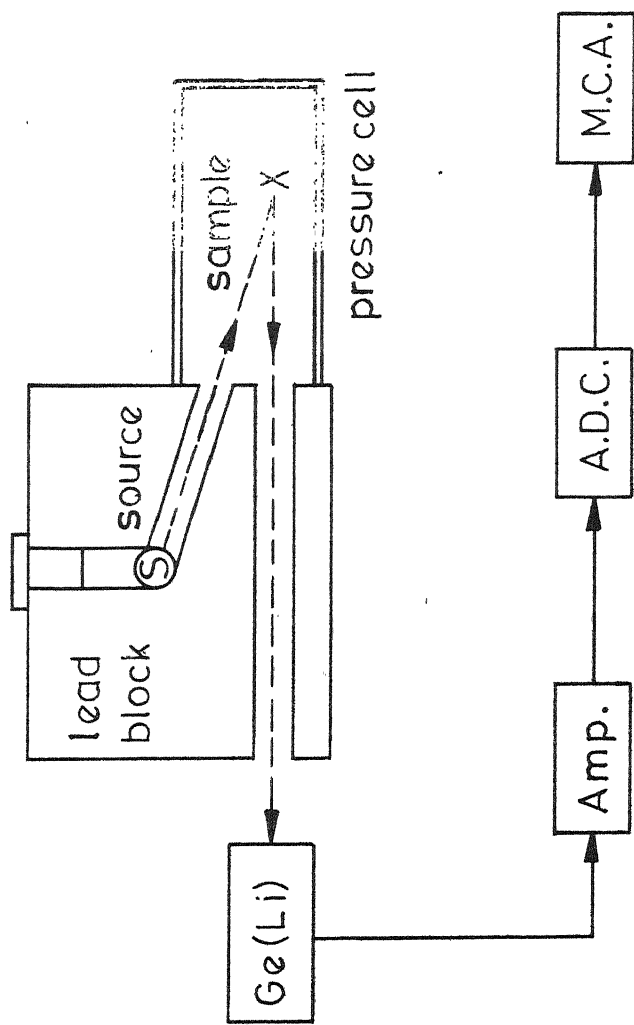


Fig. 1. : schematic diagram of the experimental set-up for Compton profile measurement.

used the 59.57 keV gamma rays from the radioisotope  $^{241}\text{Am}$  while Eisenberger and Reed [9] used the 159.0 keV gamma rays from  $^{123\text{m}}\text{Te}$ . The Compton scattering experiments carried out nowadays use nuclear gamma rays from  $^{241}\text{Am}$  or  $^{123\text{m}}\text{Te}$  or some other suitable radioisotope [3] and employ a solid state detector (e.g. Ge(Li) detector) with the associated nuclear electronics to record the Compton profile data (Fig. 1.4). The main advantages of using nuclear gamma rays are their monochromatic nature, their high energy (which allows measurements with high Z scatterers within the IA) and higher counting rates (mainly because of the use of a solid state detector which allows a simultaneous recording of different scattered energies). The details of the gamma ray Compton scattering spectrometer, design of the experiment, processing of data and calculation of errors has been discussed in the literature [2,3,9].

It may be pointed out that recently the synchrotron radiation has been used for the Compton profile studies [2,3]. However, these preliminary experiments only indicate the feasibility of such studies and more work is necessary before the synchrotron radiation becomes a routine source of the primary radiation.

One important correction to be applied to the Compton profile data arises from the possibility of multiple scattering in the sample. The effect of multiple scattering on the Compton

profile is to reduce the intensity  $J(0)$  at  $q=0$  and to broaden the profile [3]. A correction for the multiple scattering using a Monte Carlo method has been suggested [3,10]. Accurate Compton profile measurements require a choice of optimum thickness of the sample and proper correction to the data collected.

### 1.3 Some Other Experimental Methods for the Determination of EMD

#### 1.3.1 Introduction

In this section we shall briefly outline three other important experimental methods employed for the determination of the EMD. These methods have been described and compared in detail in the literature [11-15]. Our objective here is to provide a brief introduction to these methods for the sake of completeness.

#### 1.3.2 Positron Annihilation

Upon entering a material medium positrons lose their energy by ionization and excitation and become thermalised in a time ( $\sim 10^{-12}$  sec) which is less than the lifetime of positrons ( $\sim 10^{-10}$  sec or longer). Let us consider the case of metals in which such thermalised positrons annihilate with the electrons mostly in a singlet ( $^1S_0$ ) state with a lifetime  $\tau \sim 10^{-10}$  sec or higher. Such an annihilation is accompanied by the emission of two photons. The lifetime of the positron



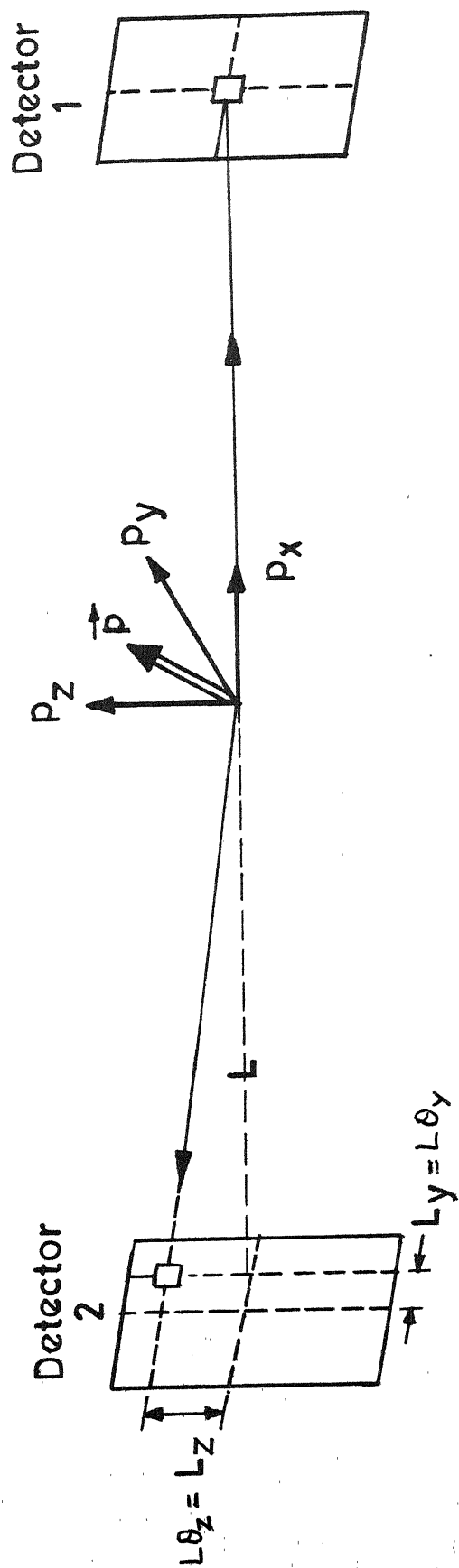


Fig. 1.5 : Schematic diagram of the experimental set-up for ACPAK measurement.

together with the direction of emission (or momentum) and energies of the annihilation photons carry information about the positron-electron state prior to annihilation. The finite momentum (in the centre-of-mass frame) of the positron-electron pair arises almost entirely out of the electron momentum (the positron being thermalised gives  $k_+ \approx 0$ ) and gives rise to the photon pair momentum  $\vec{p}$ . The finite value of  $\vec{p}$  manifests itself in two ways. The transverse component  $p_\perp$  (perpendicular to the direction of emission of the photons) gives rise to a deviation from collinearity in the path of the annihilation photons. If  $p_\perp = 0$ , the two photons are emitted exactly at  $180^\circ$  apart, but if  $p_\perp \neq 0$  the two photons deviate from collinearity such that  $\theta_z = p_z/mc$  and  $\theta_y = p_y/mc$  (Fig. 1.5). For the values of  $\vec{p}$  encountered, these angles  $\theta_z$  and  $\theta_y$  are of the order of a milliradian (one milliradian corresponds to a momentum of  $mc \times 10^{-3}$  or 0.137 atomic momentum units).

The longitudinal component  $p_\parallel$  (parallel to the direction of emission of the photons) is responsible for a change in the energy of the annihilation radiation according to the relation

$$E_\gamma = mc^2 + \frac{p^2}{8m} \pm \frac{cp_\parallel}{2} \quad (1.10)$$

Two experimental methods based on these two effects are used to study EMD by the positron annihilation method. In the first method, called the angular correlation of positron

annihilation radiation (ACPAR), one determines the angular distribution of the coincident counting rate  $N$  as a function of the angles  $\theta_z$  and  $\theta_y$ . If  $\theta_y$  is left undetermined (i.e., the detectors have a long dimension along the  $y$ -axis in the form of a long slit so that  $\theta_y \gg \theta_z$ ) one measures the  $N(\theta_z)$  curve alone and such a geometry is called the long slit geometry [12]. In an actual experiment the source of positrons is several millicuries of the radioisotope  $^{22}\text{Na}$  or  $^{64}\text{Cu}$  (which emits positrons of low energy  $< 400$  keV). The measured coincidence counting rate  $N(p_z = mc \theta_z)$  is related to the EMD,  $\rho(\vec{p})$ , through the relation

$$N(p_z) = \int_{-\infty}^{+\infty} \int \rho(\vec{p}) dp_x dp_y \quad (1.11)$$

which is same as the relation [Eq. (1.9)] between the CP,  $J(q)$  and the EMD,  $\rho(\vec{p})$ . The momentum resolution obtained by the long-slit geometry is of the order of 0.07 a.u. whereas the corresponding figure for photon Compton scattering is 0.4 a.u.

Recently the Brandeis group [3,16] has developed a multi-counter two-dimensional angular correlation apparatus with which  $N(p_y, p_z)$  curves can be measured. Their apparatus consists of a (32 x 32) matrix of rectangular NaI(Tl) counters. Such a two-dimensional curve  $N(p_y, p_z)$  measures a line integral of the EMD through the relation

$$N(p_y, p_z) = \int_{-\infty}^{+\infty} \rho(\vec{p}) dp_x \quad (1.12)$$

As compared to the long slit geometries the two-dimensional ACPAR curves provide a greater wealth of information. Various other geometries have been used in designing an ACPAR measurement and these are described in the literature [11,12].

Although the positron annihilation experiments offer a better momentum resolution when compared to photon Compton scattering and a choice of different geometries, they suffer from two limitations. Firstly, the crystalline samples used for positron annihilation measurements must be free from defects otherwise these defects can trap positrons and alter the angular correlation curves [11,17]. Secondly, the theoretical interpretation of the positron results requires a knowledge of the positron wavefunction and positron-many electron correlation effects. In spite of these limitations the experimental data obtained by the positron annihilation studies of transition metals have compared well with the results of bandstructure calculation of the EMD [18].

### 1.3.3 Electron Compton Scattering

Inelastic scattering of fast (20-50 keV) electrons is termed as electron Compton scattering or electron impact spectroscopy. Although such measurements were carried out in the 1930's this technique lay dormant until about 10 years ago when the new developments in the theory and experiment helped to revive this field [13,19]. In principle,

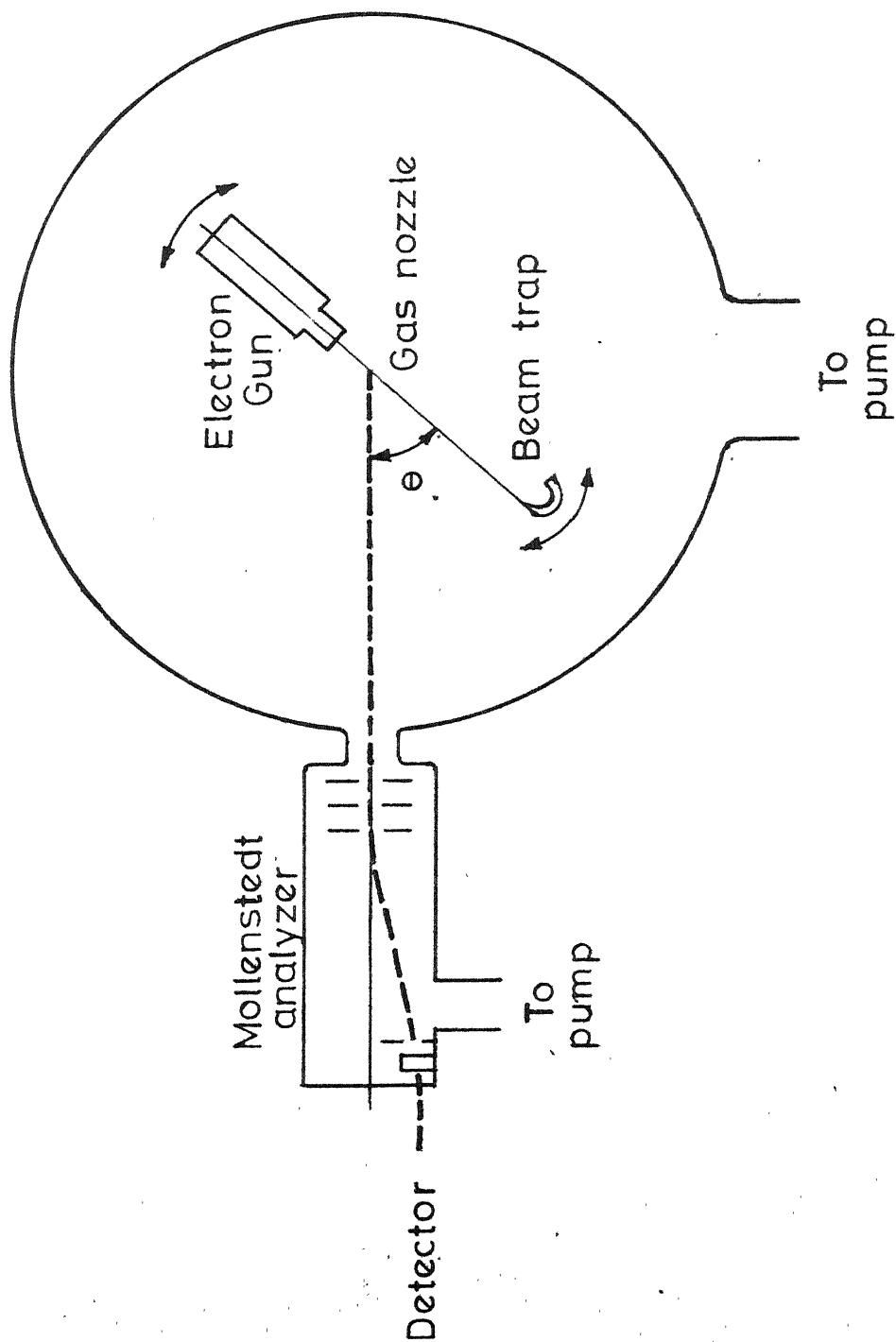


Fig. 1.6 : Schematic diagram of the experimental set-up for electron Compton scattering.

the experimental method to study the electron Compton scattering from gaseous samples consists of shooting a collimated electron beam (incident energies of the order of 20-50 keV) at the gaseous sample which is injected in the form of a narrow jet in an evacuated chamber (Fig. 1.6). The scattered electrons are energy-analyzed by a Mollenstedt velocity analyzer and counted by a Si solid state detector to obtain the  $I(E)$  versus  $E$  curve (or the electron Compton profile). The scattering angle can be changed from  $0^\circ$  to  $140^\circ$  by rotation. In such a measurement of the EMD, a resolution of 2-5 eV (equivalent to a momentum resolution of 0.01-0.03 a.u.) is usually obtained. In addition to such good momentum resolution, the counting rates are quite high and the final accuracy is of the order of 1% or so.

There are some theoretical assumptions and corrections which restrict the theoretical interpretation of the data obtained by electron Compton scattering [15,19]. The first basic approximation consists in applying the Born approximation to describe the inelastic scattering process. This approximation is certainly valid for small atoms and molecules. Secondly, the binary encounter approximation is used to calculate the differential cross section. The latter approximation assumes the final state of the electron to be taken as a plane wave and is analogous to the IA used in the photon Compton scattering. Next the cross section calculated using

the above approximations has to be corrected for (a) the relativistic effects and (b) the exchange and interference between the incident and scattered electrons.

It has been shown that within the above framework the differential cross section can be written [13] as

$$\frac{d^2\sigma}{d\Omega dE} = \frac{2k_s [1 - E(1 - \beta^2)^{1/2}/2c^2]}{k_i(1 - \beta^2)[K^2 - E^2/4c^2]^2} F_{ex} J(q) \quad (1.13)$$

where  $\vec{k}_i$  and  $\vec{k}_s$  describe the wavevectors of the incident and scattered electrons,  $E$  is the energy loss on scattering,  $\vec{K}$  is the momentum transfer,  $\vec{K} = \vec{k}_i - \vec{k}_s$  and  $q = [E(1 - E/4c^2) - K^2]$ . The function  $F_{ex}$  takes into account the exchange and interference corrections and

$$F_{ex} \approx 1 - \frac{K^2}{k_s^2} + \frac{K^4}{k_s^4} + \frac{2K^4 q^2}{k_s^6} \quad (1.14)$$

while  $J(q)$  is the Compton profile which, for the case of isotropic EMD  $\langle \rho(p) \rangle$ , assumes the following form

$$J(q) = 2\pi \int_{|q|}^{\infty} \langle \rho(p) \rangle p dp \quad (1.15)$$

Uptill now the usefulness of the electron Compton scattering technique for the study of EMD has been restricted to the gaseous samples of the elements like H and He. In terms of the momentum resolution, statistical accuracy and counting rates available, this method is definitely superior to other methods for studying gaseous samples of low  $Z$ . However, this

method has serious experimental and theoretical difficulties for extending it to heavier gases (e.g. Kr, Xe etc.) or to the bulk (or solid) samples (where the multiple scattering of electrons can be a serious disadvantage).

#### 1.3.4 (e,2e) Method

In the photon (and electron) Compton scattering experiments described earlier the information carried by the recoil electron is lost because only the energy of the scattered photon (or electron) is analyzed. In the so-called (e,2e) method the energy and momentum of the incident electron as well as the knocked out electron (both detected in coincidence) are determined. The experimental details and the theoretical framework of the (e,2e) method are reviewed by McCarthy and Weigold [15]. The basic geometry of the (e,2e) method is shown in Fig. 1.7. The incident electron having momentum  $\vec{k}_0$  and energy  $E_0$  knocks out an electron from the target. The two electrons (scattered and knocked out) coming out with momenta  $\vec{k}_A$  and  $\vec{k}_B$  and having energies  $E_A$  and  $E_B$  respectively are detected in coincidence and the coincidence counting rate can be measured as a function of the parameters  $E_0$ ,  $E_A$ ,  $E_B$ ,  $\theta$  and  $\phi$  (Fig. 1.7). The results of the measurements are analyzed in the framework of the 'distorted wave off-shell impulse approximation' [15] in which one uses slightly distorted plane waves to describe the incoming and the two outgoing electrons and the distortion is calculated within



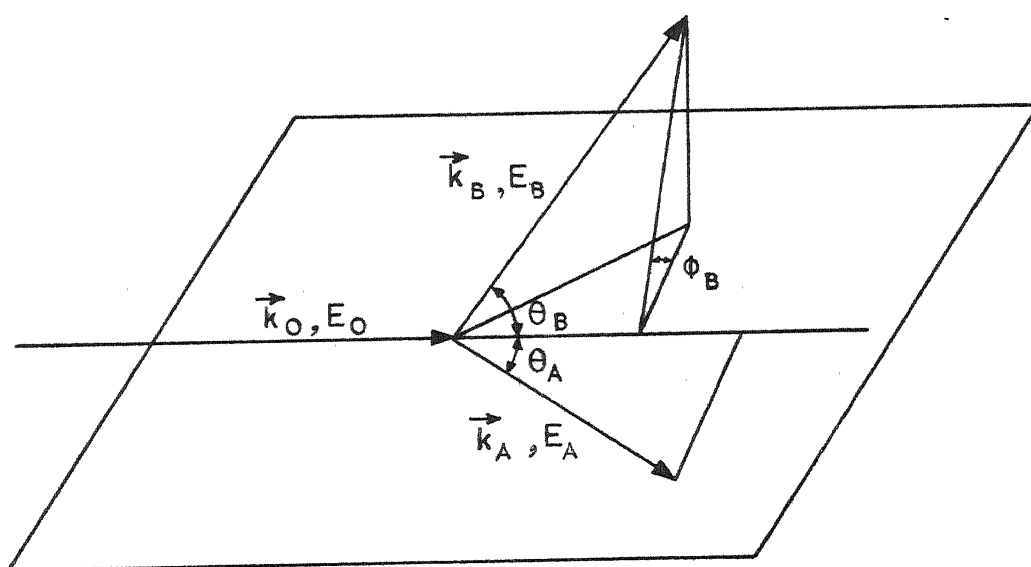


Fig. 1.7 :  $(e, 2e)$  scattering.

the eikonal approximation. The differential cross section is then calculated [13] from

$$\begin{aligned}
 \frac{d^3\sigma}{d\Omega_A d\Omega_B dE_A} &= N b_{nl}^2 \left( \frac{2me^2}{\hbar^2} \right) \frac{2\pi\eta}{[\exp(2\pi\eta)-1]} \\
 &\times \left\{ \frac{1}{|\vec{k}-\vec{k}'|^4} + \frac{1}{|\vec{k}+\vec{k}'|^4} - \frac{1}{|\vec{k}-\vec{k}'|^2 |\vec{k}+\vec{k}'|^2} \right. \\
 &\times \cos \left[ \eta \ln \left( \frac{|\vec{k}+\vec{k}'|^2}{|\vec{k}-\vec{k}'|^2} \right) \right] \left. \right\} |x_{nl}(\vec{K})|^2
 \end{aligned} \tag{1.16}$$

where  $b_{nl}$  is the spectroscopic factor and

$$N = \exp [-(k_O \gamma_O + k_A \gamma_A + k_B \gamma_B) R_N]$$

$$\eta = me^2 / \hbar^2 k'$$

$$\vec{k} = (\vec{K}_O - \vec{K}), \quad \vec{k}' = (\vec{K}_A - \vec{K}_B)$$

$$\vec{K} = \vec{K}_O - \vec{K}_A - \vec{K}_B$$

$$\vec{K}_i = (1 + \beta + i\gamma) \vec{k}_i, \quad i = O, A, B$$

and the subscripts O, A, B stand for the incoming and two outgoing electrons.

The cross section (1.16) is thus seen to be directly proportional to the EMD itself and not to a single (or double) integral of the EMD as in the previous methods. Apart from this major advantage, another advantage of this technique is that one can determine the EMD,  $\rho_{nl}(\vec{p})$ , due to each individual

orbital (nl). In spite of these advantages, this method has so far found limited applications because of the following experimental difficulties: (a) only gaseous samples can be studied and therefore only isotropic (or radial) momentum distributions can be determined. (b) Owing to the low counting rates from the core orbitals they cannot be studied and only the outer electron states can be examined. In view of these difficulties the (e,2e) method has been so far applied only to gases and thin films.

#### 1.3.5 Comparison of the Various Experimental Methods for the Determination of the EMD

The main advantages as well as the limitations of each of the above four methods have already been pointed out in the previous discussion. In Table 1.1 we provide a general comparison of the four methods described above. It is now well recognised that in spite of its moderate resolution, the technique of photon Compton scattering is the best single method suited to study the effect of electron wavefunctions on the EMD in a variety of substances. The positron annihilation method offers the advantages of superior momentum resolution, choice of geometry, possibility of measuring the two-dimensional ACPAR curves etc. but it is restricted in the theoretical interpretation available. The positron annihilation technique is more suited as a method to investigate the Fermi surface of metals and metal alloys. The other two

Table 1.1: Comparison of different methods

	Photon Compton Scattering	Positron annihilation	Electron Compton Scattering	(e, 2e)
Basic process	Inelastic scattering of photons	Annihilation of $e^+e^-$	Inelastic scattering of electrons	Knock out of an electron by an incident electron
Typical Momentum Resolution(a.u.)	0.2-0.5	0.07	0.01	0.1
Data collection efficiency	Very high	Moderate	Very high for small K	Moderate
EMD information provided	$J(p_z) = \iint \rho(\vec{p}) dp_x dp_y$	$N(p_z) = \iint \rho(\vec{p}) dp_x dp_y$ or $N(p_y, p_z) = \int \rho(\vec{p}) dp_x$	$J(p_z) = \iint \rho(\vec{p}) dp_x dp_y$	$\rho_n$ separately for each orbital (nl)
Restriction on samples	No restriction although better for low Z, optimum thickness necessary to avoid multiple scattering	No restrictions on Z. Samples should have minimum number of defects to avoid positron trapping.	Gases, low Z	Gases, low binding energies
Other difficulties for theoretical interpretation	Corrections to data necessary, esp. multiple scattering	Need to know positron wave function, $e^+e^-$ many body effects	Solids and liquids not studied so far. Theoretical approximations important.	Solids and liquids not studied so far. Theoretical approximations important.

methods, electron Compton scattering and  $(e,2e)$  scattering have not yet proved their complete potential but it is doubtful whether they can ever be used to study the bulk (or solid) samples. The best approach seems to study a particular sample both by photon Compton scattering and positron annihilation and combine these results to determine the EMD in the system.

#### 1.4 Theoretical Calculation of the Electron Momentum Density

##### 1.4.1 Choice of the Electron Wavefunction

The first step in the calculation of the EMD,  $\rho(\vec{p})$ , is to choose the electron wavefunction appropriate for the system under study. As a crude approximation one could use a free-electron model or free atom wavefunctions [3]. However, it has now been demonstrated [3] that for metals it is essential to make a bandstructure calculation employing one of the standard (e.g. OPW, APW, KKR or other) methods. For other solids (e.g. LiF) one may use a method based on the linear combination of atomic orbitals [LCAO]. In the case of the EMD for positron annihilation it is required to know the positron wavefunction as well. The positron wavefunction is usually determined by the Wigner-Seitz method or the plane-wave expansion method or by the positron pseudopotential method.

### 1.4.2 Electron-electron Correlation

Usually the bandstructure calculations of the electron wavefunctions are performed within the independent particle model. In this model the electron-electron interactions are reduced to single particle potentials. The electron-electron interaction arising from the antisymmetry requirement of the electron wavefunction is termed the exchange correlation part and that arising from the Coulombic repulsion between the electrons is called the pure electron-electron correlation. It has been shown [3] that the electron correlations can significantly affect the EMD and the CP curves for the simple [e.g. Li, Na, Al, ...] metals. In the case of transition metals one usually neglects the pure electron-electron correlation effect. In the present calculation we have taken into account the exchange correlation explicitly and neglected the pure electron correlation.

### 1.4.3 Theoretical Models

In the following sections we shall briefly outline the theoretical methods for calculating the EMD for a free-electron gas, free atoms and metallic solids.

#### (A) Free electron gas

The EMD,  $\rho(\vec{p})$ , for a non-interacting electron gas is isotropic in nature (i.e.  $\rho(\vec{p}) = \langle \rho(p) \rangle$ ) and at  $T=0^\circ\text{K}$  it assumes a constant value up to  $p \leq p_F$  (where  $p_F$  is the Fermi

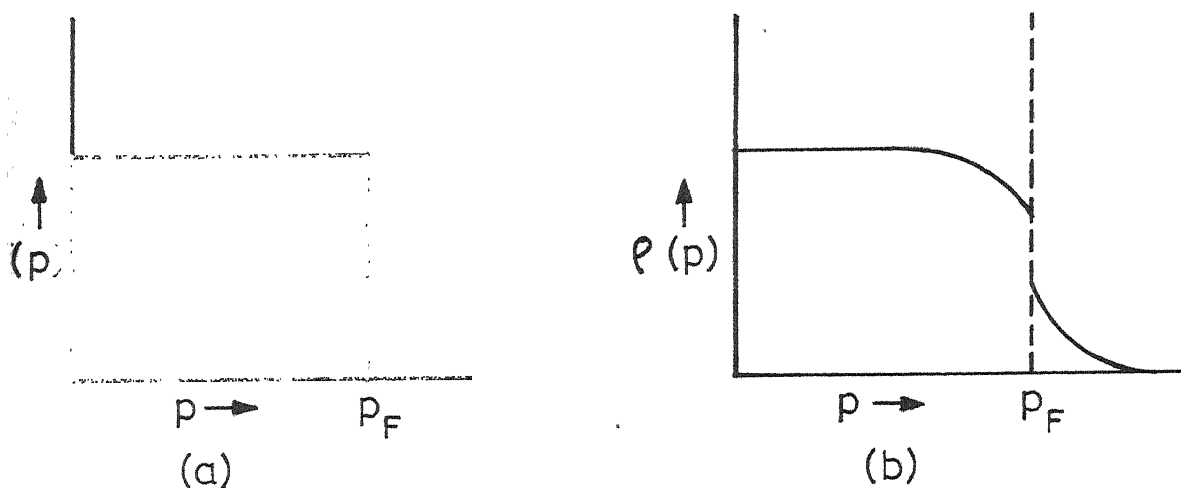


Fig. 1.8: Fermi distribution at  $T = 0$  °K of  
 (a) free electron gas (b) interacting electron gas.

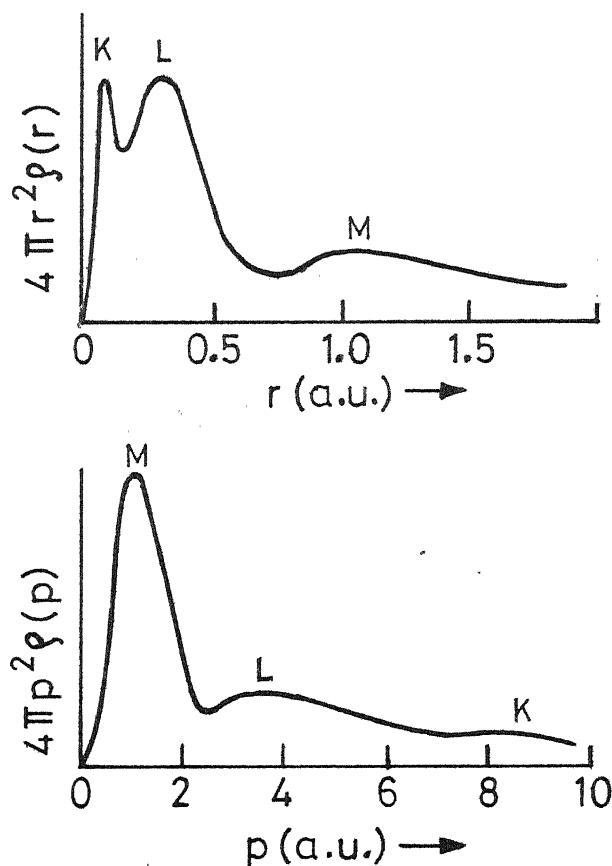


Fig. 1.9: Reciprocity of the radial charge density distribution and momentum density distribution for the different electronic orbitals of argon.

momentum) and it drops to zero in a discontinuous manner (Fig. 1.8a). The corresponding Compton profile is parabolic in nature and is given by

$$\begin{aligned} J(p_Z) &= 2\pi (p_F^2 - p_Z^2) \text{ for } p_Z \leq p_F \\ &= 0 \quad \text{for } p_Z > p_F \end{aligned} \quad (1.17)$$

The effect of taking the electron-electron correlations into account (i.e. interacting electron gas) is to transfer a part of the occupied states (lying just below  $p=p_F$ ) to the higher momentum region (just above  $p = p_F$ ) as shown in Fig. 1.8b. This results in a smoothening of the discontinuity in the EMD,  $\rho(\vec{p})$ , at  $p = p_F$  and an appearance of a tail beyond it.

#### (B) The free atom

To gain an insight into the EMD contributions by atomic orbitals we have compared in Fig. 1.9 the radial charge distribution in argon in the position ( $\vec{r}$ ) space and the EMD in the momentum space. The reciprocity between the position and momentum space (i.e. a narrow function in the  $\vec{r}$ -space becomes a broad function in the  $\vec{p}$ -space and vice versa) is brought out by these distributions. Thus, for example, the EMD for the M-shell electrons appears sharp although its position charge density appears diffuse.



While comparing the experimental Compton profile data with the band theoretical results one needs to know the contribution to the EMD from the inner core orbitals which are free-atom-like. This enables one to compare only the 'band-electron' profiles. The EMD due to the atomic orbital (nl) is assumed to be isotropic and is usually calculated from the formula

$$\rho_{nl}(p) = \frac{2(2l+1)}{4\pi} \left(\frac{2}{\pi}\right) \left| \int_0^\infty dr r^2 P_{nl}(r) j_l(pr) \right|^2 \quad (1.18)$$

where  $(P_{nl}/r)$  are the atomic wavefunctions (say, for example, those calculated by Herman and Skillman [20]). Recently, Biggs et al. [21] have published Tables of theoretical (Hartree-Fock) Compton profiles for the atomic orbitals of various elements. The various aspects of the atomic Compton profiles are discussed by Menzelsohn and Smith [22].

### (c) Solids

In a solid, the Compton profile is sensitive to the EMD (and the wavefunctions) of the outer electrons and thus provides a valuable technique to study the solids where these outer (or conduction) electrons are responsible for the bonding. The discussion of the EMD in solids can be divided according to the type of solid (e.g. metal, alloy, metal compound, covalent crystal, ionic crystal etc.). In an excellent review article Berggren et al. [23] have reviewed

the theoretical and experimental studies of the Compton profiles of solids. Their review neatly summarises the situation regarding the 3d transition metals, the area of our present interest. The free-electron gas or a free-atom model is known to give a poor description of the EMD and CP of 3d transition metals primarily because of the complicated effects of the (4s+3d) electrons. The disagreement occurs mainly in the low momentum region where the major contributions come from the outermost electrons.

Berggren [24] in 1972 applied the renormalized-free-atom (RFA) model [25] for the calculation of the EMD and CP in V. In the RFA model one proceeds as follows. The free-atom (e.g. Hartree-Fock) wavefunctions are truncated at the radius  $r_{WS}$  of the Wigner-Seitz (WS) sphere and then renormalized to unity within the WS sphere. Such a procedure takes into account the fact that in a solid the electron wavefunctions are contained in a cell. It has been shown [25] that such RFA wavefunctions provide a good estimate of some of the band-structure properties of the 3d transition metals. The extension of the RFA model for the calculation of the EMD and CP is described by Berggren [24] and it has been shown to give satisfactory agreement with experiment for the transition metals like V [23], Ti [23], Fe [25], Ni [26] and Cu [26]. In spite of its success the main limitation of the RFA model is that it can provide only a gross description of the CP for

the polycrystalline samples but cannot provide a proper description of the finer features like the anisotropy in the directional profiles (from single crystals). In the transition metals (particularly for a metal like V for which the 3d band is incompletely filled) the topology of the Fermi surface and the complicated nature of the 3d wavefunctions is reflected in the anisotropy in the EMD and CP. It is, therefore, essential to carry out the calculations of the EMD with the help of some standard bandstructure methods.

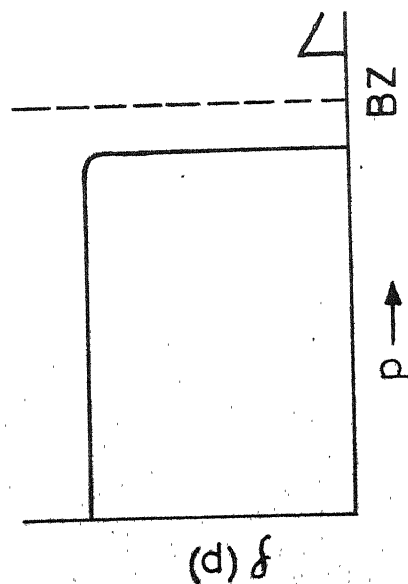
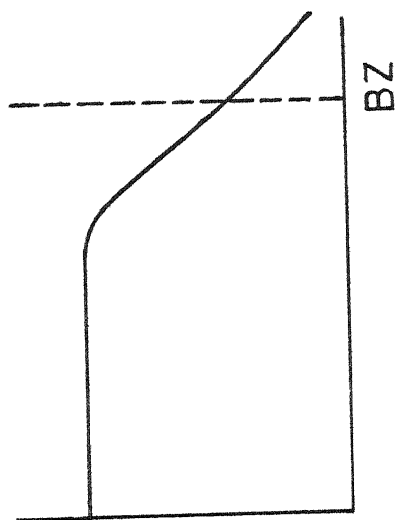
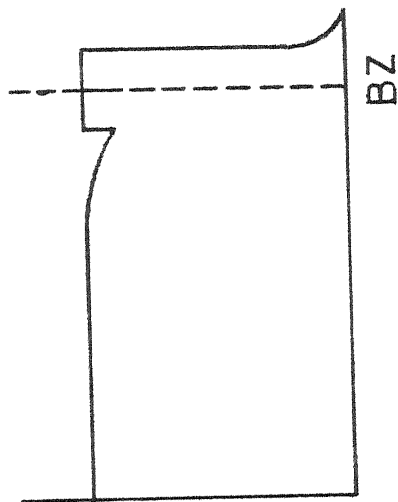
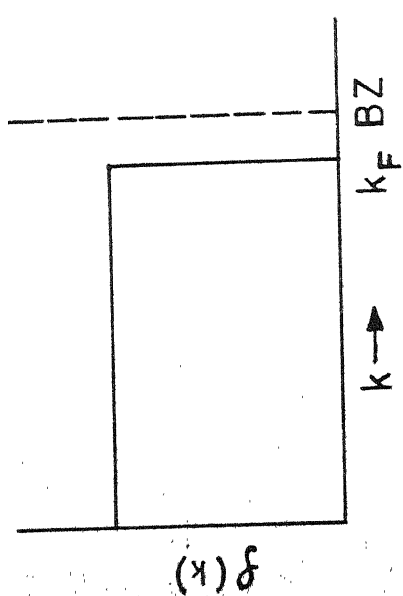
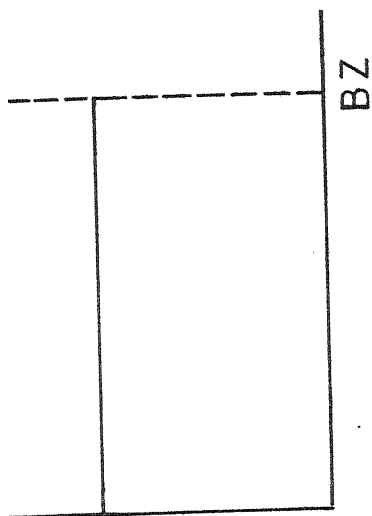
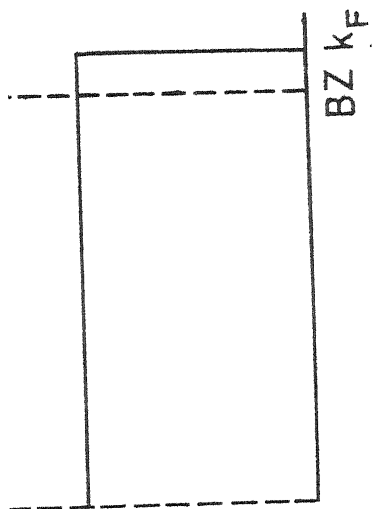
As mentioned above, the bandstructure calculations of the EMD in a solid are usually carried out in the framework of independent particle model (IPM) in which the expression for the EMD  $\rho(\vec{p})$  is expressed as

$$\rho(\vec{p}) = \sum_{j, \vec{k}, i}^{\text{occ}} f(\vec{k}, j) |A_j(\vec{k}, \vec{p})|^2 \delta(\vec{p} - \vec{k} - \vec{K}_i) \quad (1.19)$$

In Eq. (1.19)  $f(\vec{k}, j)$  is the Fermi-Dirac distribution function for an electron in state  $\vec{k}$  and band  $j$  such that at  $T = 0^\circ\text{K}$ ,  $f(\vec{k}, j) = 1$  if the state  $(\vec{k}, j)$  is occupied and  $f(\vec{k}, j) = 0$  if the state  $(\vec{k}, j)$  is unoccupied. The set  $\{\vec{K}_i\}$  is the set of reciprocal lattice vectors and

$$A_j(\vec{k}, \vec{p}) = \int_{\text{cell}} e^{-i\vec{p} \cdot \vec{r}} \psi_{\vec{k}, j}(\vec{r}) d\vec{r} \quad (1.20)$$

In Eq. (1.19) the summations over  $j$ ,  $\vec{k}$  and  $\vec{K}_i$  take into account the sum over occupied states and the normal ( $\vec{K}_i = 0$  and  $\vec{p} = \vec{k}$ ) as well as the Umklapp ( $\vec{K}_i \neq 0$ ,  $\vec{p} = \vec{k} + \vec{K}_i$ ) processes



(a)

(b)

(c)

(d)

(e)

(f)

FIG. 1.10 : The BMD in p-space,  $f(p)$ , obtained from the BMD in the first BZ,  $f(k)$ , through overlap processes for different positions of the Fermi level (one dimensional case).

thus bringing out the difference between the real physical momentum  $\vec{p}$  and the crystal momentum  $\vec{k}$ .

An electron in a state  $\vec{k}$ , thus contributes not only at  $\vec{p} = \vec{k}$  but also at other  $\vec{p} = \vec{k} + \vec{K}_i$  with an amplitude  $A_j(\vec{k}, \vec{p})$ . The importance of the Umklapp ( $K_i \neq 0$ ) coefficients  $A_j(\vec{k}, \vec{p})$  (also termed in the literature as high-momentum-components-HMC - or the high-Fourier-components HFC) can be illustrated by following Berko and Plaskett [27].

For the sake of illustration let us consider the simple case of nearly-free-electrons (NFE) in the one-dimensional model. A comparison of the  $\vec{k}$ - and  $\vec{p}$ -space distributions  $\rho(\vec{k})$  and  $\rho(\vec{p})$  is shown in Fig. 1.10 for the following three cases: (a) Fermi surface lying in the first zone, (b) No Fermi surface;  $\rho(\vec{k})$  distribution touching the boundary of the Brillouin zone (BZ) and (c) Fermi surface in the second band (shown in the extended zone scheme). It is observed from Fig. 1.10 that the breaks in the EMD,  $\rho(\vec{p})$ , occur not only in the first zone ( $K_i=0$ ) but also in the higher ( $K_i \neq 0$ ) zones although with a reduced Umklapp amplitude  $A_j(\vec{k}, \vec{p})$ . In the case of a transition metal the EMD (and hence the CP) is therefore determined by the Fermi surface topology and the  $\vec{k}$ - (and  $\vec{p}$ -) dependence of  $A_j(\vec{k}, \vec{p})$ . There is also an important effect due to the symmetry selection rule [28] which we shall discuss in Chapter 4. These considerations show that in order to understand the basis of the Compton profiles in a

metal, the theoretical results of the EMD have to be carefully examined in terms of its bandstructure and Fermi surface.

### 1.5 Comparison Between Theory and Experiment

There are two possible approaches to compare the experimentally measured Compton profiles with theoretical results. In the first method one starts with the theoretical EMD,  $\rho(\vec{p})$  and obtains the Compton profile  $J(p_z)$  from the following relation:

$$J(p_z) = \iint \rho(\vec{p}) \, dp_x \, dp_y \quad (1.21)$$

The integration involved in (1.21) requires a knowledge of the EMD,  $\rho(\vec{p})$ , at several  $\vec{p}$ -points in the momentum space and therefore involves a large computational effort. An approximate but faster way of computing the integral (1.21) is to expand  $\rho(\vec{p})$  in terms of cubic harmonics. We have followed the latter approach to calculate  $J(p_z)$  and this method would be described in Chapter 5.

Another method consists of unfolding or inverting the EMD,  $\rho(\vec{p})$ , from the experimentally measured set of the directional profiles  $J_{hkl}(p_z)$  (i.e. for a set of  $\{hkl\}$  single crystal directions) through Eq. (1.21). Two such methods have been suggested in the literature by Mijnaerends [29] and Mueller [30]. The results of the 'unfolding' analysis lead to the  $\rho(\vec{p})$  distributions which can then be compared with the

theoretical distributions. These methods of the reconstruction of the EMD are reviewed by Mijnaerends [31].

### 1.6 Motivation Behind the Present Work

It was pointed out earlier that the technique of photon Compton scattering is well-suited for testing the electron wavefunctions via the EMD. For ferromagnetic iron Mijnaerends [32] has compared the EMD obtained by unfolding the experimental positron annihilation data with the theoretical EMD, calculated from the bandstructure of Wood [33] and Wakoh and Yamashita [34]. His results demonstrated that the experimental data support the bandstructure of Fe by Wood [33].

Similar tests can be carried out on other metals, especially those transition metals for which the Fermi level lies among the d bands. The character of the d wavefunctions, which is mainly responsible for the anisotropy in the EMD (and CP) can provide a sensitive test for distinguishing among different bandstructures. One such transition metal is vanadium in which the d bands are incompletely filled. The results of bandstructure and Fermi surface of V (described in detail in Chapter 2) show interesting changes with respect to the different crystal potentials used in the literature. The 5 band electrons from the  $(3d)^n(4s)^{5-n}$  configuration fill up the entire first, most of the second and about half of the third conduction band in V. As a result the Fermi surface (FS)

of V shows a complicated structure and the FS topology (and the bandstructure) is sensitive to the crystal potential and the bandstructure method used in the calculation. We, therefore, thought it interesting to undertake a bandstructure calculation of the EMD in V and to examine the effect on the EMD by changing the crystal potential. Although the Compton profiles of metallic V have been theoretically calculated by Wakoh and Yamashita [35], their work does not give any details of the behaviour of the EMD itself. In the present work we have tried to examine the EMD in terms of the bandstructure and FS effects. In other words we treat the EMD as one more ground-state property (similar to electronic specific heat, susceptibility etc.) predicted from the bandstructure calculations. We have also extended the results for the EMD to obtain the directional Compton profiles and their anisotropies.

The experimental Compton profile data on polycrystalline Ti was analyzed by Berggren et al. [23] in terms of the RFA model and the results were interpreted to show that the electron configuration of Ti is closer to  $(3d)^2(4s)^3$  rather than  $(3d)^3(4s)^1$ . One of the early calculations by Mattheiss [36] has shown that the bandstructure of V changes considerably if the electron configuration is changed from  $(3d)^3(4s)^2$  to  $(3d)^4(4s)^1$ . In order to examine the changes brought in the EMD (as well as in the directional CP curves) by the changes in the outer electron configuration, we have calculated the



EMD using two crystal potentials one for the electron configuration  $(3d)^3(4s)^2$  and other for  $(3d)^4(4s)^1$ . A third type of potential was also used. These details would be discussed in the following chapters.

Recognising the interest in the field of EMD, the International Union of Crystallography formed a Special Commission on Electron Charge, Spin and Momentum Density in 1972. A special project was initiated by this Commission in 1975 to determine the accuracy of the theoretical Compton profiles and X-ray scattering factors for metallic V. The main object in this project has been to compare the results of various theoretical methods and to determine their relative accuracy thus providing the experimentalists a basis for comparison.

Our research group joined this International project and the present work was undertaken with this object in mind. The standard lattice potential of metallic V to be used for this project was prepared by Mijnaarends [37] for the electron configuration  $(3d)^3(4s)^2$ . We decided to extend the scope of this project by calculating the EMD and CP in V for two other crystal potentials besides this standard potential.

Recently the electron structure of the hydrides (and deuterides) of the transition metals have invoked considerable interest. In the metal hydrides the electronic states of the outer or conduction electrons are modified by the dissolved

hydrogen (or deuterium). The technique of photon Compton scattering provides a sensitive method to probe the conduction electron states (via the EMD) of a metal hydride and recently the Compton profiles of hydrides and deuterides of niobium [i.e.  $\text{NbH}_x$  and  $\text{NbD}_x$ ] have been investigated in detail [38]. We have therefore found it interesting to extend our theoretical results on the EMD in pure V to  $\text{VD}_x$  to calculate the EMD and directional Compton profiles in  $\text{VD}_x$ . It is well known that the group VB metals V and Nb have similar bandstructure and Fermi surface topologies. Hence a calculation of the EMD in  $\text{VD}_x$  and its comparison with  $\text{NbD}_x$ , as well as with experiment, can provide valuable information about the electronic structure of transition metal hydrides.

Keeping these objectives in mind we have calculated the bandstructure and EMD in V applying Hubbard's fast approximation scheme for three different types of the crystal potential. Chapter 2 provides a review of the bandstructure and Fermi surface of V as reported in the literature and summarises the motivation behind our work. A brief description of the Hubbard-Mijnarends method of calculating the bandstructure and EMD is given in Chapter 3. The theoretical results of our calculations are presented in Chapter 4 where these results for the EMD are analyzed in terms of the bandstructure and FS. Directional Compton profiles and their anisotropies are

obtained from the EMD and are presented in Chapter 5. The extension of our results to vanadium aceturide ( $VD_x$ ) and the calculation of the directional Compton profiles in  $VD_x$  are discussed in Chapter 6.

## REFERENCES

1. M. Cooper, Adv. Phys. 20, 453 (1971).
2. M. J. Cooper, Contemp. Phys. 18, 489 (1977).
3. B. Williams, ed. Compton Scattering, McGraw-Hill, London, 1977.
4. I. R. Epstein, MTP International Review of Science, Physical Chemistry, Series II, Theoretical Chemistry, 145 (1975).
5. P. M. Platzman and N. Tzoar, Phys. Rev. 129, A410 (1965).
6. P. Eisenberger and P. M. Platzman, Phys. Rev. A2, 415 (1970).
7. R. Currat, P. D. DeCicco and R. J. Weiss, Phys. Rev. B4, 4256 (1971).
8. J. Felsteiner, R. Fox, and S. Kahana, Phys. Lett. A33, 442 (1970); Solid State Commun. 9, 61 (1971).
9. P. Eisenberger and W. A. Reed, Phys. Rev. A5, 2085 (1972).
10. V. Halonen, B. G. Williams and T. Paakkari, Phys. Fenn. 10, 107 (1975); A. C. Tanner and I. R. Epstein, Phys. Rev. A14, 328 (1976).
11. R. N. West, Adv. Phys. 22, 263 (1973).
12. R. M. Singru, Phys. Status Solidi (a) 30, 11 (1975).
13. W. A. Reed, Acta Crystallogr. A32, 576 (1976).
14. B. G. Williams, Physica Scripta 15, 92 (1977).
15. J. E. McCarthy and E. Weigold, Phys. Reports 27C, 275 (1976).
16. S. Berko and J. Mader, Appl. Phys. 5, 287 (1975).  
S. Berko, M. Haghgoie and J. J. Mader, Phys. Lett. A63, 335 (1977).
17. W. Triftshäuser, in Festkörperprobleme (Advances in Solid State Physics), Volume XV, ed. H. J. Queisser, Pergamon/Vieweg, Braunschweig, 1975, p. 381.

18. P. E. Mijnaerends, 'Progress in Positron Fermi Surface and Momentum Density Work', Report RCM-76-089, Reactor Centrum Nederland, Petten (N.H.), The Netherlands, 1976 (Unpublished).
19. R. A. Bonham and H. Fink, High Energy Electron Scattering, Van Nostrand Reinhold Co., New York, 1974.
20. F. Herman and S. Skillman, Atomic Structure Calculations, Prentice-Hall, Englewood Cliffs, New Jersey, 1963.
21. F. Biggs, L. B. Mendelsohn and J. B. Mann, Atomic Data and Nuclear Data Tables 16, 201 (1975).
22. L. Mendelsohn and V. H. Smith in Compton Scattering, ed. B. Williams, McGraw-Hill Inc. London, 1977, p. 102.
23. K.-F. Berggren, S. Manninen, T. Paakkari, O. Aikala and K. Hansikka, in Compton Scattering, ed. B. Williams, McGraw-Hill Inc. London, 1977. p. 139.
24. K.-F. Berggren, Phys. Rev. B6, 2156 (1972).
25. L. Hodges, R. E. Watson and H. Ehrenreich, Phys. Rev. B5, 3953 (1972).
26. D. G. Kanhere and R. M. Singru, J. Phys. F5, 1146 (1975).
27. S. Berko and J. S. Plaskett, Phys. Rev. 112, 1877 (1958).
28. P. E. Mijnaerends, Physica 63, 235 (1973).
29. P. E. Mijnaerends, Phys. Rev. 160, 512 (1967).
30. F. M. Mueller, Phys. Rev. B15, 3039 (1977).
31. P. E. Mijnaerends in Compton Scattering, ed. B. Williams, McGraw-Hill Inc. London (1977), p. 323.
32. P. E. Mijnaerends, Physica 63, 248 (1973).
33. J. H. Wood, Phys. Rev. 126, 517 (1962).
34. S. Wakoh and J. Yamashita, J. Phys. Soc. Jap. 21, 1712 (1966).
35. S. Wakoh and J. Yamashita, J. Phys. Soc. Jap. 35, 1406 (1973); S. Wakoh, Y. Kubo and J. Yamashita, J. Phys. Soc. Jap. 40, 1043 (1976).

36. L. F. Mattheiss, Phys. Rev. 134, A970 (1964).
37. P. L. Mijnaerends, 'Construction of a Muffin-Tin Potential for Metallic Vanadium', Report RCN-76-010, Reactor Centrum Nederland, Petten, (N.H.), The Netherlands, 1976 (Unpublished).
38. P. Pattison, M. Cooper, M. Eolt, J. R. Schneider and W. Stump, Z. Phys. B27, 205 (1977); M. G. Alexandropoulos and W. Reed, Phys. Rev. B15, 1790 (1977); R. Lässer and B. Lengeler (Private communication).

## Chapter 2

### REVIEW OF BANDSTRUCTURE AND FERMI SURFACE STUDIES OF VANADIUM

#### 2.1 Introduction

There has been considerable interest in the electronic structure of the vanadium group (i.e. the VB isoelectronic group consisting of vanadium, niobium and tantalum) of metals. In all these three metals the outer (or conduction) electrons fill up the outermost d-states (e.g. 3d for V) only partially and the Fermi level straddles the d bands thus resulting in a complicated topology of the Fermi surface (FS). This has resulted in a number of theoretical calculations of the bandstructure and experimental investigations of the Fermi surface of the group VB metals. Before we review these theoretical and experimental studies for V (the metal of our interest) we shall outline some features of the bandstructure calculations which are of interest in the discussion of our results (Chapter 4).

The calculation of the energy levels of the electrons in a solid is based on the basic assumption (involving the Born-Oppenheimer approximation) that the electronic and

nuclear motions can be described separately and that the effect of the nuclear motion on the electrons is small and negligible. As atoms are brought together to form a crystalline solid, the potential assumes the periodicity of the crystal lattice. The calculations are carried out in the independent particle model (IPM) in which one limits the calculation to the states of a single electron in a rigid, infinite and periodic lattice. The results for the many-electron system are then derived by treating the electrons as a system of non-interacting particles in this periodic potential and applying the Fermi-Dirac statistics to accommodate them in these states. Many bulk properties of the solids can be fairly successfully described in the framework of the above model.

A critical discussion of the various approximate methods used to solve the bandstructure problem is beyond the scope of this work. Excellent review article [1] and texts [2-5] exist in the literature on this subject. In the following we shall outline only those features which are relevant for the discussion of our results. In this work, unless otherwise stated we shall follow the Hartree system of atomic units in which  $\hbar = 1$ ,  $m = 1$ ,  $e = 1$  and  $c = 137.036$ .

The Hartree-Fock-Slater equations

$$\begin{aligned} H \psi(\vec{r}) &= \left[ -\frac{\nabla^2}{2} + V_c(\vec{r}) + V_x(\vec{r}) \right] \psi(\vec{r}) \\ &= \left[ -\frac{\nabla^2}{2} + V(\vec{r}) \right] \psi(\vec{r}) = E \psi(\vec{r}) \end{aligned} \quad (2.1)$$



provide a basis for the solution of the bandstructure problem. In Eq. (2.1)  $V_x$  represents the exchange potential arising out of the fact that electrons have spin, are indistinguishable and obey the Pauli exclusion principle. On the other hand,  $V_c$  (Eq. 2.1) is the non-exchange potential experienced by the electron in the Coulomb field of all ions and all other electrons.

The next problem in the band theory is how to solve the one-electron equation. This problem can be divided into two parts: (a) the mathematical method to be used and (b) the one-electron potential,  $V(\vec{r})$  in Eq. (2.1), to be used. Any one of the methods (e.g. the matrix method, the variational formulation or Green's function method) can be taken as the mathematical method to be used. In the present work we have used Hubbard's fast approximation scheme (which is based on the KKRZ method) and it is described in the next chapter.

After making the choice of the mathematical method to be used, one has to make the important decision of selecting the initial form of the potential  $V(\vec{r})$  involved in Eq. (2.1). By employing an iterative procedure one can modify  $V(\vec{r})$  in each iteration so that a satisfactory self-consistency (SC) is achieved between the  $V(\vec{r})$  and the calculated wavefunctions. Alternately one may perform the calculation non-self-consistently (NSC). We may expect the following behaviour of  $V(\vec{r})$  as atoms are incorporated into a solid. (a) The potential

$V(\vec{r})$  remains spherically symmetric [i.e.  $V(\vec{r}) = V(r)$ ] in the region of the ionic cores, (b) The potential  $V(\vec{r})$  remains fairly constant in the interstitial regions outside the ionic cores. These ideas are incorporated in the muffin-tin (MT) type of potential which assumes  $V(\vec{r}) = V(r)$  inside spheres of radius  $r_i$  centered on each nucleus, and  $V(r) = V_0$  outside these spheres. Such a design of the MT potential makes it possible to solve the one-electron equation exactly and accurately. Within the inscribed sphere the equation gives separable solutions in polar coordinates while in the interstitial region (where  $V(\vec{r}) = V_0$ ) plane-wave solutions are used. The constant potential  $V_0$  is usually taken as the average value of the potential between the boundary of the inscribed (MT) sphere and the Wigner-Seitz cell. The radius  $r_i$  of the inscribed sphere is chosen arbitrarily so that the spheres do not overlap.

The construction of the muffin-tin crystal potential usually follows the method suggested by Mattheiss [6]. The Coulomb contribution,  $V_c(\vec{r})$  (in Eq. 2.1), is obtained as a superimposition of neutral atom Coulomb potentials (arising from the neighbouring atoms) expanded about the origin using Löwdin's alpha function expansion method [7]. Atomic orbitals and atomic potentials obtained from Hartree-Fock-Slater self-consistent field equations (e.g. Herman and Skillman [8]) are usually used. The super-imposition is done in two stages;

the Coulomb and exchange contributions are considered separately. The exchange potential term  $V_x(\vec{r})$  is usually calculated in the free-electron-exchange approximation of Slater [9,2,3] who assumed that the exchange term for the electrons in the potential field of crystal is similar to the one for electron gas and depends only on the local electronic charge density  $\rho(\vec{r})$ . The averaged exchange potential is obtained from

$$V_x(\vec{r}) = -6 \alpha \left[ \left( \frac{3}{8\pi} \right) |\rho(\vec{r})| \right]^{1/3} \quad (2.2)$$

Rydbergs

There is some arbitrariness about the proportionality constant  $\alpha$ , which can be taken as  $\alpha = 1$  (Slater's full exchange [9]) or  $\alpha = 2/3$  (Gaspar [10], Kohn and Sham [11]) or  $\alpha$  can be varied between these limits to improve the quality of the bandstructure results.

A particular bandstructure calculation is, therefore, generally characterized by (i) the particular mathematical method used (e.g. KKR, APW etc.), (ii) the self-consistency or the non-self-consistency requirements for the potential  $V(\vec{r})$ , (iii) the model for the crystal potential (e.g. muffin-tin), (iv) the electron configuration used for the outer (band) electrons in constructing the crystal potential, (v) the value of the exchange parameter  $\alpha$  used in Eq. (2.2) and so on.

The aims of the final calculation are as follows:

- (a) To calculate the energy relations  $E(\vec{k})$  versus  $\vec{k}$  along different  $\vec{k}$  directions of the single crystals of the solid.
- (b) To determine the Fermi energy  $E_F$  through the calculation of the density-of-states curve  $n(E)dE$  and use this result to construct the constant energy surface,  $E(\vec{k}) = E_F$  (i.e. Fermi surface) in the  $\vec{k}$ -space.
- (c) To determine the wavefunction  $\psi_{\vec{k},j}(\vec{r})$  describing the electron belonging to the  $j$ th band in a particular  $\vec{k}$ -state.
- (d) To combine the results of (a), (b) and (c) above to determine various physical bulk properties of the solid.

Nowadays the bandstructure problem is meant to comprehensively cover the above calculations. It is only recently that these calculations are being extended to theoretically determine the electron momentum distributions,  $\rho(\vec{p})$  (Eq. 1.18), as one more ground state property predicted from the band-structure results.

The transition metals constitute a large group of metals in the periodic table and there is considerable interest in their electronic structure and other physical properties in view of their technological applications. In the iron series (or 3d) transition metals the outer 4s electrons form a broad s band which behaves like a nearly-free-electron (NFE) conduction

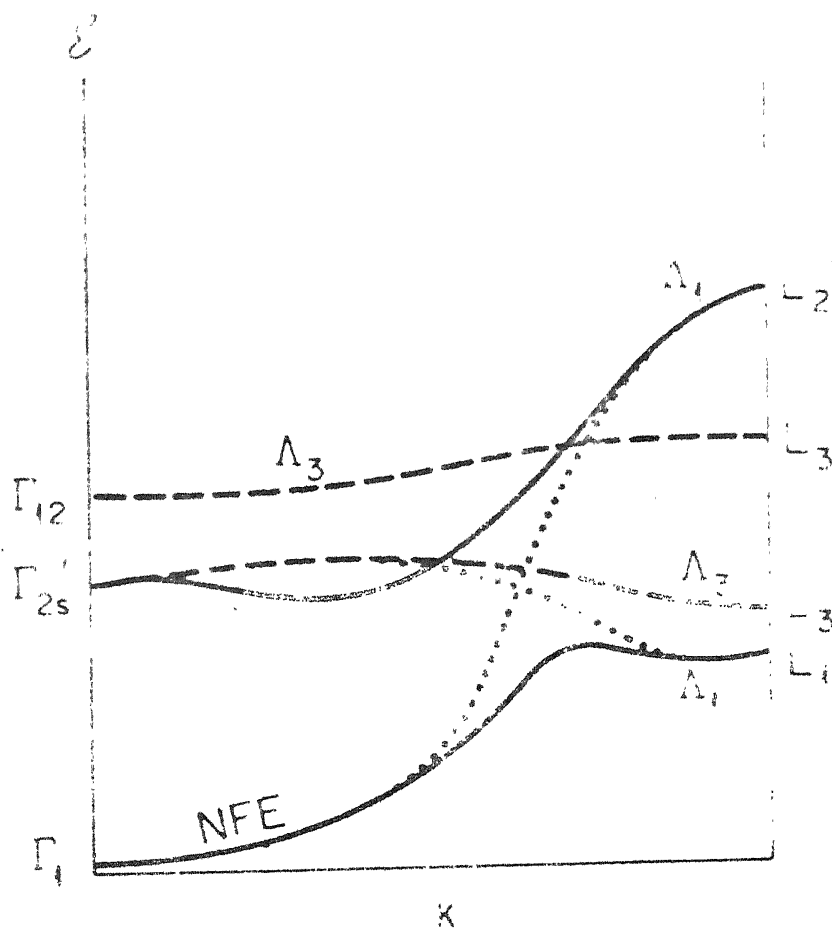


Fig. 2.1 : Hybridisation of the s and d bands for a fcc transition metal.

band in an ordinary metal. The 3d electrons form a narrow 3d-band because of the overlap with the neighbouring atoms. The narrow d band lies within the s-p (or conduction band) and hybridizes with it when they cross (Fig. 2.1). The relative positions of these bands (and therefore the bandstructure, Fermi surface and the electron wavefunctions) in the transition metals are sensitive to the choice of bandstructure method, crystal potential, outer electron configuration, exchange parameter  $\alpha$  and so on. In the present work we have investigated the sensitivity of the EMD,  $\rho(\vec{p})$  in vanadium to the choice of crystal potential (including the choice of electron configuration and the exchange parameter  $\alpha$ ).

In the next two sections we shall review the results obtained by other workers on the bandstructure and Fermi surface of vanadium. This background would be useful in discussing the results of our calculations.

## 2.2 Survey of the Bandstructure Calculations for Vanadium

The earliest bandstructure calculation on vanadium was made by Mattheiss [12] who reported the systematics of the bandstructures (along a line of symmetry) for the iron-series transition metals using a non-self-consistent (NSC) augmented-plane-wave (APW) method. His results demonstrated that for V the bandstructure (in particular the location of the d bands) is affected significantly by the change in the electron

configuration of the (3d) and (4s) shells. As the d state population in V was increased from  $(3d)^3(4s)^2$  to  $(3d)^4(4s)^1$  the d-bandwidth (e.g.  $H_{25} - H_{12}$ ) increased by about 70%.

The prediction of the nature of the Fermi surface (FS) in the vanadium group of metals (i.e. V, Nb and Ta belonging to the group VB) was first made by Mattheiss [13] himself in 1965. Assuming a rigid band model, he predicted the FS of the vanadium group of metals by using the results of three different calculations on the chromium group (i.e. Cr, Mo and W) of metals. Two of these were his own calculations for two different potentials for W and the third was based on the calculation by Wood [14] for iron. It was found by Mattheiss that in contrast to the VIB group (i.e. chromium group) metals, the FS of the VB group (i.e. vanadium group) is rather sensitive to small changes in the bandstructure. Such a behaviour arises because the  $\Gamma_{25}$  state in the case of the VB metals falls just above the Fermi level. The topology of the FS for the vanadium group of metals showed two hole sheets: one corresponding to the second band consists of a closed surface which is centred on the point  $\Gamma$  and is octahedral in character. The other sheet, arising out of the third band, consists of a jungle-gym (JG) structure of hole arms along the  $\langle 100 \rangle$  directions as well as large ellipsoids around the points N. The conclusions drawn from the results for Fe, however, showed a neck along  $\Gamma$  N in the third band; otherwise the three different

calculations predicted qualitatively similar results. Mattheiss also found that the accidental degeneracies in the (100) and (110) planes (where the inner closed hole surface contacts the outer multiply connected hole surfaces) could be removed by including the spin-orbit coupling.

Snow and Waber [15] calculated the bandstructure and the density-of-states curves for the bcc and fcc metals in the iron-series transition metals using a NSC APW method and full Slater exchange ( $\alpha=1$ ). These calculations were performed for two different configurations for the outer electrons,  $(3d)^n(4s)^2$  and  $(3d)^{n+1}(4s)^1$ , for all the metals. A comparison with the experimental results indicated that the  $(3d)^{n+1}(4s)^1$  configuration was generally more favourable.

Anderson et al. [16] calculated the bandstructure of V using the NSC APW method with the electron configuration as  $(3d)^3(4s)^2$  for two different values of the exchange parameters  $\alpha=1$  and  $\alpha=2/3$ . They found that as  $\alpha$  was increased the d-bandwidth decreased significantly. The p-like point  $N'_1$  was found to lie below the Fermi level for  $\alpha=2/3$  while it was above  $E=E_F$  for  $\alpha=1$  (full exchange). A comparison of these theoretical results with those obtained from the photoemission [17] and de Haas-van Alphen effect [18] experiments supported the  $\alpha=1$  exchange. It was also found that their results for  $\alpha=2/3$  case were qualitatively same as those of Mattheiss [12] using a full ( $\alpha=1$ ) exchange and a  $(3d)^4(4s)^1$  configuration.



Christensen [19] studied the effect of changing the population of the outer d and s shells on the bandstructure of V and Mo. The muffin-tin potentials were constructed for the case  $\alpha=1$  by using the HFS self-consistent charge densities for the two different configurations and the bandstructure was calculated by using a non-relativistic NSC APW method. It was found that for V the d-bandwidth increased dramatically when the 3d population was increased from  $(3d)^3(4s)^2$  to  $(3d)^4(4s)^1$  whereas similar changes did not occur for Mo when the 4d population was changed from  $(4d)^4(5s)^2$  to  $(4d)^5(5s)^1$ . The results of Christensen for the  $(3d)^4(4s)^1$  configuration of V agreed well with those of Mattheiss [12] for the same configuration.

The first SC calculations on V were carried out by Yasui et al. [20] using the modified tight binding (MTB) method and the OPW method for the d and s valence electrons respectively. Using the configurations  $(3d)^4(4s)^1$  two potentials were created, one for  $\alpha=1$  while another for  $\alpha = 0.725$ . The results for  $\alpha=1$  case were very different from the previous NSC calculations while the  $\alpha = 0.725$  results showed a better agreement.

Self-consistent calculations for V were also reported by Papaconstantopoulos et al. [21] who used the APW method and the  $(3d)^3(4s)^2$  configuration. Calculations were performed for the normal lattice constant ( $a_0$ ) using  $\alpha=1$  and  $\alpha=2/3$  as

well as for the reduced lattice constant ( $a = 0.95 a_0$ ) with  $\alpha = 2/3$ . It was found that their results for  $\alpha=1$  after the first iteration (NSC) were very close to the results after the last iteration (SC) for  $\alpha = 2/3$ . Such cancellation of the effects of self-consistency and exchange were also pointed out for Ni by Connolly [22] and for Cu by Snow and Waber [23]. The effect of the different values of the exchange parameter was reflected in the changes in the s,p,d,f and the interstitial (i.e. outside the inscribed sphere) components of the charge density. For the SC  $\alpha = 2/3$  case, the d-component was more pronounced than for the SC  $\alpha = 1$  case. The s-d separation and the d and s-p widths were all found to increase in going from SC  $\alpha = 1$  to SC  $\alpha = 2/3$ . The only important change observed in the level ordering was for the  $N_1'$  state which falls below  $N_4$  and  $N_1$  as the exchange parameter was reduced from  $\alpha = 1$  to  $\alpha = 2/3$ . Along  $\Gamma N$  the third band was found to dip below the Fermi level when going from  $\alpha = 1$  to  $\alpha = 2/3$ , thus giving rise to significant changes in the FS. A comparison with the experimental data from the photoemission [17] and dHvA [18] studies showed that the SC  $\alpha = 2/3$  calculations gave a better agreement compared to the SC  $\alpha = 1$ . At the same time it was found that their NSC  $\alpha = 1$  calculation for the configuration  $3d^4 4s^1$  gave slightly better agreement with experiment than SC  $\alpha = 2/3$ . Their calculations for the reduced lattice parameter ( $a = 0.95 a_0$ ) showed a significant

change in the results for the band structure and Fermi surface of V. Hattox et al. [24] performed a SC APW bandstructure calculation for V using a statistical exchange  $X_\alpha$  [3] muffin-tin approximation. They assumed a ferromagnetic bcc structure as a function of the lattice parameter and calculated the  $X_\alpha$  cohesive energy, pressure and magnetization for several values of the lattice parameter.

Wakoh and Yamashita [25] have calculated the bandstructure of V using the state-dependent potentials. Using a configuration of  $(3d)^{3.9}(4s)^{1.1}$  and the values of exchange parameter  $\alpha = 2/3$ , 0.8 and 1.0, atomic charge densities were calculated self-consistently to obtain the corresponding muffin-tin crystal potential. The modified Wigner-Seitz (MWS) potentials were also used with the parameter  $\lambda = 1.0$ , 1.4 and 2.0. The bandstructure was calculated self-consistently using the KKR method. It was found that the SC  $\alpha = 2/3$  case generally gave better agreement with the experimental results. However, the calculated values failed to match the experimental results (particularly the dimensions and shape of the FS) completely. The calculations were, therefore, done phenomenologically using a final (i.e. fitted) state-dependent potential with different energy dependence for the  $d_z$  and the  $d_{xy}$  states. The results obtained with the final state-dependent potential were thus able to reproduce the FS data and the X-ray form factor values obtained experimentally. These authors later on

extended their calculations to compute the directional Compton profiles [26] and positron angular correlation curves [27] using the same state-dependent potential. We shall discuss these results at a later stage.

Recently Boyer et al. [28] have investigated the effects of exchange and self-consistency on the bandstructure of the group VB metals V, Nb and Ta. They have calculated the density-of-states, FS areas and effective masses from the SC APW bandstructure results obtained by using Slater's [29]  $X_\alpha$  exchange approximation. In this method the value of  $\alpha$  is taken to be that for which the HFS total energy of the atom is the same as the HF total energy. For V, the value of the  $X_\alpha$  parameter previously determined as  $\alpha = 0.71556$  was used. A comparison of their results with other theoretical and experimental results showed that the SC  $\alpha = 2/3$  results agreed with the experimental results better than their  $X_\alpha$  results. It was also found that the bandstructure results for V are very sensitive to the exchange approximation used.

In a recent paper Callaway et al. [30] have reported a bandstructure calculation of the paramagnetic 3d transition metals (including V) by using the self-consistent LCGO (linear combination of Gaussian orbitals) method. They have also calculated the Compton profiles of V and these results would be discussed later.

Recently Kanhere and Singru [31] have reported a calculation of the bandstructure and EMD in the 3d metals V, Cr, Fe, Ni and Cu by using Hubbard's fast approximation scheme. By using a common method for the construction of the crystal potential, the systematics of the EMD and their relation to the respective bandstructure were pointed out.

To summarise, the results of various calculations have shown that the bandstructure of V is very sensitive to small changes in the crystal potential introduced by (i) the changes in the (3d) and (4s) outer electron configuration, (ii) variation in the exchange parameter  $\alpha$ . Besides these the other factor which seems to affect the bandstructure results is (iii) whether the calculations were performed in a self-consistent (SC) or the non self-consistent (NSC) manner. In Table 2.1 we have summarised some of these features for those bandstructure calculations which show a fair agreement with the experiments (and therefore with each other).

Some of these factors [(i) to (iii) mentioned above] affecting the bandstructure results tend to provide a cancellation effect. These are outlined below.

(a) Keeping the other factors common, a NSC  $\alpha = 1.0$  calculation is equivalent to a SC  $\alpha = 2/3$  calculation. This behaviour has been pointed out earlier in the literature [22,23].

Table 2.1 Summary of the method and parameters used in the various bandstructure calculations

Reference	Method	NSC or SC	Electron Configuration	Exchange
Mattheiss [12]	APW	NSC	$(3d)^4(4s)^1$	$\alpha=1$
Anderson et al. [16]	APW	NSC	$(3d)^3(4s)^2$	$\alpha=1$
Yasui et al. [20]	MTB+OPW	SC	$(3d)^4(4s)^1$	$\alpha=0.725$
Papaconstantopoulos et al. [21]	APW	SC	$(3d)^3(4s)^2$	$\alpha=2/3$
Wakoh and Yamashita [25]	KKR	SC	$(3d)^{3.9}(4s)^{1.1}$	$X_\alpha$ method (see text).

(b) Using the NSC APW method the results obtained by Mattheiss [12] for the case  $\alpha = 1$ ,  $(3d)^4(4s)^1$  compared well those for the case  $\alpha = 2/3$ ,  $(3d)^3(4s)^2$  by Anderson et al. [16]. This suggests that the effect of reducing the 3d population from  $(3d)^4(4s)^1$  to  $(3d)^3(4s)^2$  is compensated by decreasing  $\alpha$  from 1 to  $2/3$ .

### 2.3 Survey of the Fermi Surface Studies of Vanadium

In this section we shall briefly review the experimental studies of the Fermi surface of V. The general conclusion of the different experiments (which are not many, perhaps because of the lack of pure samples of V) support the FS topology suggested by Mattheiss [13,32].

The earliest work carried out by Alekseevskii and Egorov [33] by the magnetoresistance studies was inconclusive, but a subsequent work [34] using same techniques reported an anisotropy in the FS of V. Phillips [18] using the technique of impulsive fields studied the FS in the  $\{100\}$  crystallographic plane. By using magnetothermal oscillation techniques Parker and Halloran [35] extended their previous studies [36] and investigated the FS of V in two planes  $\{100\}$  and  $\{110\}$ . This is the most extensive FS study of V and these authors [35] have compared their results with other experimental and theoretical results.

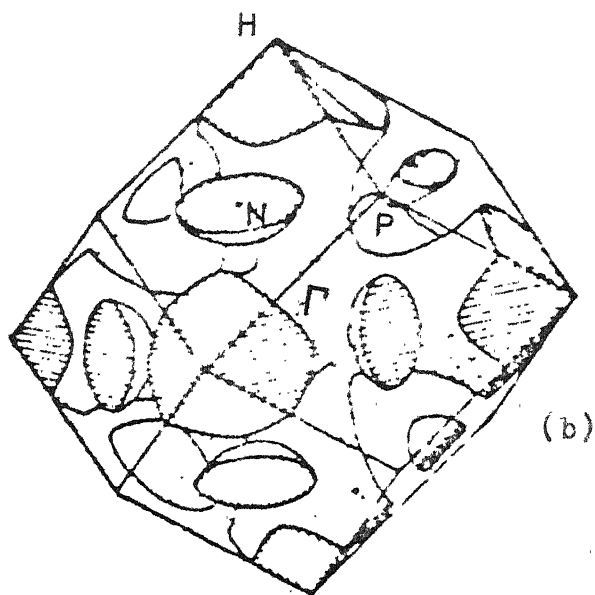
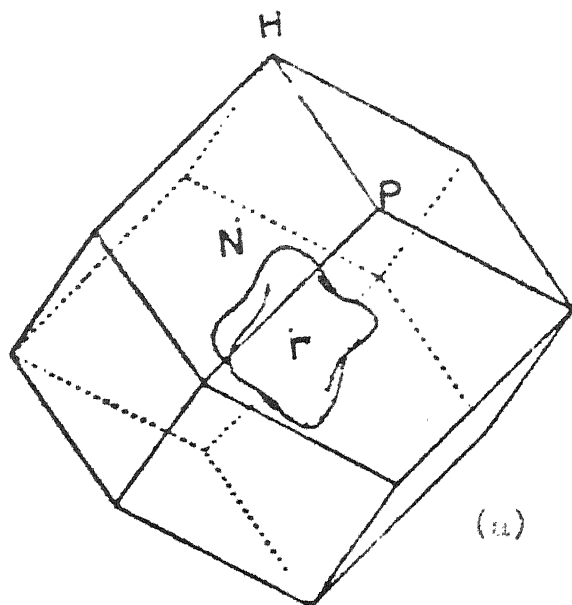


Fig. 2.2 : General features of the F3 of vanadium:  
 (a) second band octahedral hole surface  
 (b) third band hole sheets.



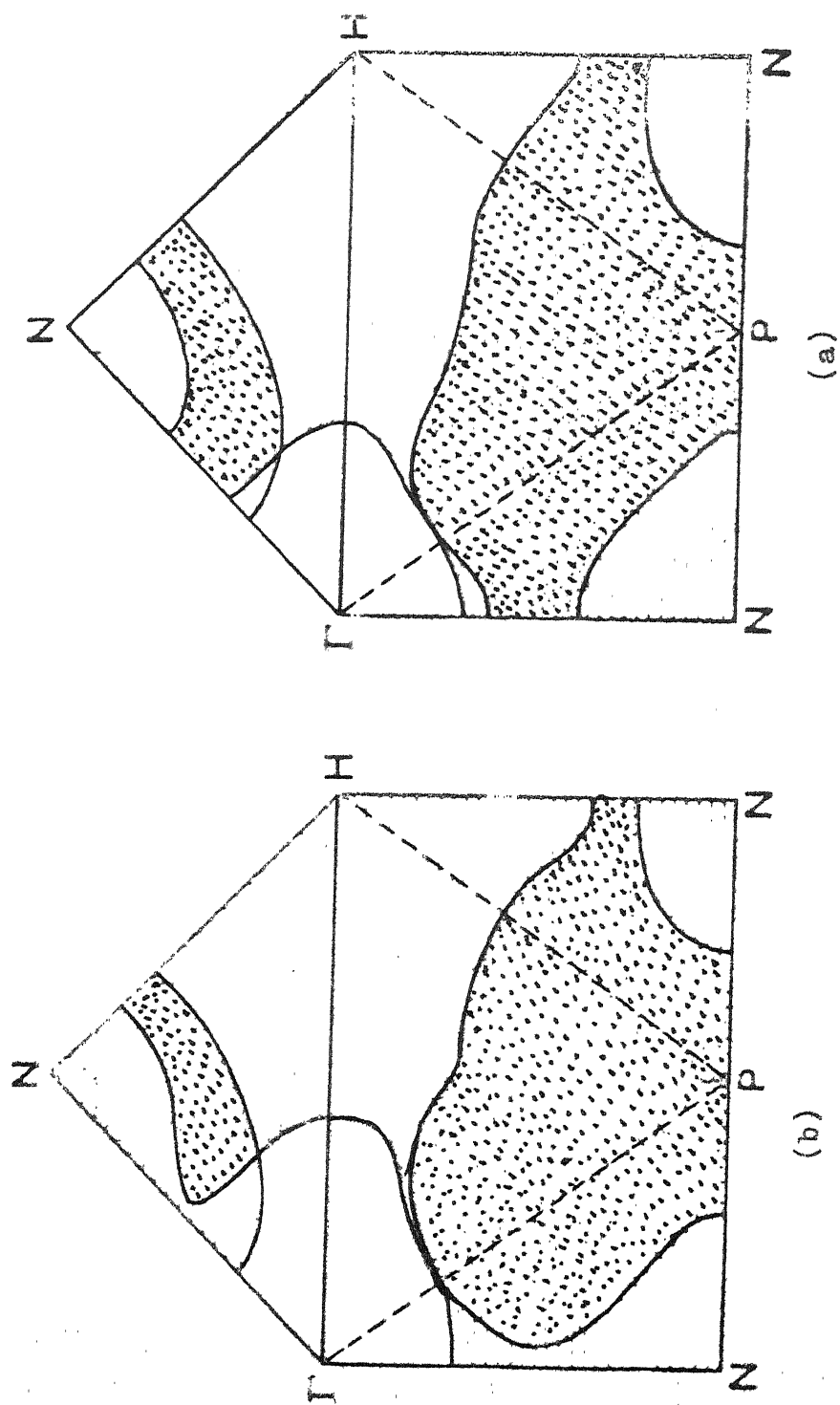


Fig. 2.3 : Fermi surface of vanadium group metals predicted by Mattheiss [12] from (a) calculations on tungsten (b) calculations on iron by Wood [14].

Different studies [34-36] agree that the general features of the FS of V is as shown in Fig. 2.2. The crosssection of the FS in the central  $\{110\}$  and  $\{100\}$  planes are shown in Fig. 2.3 as calculated by Mattheiss [12] using energy bands for tungsten (Fig. 2.3a) and iron (Fig. 2.3b).

The closed second-zone hole surface of V centered on  $\Gamma$  is shown in Fig. 2.2a. The third zone hole surface (Fig. 2.2b) is quite complicated. It consists of multiply connected hole tubes along the  $\langle 100 \rangle$  directions (which are known as the jungle-gym arms) as well as large distorted half ellipsoids centred at N. For the latter type of half ellipsoids, Parker and Halloran [35] experimentally determined the semiaxes to be 4.632, 4.405 and 3.649 nm<sup>-1</sup> along the N-P, N- $\Gamma$  and N-H directions respectively. The measured areas of these half ellipsoids [18,35] agree amongst themselves but are higher than the APW bandstructure calculations [21]. Similarly, the effective masses determined from the dHvA experiments [35] gave ( $m^*/m$ ) values which were higher than those calculated theoretically [21,28].

The model FS of V obtained by Mattheiss [13] using the energy bands of Fe predicted that the ellipsoids are connected to the jungle-gym (JG) surface by narrow necks along the  $\Gamma$ -N directions (Fig. 2.3b). The measurements of Parker and Halloran [35] indicated that such narrow necks exist along the  $\Gamma$ -N directions. For such necks to exist the third band

in V along the  $\Sigma$  direction should not cross the Fermi level but should lie above it. Bandstructure calculations (for the normal lattice constant of V) reported by different workers [21,25,28,30] all show that the third band along the  $\Sigma$  direction dips below the Fermi level and thus preclude the existence of such necks. Papaconstantopoulos et al. [21] however showed that for the reduced lattice constant  $a = 0.95 a_0$  and  $\alpha = 2/3$  the ellipsoids connect the JG arms and estimated that the contact should occur at an applied pressure of 135 kbars.

In the next section we shall point out that this point of disagreement (i.e. existence of necks) between experiment and theory can perhaps be resolved by a carefully designed measurement of the directional Compton profiles of V.

#### 2.4 Survey of the Compton Profile Studies of V

The EMU and the Compton profiles of V have been studied both experimentally and theoretically. These studies were inspired by the early studies of Weiss and De Marco [37] who measured the X-ray diffraction of V paired reflections and obtained a  $e_g/t_{2g}$  population ratio of about 0.19/0.81 for the electron states in V. Using this population ratio Weiss [38] calculated the directional Compton profiles of V. This calculation indicated an anisotropy in the Compton profiles, the difference between  $J_{100}(0)$  and  $J_{111}(0)$  being about 8%.

Phillips [39] measured the Compton profiles of single-crystal vanadium samples using 17.4 keV Mo- $K_\alpha$  X-rays and observed that the anisotropy at  $J(0)$  was very small. Gamma-ray Compton profiles were later measured by Terasaki et al. [40] and Paakkari et al. [41] and these studies showed that the anisotropy was measurable but was smaller than predicted by Weiss' model [38]. These experiments showed that the difference  $\Delta J = [J_{100}(0) - J_{111}(0)]$  was about 2% and the anisotropy curves  $\Delta J(p_z)$  showed a structure (submaxima and minima) which could not be explained by the calculations of Weiss [38]. A systematic measurement of the Compton profiles of the polycrystalline samples of V, Cr, Ni, Cu and Zn was reported by Manninen and Paakkari [42] but later experimental work [43,44] showed that the multiple scattering effects are important. Experimental Compton profiles for polycrystalline V corrected for the multiple scattering effects showed a close agreement [43] with a theoretical Compton profile calculated from the RFA model [45] in which only 4s electrons in an outer electron configuration  $(3d)^3(4s)^2$  are normalised.

Wakoh and Yamashita [26] performed a detailed calculation of the directional Compton profiles of V using the KKR bandstructure method and a state-dependent crystal potential [25]. A comparison of the theoretical anisotropies  $\Delta J(p_z) = [J_{hkl}(p_z) - J_{h'k'l'}(p_z)]$  obtained by these workers showed a

fair agreement with the experimental results of Terasaki et al. [40]. The spherically averaged Compton profile (due to the band electrons) obtained from these calculations showed a better agreement with the measured profile of Paakkari et al. [41] rather than that of Phillips [39]. Although Wakoh and Yamashita [26] presented the theoretical contributions by the first, second and third band to the Compton profiles along the  $\langle 100 \rangle$ ,  $\langle 110 \rangle$  and  $\langle 111 \rangle$  directions and discussed their results in terms of the bandstructure and FS of V, they do not describe the behaviour of the EMD,  $\rho(\vec{p})$  itself. In a later work, Wakoh et al. [46] repeated these calculations by using the APW method and obtained results which were qualitatively similar to their earlier work [26].

Recently Kanhere and Singru [31] discussed the systematics of the EMD,  $\rho(\vec{p})$ , in the 3d transition metals V, Cr, Fe, Ni and Cu and explained the behaviour of the EMD in terms of the respective bandstructure. However, this analysis was restricted only to the three symmetry directions  $\langle 100 \rangle$ ,  $\langle 110 \rangle$  and  $\langle 111 \rangle$ . The recent calculation by Callaway et al. [30] using the LCGO method concerns itself only with the spherically averaged Compton profile from polycrystalline V.

One of the main objectives of the present work is to gain an insight into the EMD,  $\rho(\vec{p})$ , of V in terms of its bandstructure and FS. If the narrow necks along  $\Gamma$ -N (connecting

the JG arms to the ellipsoids) exist the EMD,  $\rho(\vec{p})$ , along  $r \Sigma N$  should be radically different and this behaviour should be reflected in the directional Compton profiles and their anisotropies. This aspect would be discussed further in Chapters 4 and 5.

REFERENCES

1. J. M. Ziman, Solid State Physics, Eds. H. Ehrenreich, F. Seitz and D. Turnbull, Vol. 26, Academic Press, New York, 1976, p. 1.
2. G. C. Fletcher, The Electron Band Theory of Solids, North-Holland Publishing Co. Amsterdam-London, 1971.
3. J. Callaway, Quantum Theory of the Solid State, Part A and B, Academic Press, New York, 1974.
4. C. M. Quinn, An Introduction to the Quantum Chemistry of Solids, Clarendon Press, Oxford, 1973.
5. L. Pincherle, Electronic Energy Bands in Solids, Macdonald, London, 1971.
6. L. F. Mattheiss, Phys. Rev. 133, A1399 (1964).
7. P.-O. Löwdin, Adv. Phys. 5, 1 (1956).
8. F. Herman and S. Skillman, Atomic Structure Calculations, Prentice Hall, Englewood Cliffs, New Jersey, 1963.
9. J. C. Slater, Phys. Rev. 81, 385 (1951).
10. R. Gaspar, Acta. Phys. Acad. Sci. Hung. 3, 263 (1954).
11. W. Kohn and L. J. Sham, Phys. Rev. 140, A1133 (1965).
12. L. F. Mattheiss, Phys. Rev. 134, A970 (1964).
13. L. F. Mattheiss, Phys. Rev. 139, A1893 (1965).
14. J. H. Wood, Phys. Rev. 126, 517 (1962).
15. E. C. Snow and J. T. Waber, Acta Metall. 17, 623 (1969).
16. J. R. Anderson, J. W. McCaffrey and D. A. Papaconstantopoulos, Solid St. Commun. 7, 1439 (1969).
17. D. W. Eastman, Solid St. Commun., 7, 1697 (1969).
18. R. A. Phillips, Phys. Lett. A36, 361 (1971).

19. N. E. Christensen 'Energy Band Structure of Molybdenum and Vanadium', Report No. 95, The Technical University of Denmark, Lyngby, Denmark, 1971 (Unpublished).
20. M. Yasui, E. Hayashi and M. Shimizu, J. Phys. Soc. Jap. 29, 1446 (1970).
21. D. A. Papaconstantopoulos, J. R. Anderson and J. W. McCaffrey, Phys. Rev. B5, 1214 (1972).
22. J. W. D. Connolly, Phys. Rev. 159, 415 (1967).
23. E. C. Snow and J. T. Waber, Phys. Rev. 157, 570 (1967).
24. T. M. Hattox, J. B. Conklin, J. C. Slater and S.B. Trickey, J. Phys. Chem. Solids 34, 1627 (1973).
25. S. Wakoh and J. Yamashita, J. Phys. Soc. Jap. 35, 1394 (1973).
26. S. Wakoh and J. Yamashita, J. Phys. Soc. Jap. 35, 1406 (1973).
27. S. Wakoh, Y. Kubo and J. Yamashita, J. Phys. Soc. Jap. 38, 416 (1975).
28. L. L. Boyer, D. A. Papaconstantopoulos and B. M. Klein, Phys. Rev. B15, 3685 (1977).
29. J. C. Slater in Advances in Quantum Chemistry, Ed. P.-O. Löwdin, Vol. 6, Academic Press, New York, 1972, p. 1.
30. J. Callaway, D. Laurent and C. S. Wang, Phys. Rev. B15 (1978), In press.
31. D. G. Kanhere and R. M. Singru, J. Phys. F7, 2603 (1977).
32. L. F. Mattheiss, Phys. Rev. B1, 371 (1970).
33. N. E. Alekseevskii and V. S. Egorov, Zh. Eksp. Teor. Fiz. Pis'ma Red. 1, 141 (1965) [JETP Lett. 1, 141 (1965)].
34. K. S. Nelson, J. L. Stanford and F. A. Schmidt, Phys. Lett. A28, 402 (1968).
35. R. D. Parker and M. H. Halloran, Phys. Rev. B9, 4130 (1974).
36. R. D. Parker, J. C. Abele and M. H. Halloran, Bull. Am. Phys. Soc. 16, 838 (1971).



37. R. J. Weiss and J. J. De Marco, Phys. Rev. 140A, 1223 (1965).
38. R. J. Weiss, Philos. Mag. 14, 403 (1966).
39. W. C. Phillips, Phys. Rev. B7, 1047 (1973).
40. O. Terasaki, T. Fukamachi, S. Hosoya and D. Watanabe, Phys. Lett. 43A, 123 (1973).
41. T. Paakkari, S. Manninen, O. Inkinen and E. Liukkonen, Phys. Rev. B6, 351 (1972).
42. S. Manninen and T. Paakari, Phys. Fenn. 9, 129 (1974).
43. T. Paakkari, S. Manninen and K.-F. Berggren, Phys. Fenn. 10, 207 (1975).
44. V. Halonen et al. in 'Compton Scattering', ed. B. Williams, McGraw-Hill Inc. London, 1977, p. 79.
45. K.-F. Berggren, Phys. Rev. B6, 2156 (1972).
46. S. Wakoh, Y. Kubo and J. Yamashita, J. Phys. Soc. Jap. 40, 1043 (1976).

## Chapter 3

### THE APPROXIMATE CALCULATION OF ELECTRON BANDSTRUCTURE AND MOMENTUM DENSITY

#### 3.1 Introduction

It may be recalled from Eq. (1.18) that the electron momentum density (EMD),  $\rho(\vec{p})$ , in the independent particle model is calculated [1] from

$$\rho(\vec{p}) = \sum_{j, \vec{k}, i}^{\text{occ}} f(\vec{k}, j) |A_j(\vec{k}, \vec{p})|^2 \delta(\vec{p} - \vec{k} - \vec{K}_i) \quad (3.1)$$

where the various symbols are already explained in §1.4.

This involves the calculation of the matrix elements

$$A_j(\vec{k}, \vec{p}) = \int_{\text{cell}} e^{-i\vec{p} \cdot \vec{r}} \psi_{\vec{k}, j}(\vec{r}) d\vec{r}$$

for each  $j$  and  $(\vec{k}, \vec{p})$ .

In a typical computation, one has to evaluate the EMD,  $\rho(\vec{p})$ , at several (usually > 500) momenta values of  $\vec{p}$  involving many combinations of  $\vec{k}$  and  $\vec{K}_i$  to form  $\vec{p} = \vec{k} + \vec{K}_i$ . Such computations can be very time-consuming if a standard (and more

accurate) bandstructure method like the APW or KKR method is used to calculate the electron wavefunctions  $\psi_{\vec{k},j}$ , the bandstructure  $E(\vec{k})$  and the EMD  $\rho(\vec{p})$ . It is, therefore, useful to employ a rapid but approximate method to compute the above quantities. Such a fast approximate scheme for transition metals was first proposed by Hubbard [2]. This method does not contain any arbitrary parameters and it has shown to provide an overall accuracy of about 0.005-0.01 Ry. for the bandstructure results. Mijnaerends [1,3] further developed this method for the calculation of the EMD. Application of the Hubbard-Mijnaerends fast approximate method for the calculation of the EMD in the transition metals like Fe [1], Ni [4], Cu [1,5], Pd [6] and Ag [6] has met with significant success when the theoretical results are compared with experiment. In view of these successes and the availability of computer programs<sup>ⓧ</sup> and its suitability and speed for the computer system (IBM 7044/1401) located at this Institute, we have adopted this method for the calculation of the EMD,  $\rho(\vec{p})$ , in vanadium. In the following section we give a brief outline of this method, the details of which are described elsewhere [2,7,8].

---

<sup>ⓧ</sup> These computer programs were generously made available to us by Dr. P. E. Mijnaerends. We are indebted to him for his kind help.

### 3.2 Hubbard's Fast Approximate Scheme

In the case of transition metals the electron band-structure can be described as hybrids of nearly-free-electron (NFE)-like (or plane-wave-like) bands with narrow d bands of tight-binding nature. Ziman [9] has reviewed various approximate schemes using the above concept. One such convenient scheme is that due to Hubbard [2] and it is based on the Green's function [9] or Korringa [10], Kohn and Rostoker [11] (i.e. KKR) method of bandstructure calculations. The Green's function or the KKR method determines the bandstructure through the calculation of the energy-dependent phase shifts arising from the scattering of electrons from the atomic potential (usually of the muffin-tin type).

Ziman [12] reformulated the KKR method and obtained the determinantal equation

$$(k_n^2 - \epsilon) B_n + \sum_{n'} \Gamma_{nn'} B_{n'} = 0 \quad (3.2)$$

where  $k_n = |\vec{k}_n|$  and  $\vec{k}_n = \vec{k} + \vec{K}_n$ ,  $\vec{K}_n$  being the reciprocal lattice vectors, and  $\epsilon$  is the Bloch energy eigenvalue for the electron in a state  $k$ .

It was shown by Lloyd [13] that  $B_n$  are the coefficients of the pseudo-wavefunction  $\psi_{ps}$  such that

$$\psi_{ps}(\vec{r}) = (1/\tau)^{\frac{1}{2}} \sum_n B_n \exp(i\vec{k}_n \cdot \vec{r}) \quad (3.3)$$

throughout the atomic polyhedron (of volume  $\tau$ ). In the interstitial region outside the inscribed spheres, the Bloch wavefunction is given by the same expression, i.e.

$$\psi_{\vec{k}}(\vec{r}) = (1/\tau)^{\frac{1}{2}} \sum_n B_n \exp(i\vec{k}_n \cdot \vec{r}) \quad (3.4)$$

The matrix elements  $\Gamma_{nn'}$  are given [14] by

$$\Gamma_{nn'} = \frac{4\pi}{\tau} \sum_l (2l+1) r_l^2 \gamma_l j_l(k_n r_l) j_l(k_{n'} r_l) P_l(\cos \theta_{nn'}) \quad (3.5)$$

where

$$\gamma_l = \frac{-\tan \eta_l}{kr_l^2 j_l(kr_l) [j_l(kr_l) - (\tan \eta_l) n_l(kr_l)]} \quad (3.6)$$

$k = \sqrt{\epsilon}$ ,  $\theta_{nn'}$  is the angle between  $\vec{k}_n$  and  $\vec{k}_{n'}$ ,  $r_l$  is a radius in the interval  $(0, r_i)$ ,  $r_i$  being the muffin-tin radius;  $\eta_l$  is the phase shift of the  $l$ th partial wave scattered from the atomic potential while  $j_l$ ,  $n_l$  are the spherical Bessel and Neumann functions respectively.

Excepting the case when  $j_l(kr_l)$  or  $[j_l(kr_l) - (\tan \eta_l) n_l(kr_l)]$  is close to zero for some value of  $l$  we shall have  $\gamma_l$  and therefore  $\Gamma_{nn'}$  to be small. It has been suggested by Pendry and Capart [15] that in order to avoid

the large values, one should choose  $r_l$  at the zero of  $n_l(kr_l)$  if there is a zero in  $(0, r_i)$ , otherwise  $r_l$  should be chosen at  $r_l = r_i$ , the radius of the inscribed sphere. The case of  $r_l$  being different from  $r_i$  will occur only for  $l = 0$ .

It has been shown by Hubbard [2,7] that in the case of transition metals there occurs a narrow resonance for  $\tan \eta_l$  and hence also for  $\gamma_l$  for the d bands corresponding to  $l = 2$ . For the case of a single resonance at  $k^2 = \epsilon_0$  for  $l = \lambda$  ( $\lambda$  being 2 for the d bands of a transition metal) one can write [2]

$$\gamma_l = \gamma_l' - \frac{\delta_{\lambda\lambda} \Gamma}{\epsilon_0 - k^2} \quad (3.7)$$

where  $\Gamma$  is the width of the resonance and  $\gamma_l'$  is the residue, thus making  $\gamma_l'$  always small.

Ziman's determinantal equation (Eq. 3.2) can now be written as

$$\begin{pmatrix} K + V - \epsilon I & B \\ B^* & (\epsilon_c - \epsilon) I \end{pmatrix} \begin{pmatrix} A \\ C \end{pmatrix} = 0 \quad (3.8)$$

where the matrix elements of the various submatrices are written as

$$K_{nn'} = k_n^2 \delta_{nn'} \quad (3.9a)$$

$$V_{nn'} = -\left(\frac{4\pi}{\tau}\right) \sum_l (2l+1) r_l^2 \gamma_l' j_l(k_n r_\lambda) j_l(k_{n'} r_\lambda) P_l(\cos \theta_{nn'}) \quad (3.9b)$$

$$h_{nm} = -4\pi r_\lambda (r/\tau)^{\frac{1}{2}} j_\lambda(k_n r_\lambda) Y_{\lambda m}(\hat{k}_n) \quad (3.9c)$$

and

$$a_m = \frac{4\pi r_\lambda}{\varepsilon_0 - \varepsilon} (r/\tau)^{\frac{1}{2}} \sum_n j_\lambda(k_n r_\lambda) Y_{\lambda m}^*(\hat{k}_n) B_n \quad (3.9d)$$

with  $m = -\lambda, -\lambda + 1, \dots, \lambda$

In Eq. (3.8) the column matrix  $\mathbb{A}$  describes the resonant behaviour while  $\mathbb{B}$  contains the non-resonant part of the wavefunctions.

By following a procedure suggested by Heine [16], Hubbard [2] was able to reduce Eq. (3.8) to an equation of lower order. This procedure consisted in dividing  $\vec{k}_n$  into two sets:

(a) A preferred set 'P' which consists only of the chosen (few in number)  $\vec{k}_n$  for which  $k_n^2$  has values in or near the energy values of our interest. Usually the set P consists of a few of the smallest reciprocal lattice vectors.

(b) A remainder set 'R' which consists of those  $\vec{k}_n$  which are not included in the set P.

By introducing the approximations  $\mathbb{V}_{PR} = \mathbb{V}_{RP} = 0$  and by neglecting  $\mathbb{V}_{RR}$  in comparison with  $(k_n^{(R)})^2 - \varepsilon$ , Eq. (3.8) can be split up as

$$\begin{pmatrix} \mathbb{K}_P + \mathbb{V}_{PP} - \varepsilon \mathbb{I} & \mathbb{H}_P \\ \mathbb{H}_P^* & \mathbb{A} - \varepsilon \mathbb{I} \end{pmatrix} \begin{pmatrix} \mathbb{B}_P \\ \mathbb{A} \end{pmatrix} = 0 \quad (3.10a)$$

and

$$\left( \mathbf{k}_R - \varepsilon \cdot \mathbf{I} \right) \mathbf{E}_R + \mathbf{H}_R \mathbf{A} = 0 \quad (3.10b)$$

where the square matrix  $\mathbf{A}$  is given by

$$A_{mm'} = \varepsilon_0 \delta_{mm'} - \frac{(4\pi)^2}{\tau} r_\lambda^2 r \sum_n^{(R)} \frac{j_\lambda^2(k_n r_\lambda)}{k_n^2 - k^2} \times Y_{\lambda m}(\hat{k}_n) Y_{\lambda m'}^*(\hat{k}_n) \quad (3.11)$$

the sum  $\sum_n^{(R)}$  being carried out over all the vectors of the remainder set  $R$ . A prescription to calculate the sum  $\sum_n^{(R)}$  is given by Hubbard [2] as follows

$$\sum^{(R)} = \sum^{(S)} + \frac{\delta_{mm'}}{r_\lambda \tau_k} \left[ \frac{1 - \cos X}{X} + \frac{1}{2}\pi - \text{Si}(X) \right]_{X=2k_0 r_\lambda} \quad (3.12)$$

where  $\sum^{(S)}$  is a sum similar to the second term in Eq. (3.11) but now over the first few shells of reciprocal-lattice vectors except those of the preferred set 'P',  $\text{Si}(X)$  is the sine-integral  $\int_0^X (\sin t/t) dt$ ,  $\tau_k$  is the volume of the unit cell in reciprocal space, and  $(4\pi k_0^3/3\tau_k) = N$ ,  $N$  being the total number of reciprocal lattice vectors included in  $P$  and in the sum  $\sum^{(S)}$ . The determinantal equation (Eq. 3.10a) resembles in form the equation used in model pseudo-potential schemes [16,17]. The physical significance of the



various submatrices in Eq. (3.10a) is as follows. The submatrix  $V$  describes the nearly-free-electron (NFE) part of the (s-p) conduction band while the submatrix  $A$  (5x5 in size) describes the d-bands. The hybridization between these bands is contained in the off-diagonal matrices  $B$  and  $B^*$ . The submatrices  $A$  and  $V$  depend on energy. The energy dependence of  $A$  and  $V$  can be suitably approximated to remove the energy dependence of the matrix  $M$  in

$$[ M(\epsilon) - \epsilon I ] \begin{pmatrix} B \\ A \end{pmatrix} = 0 \quad (3.13)$$

which is an equivalent form of (3.10a). The idea is thus to reduce the problem to that of diagonalization.

Hubbard [2] has indicated the procedure for this. In outline it consists in setting

$$M(\epsilon) - \epsilon I \approx M_1 - \epsilon M_2 \quad (3.14)$$

such that  $M_1$  and  $M_2$  do not depend on  $\epsilon$ , and writing

$$\hat{x} = \begin{pmatrix} B \\ A \end{pmatrix} \quad \text{and} \quad y = M_2^{-\frac{1}{2}} \hat{x}$$

to obtain

$$[ M_2^{-\frac{1}{2}} M_1 M_2^{-\frac{1}{2}} - \epsilon I ] y = 0 \quad (3.15)$$

as an equivalent form of Eq. (3.10a).

By comparing Eq. (3.15) and (3.10a) we note that the problem has now been put into a secular form which can be solved by standard methods of matrix algebra.

### 3.3 Calculation of Electron Wavefunctions and Momentum Density

In the previous section we have given a bare outline of Hubbard's fast approximation scheme. In this section we shall outline how one obtains electron wavefunction  $\psi_{\vec{k}}(\vec{r})$  and momentum density  $\rho(\vec{p})$  in the Hubbard-Mijnarends method [1,3].

In the case of a muffin-tin type of crystal potential the electron wavefunction,  $\psi_{\vec{k}}(\vec{r})$ , can be expanded in two different ways [13] in the two regions. Inside the inscribed sphere ( $r < r_i$ ) the wavefunction can be expanded in terms of spherical harmonics  $Y_L(\hat{r})$  with  $L \equiv (l, m)$  as follows.

$$\psi_{\vec{k}}(\vec{r}) = \frac{4\pi}{(\tau)^{\frac{1}{2}}} \sum_L i^l \frac{R_l(r)}{R_l(r_i)} X_L Y_L(\hat{r}) \quad (3.16)$$

In the region ( $r > r_i$ ) between the muffin-tin spheres, the electron wave function is expanded in terms of plane waves with  $B_n$  as the coefficients

$$\psi_{\vec{k}}(\vec{r}) = \frac{1}{(\tau)^{\frac{1}{2}}} \sum_n B_n \exp[i(\vec{k} + \vec{K}_n) \cdot \vec{r}] \quad (3.17)$$

The coefficients  $X_L$  in Eq. (3.16) are determined by applying

the continuity condition on  $\psi_{\vec{k}}(\vec{r})$  at  $r=r_i$  to obtain

$$X_L = \sum_n B_n j_l(k_n r_i) Y_L^{\vec{k}} \quad (3.18)$$

One will have to use all  $l$ -values upto infinity to achieve a perfect matching at  $r = r_i$ . In practical computations one truncates the expansion in Eq. (3.16) [and hence in Eq. (3.18)] at a finite value of  $l$  (usually  $l_{\max} = 3$ ) and this gives rise to a slight discontinuity at  $r=r_i$ .

In the fast approximation scheme of Hubbard [1-3] the expression for  $A_j(\vec{k}, \vec{p})$  can be simplified by using Eq. (3.16) and (3.17) to obtain

$$\begin{aligned} A_j(\vec{k}, \vec{p}) = & \sum_n B_n \delta(\vec{k}_n - \vec{p}) - \frac{4\pi r_i^2}{\tau} \frac{j_l(|\vec{k}_n - \vec{p}| r_i)}{|\vec{k}_n - \vec{p}|} \\ & + \frac{(4\pi)^2}{\tau} \sum_l \sum_m \frac{X_{lm}}{R_l(r_i)} Y_{lm}(\vec{p}) \int_0^{r_i} j_l(pr) R_l(r) r^2 dr \end{aligned} \quad (3.19)$$

In the present calculations for vanadium we have used Eq. (3.1) and (3.19) as the basis to compute the EMD,  $\rho(\vec{p})$  due to the band  $(3d)^n(4s)^{5-n}$  electrons. The EMD due to the inner or core electron  $[(1s)^2(2s)^2(2p)^6(3s)^2(3p)^6]$  states can be calculated by using Hartree-Fock wavefunctions and such results are available in literature [18].

### 3.4 Computational Details

The course of the present computations progressed along the following stages.

#### 3.4.1 Calculation of the muffin-tin crystal potential for vanadium

The starting point of our calculation was the choice of a muffin-tin potential. Using the lattice constant  $a$  for metallic b.c.c. V as  $a = 5.74509$  a.u. and the radius of inscribed sphere  $r_i = 2.4877$  a.u. we have done complete calculations for two different muffin-tin potentials for V. The first one (called V1 hereafter) was taken from the calculation of Mijnders [19]. This potential  $V_1(r)$  was constructed by Mijnders by using neutral-free-atom charge densities for the  $(3d)^3(4s)^2$  electron configuration obtained by a relativistic calculation [19,20]. The exchange potential was included with  $\alpha = 2/3$ , following Gaspar, Kohn and Sham [21]. Using Löwdin alpha expansion [22] atomic charge densities upto 13th nearest neighbours were superimposed. The potential was not made self-consistent. The constant potential between the inscribed spheres  $V_0$  was obtained as  $V_0 = -1.7106$  Ry. The potential was constructed on a Herman-Skillman mesh [23]. The quantity  $rV_1(r)$  normalised to unity at  $r = 0$  on a coarse mesh is shown in Table 3.1.

Table 3.1. The normalised muffin-tin potential ( $rV_l(r)/2Z$ )

Sl. No.	r in a.u.	$rV_l(r)/2Z$
1	0.00000	1.00000
2	0.00194	0.99333
3	0.00389	0.98659
4	0.00778	0.97297
5	0.01167	0.95940
6	0.01945	0.93283
7	0.02724	0.90743
8	0.04280	0.86063
9	0.05837	0.81859
10	0.08950	0.74545
11	0.12063	0.68374
12	0.18289	0.58433
13	0.24516	0.50756
14	0.36968	0.39711
15	0.49421	0.31822
16	0.74326	0.21103
17	0.99231	0.14012
18	1.49042	0.06129
19	1.98853	0.02303
20	2.98474	0.00132

A second type of muffin-tin potential (designated V2) was constructed by us following the method of Bhatnagar [24]. We employed an electron configuration  $(3d)^4(4s)^1$  and full Slater exchange  $\alpha=1$ . Our efforts to use  $\alpha = 2/3$  for this calculation of V2 (configuration  $3d^4 4s^1$ ) were not successful because of the computational difficulties in the Hubbard scheme. This point would be taken up again in the next Chapter when we shall discuss the results of our calculations. For the case of V2 the neutral free-atom-charge densities were calculated employing the wavefunctions of Herman and Skillman [23]. Löwdin's alpha expansion scheme [22] was again used to superimpose charge densities upto 13th nearest neighbours. No attempt was made to make the potential self-consistent. The constant interstitial potential was obtained as  $V_{02} = -1.5896$  Ry. Table 3.2 tabulates normalised  $rV2(r)$  for this second potential.

Towards the end of our computations we received the numerical values of the self-consistent muffin-tin potential used by Papaconstantopoulos et al. [25]. This potential (called hereinafter as V3) used the Gaspar-Kohn-Sham exchange parameter  $\alpha = 2/3$  and was constructed for the normal lattice constant ( $a = 5.713$ , the value used in Ref. 25).

In Table 3.3 we have summarised some important numerical data about the three potentials V1, V2 and V3. As explained

Table 3.2 . Normalised muffin-tin potential ( $rV_2(r)/2Z$ )

Sl.No.	r in a.u.	( $rV_2(r)/2Z$ )
1	0.00000	1.00000
2	0.00194	0.99405
3	0.00389	0.98799
4	0.00778	0.97566
5	0.01167	0.96319
6	0.01945	0.93836
7	0.02724	0.91418
8	0.04280	0.86861
9	0.05837	0.82679
10	0.08950	0.75512
11	0.12063	0.69137
12	0.18289	0.59301
13	0.24516	0.51596
14	0.36968	0.40111
15	0.49421	0.31849
16	0.74326	0.21107
17	0.99231	0.13985
18	1.49042	0.05861
19	1.98855	0.01813
20	2.93474	-0.00216

Table 3.3. Numerical constants for the three potentials for V.

Parameter	$V_1$	$V_2$	$V_3$
a, the lattice const. (a.u.)	5.74509	5.74509	5.713 <sup>‡</sup>
$r_i$ , the muffin-tin radius (Kept as $\frac{1}{2}$ the nearest neighbour distance)(a.u.)	2.4877	2.4877	2.4738 <sup>‡</sup>
Constant potential between the muffin-tin spheres (Ry.)	-1.7106	-1.5896	-1.5498 <sup>‡</sup>
$E_F$ , the Fermi Energy with respect to the zero of the muffin-tin potential (Ry.)	0.746	0.774	0.777 <sup>‡‡</sup>
$\epsilon_d$ , the mean d band energy (the energy at which $\tan \eta_1$ goes through a resonance (Ry.))	0.838	0.863	0.849 <sup>‡‡</sup>
Width of the resonance (Ry.)	0.212	0.184	0.193 <sup>‡‡</sup>

<sup>‡</sup> Taken from Papaconstantopoulos et al. [25]

<sup>‡‡</sup> Obtained by us by using the muffin-tin potential of Papaconstantopoulos [25] in the approximate method of Hubbard [2].



in Chapters 1 and 2 the aim of the present work has been to examine the sensitivity of the EMD,  $\rho(\vec{p})$  and the directional Compton profiles  $J_{hkl}(p_z)$  to the choice of crystal potential, electron configuration etc.

### 3.4.2 Calculation of Phase Shifts and Radial Wavefunctions

After choosing a particular muffin-tin potential for  $V$ , it was interpolated on an Herman-Skillman mesh [23] using  $\Delta x = 0.0003125$ . The next step was the calculation of phase shifts  $\eta_l(E)$  (see Eq. (3.6)), in the energy range  $E = 0.0$  to  $2.0$  Ry, at about 200 energy values situated at an energy interval of  $0.01$  Ry. Values of  $R_l(r)$ , the radial part of the wavefunction was stored on a magnetic tape for further use.

### 3.4.3 Calculation of Energy Eigenvalues ( $E_n$ ), wavefunctions (i.e. $B_n$ and $X_L$ coefficients) and momentum density

The phase shifts  $\eta_l(E)$  and the radial wavefunctions  $R_l(r)$  having been determined we now proceeded to calculate  $E_n$ ,  $B_n$ ,  $X_L$  and  $\rho(\vec{p})$  at each selected  $\vec{k}$ -value by using the scheme [see Eqs. 3.1 to 3.19] described in §3.5. Within the inscribed sphere the wavefunction expansion (Eq. 3.16) was truncated at  $l_{\max} = 3$  while in the interstitial region 141 plane waves were used (Eq. 3.17) to expand the wavefunction.

In his original calculation on the 3d transition metals, Hubbard [2,3] had used  $n_p = 7$  ( $n_p$  being the number of vectors in the preferred set P) for the bcc structures and  $n_p = 4$  for the fcc structures. Later on Kaga [26] compared the results of band structure calculations performed on Pd using the KKR method and Hubbard's method and showed that for Pd the number  $n_p$  should be higher than 4. The results of Kanhere [27] and Harthoorn [8] showed that increasing  $n_p$  from 4 to 14 changed the  $E(\vec{k})$  and  $\rho(\vec{p})$  values significantly for Pd but for Ag the change was within the tolerable limit (e.g.,  $\Delta E \leq 0.01$  Ry, which is the accuracy of the Hubbard's method).

We examined the effect of  $n_p$  on the  $E(\vec{k})$  and  $\rho(\vec{p})$  values obtained for V using the potential VI. It was found that in going from  $n_p = 7$  to  $n_p = 14$  the changes were significant but increasing  $n_p$  from 14 to 19 resulted in less serious differences. Some typical results are shown in Table 3.4. It should be pointed out that the calculations for  $n_p = 19$  were performed at the IBM 370 computer at Kernforschungsanlage Jülich, West Germany [28] which had the requisite larger memory. The effect of changing  $n_p$  on the important energy gaps in V is shown in Table 3.5. The results of Tables 3.4 and 3.5 show that changing  $n_p$  from 14 to 19 causes energy changes within the accuracy of Hubbard's approximate scheme except for the points P where

Table 3.4. Effect of the number ( $n_p$ ) of preferred vectors on energy values of  $V^{\#}$  at some symmetry points.(Energy<sup>##</sup> in Ry.)

		1	2	3	4	5	6
	$n_p$	$\Gamma_1$	$\Gamma_{25'}$	$\Gamma_{25'}$	$\Gamma_{25'}$	$\Gamma_{12}$	$\Gamma_{12}$
F	14	0.225	0.795	0.795	0.795	0.941	0.941
	19	0.228	0.800	0.800	0.800	0.944	0.944
		$H_{12}$	$H_{12}$	$H_{25'}$	$H_{25'}$	$H_{25'}$	$H_{15}$
H	14	0.502	0.503	1.053	1.055	1.055	1.462
	19	0.503	0.503	1.054	1.057	1.057	1.471
		$N_1$	$N_2$	$N_1'$	$N_1$	$N_4$	$N_3$
N	14	0.474	0.670	0.818	0.942	0.971	1.086
	19	0.468	0.673	0.823	0.944	0.972	1.086
		$P_4$	$P_4$	$P_4$	$P_3$	$P_3$	$P_4$
P	14	0.659	0.664	0.666	0.975	0.975	1.400
	19	0.651	0.654	0.654	0.977	0.977	1.282

\* Potential used was V1.

\*\* Values given with respect to the zero of the muffin-tin potential.

Table 3.5. Effect of  $n_p$  on the energy gaps in V.

		Case VI	
		$n_p = 14$	$n_p = 19$
s-d separation	$\Gamma_{25'} - \Gamma_1$	0.570 Ry.	0.572 Ry.
	$H_{25'} - \Gamma_1$	0.830	0.829
d bandwidth	$H_{25'} - H_{12}$	0.552	0.554
	$\Gamma_{12} - \Gamma_{25'}$	0.146	0.146
s-p bandwidth	$N_1' - \Gamma_1$	0.593	0.596
	$H_{15} - \Gamma_1$	1.237	1.243
Occupied bandwidths	$E_F - \Gamma_1$	0.521	0.517
	$E_F - H_{12}$	0.244	0.241

Table 3.5. Effect of the number of preferred vectors  $n_p$  on the EMD of vanadium. Results for some symmetry points  $\vec{k} = \vec{p}$ .

	$n_p$	1	2	3	4	5	6	Total
Γ	14	0.686	-	-	-	-	-	0.686
	19	0.678	-	-	-	-	-	0.678
H	14	0.238	-	-	-	-	0.346	0.238
	19	0.224	0.014	-	-	-	0.344	0.238
N	14	0.200	-	0.385	0.001	-	-	0.200
	19	0.200	-	0.383	0.002	-	-	0.200
P	14	0.343	-	0.013	-	-	0.088	0.356
	19	0.380	-	-	-	-	0.077	0.380

Table 3.7. The set of preferred vectors in units of  $2\pi/a$ .  
In the calculations only the first 14 were used.

---

1	(0,0,0)
2	(0,-1,1)
3	(0,-1,-1)
4	(0,-2,0)
5	(1,-1,0)
6	(-1,-1,0)
7	(-1,0,-1)
8	(-1,1,0)
9	(1,0,1)
10	(1,0,-1)
11	(-1,0,1)
12	(1,1,0)
13	(0,1,1)
14	(0,1,-1)

---

15	(2,0,0)
16	(-2,0,0)
17	(0,2,0)
18	(0,0,2)
19	(0,0,-2)

---

the changes are larger. In Table 3.6 we have shown the effect brought in the EMD,  $\rho_j(\vec{p})$ , due to the individual bands by changing  $n_p$  from 14 to 19. Again these changes are minor at the points  $\Gamma$ , H, N but are serious at the point P. As the memory limitations of the computer (IBM 7044) at IIT Kanpur restricted us from using a larger preferred set we carried out our calculations for  $n_p = 14$ .

The set of the 14 preferred vectors used in our calculations are tabulated in Table 3.7 which also shows the vector numbers 15 to 19 (i.e. the set of 19 vectors) used in testing the effect of  $n_p$ . It should be remembered that by using the set of only 14 vectors we have calculated the EMD within a certain accuracy. However, the inaccuracies (or uncertainties) brought by this limited set is within the limitations of the Hubbard-Mijnarends method.

The results of our calculations for the cases V1, V2 and V3 are discussed in the following chapters. We have used about 80  $\vec{k}$ -points in the 1/48th part of the Brillouin zone (Figs. 3.1 and 3.2) and by choosing suitable  $\vec{k}_i$  vectors we have calculated  $\rho(\vec{p})$  for about 700  $\vec{p}$ -points in the (100) and (110) planes.

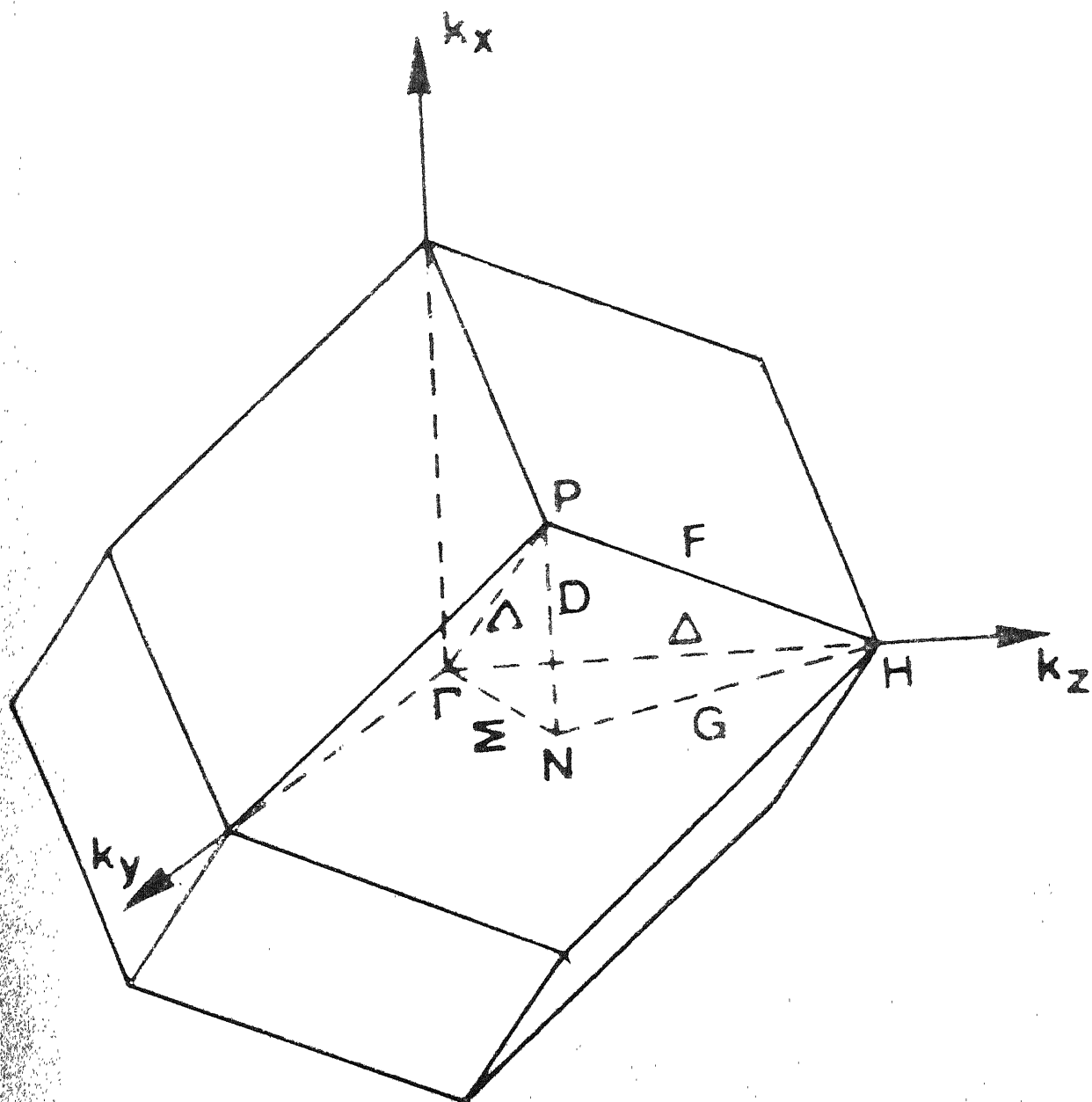


Fig. 3.1 : The 1/48 th part of the first BZ for a bcc metal.



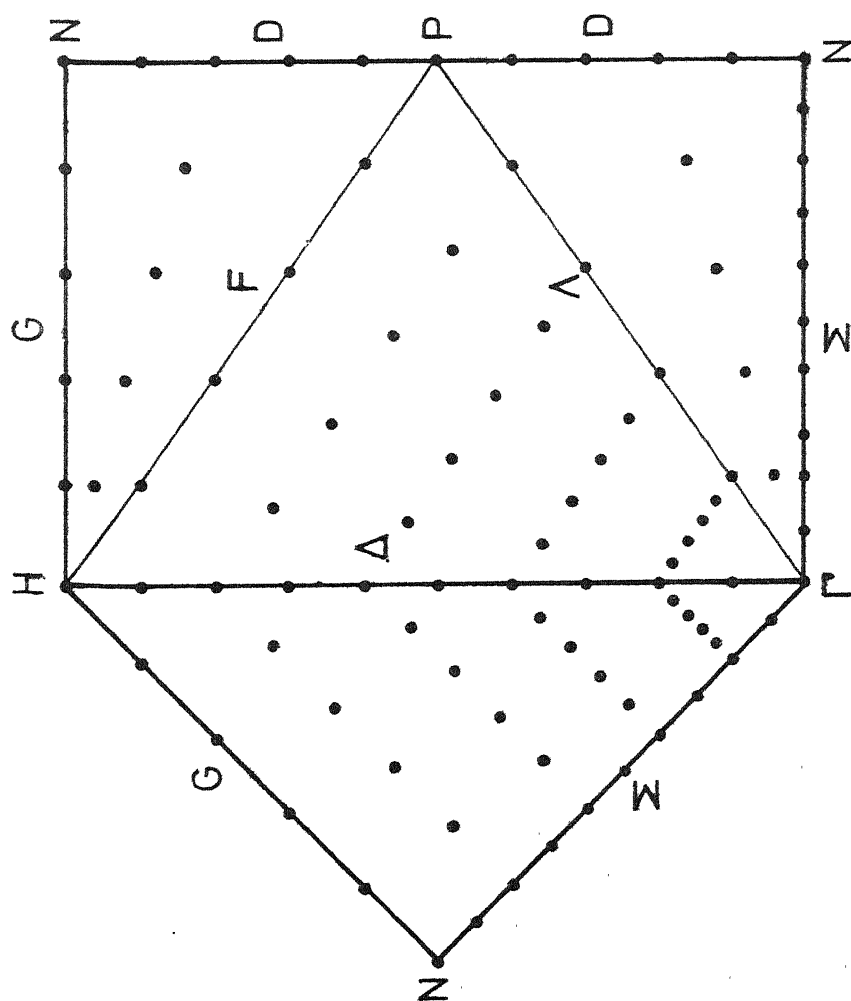


Fig. 3.2 : The  $k$  points in the (100) and (110) planes involved in the calculations of EMD.

19. P. E. Mijnders, 'Construction of a Muffin-Tin Potential for Metallic Vanadium', Report RCN-76-C10, Reactor Centrum Nederland, Petten (N.H.), The Netherlands, 1975. (Unpublished).
20. J. P. Desclaux, Comp. Phys. Comm. 1, 216 (1969) gives a non-relativistic version of this program.
21. R. Gaspar, Acta Phys. Acad. Sci. Hung. 3, 263 (1954); W. Kohn and L. J. Sham, Phys. Rev. 140, A1133 (1965).
22. P. Löwdin, Adv. Phys. 5, 1 (1956), L. F. Mattheiss, Phys. Rev. 133, A1399 (1964).
23. F. Herman and S. Skillman, Atomic Structure Calculations, Prentice Hall, Inc. Englewood Cliffs., New Jersey, 1963.
24. S. Bhatnagar, Phys. Rev. 183, 657 (1969). We are grateful to Dr. S. Tewari (née Bhatnagar) for giving us the computer programs for this calculation.
25. D. A. Papaconstantopoulos, J. R. Anderson and J. W. McCaffrey, Phys. Rev. B5, 1214 (1972).
26. H. Kaga, Phys. Lett., 37A, 373 (1971).
27. D. G. Kanhere, Ph.D. Thesis, Indian Institute of Technology Kanpur (1976); Unpublished.
28. R. M. Singru (Private communication).

## Chapter 4

### ELECTRON MOMENTUM DISTRIBUTION IN VANADIUM: RESULTS AND DISCUSSION

#### 4.1 Introduction

In this Chapter we shall present and discuss the results of our calculations of the bandstructure, Fermi surface (FS) and electron momentum distribution (EMD) in metallic V. The starting point of the calculation was a choice of the muffin-tin crystal potential for metallic V. As explained in §3.4.1, we chose three types of potentials, the basic parameters of which are summarised in Table 4.1. Perhaps it might have been more appropriate to choose  $\alpha=2/3$  while constructing the potential V2 so as to examine the effect of changing the electron configuration alone. Although such a crystal potential for the configuration  $(3d)^4(4s)^1$  and  $\alpha = 2/3$  was constructed by us, we met with serious computational difficulties in calculating the bandstructure using such a potential. These difficulties arise out of the following considerations.

As pointed out in §2.2 the width of the d band in V is increased when the configuration is changed from  $(3d)^3(4s)^2$

Table 4.1. Different muffin-tin crystal potentials  
(for metallic V) used in the present work.

Our label	Reference	Electron configuration	Exchange parameter	Lattice constant $a$ (a.u.)
V1	Mijnarends [1]	$(3d)^3(4s)^2$	$\alpha = 2/3$	5.74509
V2	Present work <sup>‡</sup>	$(3d)^4(4s)^1$	$\alpha = 1$	5.74509
V3	Papaconstantou- poulos [2] <sup>φ</sup>	$(3d)^3(4s)^2$	$\alpha = 2/3$	5.713

<sup>‡</sup> The method of construction of this potential has been given in §3.4.1 and is described by Bhatnagar [3].

<sup>φ</sup> This crystal potential has been constructed in a self-consistent manner.

to  $(3d)^4(4s)^1$ . Similarly the width of the d band is increased by decreasing  $\alpha$  from 1 to  $2/3$  keeping the configuration same. These considerations suggest that in going from the case V1 (where  $\alpha = 2/3$ , and  $(3d)^3(4s)^2$ ) to the case where  $\alpha = 2/3$  and the configuration is  $(3d)^4(4s)^1$  the d band would become much broader. The fast approximate scheme of Hubbard [4] is based on the main assumption that the d bands are narrow. In the case of the 3d metals the d bandwidth for Cu is  $\sim 0.27$  Ry. while for V it is  $\sim 0.55$  Ry. [5]. Thus the case of V falls just near the limit of Hubbard's approximation scheme. If the d band in V, for some crystal potential, becomes much broader than 0.55 Ry. the d band becomes more delocalised and the main assumptions underlying the scheme of Eq. (3.2)-(3.19) break down, giving rise to computational difficulties. In fact our attempts to use Hubbard's fast approximate scheme to calculate the bandstructure of Nb for the case  $\alpha = 2/3$ ,  $(4d)^3(5s)^2$  (which is known to give d bandwidth  $\sim 0.75$  Ry. ) also met with similar difficulties.

To surmount these computational difficulties we used a value of  $\alpha = 1$  in constructing the potential V1. In going from V1 to V2 the increase in the d population and the increase in  $\alpha$  have opposing effect on the d bandwidth and in fact our results [Table 4.2] indicated that the d bandwidth for the case V2 was narrower (by  $\sim 0.04$  Ry.) when compared to that for V1.

The present results for the EMD and Compton profiles (to be discussed later) obtained from the potentials V1 and V2 show similarities and suggest that experimentally one may not be able to distinguish between the cases V1 and V2. Recently, a comparison of the experimental Compton profile data for some 3d metals has been made with the RFA model calculations [6] to conclude that a particular electron configuration [o.g., Ti:(3d)<sup>2</sup>(4s)<sup>2</sup>, V:(3d)<sup>3</sup>(4s)<sup>2</sup>] is supported by the Compton profile data. The results of our calculation would show that for a more realistic comparison with the experiment, a bandstructure calculation (involving a choice of the electron configuration as well as the exchange parameter) is necessary. It will be shown that although crystal potentials can be different, the electron configuration and the exchange parameter  $\alpha$  can combine to give similar results for the EMD. Besides this effect, the sensitivity of the EMD in V to the bandstructure and FS will be discussed in detail.

#### 4.2 Energy Bands and Bandwidths

The bandstructure diagrams obtained by us along the principal symmetry directions of V using the crystal potentials V1, V2 and V3 are shown in Figs. 4.1-4.6. There is a close similarity in the results for the cases V1 and V2 while the results for V3 are also similar except along the

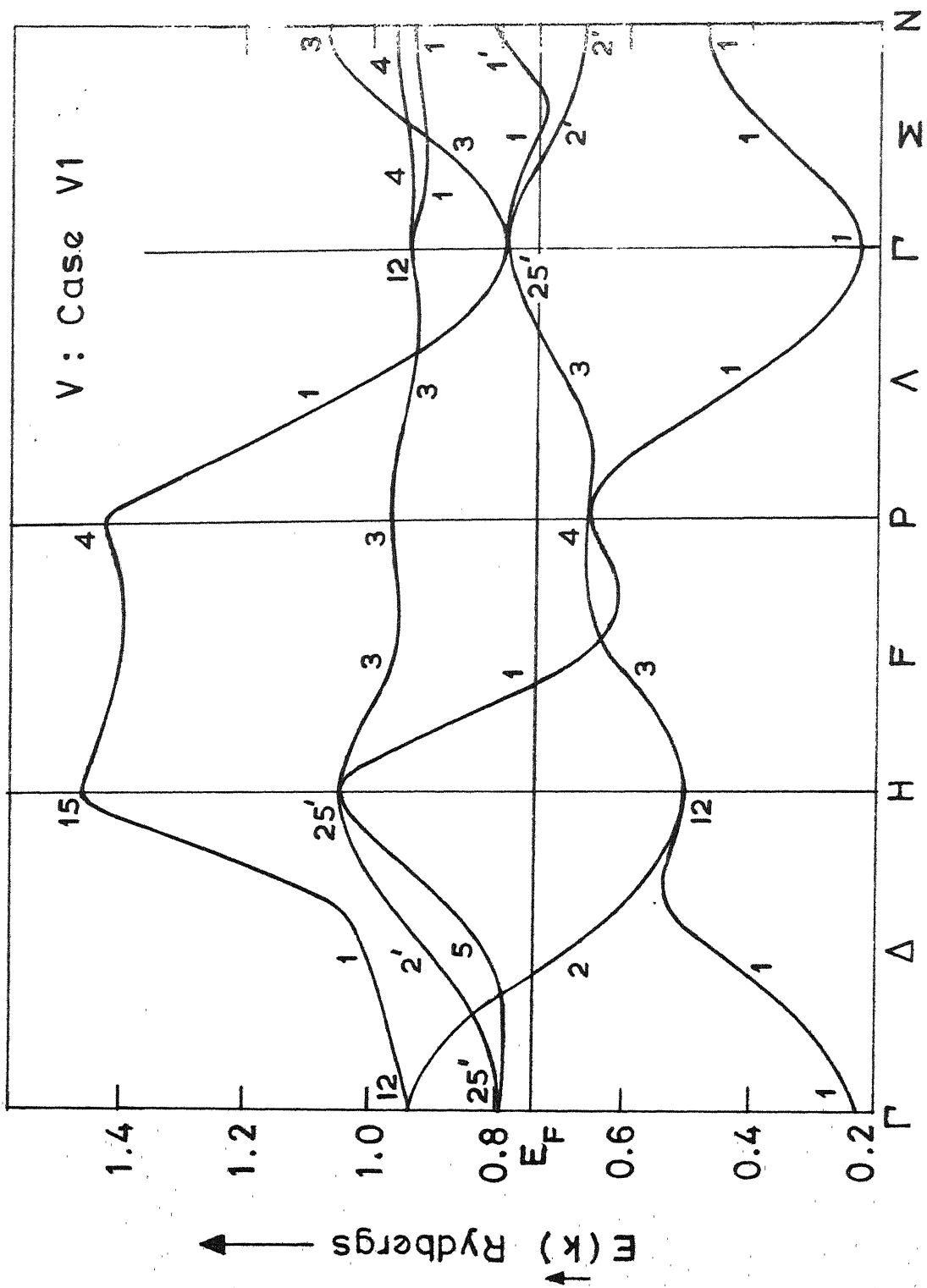
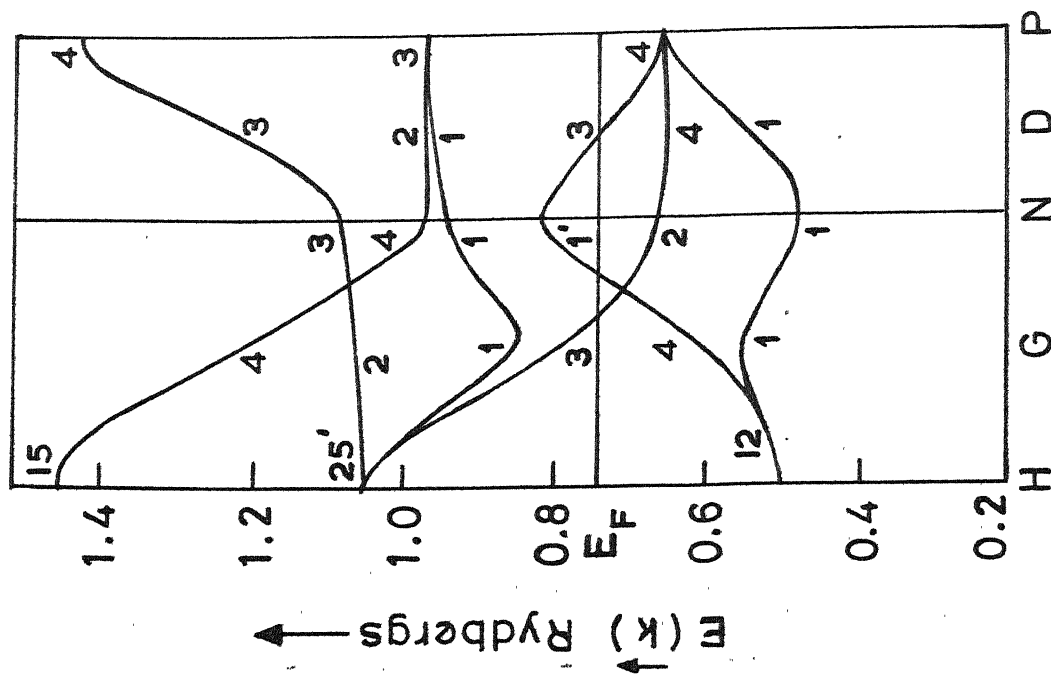


Fig. 1.1: The energy bands of vanadium along the principal



V : Case V1

Fig. 4.2 : The energy bands of vanadium along the principal symmetry



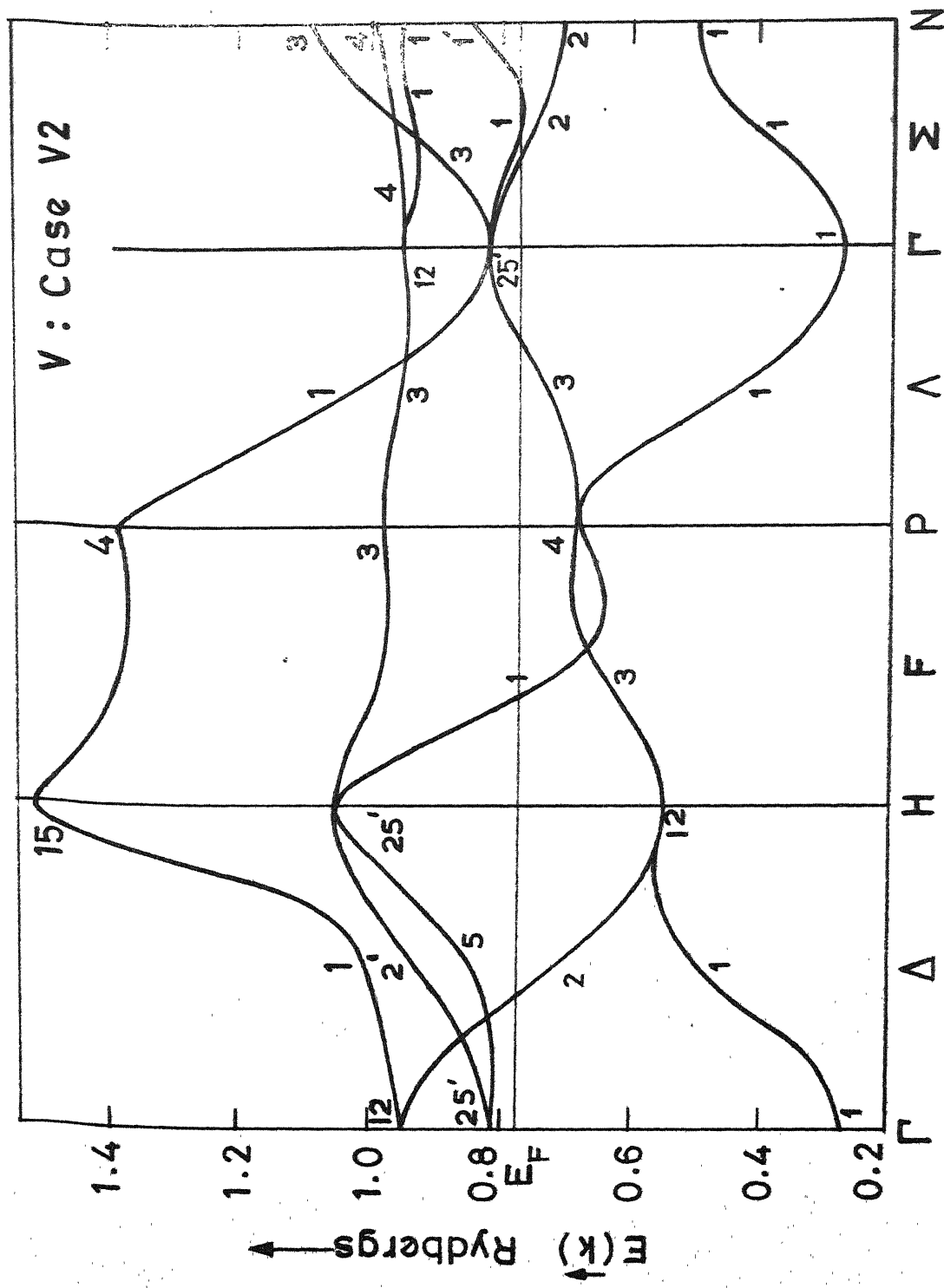


Fig. 4.3 : The energy bands of vanadium along the principal

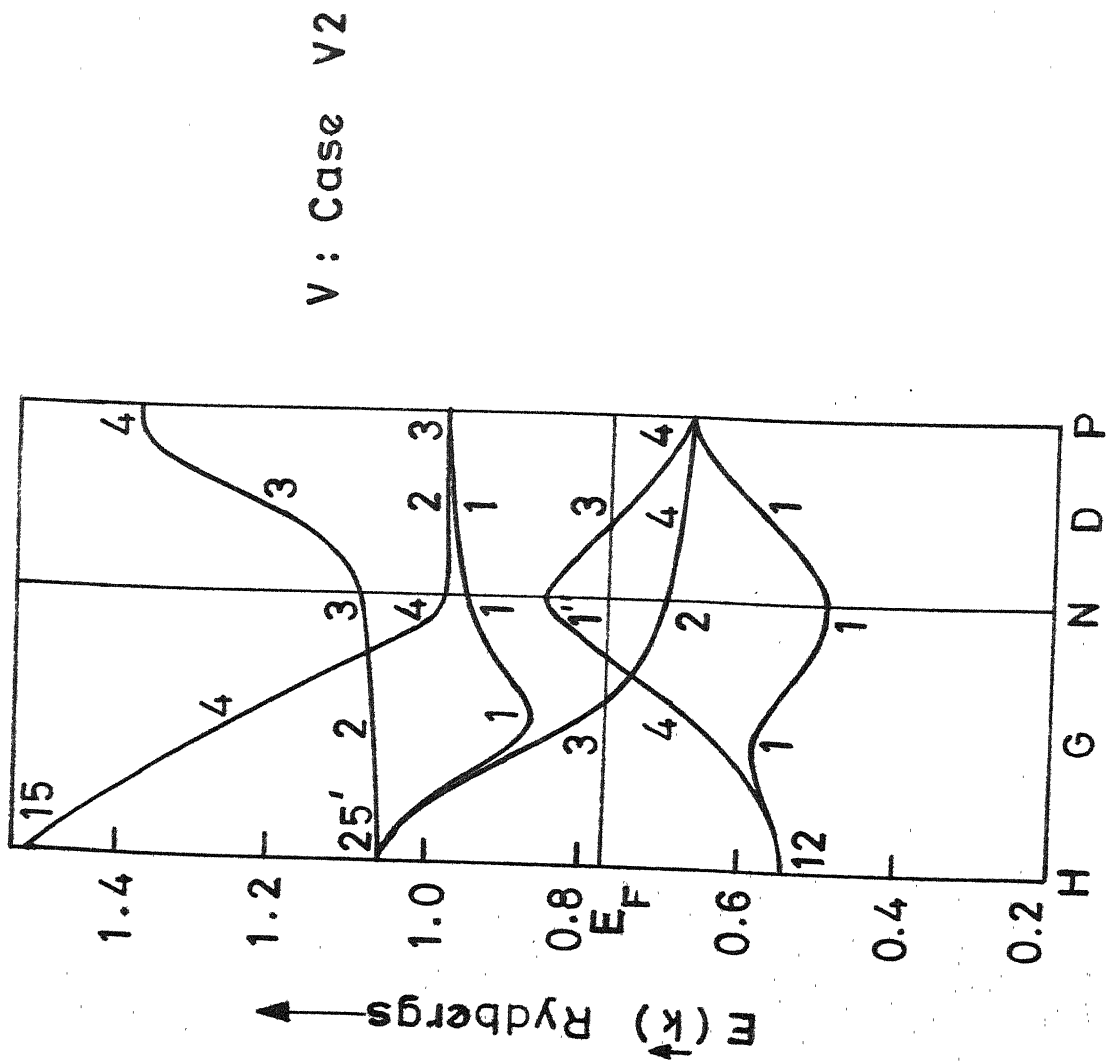


Fig. 4.4 : The energy bands of vanadium along the principal

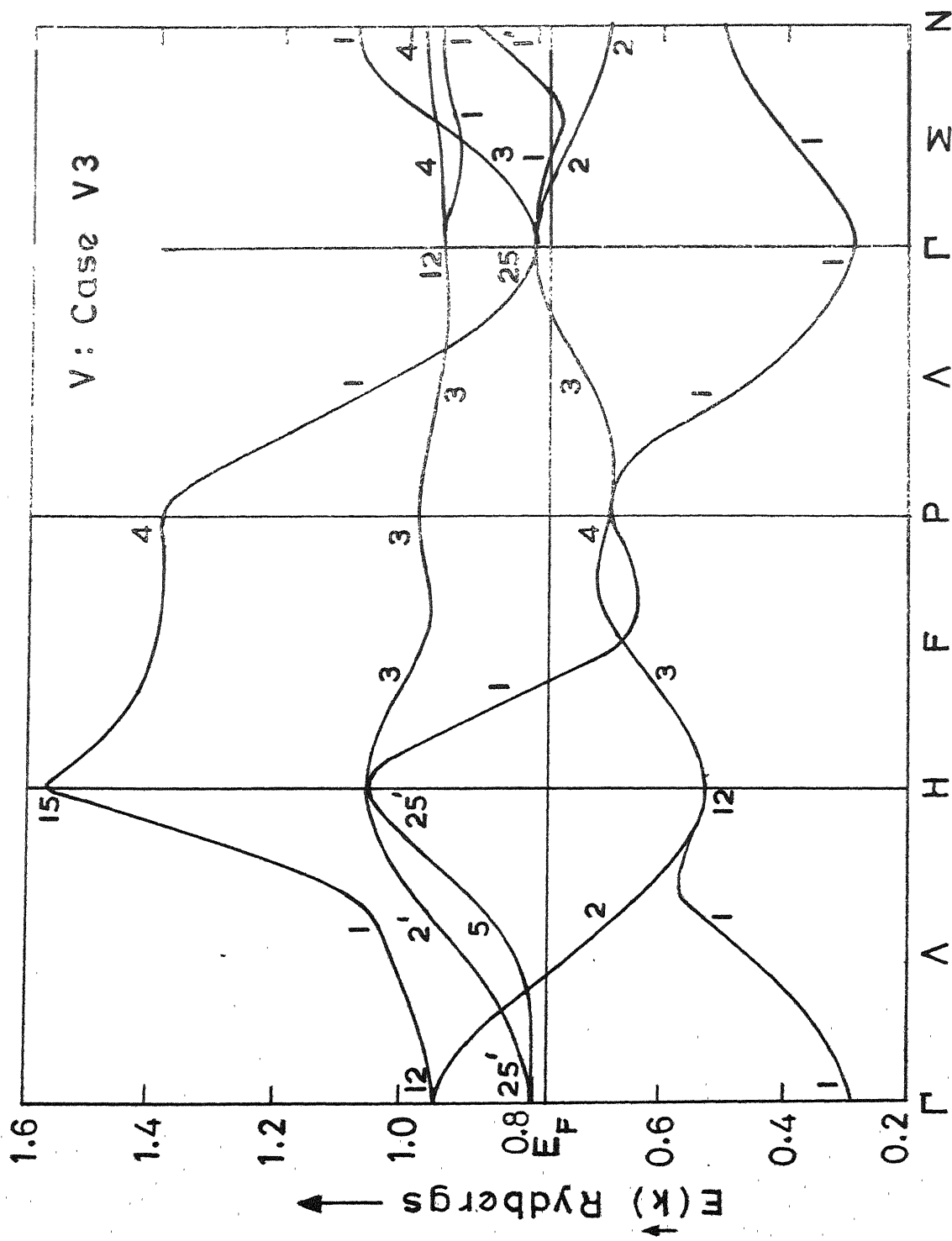


Fig. A.5 : The energy bands of vanadium along the principal symmetry axes (see Fig. 1).

V : Case V3

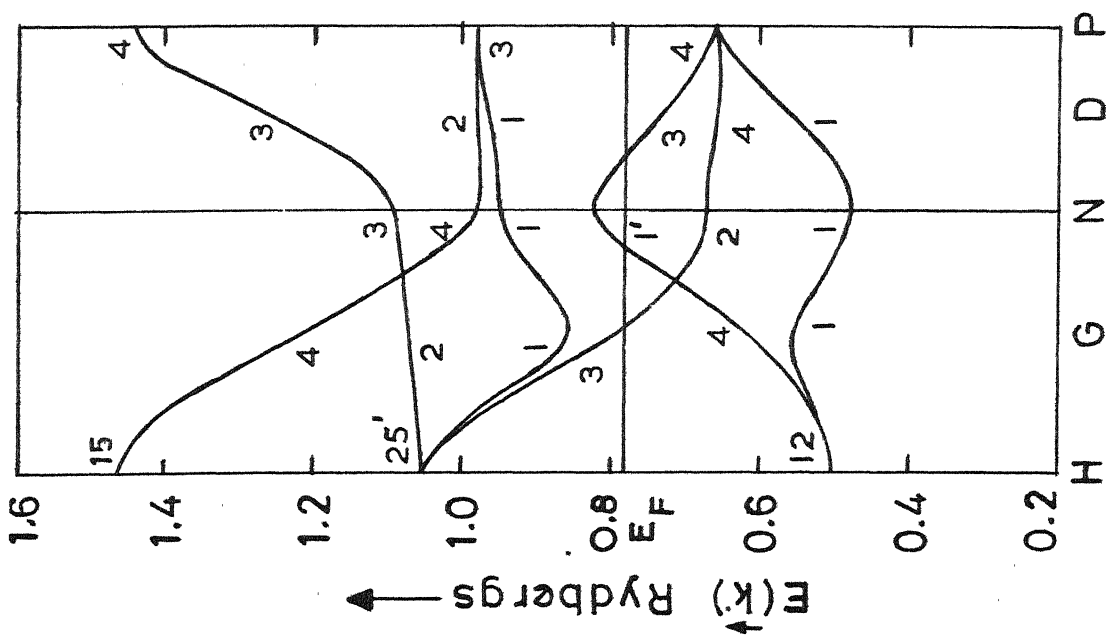


Fig. 2.5 : The energy bands of vanadium along the principal symmetry axes (case V3).

Table 4.2. Comparison of energy bandwidths (in Rydbergs) for V

Method and reference	s-d separation		d bandwidth		s-p bandwidth	
	$\Gamma_{25'} - \Gamma_1$	$H_{25'} - \Gamma_1$	$H_{25'} - H_{12}$	$\Gamma_{12} - \Gamma_{25'}$	$N_1 - \Gamma_1$	$H_{15} - \Gamma_1$
APW Papaconstantopoulos et al. [2]	0.543	0.791	0.535	0.140	0.583	1.220
KKR Wakoh and Yamashita [7]	0.521	-	0.437	0.157	0.580	-
Present work case V1*	0.570	0.830	0.552	0.146	0.593	1.237
Present work case V2	0.554	0.793	0.515	0.134	0.585	1.250
Present work case V3	0.514	0.768	0.531	0.142	0.608	1.277
Present work case V4**	0.446	0.653	0.438	0.120	0.565	1.228

\* These results are different from those reported by Mijnaerends [1] because the value of  $n_p$  (number of preferred vectors) in the two calculations are not same. See §3.4.3 for details.

\*\*  $(3d)^3(4s)^2$ ;  $\alpha = 1$ .

Table 4.3. Energy values for the various symmetry points (energies given in Rydbergs with respect to the zero of the muffin-tin potential).

a)  $\Gamma$

Reference	$\Gamma_1$	$\Gamma_{25'}$	$\Gamma_{12}$	$E_F$
$V1^\#$	0.225	0.795	0.941	0.746
$V2^\#$	0.263	0.817	0.951	0.774
$V3^\#$	0.288	0.802	0.944	0.777
Ref.[2]	0.269	-	-	-

b) H

Reference	$H_{12}$	$H_{25'}$	$H_{15}$
$V1^\#$	0.502	1.055	1.462
$V2^\#$	0.541	1.056	1.513
$V3^\#$	0.525	1.056	1.563
Ref.[2]	0.525	-	-

c) N

Reference	$N_1$	$N_2$	$N_1'$	$N_1$	$N_4$	$N_3$
$V1^\#$	0.474	0.670	0.818	0.942	0.971	1.086
$V2^\#$	0.500	0.702	0.848	0.950	0.979	1.085
$V3^\#$	0.495	0.684	0.896	0.944	0.973	1.087
Ref.[2]	0.523	0.692	-	-	-	-

d) P

Reference	$P_4$	$P_3$
$V1^\#$	0.664	0.975
$V2^\#$	0.680	0.982
$V3^\#$	0.680	0.976
Ref.[2]	0.680	-

$^\#$  Present work.

$\Sigma$  direction and their general features compare well with the band structure of V reported by Papaconstantopoulos [2] using the APW method and by Wakoh and Yamashita [7] using the KKR method. A detailed comparison between various results is made in terms of the bandwidths in Table 4.2 and in terms of the  $E(\vec{k})$  values in Table 4.3. Comparing the results for the cases V1 and V2 we note that the potential V1 produces larger d bandwidth and s-d separation. Potential V3 resulted in smaller s-d separation. We have also calculated the d bandwidth for the fourth type of crystal potential V4 involving the case  $(3d)^3(4s)^2$ ,  $\alpha = 1$  (results shown in Table 4.2). These results indicated that the increase in the d bandwidth in going from  $(3d)^3(4s)^2$ ,  $\alpha = 1$  to  $(3d)^4(4s)^1$ ,  $\alpha = 1$  is smaller than in going from  $(3d)^3(4s)^2$ ,  $\alpha = 1$  to  $(3d)^3(4s)^2$ ,  $\alpha = 2/3$ . It is thus seen that the bandstructure of V responds more sensitively to the changes in the exchange parameter  $\alpha$  than to the changes in the 3d population. We found that the d bandwidth increases in the following order: (i)  $(3d)^3(4s)^2$ ,  $\alpha = 1$ , (ii)  $(3d)^4(4s)^1$ ,  $\alpha = 1$ , (iii)  $(3d)^3(4s)^2$ ,  $\alpha = 2/3$  and (iv)  $(3d)^4(4s)^1$ ,  $\alpha = 2/3$ . In the last case the d bandwidth goes beyond the limits of the applicability of the Hubbard's approximation scheme.

Comparing the results (Table 4.2) for the same potential (V3) obtained by the APW method (2) and by the present calculations we find that although the d bandwidth is about the same,

our results show a smaller s-d separation and larger s-p bandwidth. These differences are perhaps arising out of the different accuracies of the APW method and Hubbard's fast approximation scheme.

### 4.3 Fermi Surface of Vanadium

In view of the limited accuracy (0.005-0.01 Ry.) of our bandstructure calculation we adopted an approximate method due to Burdick [8] to determine the Fermi energy,  $E_F$ . Using a three-dimensional mesh of 56  $\vec{k}$ -points in 1/48th part of the Brillouin zone we calculated the  $E(\vec{k})$  values for the lowest 6 bands. These energy values were arranged in an array of ascending order, by giving each  $\vec{k}$  an appropriate weight arising from the number of like vectors  $N(\vec{k})$  for each  $\vec{k}$ . Starting from the bottom of the array the energy values  $E(\vec{k})$  of the  $[N(\vec{k})x\frac{1}{2}xn_b]$ th and the next state (where  $n_b$  = number of band electrons,  $n_b = 5$  for V) were found. The average of these two values was taken as the Fermi energy  $E_F$  and is shown in Table 4.3. The density-of-states histogram (using  $\Delta E = 0.02$  Ry.) for the case V1 is shown in Fig. 4.7 and it shows the same general features as that obtained by a detailed calculation [9]. Using these values of  $E_F$  and our bandstructure results we obtained the Fermi surface of V graphically. The central crosssection of the FS in the (100) and (110) planes of V for the cases V1, V2



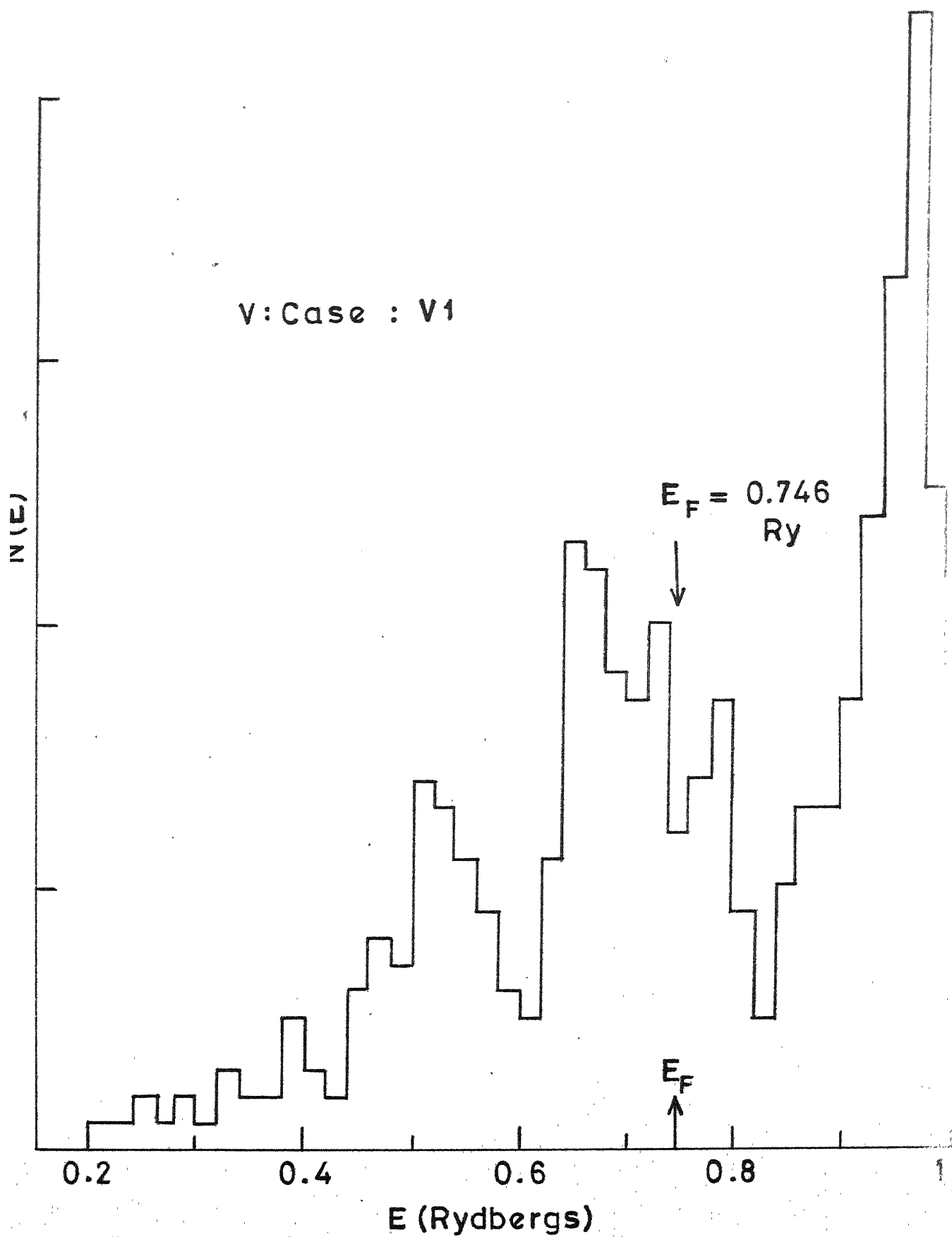


Fig. 4.7 : The density of states histogram for vanadium (case V1).

# Fermi surface of V: Case V1

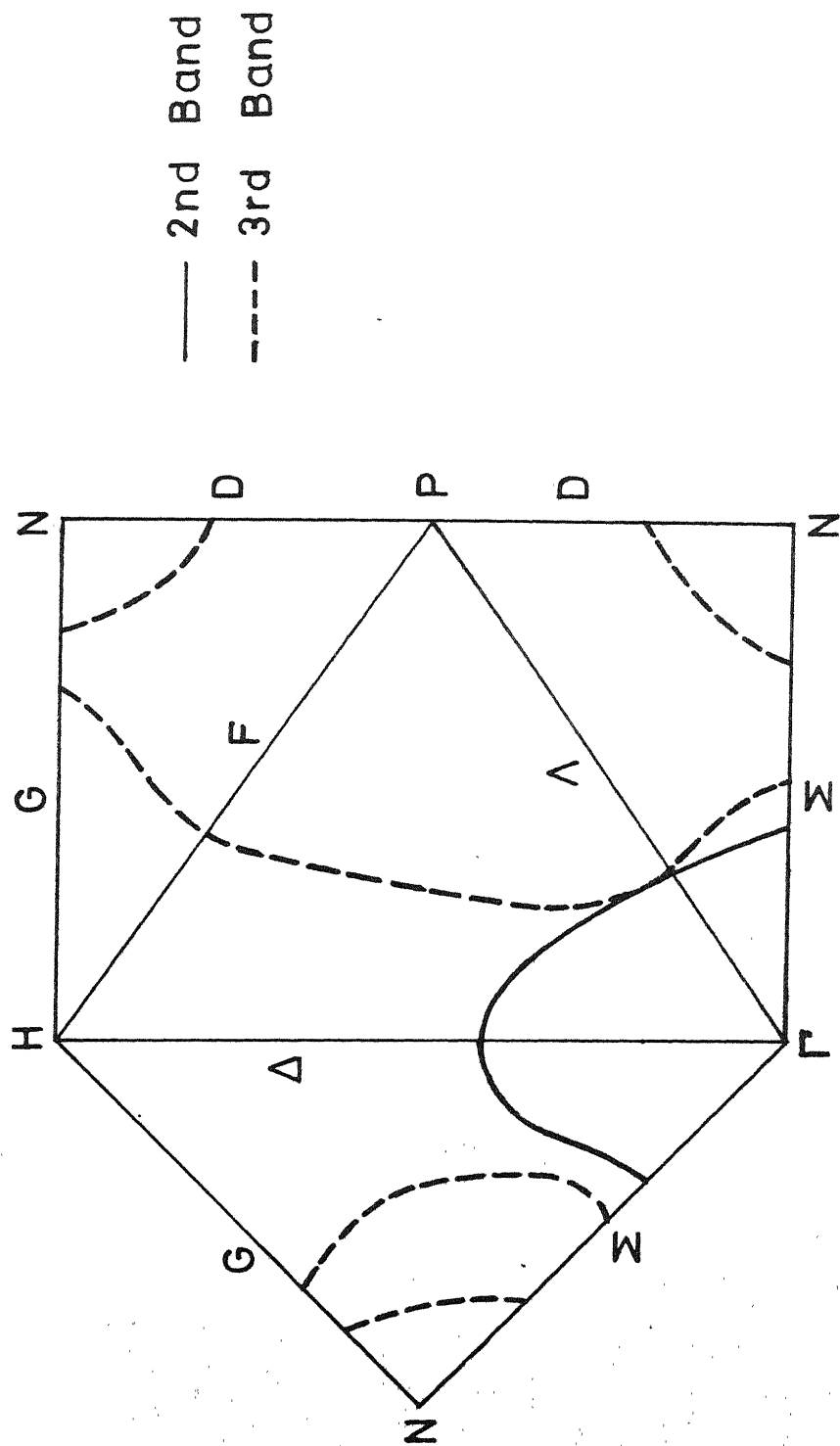


Fig. 4.3 : The cross-section of the  $F^*$  of vanadium in the (100) and (110) planes (case V1).

# Fermi surface of V: case V2

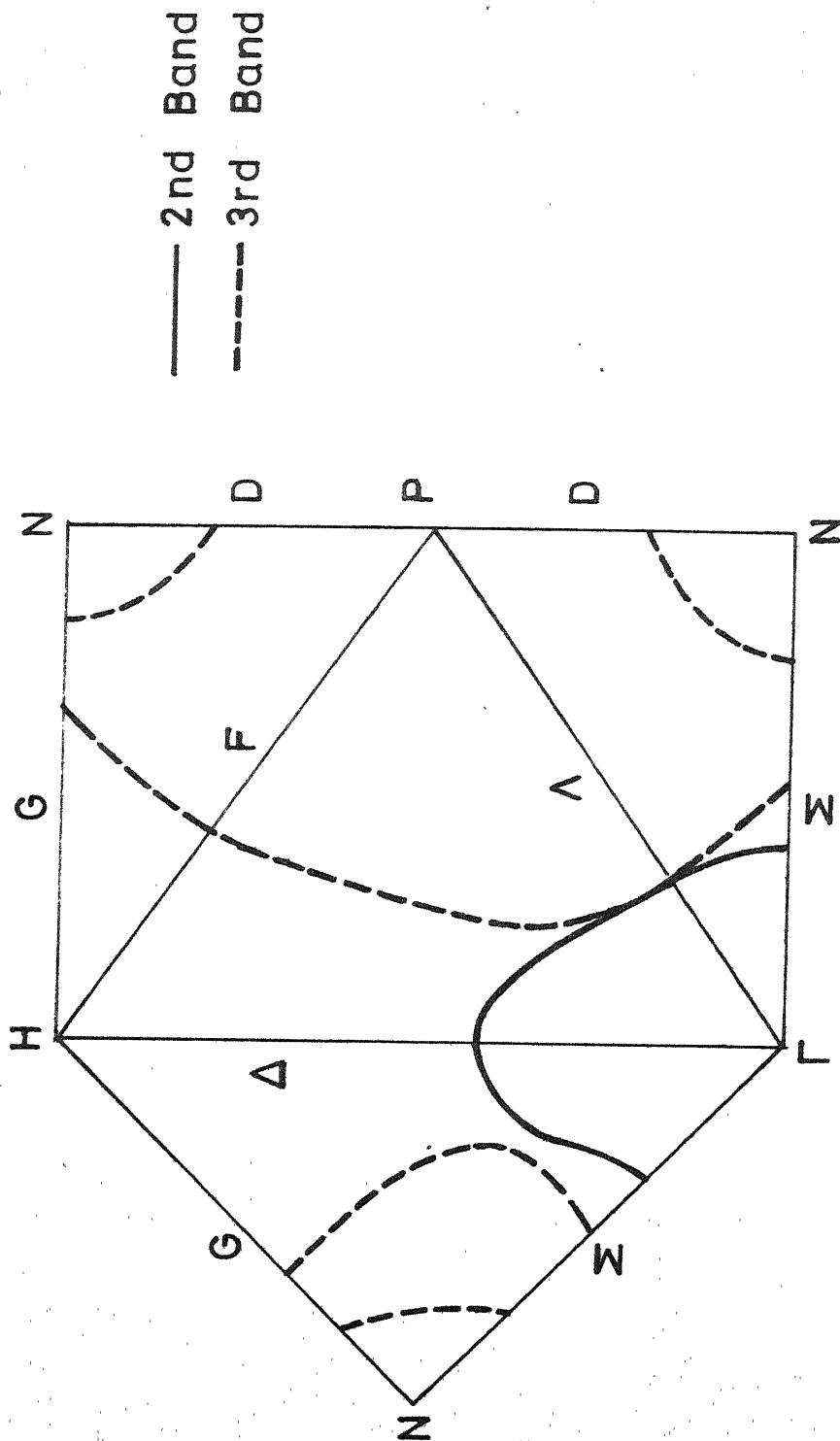


Fig. 4.9 : The cross-section of the FS of vanadium in the (100) and (110) planes (case V2).

# Fermi surface of V: case V3

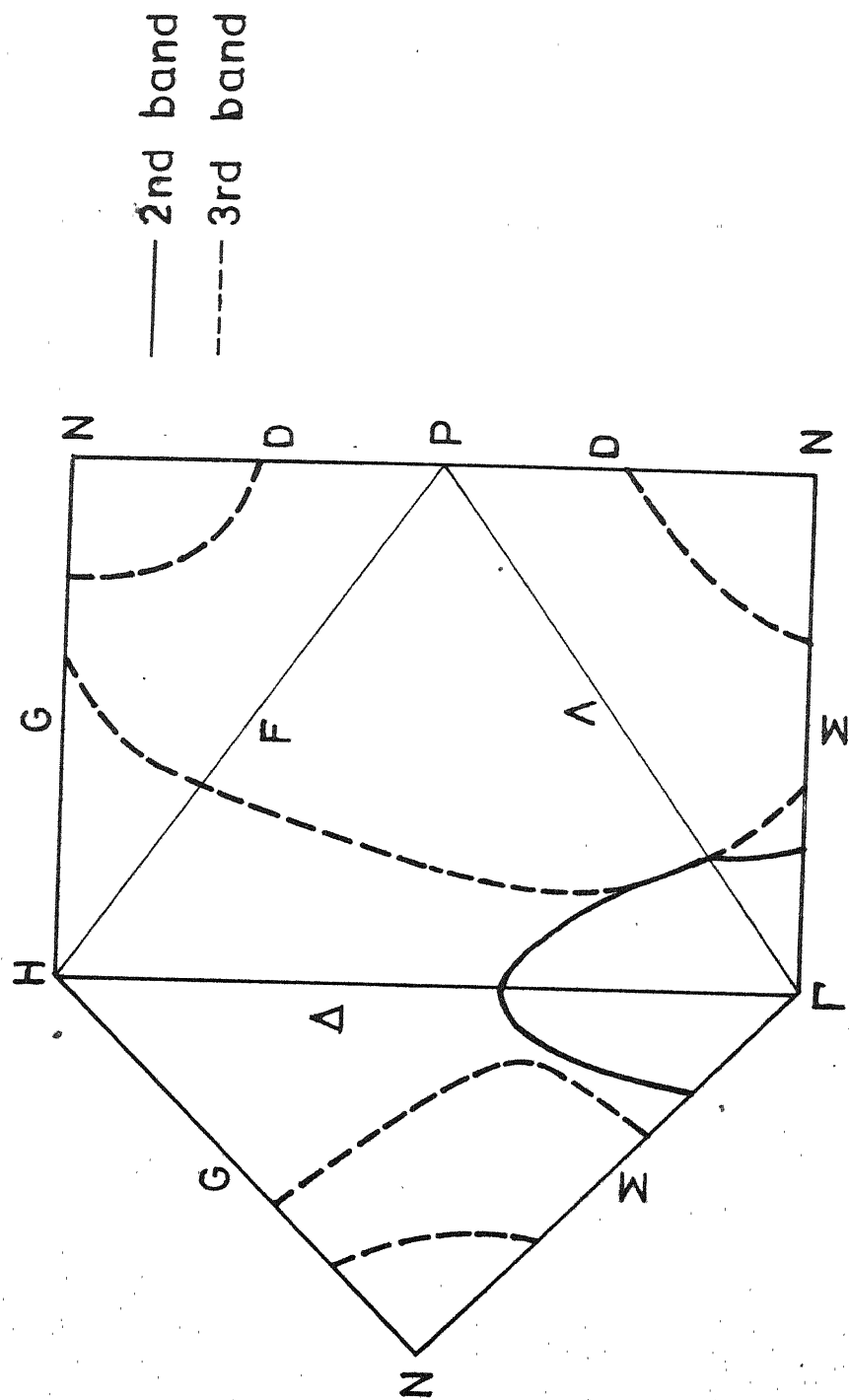


Fig. 4.10 : The cross-section of the FS of vanadium in the (100) and (110) planes (case V3).

and V3 is shown in Figs. 4.8, 4.9 and 4.10 respectively. Except for some minor differences the FS results for the cases V1, V2 and V3 agree with each other and display the familiar features (i.e.  $\Gamma$ -centered octahedral hole surface, jungle-gym hole arms and N-centered hole ellipsoids as described in Chapter 2) common to the FS of the group VB metals. When compared to the results obtained by Mattheiss [10] using the bands for W and by Wakoh and Yamashita [7], the present results show similar topology except for the accidental degeneracy in the (100) plane (between the second and third band) which is not observed by us. In this respect our results agree better with the FS topology obtained by Papaconstantopoulos et al. [2].

We have not calculated the FS areas of various orbits etc. as we were not primarily concerned with the de Haas-van Alphen data. However, a rough estimate of the size and the shape of the ellipsoid centered on N can be obtained from the ratio of the semiaxes along the N-P, N- $\Gamma$  and N-H directions. We obtained the ratios  $N-\Gamma/N-P = 0.92$  and  $N-\Gamma/N-H = 1.34$  for the case V1 and  $N-\Gamma/N-P = 0.87$  and  $N-\Gamma/N-H = 1.33$  for the case V2. For V3, the corresponding values were 0.90 and 1.40 respectively. These values may be compared with the values  $N-\Gamma/N-P = 0.946$  and  $N-\Gamma/N-H = 1.21$  obtained experimentally by Parker and Halloran [11]. In view of the approximate nature of our method, these differences are not so serious.

It may be pointed out that in all the three cases V1, V2 and V3, we observe the higher  $\Sigma_1$  band dipping below the Fermi level (Figs. 4.1, 4.3 and 4.5) by an amount varying between 0.010-0.020 Ry. The present results for the three bandstructures, therefore, do not support the possibility of narrow necks (along  $\Gamma$ -N) connecting the jungle-gym hole arms to the ellipsoids (see §2.3).

#### 4.4 Electron Momentum Distribution in Vanadium

##### 4.4.1 Introduction

We shall now discuss the results of the electron momentum distributions (EMD) obtained by us for the crystal potentials V1, V2 and V3, in terms of their bandstructure. Such a discussion becomes more meaningful when it is carried out on the basis of the symmetry direction involved and towards this aim we shall present our results according to the symmetry direction (i.e.  $\langle 100 \rangle$  etc.) involved.

As discussed in §1.4.3 the total EMD

$$\rho(\vec{p}) = \sum_j^{\text{occ}} \rho_j(\vec{p}) \quad (4.1)$$

(where  $j$  is the band index) at a point  $\vec{p} = \vec{k} + \vec{K}_1$  is determined by  $|A_j(\vec{k}, \vec{p})|^2$  [see Eq. (1.18)]. The magnitude of  $|A_j(\vec{k}, \vec{p})|^2$  is, in turn, determined by the nature of the band wavefunction  $\psi_{\vec{k}, j}^{\vec{p}}(\vec{r})$ , through Eq. (1.19), as well as by the

reciprocal lattice vector  $\vec{K}_i$  involved in constructing the momentum vector  $\vec{p} = \vec{k} + \vec{K}_i$ . A third important effect on the  $|A_j(\vec{k}, \vec{p})|^2$  was not discussed in Chapter 1 and it arises from the group theoretical selection rule pointed out by Mijnaerends [12,13]. To understand this rule one writes  $A_j(\vec{k}, \vec{p})$  as

$$A_j(\vec{k}, \vec{p}) = N \sum_i \delta(\vec{p} - \vec{k} - \vec{K}_i) \int_{\text{cell}} e^{-i\vec{p} \cdot \vec{r}} \psi_{\vec{k}, j}(\vec{r}) d\vec{r} \quad (4.2)$$

The symmetry properties of  $A_j(\vec{k}, \vec{p})$  are determined by the behaviour of  $A_j$  under the operations  $R$  of  $G_0(\vec{k})$ , the group of  $\vec{k}$  [14]. The function  $\psi_{\vec{k}, j}$  is the basis function for the irreducible representation  $r^j$  of  $G_0$ . The integral in Eq. (1.19) will then be non-vanishing only if the term  $\exp(-i\vec{p} \cdot \vec{r})$  contains a part which transforms according to the same representation. To test this we define a projection operator

$$\mathcal{P}^j = (l_j/h) \sum_R x^j(R)^* P_R \quad (4.3)$$

where  $l_j$  denotes the dimension of  $r^j$ ,  $h$  is the order of  $G_0(\vec{k})$ ,  $x^j(R)$  indicates the character of the operation  $R$  for this representation and  $P_R$  is the operator corresponding to  $R$ . The projection operator  $\mathcal{P}^j$ , by operating on a function  $\phi_{\vec{p}}$ , will project out of  $\phi_{\vec{p}}$  that part which belongs to  $r^j$ . If it so happens that  $\mathcal{P}^j \exp(-i\vec{p} \cdot \vec{r}) = 0$ , the exponential term does not contain such a part and  $A_j(\vec{k}, \vec{p}) = 0$  for this

particular  $\vec{p}$ . If however  $\oint \vec{j} \exp(-i\vec{p} \cdot \vec{r}) \neq 0$  the symmetry considerations allow  $A_j(\vec{k}, \vec{p})$  to be non-vanishing. Application of this selection rule is very important while analyzing the effects of bandstructure on the EMD due to the individual bands.

The above selection rule when applied to the bcc structure (cubic space group  $O_h^9$ ) gives the following interesting results [13]. For a  $\vec{p}$ -direction along the  $\langle 100 \rangle$  direction (if  $\vec{p} = \vec{k}$  in the first zone or  $\vec{p}$  is parallel to  $\vec{k}$  in a higher zone) only the bands of  $\Delta_1$  symmetry will give a non-vanishing contribution (during its occupied part) to  $A_j(\vec{k}, \vec{p})$  while the other  $\Delta$  bands (e.g.  $\Delta_2$ ,  $\Delta_5$ , etc.) will give  $A_j(\vec{k}, \vec{p})$  which is identically zero. Along the  $\langle 110 \rangle$  direction only the  $\Sigma_1$  bands and along the  $\langle 111 \rangle$  direction only the  $\Lambda_1$  band (between  $\Gamma$  and P) and  $F_1$  band (between P and H) may contribute to  $A_j(\vec{k}, \vec{p})$ . A more detailed discussion of the effects of this selection rule is given by Harthoorn and Mijnaerends [13] and we have summarised in Table 4.4 some of their results which are relevant for our discussion.

To summarise, therefore, the partial contribution to the momentum density at momenta  $\vec{p}$ , due to an electron belonging to the  $j$ th band is determined by the following considerations:

- (i) The relation  $\vec{p} = \vec{k} + \vec{K}_1$ ,
- (ii) Whether the  $j$ th band is occupied or unoccupied at  $\vec{k}$ ,



Table 4.4. Some<sup>\*</sup> energy bands allowed by the symmetry selection rule to contribute to the EMD at momenta  $\vec{p}$  for the bcc lattice. Based on Ref. [13].

$p_x$	$\vec{p}$		Observable bands
	$p_y$	$p_z$	
0	0	$\xi$	$A_1, H_1, H_{12}, H_{15}$
0	$\xi$	$\xi$	$\Sigma_1, N_1, N_1^i$
$\xi$	$\xi$	$\xi$	$A_1, H_1, H_{15}, H_{21}, H_{25},$ $P_1, P_4, F_1$
0	$\xi$	$\eta$	$(\Gamma HN)_+$
$\xi$	$\eta$	$\eta$	$(\Gamma HP)_+, (\Gamma NP)_+$
$\xi \neq 0, \eta \neq 0$			

<sup>\*</sup>List not exhaustive. See Ref. [13] for a more exhaustive tabulation.

- (iii) Nature of the wavefunction  $\psi_{\vec{k}, j}(\vec{r})$ ,
- (iv) Whether the selection rule allows the  $j$ th band (having a particular symmetry) to contribute to  $A_j(\vec{k}, \vec{p})$  or not.

We shall apply the above considerations while analyzing the results of the EMD.

#### 4.4.2 EMD along the $\langle 100 \rangle$ direction

The EMD,  $\rho(\vec{p})$ , along the  $\langle 100 \rangle$  direction in V is shown in Figs. 4.11, 4.12 and 4.13 for the potentials V1, V2 and V3 respectively. The relevant bandstructure (along the  $\Delta$  direction) is shown in the inset of each figure. Same units and scales are used in the  $\rho(\vec{p})$  and  $E(\vec{k})$  plots throughout. It is observed that V1, V2 and V3 which result in similar bandstructure also yield similar results for the EMD. As pointed out in the previous section only the  $\Delta_1$  band is allowed by the selection rule to contribute to the EMD [through  $A_j(\vec{k}, \vec{p})$ ]. In all the three cases V1, V2 and V3 the higher  $\Delta_1$  band remains unoccupied throughout as one goes from  $\Gamma$  to H along  $\Delta$ . The total EMD, therefore arises only from the lowest  $\Delta_1$  band. Since this band never crosses the Fermi level, there are no sharp discontinuities in the EMD curve which shows a smooth momentum dependence. It should be noted that there is a crossing of the second band (from the bottom)

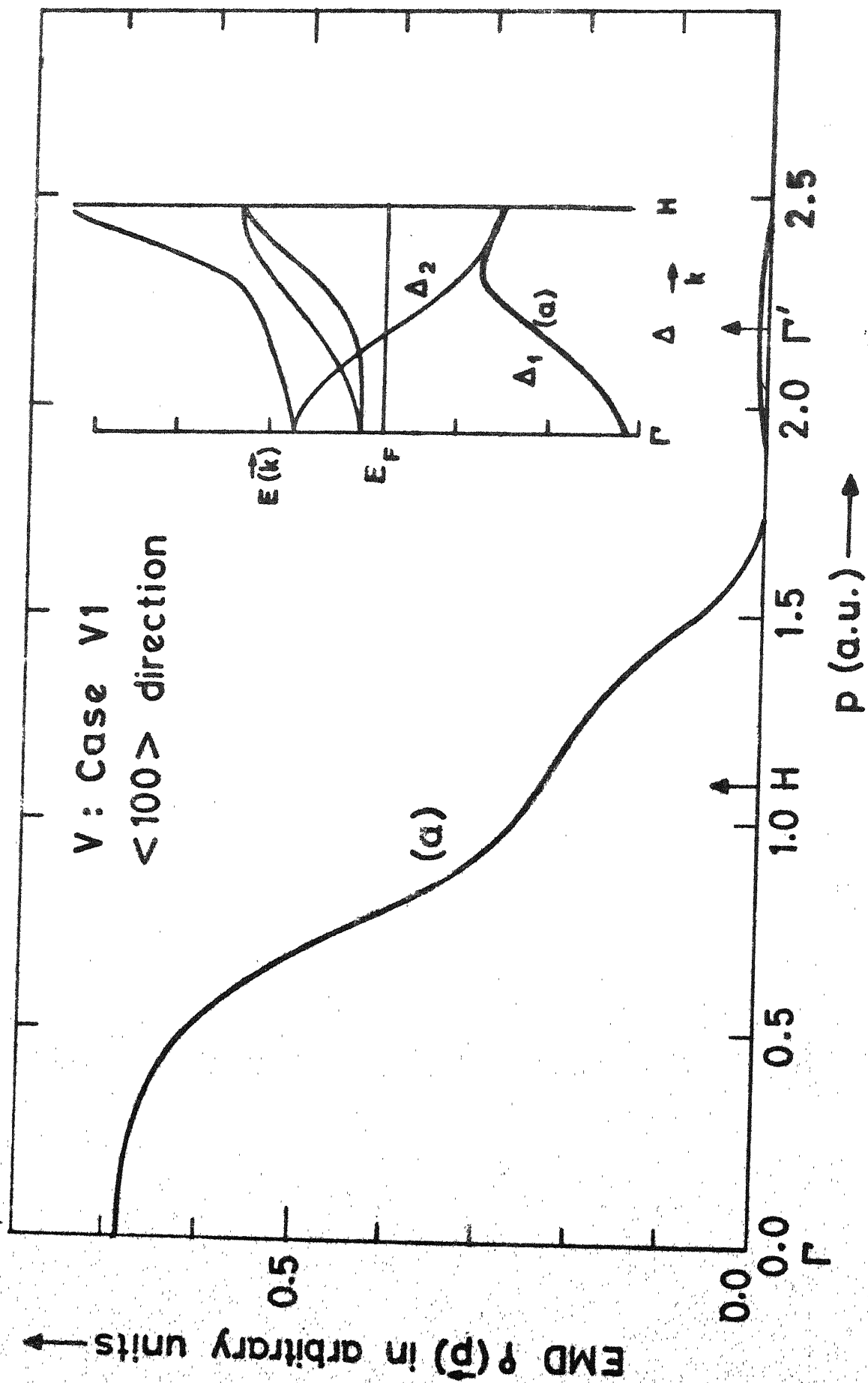


FIG. 4.11 : The EMD along the  $\langle 100 \rangle$  direction for vanadium (case V1).

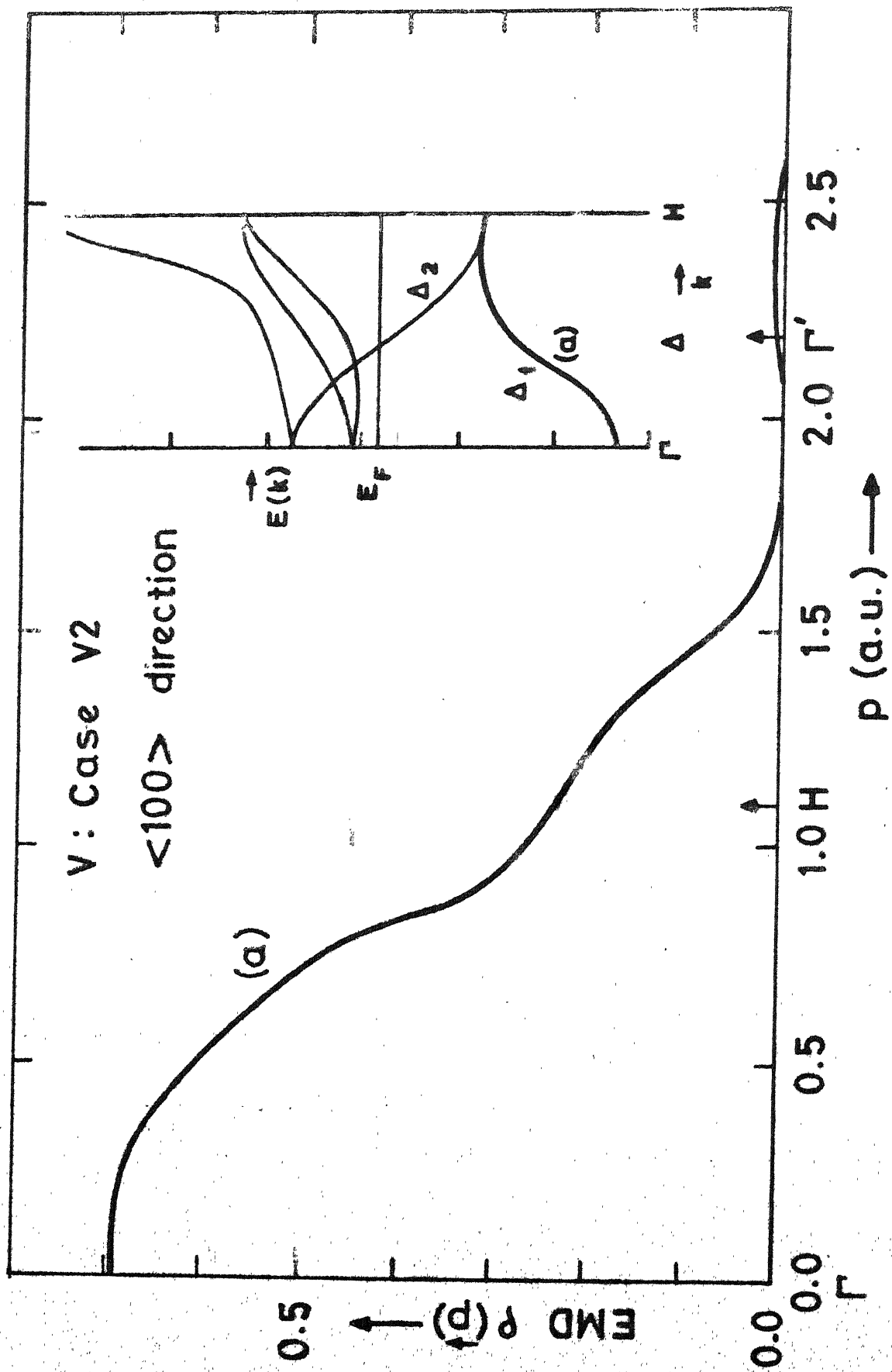


Fig. 4.12 : The EMD along the  $\langle 100 \rangle$  direction for vanadium (case V2).

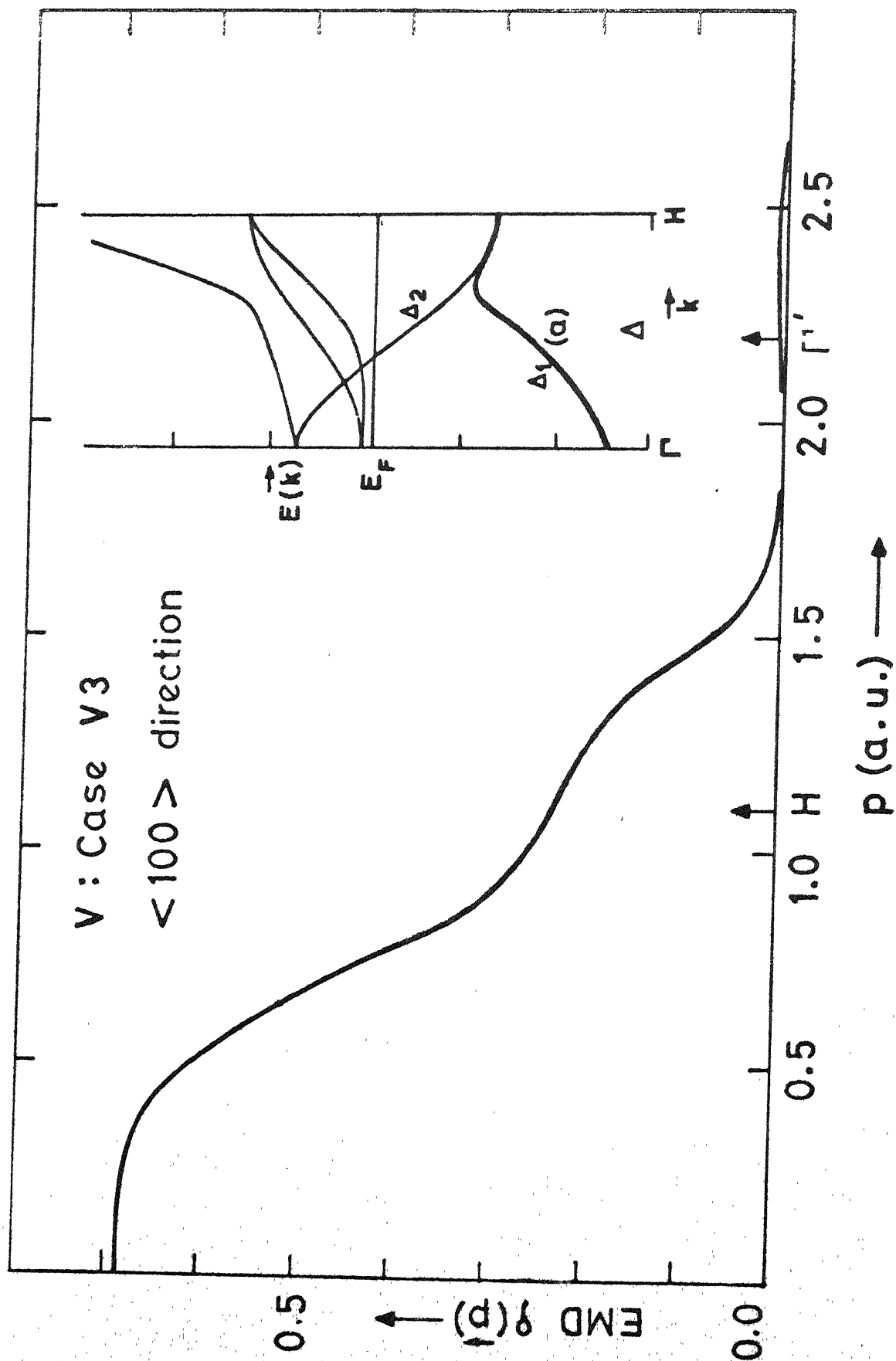


Fig. 4.13 : The EMD along the  $\langle 100 \rangle$  direction for vanadium (case V3).

with the Fermi level but the symmetry of this band being  $\Delta_2$ , it is forbidden by the selection rule to contribute to the EMD.

Along the  $\langle 100 \rangle$  direction the FS of V is known to exhibit (Figs. 4.8-4.10) interesting features, that is, the  $\Gamma$ -centered octahedral hole surfaces and the jungle-gym (JG) hole tubes (arms). It may appear surprising that the EMD along the  $\langle 100 \rangle$  direction (Figs. 4.11-4.13) is relatively smooth and does not reflect these interesting features of the FS. To appreciate this one should remember that these two sheets of the FS in V arise from the second band (symmetry  $\Delta_2$ ) and the third band (symmetry  $\Delta_5$ ). The symmetry character of both the second and third band is such that they are forbidden by the selection rule to contribute to the EMD. On the top of this the third band is totally unoccupied. In other words, it is only the filled electron surfaces (and not the empty hole surfaces) which can contribute to the EMD provided that they are allowed to do so by the symmetry selection rule.

It would be interesting to further examine these effects of the symmetry selection rule by looking at the EMD,  $\rho(\vec{p})$ , along a  $\vec{p}$ -direction which is removed from the  $\langle 100 \rangle$  direction but still lies in the (100) plane. One such  $\vec{p}$ -direction marked by A in Fig. 4.14 is such that  $\vec{p} \equiv (p_x, p_y, p_z) \equiv (\xi, \eta, 0)$ . The EMD in the first Brillouin zone (BZ) along this  $\vec{p}$ -direction is shown in Fig. 4.15 along with the relevant bandstructure.

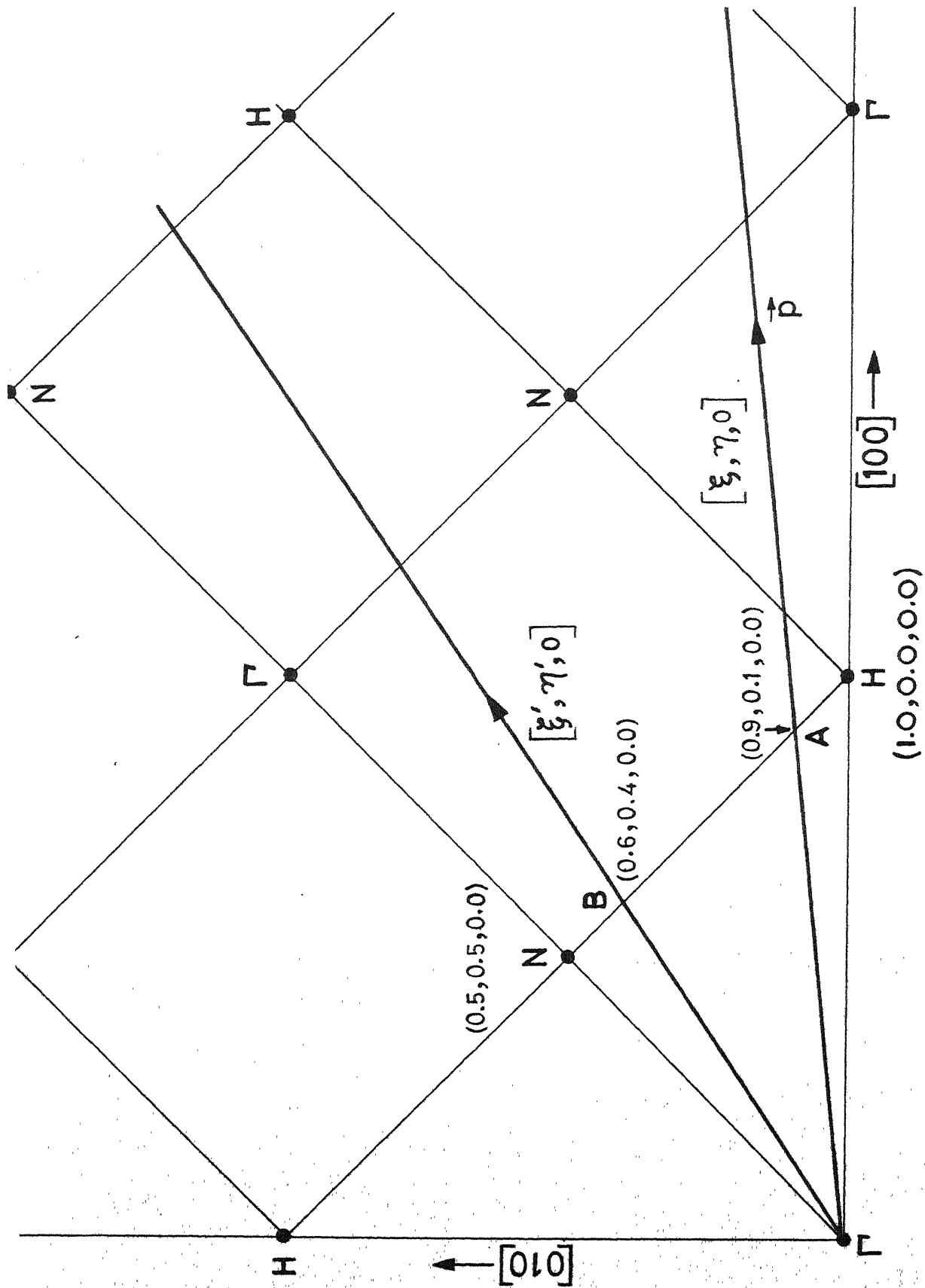


Fig. A.14 : The  $\vec{p}$  directions  $\Gamma A$  near the  $\langle 100 \rangle$  direction and  $\Gamma B$  near the  $\langle 110 \rangle$  direction.

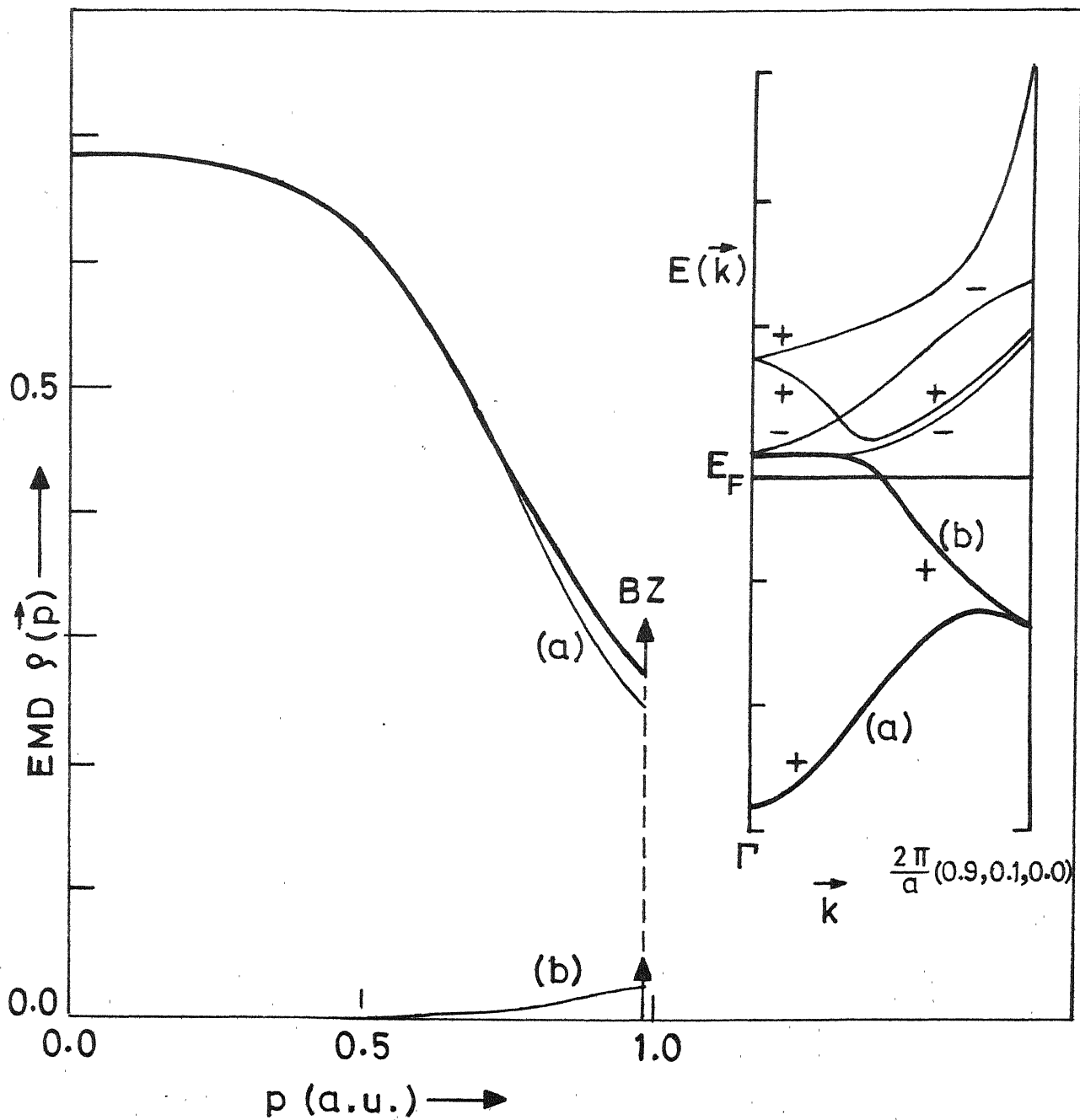


Fig. 4.15: The EMD along the direction  $\Gamma A$ .



It will be observed that the second band has now lost its higher symmetry ( $\Delta_2$ ) and has assumed a lower symmetry which is now (+). Application of the symmetry selection rule (Table 4.4) allows the (+) bands from the  $\Gamma$ HN plane to contribute along the  $\langle \xi, \eta, 0 \rangle$  direction. This effect is seen from the partial EMD contributed by the second band (during its occupied part) to the total EMD.

#### 4.4.3 EMD along the $\langle 110 \rangle$ direction

The results for the EMD along the symmetry direction  $\langle 110 \rangle$  for the cases V1, V2 and V3 are shown in Figs. (4.16)-(4.18) along with the corresponding bandstructure. When compared to the  $\langle 100 \rangle$  direction, these results show a more interesting behaviour. Along the  $\langle 110 \rangle$  direction, the symmetry selection rule allows only the  $\Sigma_1$  bands to contribute to the EMD. Besides the lower  $\Sigma_1$  [marked by (a) in the bandstructure of Figs.(4.16)-(4.18)] the next higher  $\Sigma_1$  band [marked by (b) in Figs. (4.16)-(4.18)] can also contribute while the  $\Sigma_2$  band (second band from the bottom) is forbidden by the selection rule. In our bandstructure results the higher  $\Sigma_1$  (or the 'b') band dips below the Fermi level and thus remains unoccupied except in the central region along  $\Gamma$ -N. It is only in this central occupied region that band (b) contributes to the total EMD (see the curves of the partial EMD marked by (a) and (b)) and this explains the

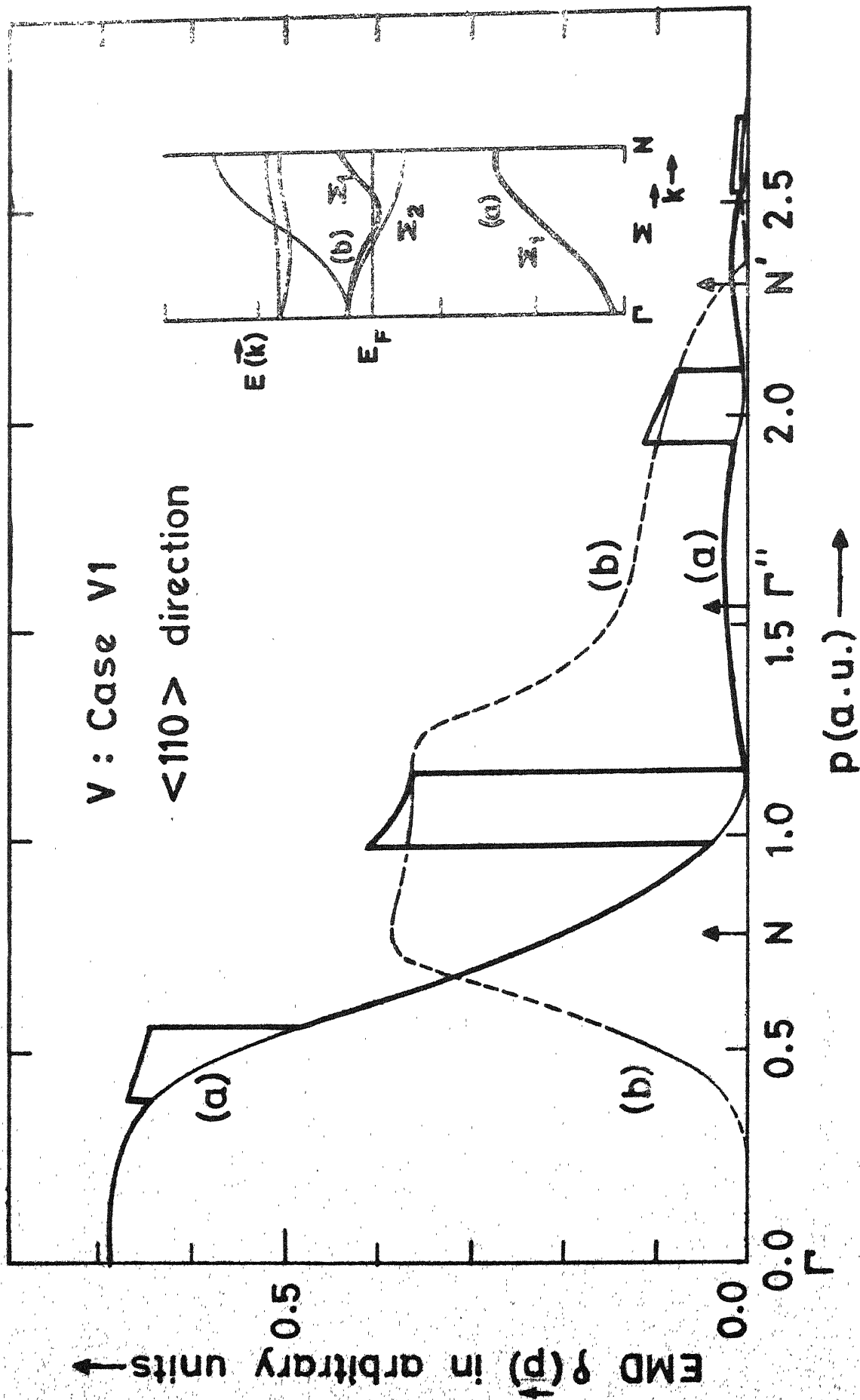


Fig. 4.16 : The EMD along the  $\langle 110 \rangle$  direction (case V1).

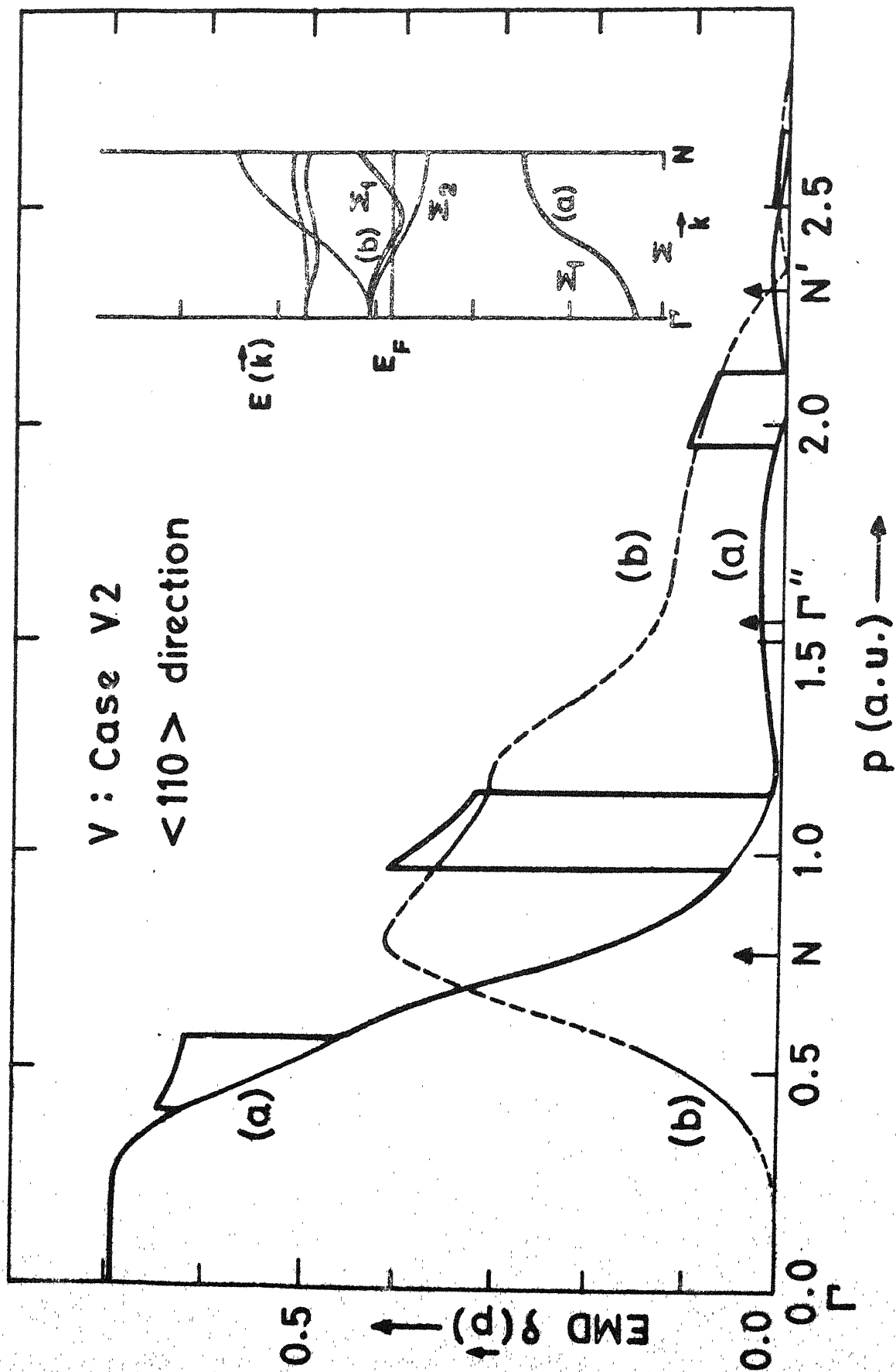


Fig. 4.17 : The EMD along the  $\langle 110 \rangle$  direction (case V2).

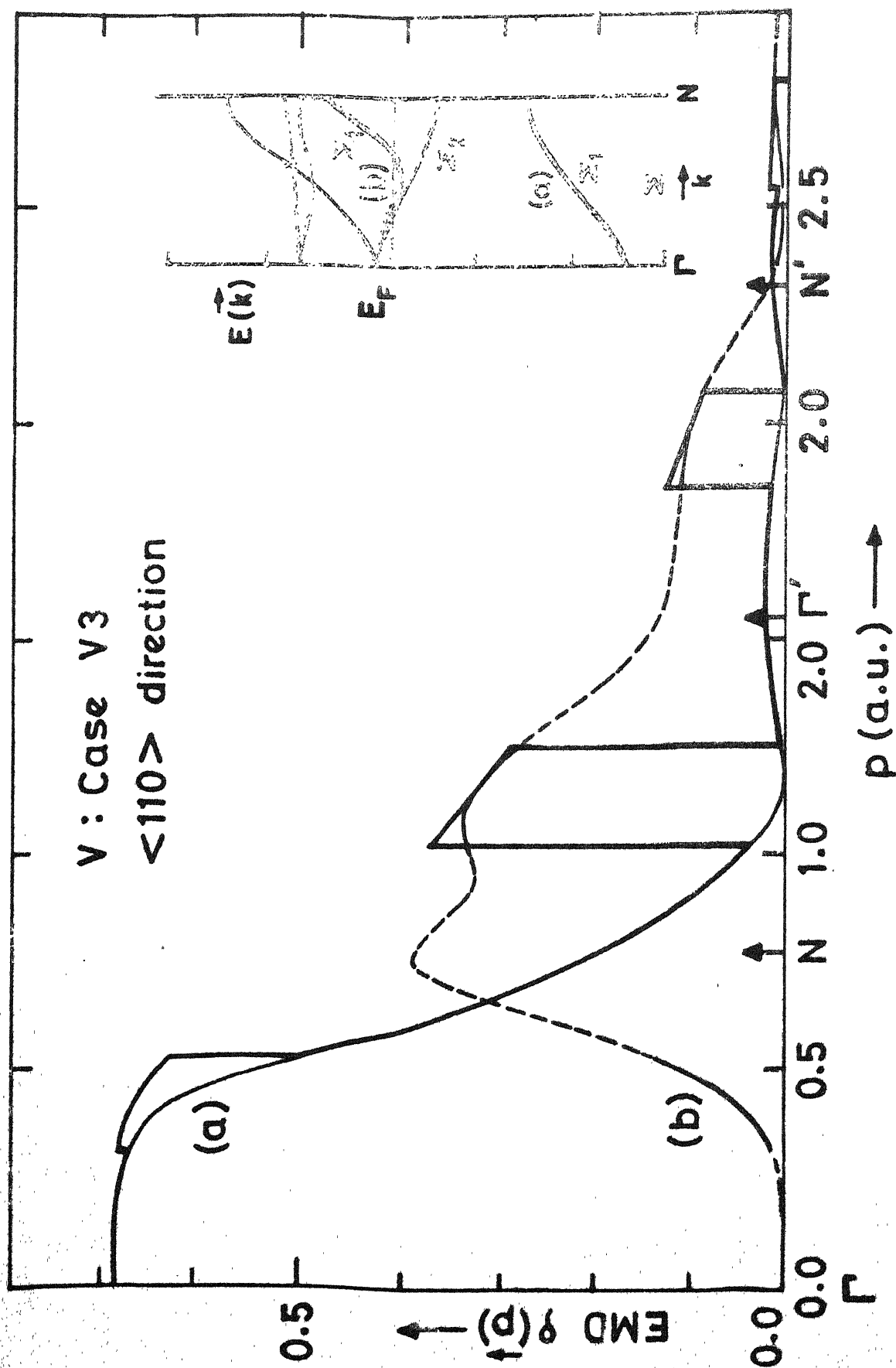


Fig. 4.18: The EMD along the  $\langle 110 \rangle$  direction (case V3).

'spikes' and the sharp discontinuities seen in Figs. 4.16-4.18. The thinly drawn curves (a) and (b) in these figures denote the partial EMD,  $\rho_j(\vec{p})$ , while the thickly drawn curve shows the total EMD,  $\rho(\vec{p}) = \sum_j \rho_j(\vec{p})$ . The behaviour of the partial EMD curves provide a good insight into the combination of effects mentioned at the end of §4.4.1. It will be noticed that the dipping of the  $\Sigma_1$  band below the Fermi level is shown as the discontinuities in the total EMD curve not only in the first BZ ( $p \sim .35$  a.u.,  $0.51$  a.u.) but also in the higher ( $p \sim 1.06$  a.u.,  $0.90$  a.u.) zones through the Umklapp images of the FS (Fig. 4.16). The width of the spikes in Figs. 4.16-4.18 is determined by the amount of 'dipping' shown by the  $\Sigma_1$  band while the height of the spikes will be decided by the momentum eigenfunction of  $\psi_{\vec{k},j}(\vec{r})$  through  $|A_j(\vec{k}, \vec{p})|^2$ . In terms of the FS topology, as one goes from  $\Gamma$  to N, the first crossing of the  $\Sigma_1$  band with the Fermi level determines the dimensions of the JG hole-tube arms while the second crossing determines the semiaxis of the hole ellipsoid centered at N. If the model of the FS in which the JG hole arms and the hole ellipsoids are connected by a narrow neck (narrow neck model) is valid, the corresponding bandstructure could be somewhat similar to that shown in the inset in Fig. 4.19. We have calculated the EMD (along  $\langle 110 \rangle$  direction) for such a model by lowering the Fermi level by about  $0.05$  Ry. from its position for the case VI. These results are shown

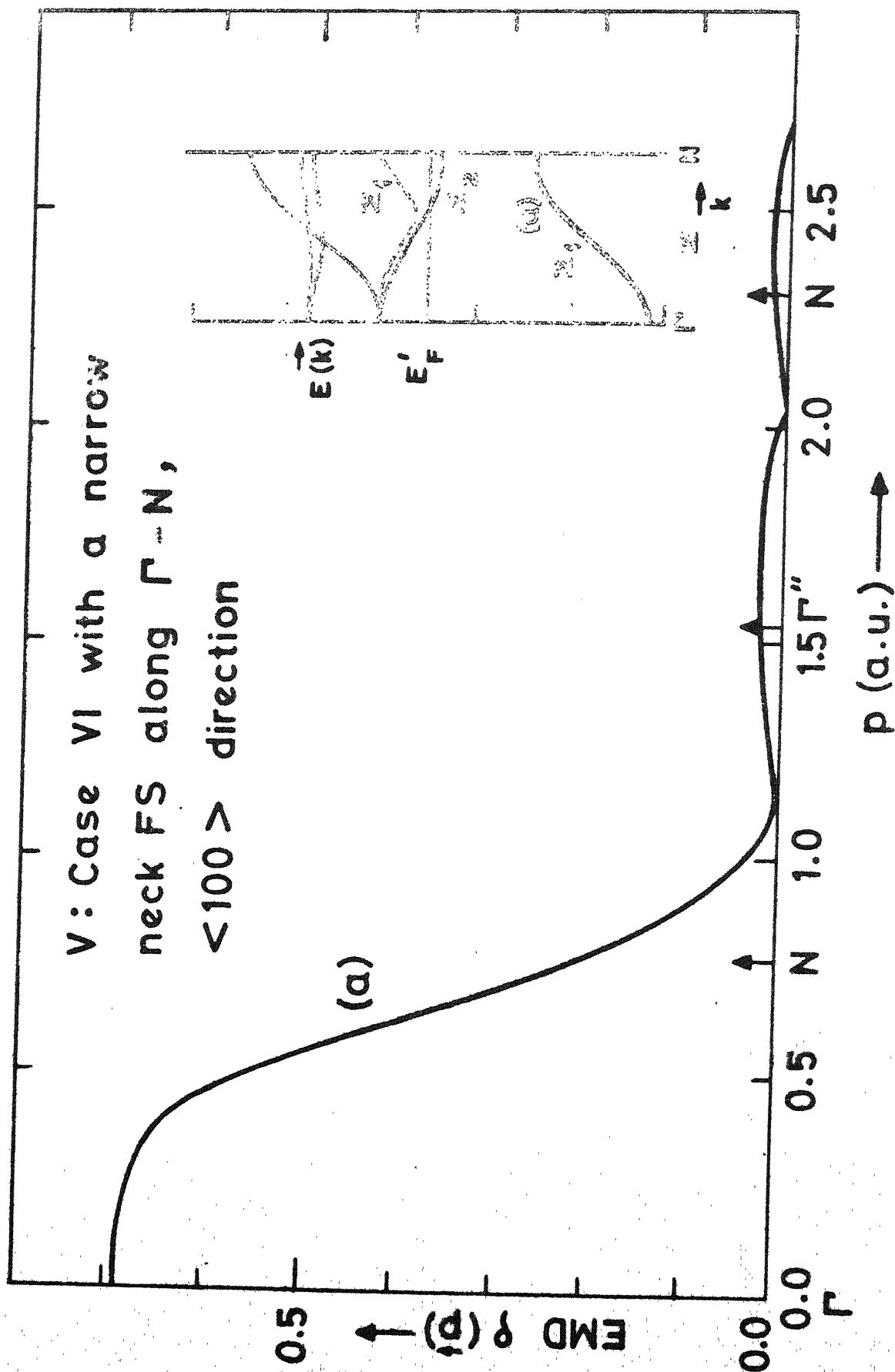


Fig. 4.19: The EMD along the  $\langle 110 \rangle$  direction for Fermi level dipping below the  $\Sigma_1$  band (case VI)

in Fig. 4.19. A comparison of the results in Figs. 4.19 and 4.16 show that the EMD along the  $\langle 110 \rangle$  direction changes drastically if the narrow neck model is accepted.

Mijnarends [15,16] and Mueller [17] have proposed inversion methods to reconstruct the EMD,  $\rho(\vec{p})$ , by inverting (or unfolding) a set of experimentally measured Compton profiles  $J_{hkl}(p_z)$  for several directions (hkl) through the equation

$$J(p_z) = \iint \rho(\vec{p}) dp_x dp_y \quad (4.4)$$

Such an unfolding or inversion procedure has not yet been reported for the directional Compton profiles measured from V single crystals. We feel that such an unfolding of the  $\rho(\vec{p})$  from the experimental data for V should be undertaken so as to obtain, for example, the  $\rho(\vec{p})$  along the  $\langle 110 \rangle$  direction. The results of our calculations (Figs. 4.16 and 4.19) would then provide a basis to indicate whether the Compton profile data supports a FS model with or without the neck. Further in case the experimental results rule out the existence of these necks, the positions (p-values) of the discontinuities (measured from  $\Gamma$  or N) observed in the unfolded  $\rho_{110}(\vec{p})$  curves can provide some information about the dimensions of the JG hole arms and the N-centered hole ellipsoids.

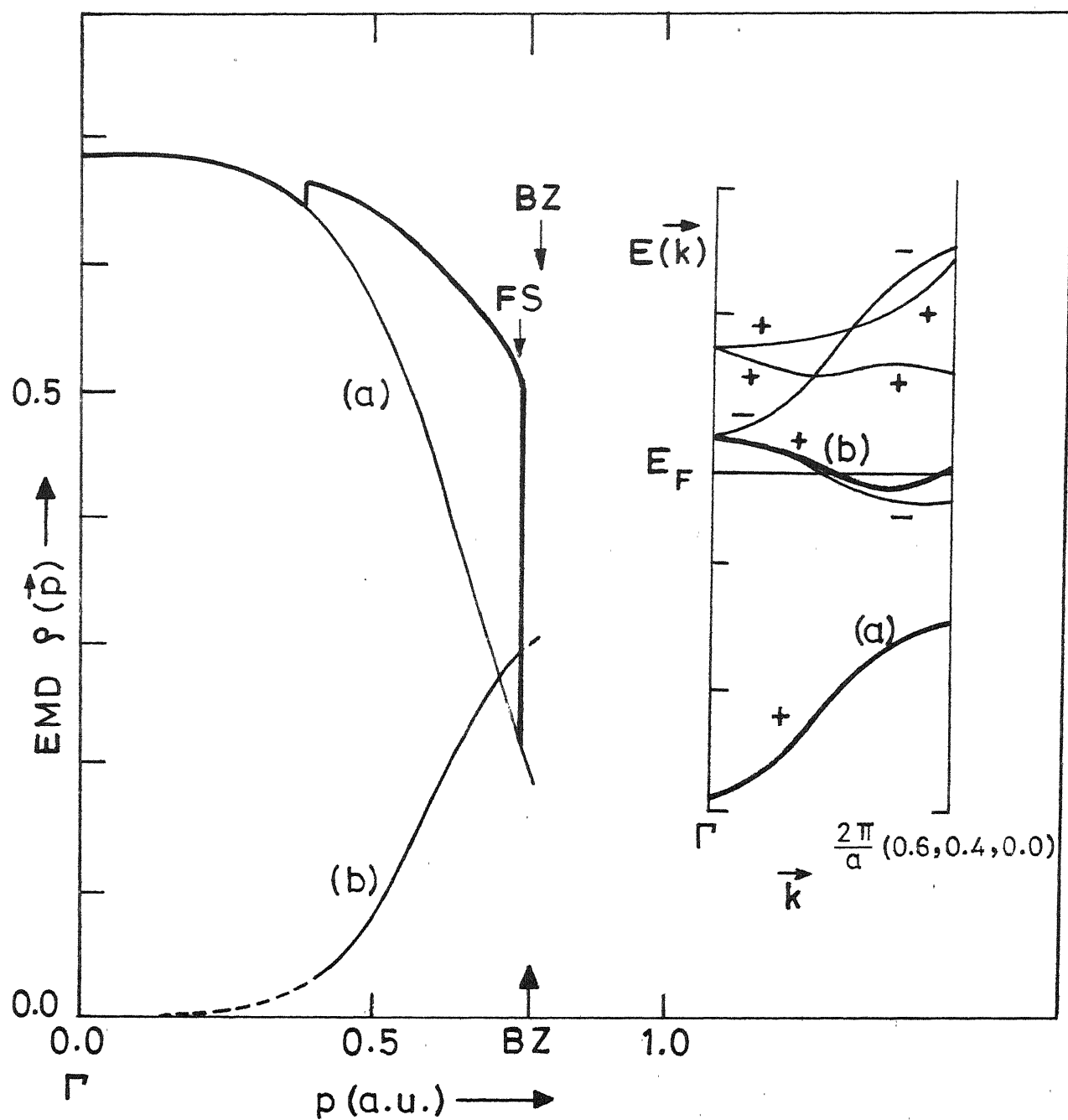


Fig. 4.20 : The EMD along the direction  $\Gamma B$ .



We have also examined the effect of the symmetry selection rule on the second band from the bottom. Along the  $\langle 110 \rangle$  direction this band has a  $\Sigma_2$  character and is forbidden to contribute (Table 4.4) as borne out by Fig. 4.16. If the  $\vec{p}$ -direction is moved away from the  $\langle 110 \rangle$  direction but still limited in the  $(110)$  plane the  $\Sigma_1$  and  $\Sigma_2$  bands assume a lower symmetry (+) and (-) respectively. The selection rule (Table 4.4) allows only the (+) bands in the  $(\Gamma\text{HN})$  plane to contribute for  $\vec{p} = (\xi, \eta, 0)$  direction. Thus the second band gives no contribution to the EMD even along the  $\vec{p} = (\xi, \eta, 0)$  direction (marked by B in Fig. 4.14) as shown by the results of our calculation (Fig. 4.20).

#### 4.4.4 EMD along the $\langle 111 \rangle$ direction

The plots of the EMD along the  $\langle 111 \rangle$  direction in V are presented in Figs. 4.21-4.23 for the crystal potentials V1, V2 and V3 respectively. In a bcc structure the direction  $\langle 111 \rangle$  proceeds along  $\Gamma\text{-A-P-F-H-F-P-A-}\Gamma$  in the succeeding zones and we have therefore shown the bandstructure along the A and F directions in the inset of Figs. 4.21-4.23. The symmetry selection rule (Table 4.4) allows only the  $\Lambda_1$  and  $F_1$  bands to contribute to the EMD along the  $\langle 111 \rangle$  direction and this effect is observed in our results. The sharp discontinuities in the EMD curves observed at  $p \sim 1.5$  a.u. and  $p \sim 2.25$  a.u. arise from the crossing of the  $F_1$  band with the Fermi level

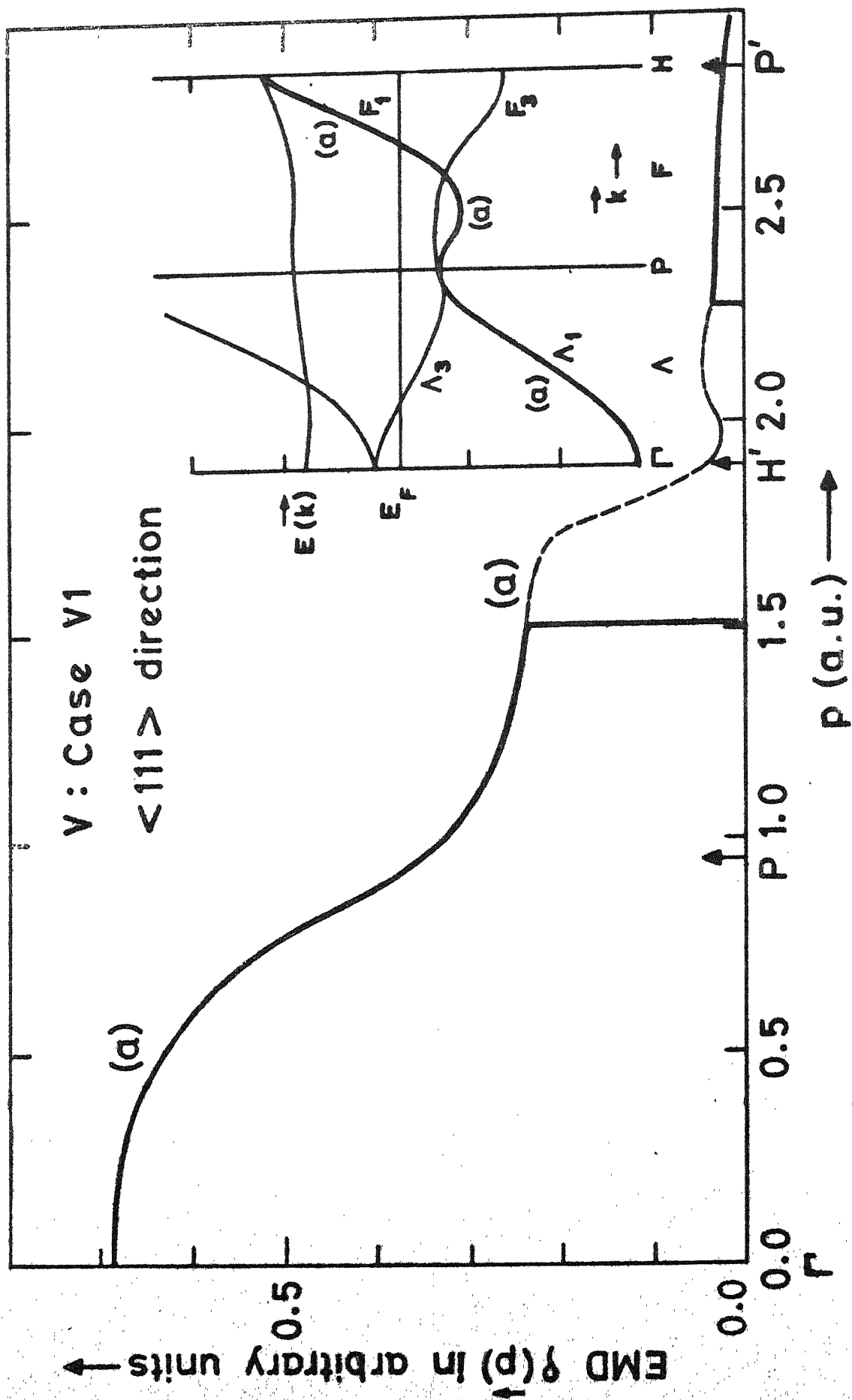


FIG. 4.21 : The EMD along the  $\langle 111 \rangle$  direction (case V1).

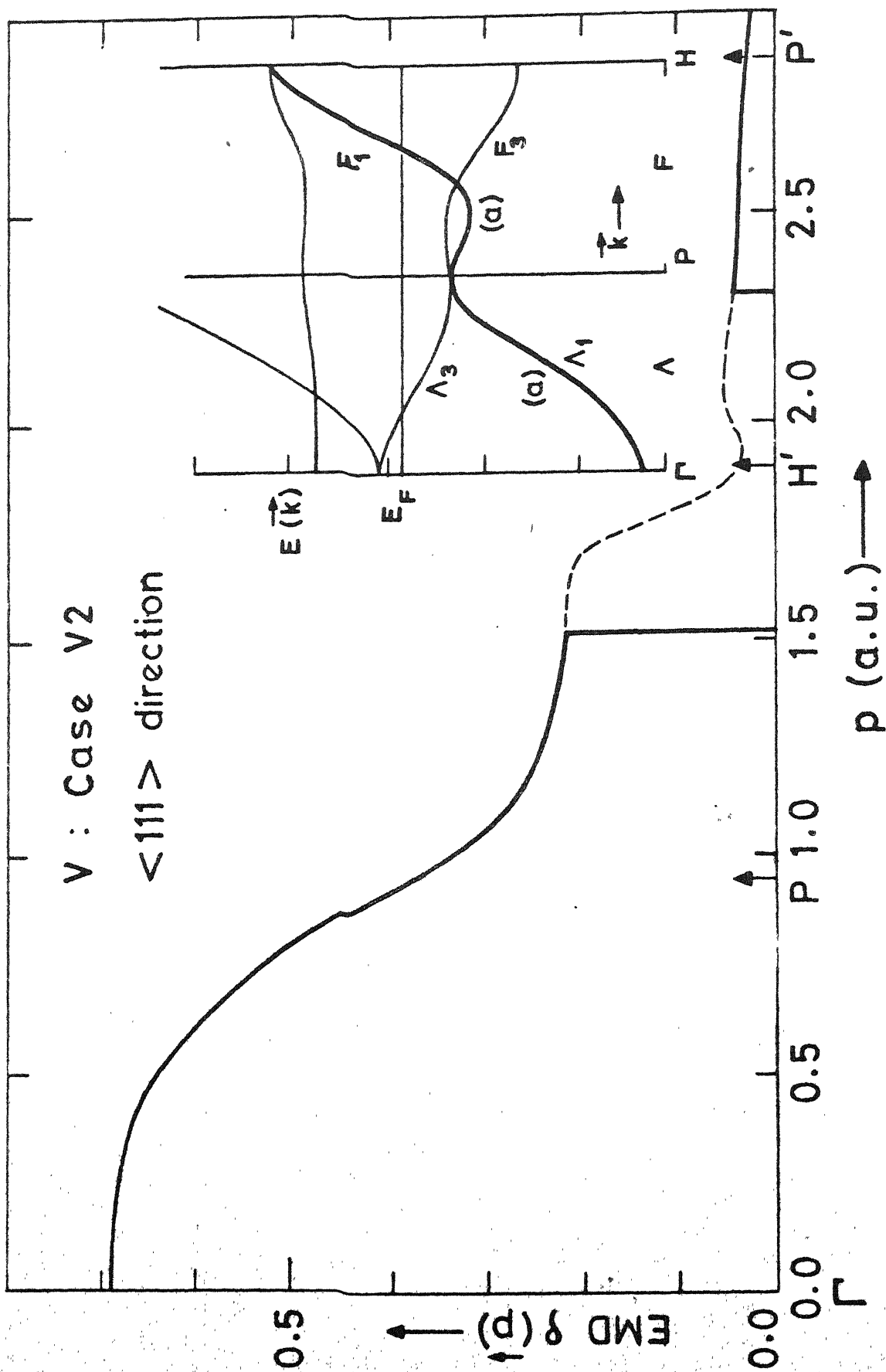


Fig. 4.22 : The EMD along the  $\langle 111 \rangle$  direction (case V2).

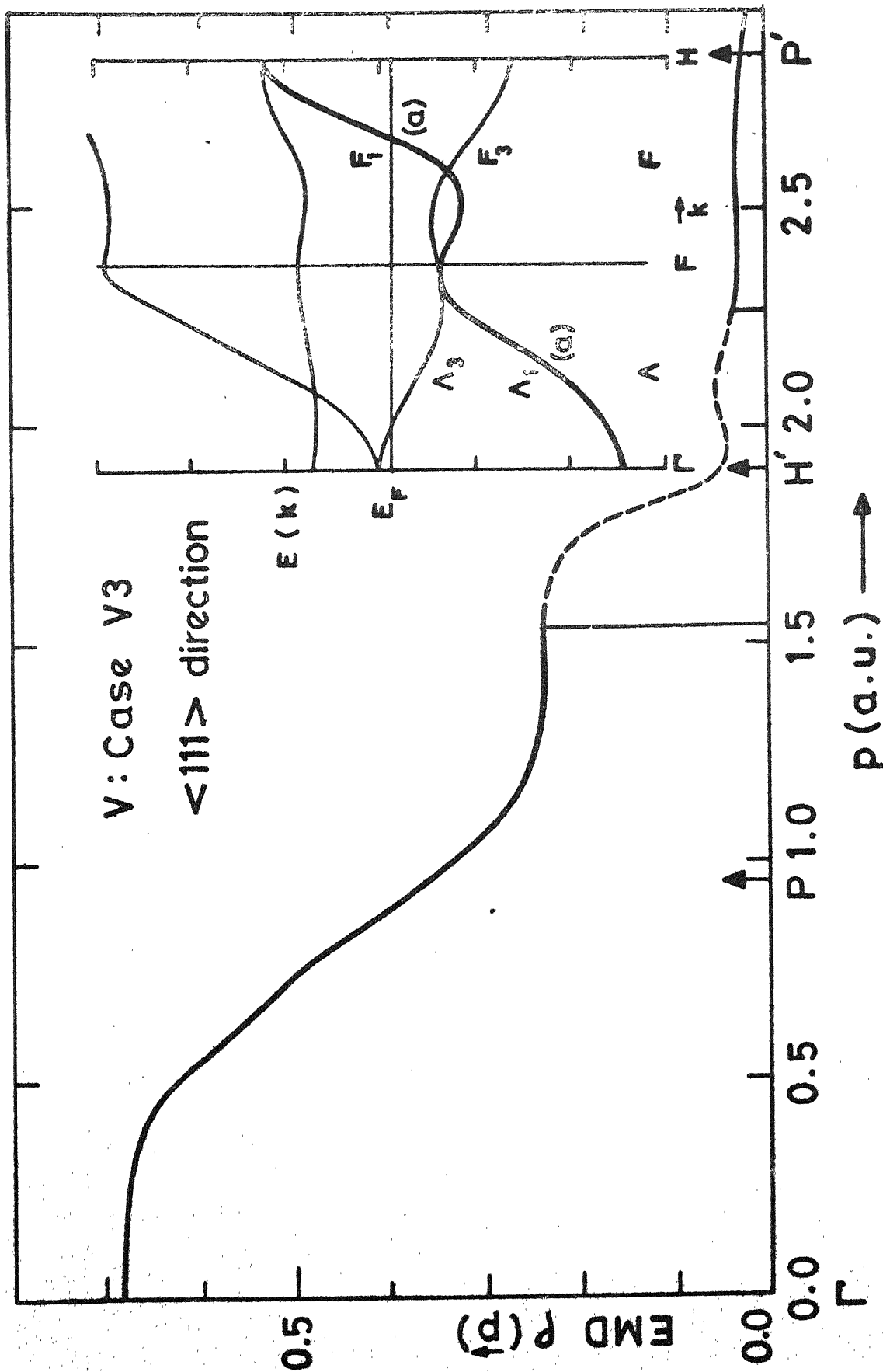


Fig. 4.23 : The EMD along the  $\langle 111 \rangle$  direction (case V3).

and hence it is seen in the second and third BZ. In the first BZ no such discontinuity is observed because the  $\Lambda_1$  band is occupied throughout this zone. The position (i.e. p-values) of the discontinuities (at  $p \sim 1.5$  a.u. and 2.25 a.u.) can provide us with the dimensions of the JG hole arms along the H-P direction. As pointed out in the previous section, the experimental Compton profile data, if unfolded to obtain  $\rho_{111}(\vec{p})$ , can help us to determine these dimensions of the FS. The  $\rho(\vec{p})$  distributions for the three cases V1, V2 and V3 (Figs. 4.21-4.23) show similar features.

#### 4.4.5 EMD along some other directions in the (100) and (110) planes

In order to get a better insight into the anisotropic nature of the EMD in V we have calculated the  $\rho(\vec{p})$  values for the case V1 along nine other (besides the  $\langle 100 \rangle$ ,  $\langle 110 \rangle$  and  $\langle 111 \rangle$ )  $\vec{p}$ -directions lying in the (100) and (110) planes. These twelve  $\vec{p}$ -directions are shown in Fig. 4.24 where they are marked as 1, 2...12. The components ( $p_x, p_y, p_z$ ) of each  $\vec{p}$  vector are shown in Table 4.5 where the ( $p_x, p_y, p_z$ ) refer to the intersection of the  $\vec{p}$ -direction with the first zone face. Each of the  $\vec{p}$ -directions is formed by joining the point  $r$  to the point ( $p_x, p_y, p_z$ ).

The plots of the EMD for the directions 1, 6 and 11 (i.e., the principal symmetry directions) are already shown

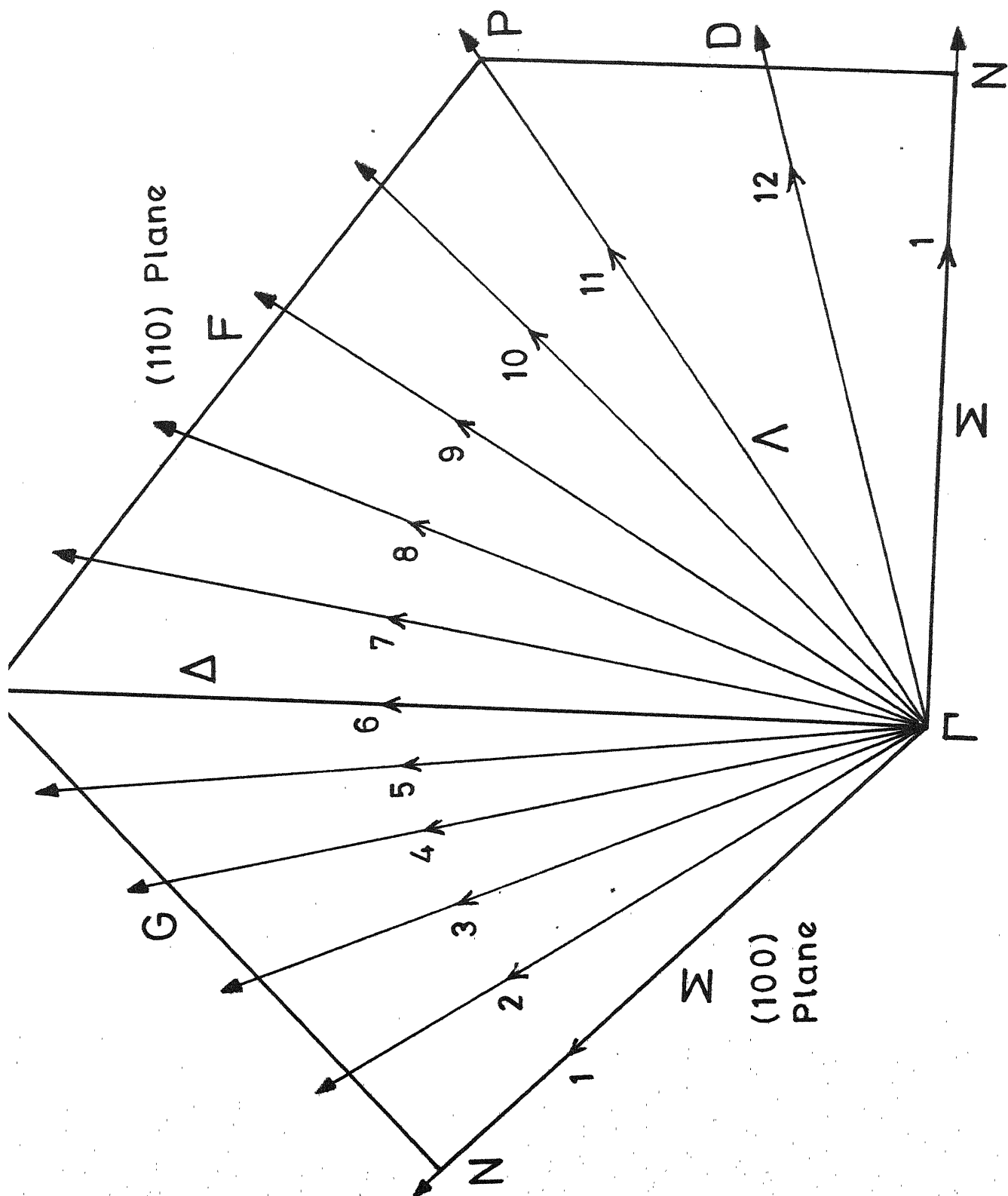


Table 4.5. Specification of the components of the twelve  $\vec{p}$  directions shown in Fig. 4.24. The values  $(p_x, p_y, p_z)$  denote a point on the zone face.

Label of the $\vec{p}$ direction (Fig. 4.24)	$\vec{p}$ in units of $2\pi/a$		
	$p_x$	$p_y$	$p_z$
1	0.5	0.5	0.0
2	0.6	0.4	0.0
3	0.7	0.3	0.0
4	0.8	0.2	0.0
5	0.9	0.1	0.0
6	1.0	0.0	0.0
7	0.9	0.1	0.1
8	0.8	0.2	0.2
9	0.7	0.3	0.3
10	0.6	0.4	0.4
11	0.5	0.5	0.5
12	0.5	0.5	0.2

V: Case V1

$\vec{p}$  along direction 2

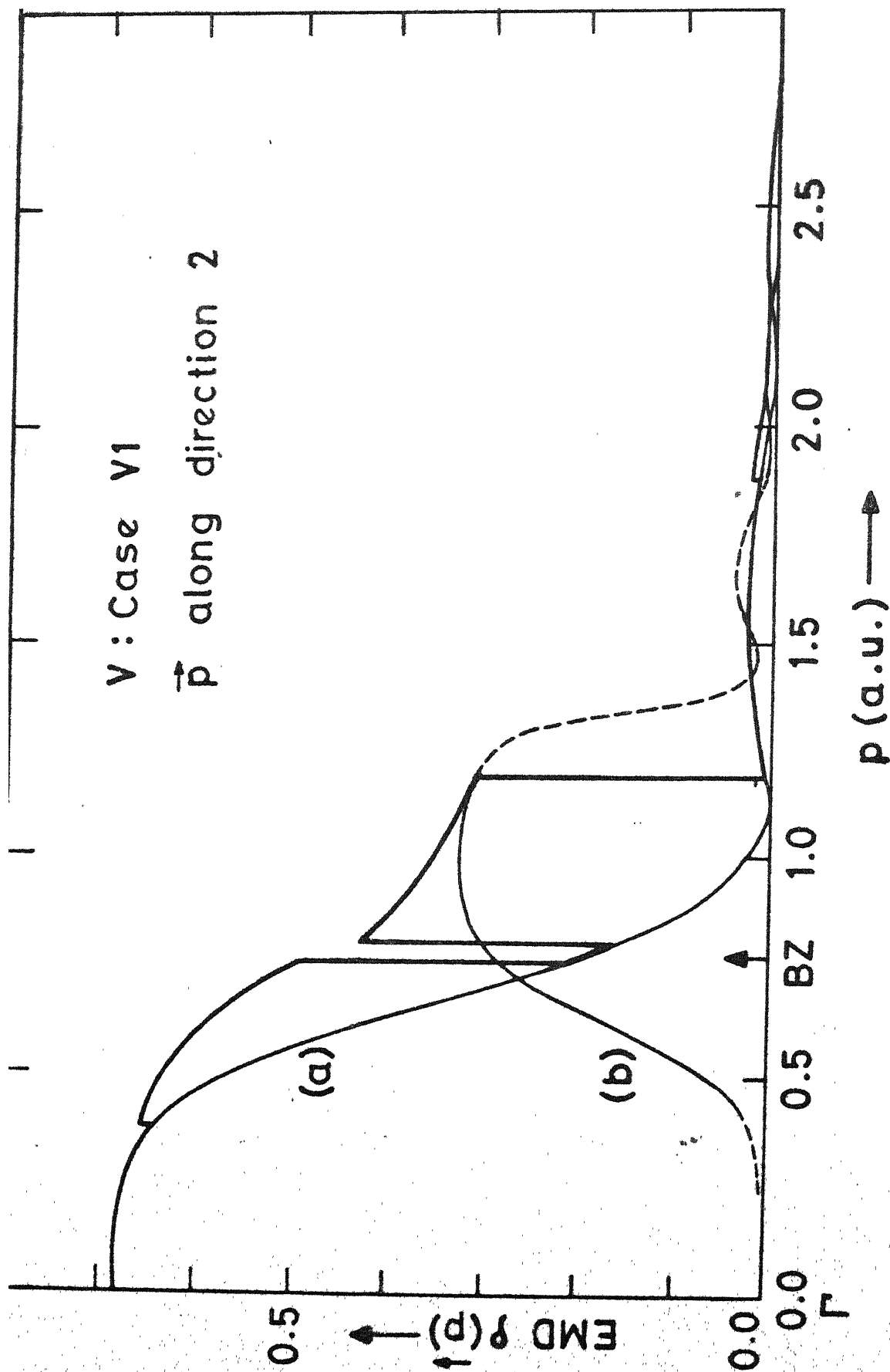


Fig. 4.25 : The EMD along direction 2.



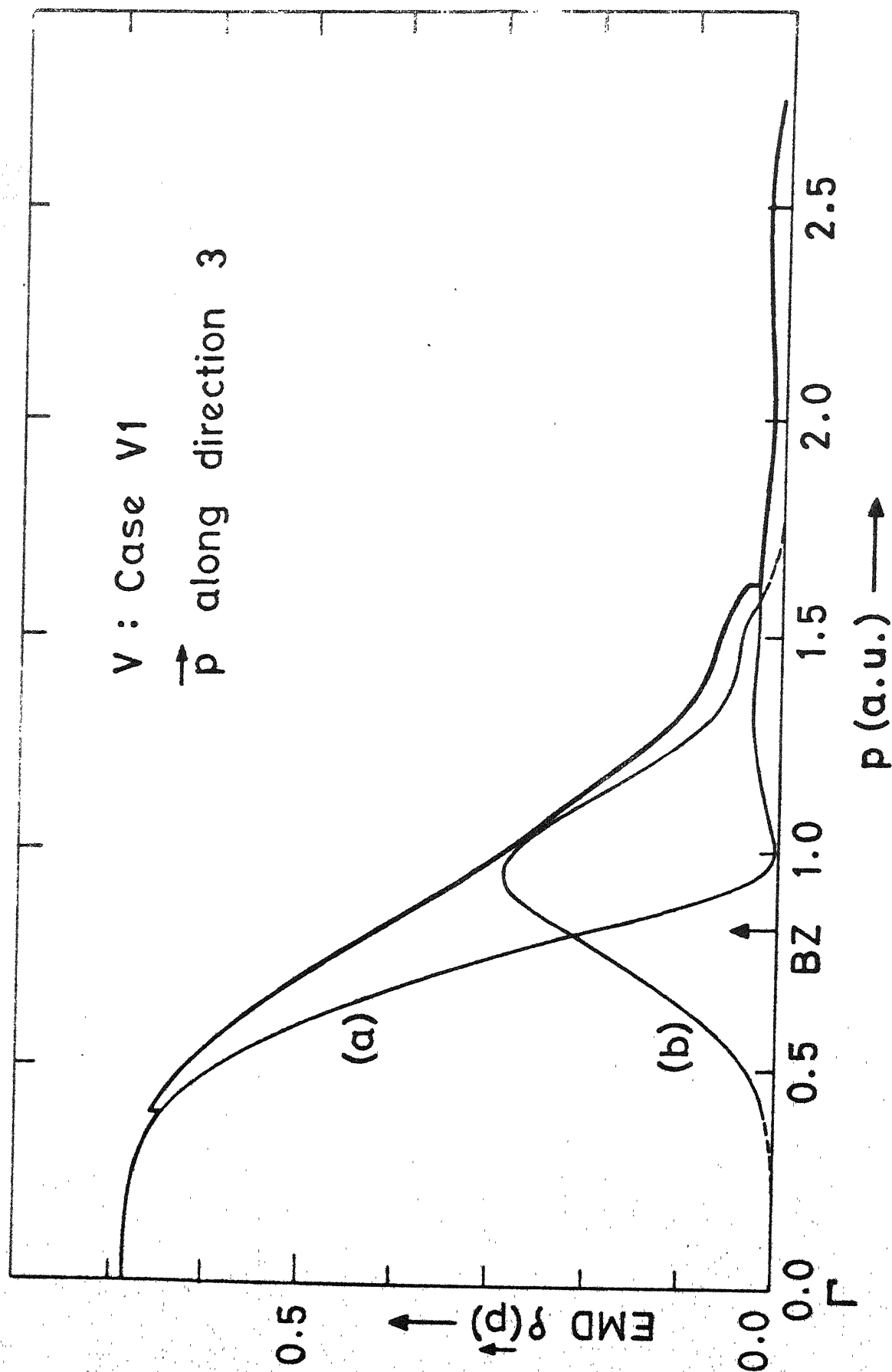


Fig. 4.26 : The EMD along direction 3.

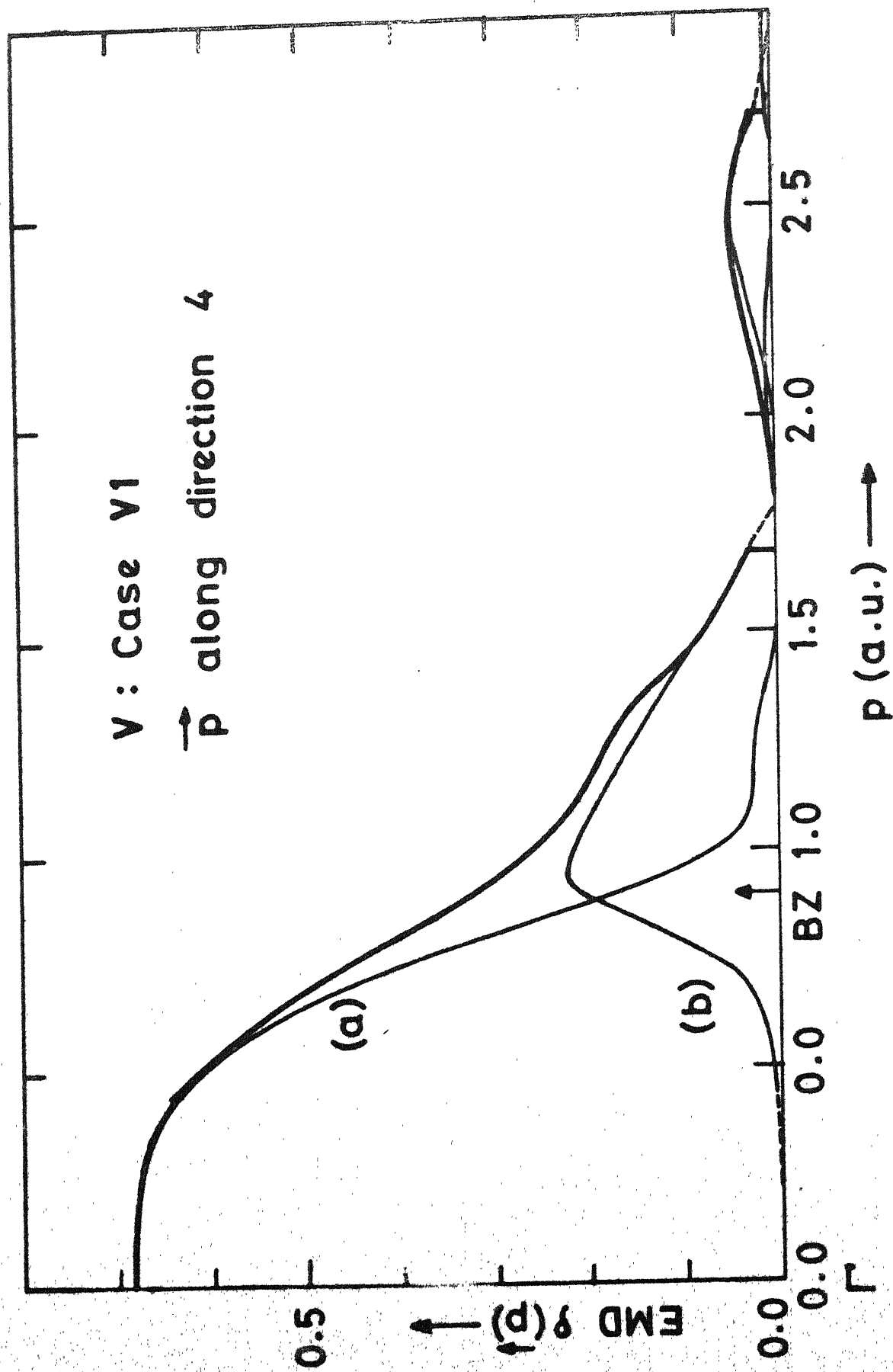


Fig. 4.27 : The EMD along direction 4.

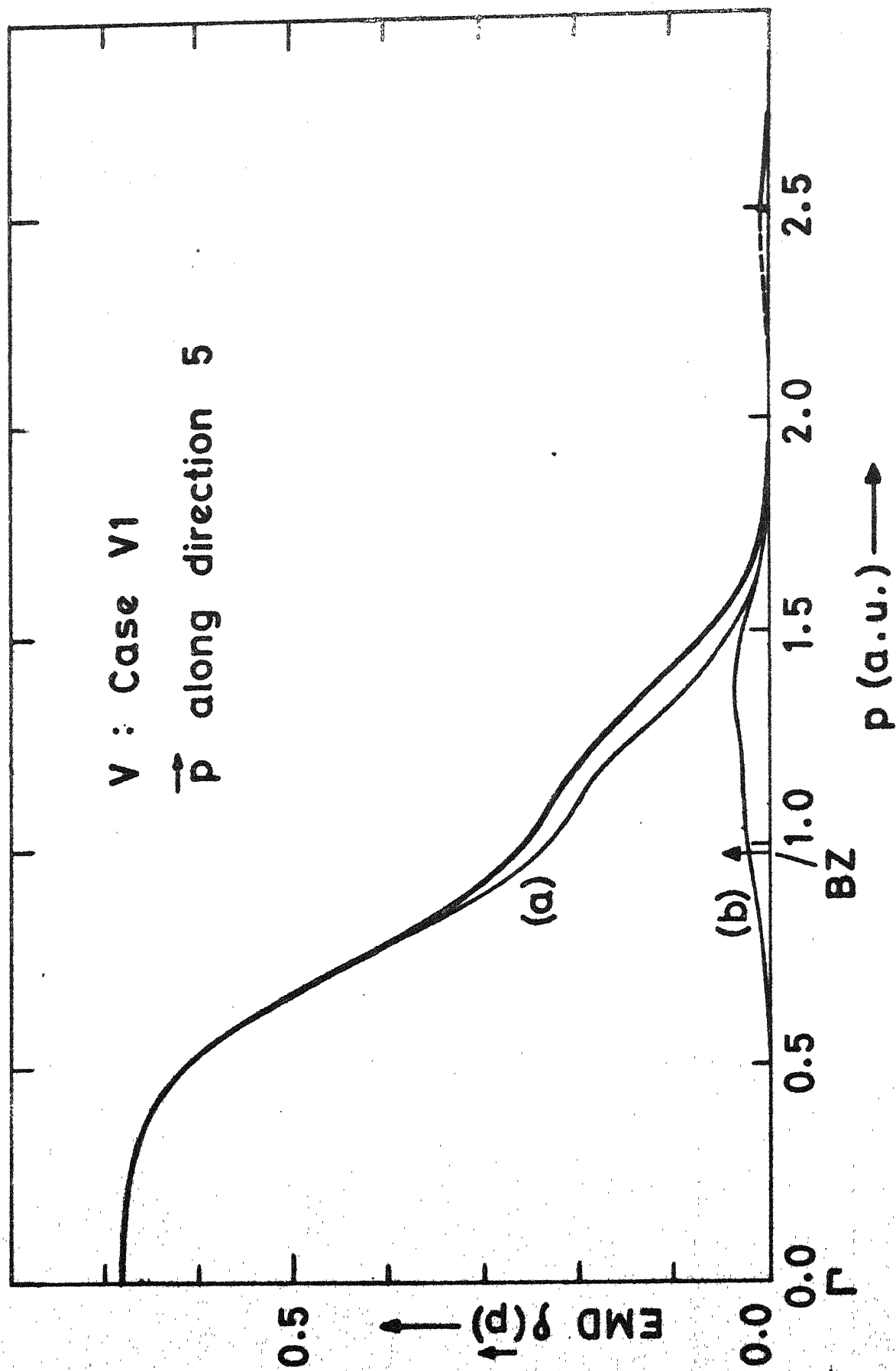


Fig. 4.28 : The EMD along direction 5.

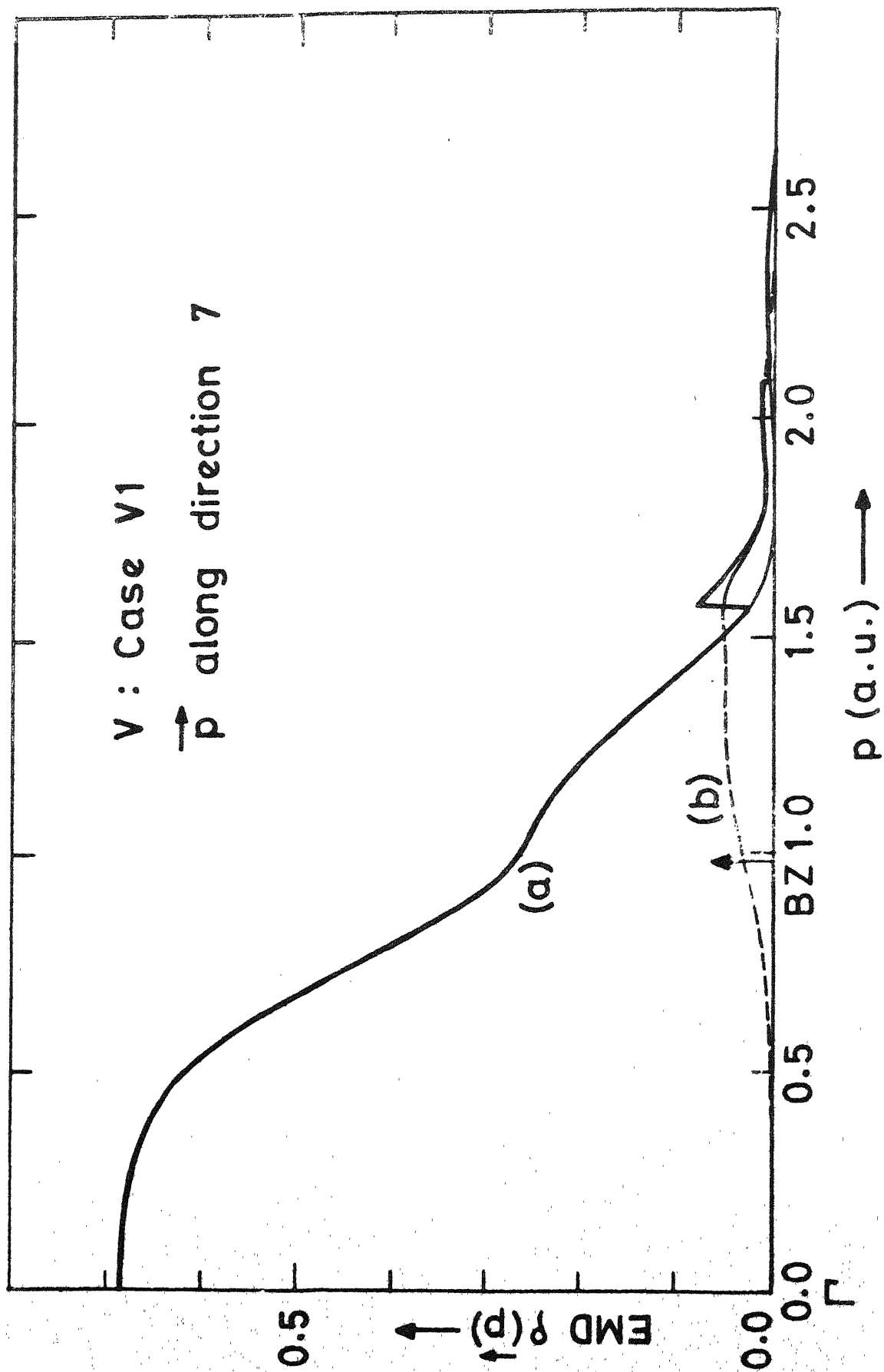


FIG. 1.29 : The EMD along direction 7.

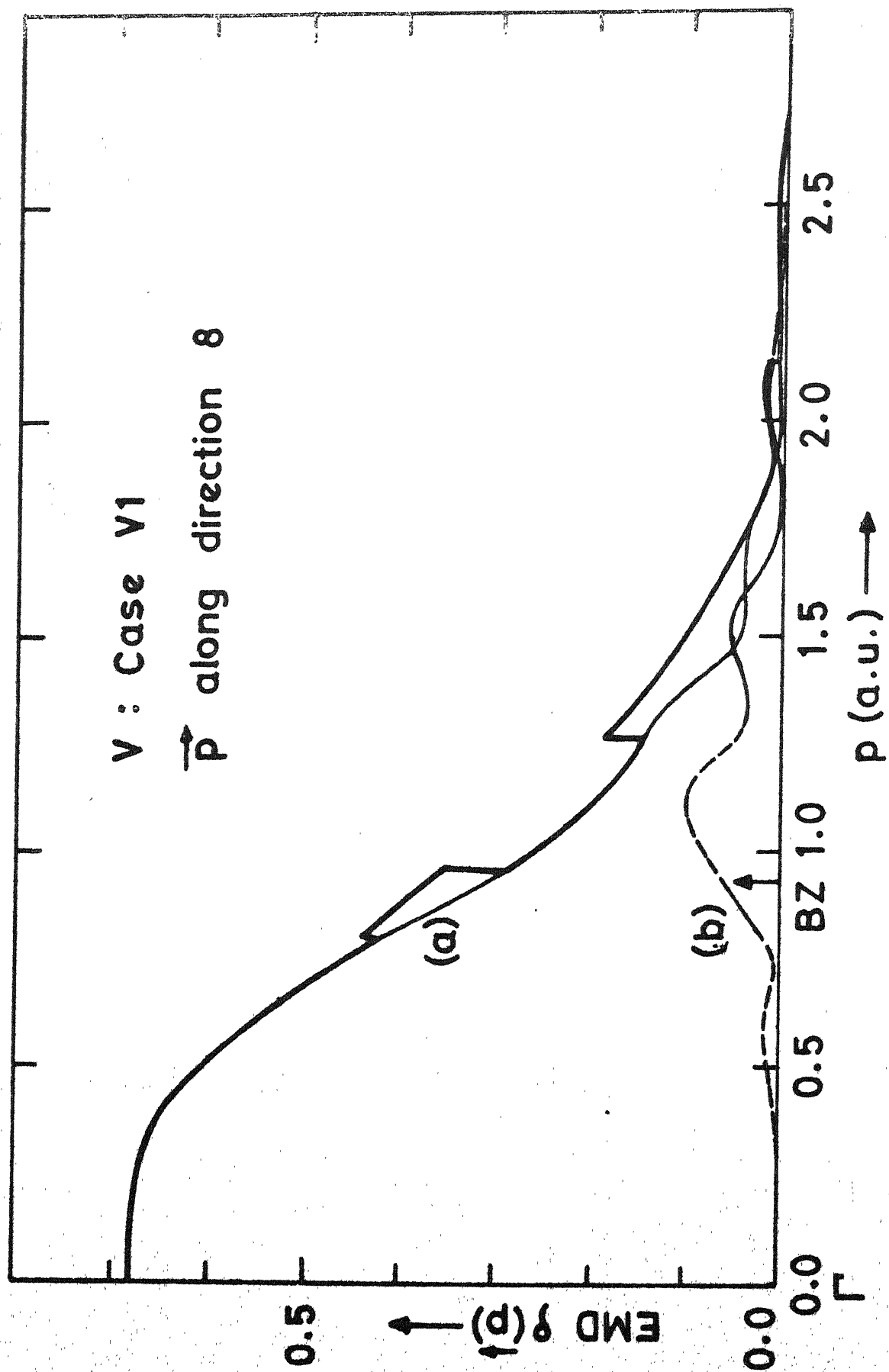


FIG. 4.50 : The EMD along direction 8.

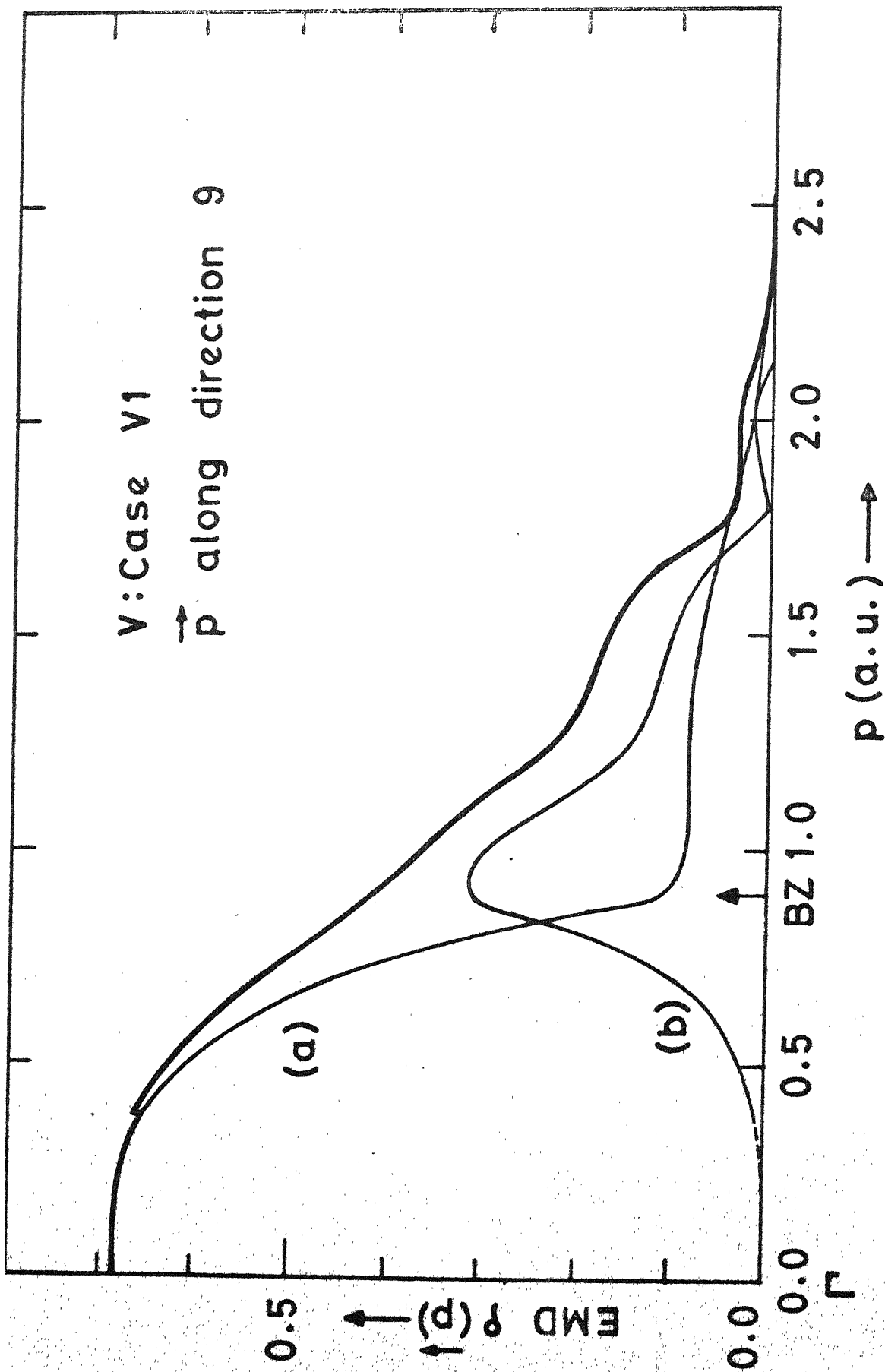


Fig. 4.31 : The EMD along direction 9.

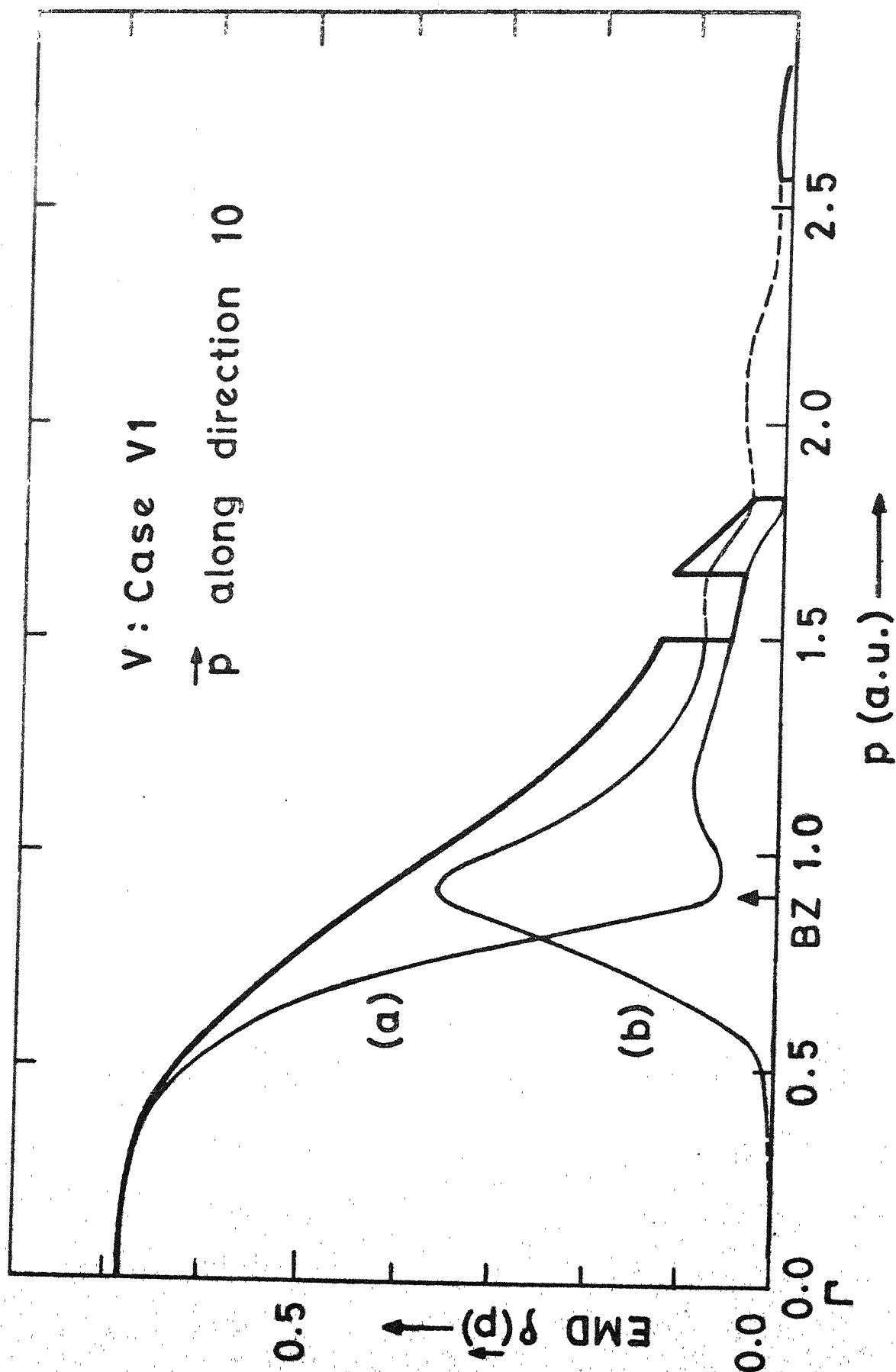


FIG. 4.32 : The EMD along direction 10.

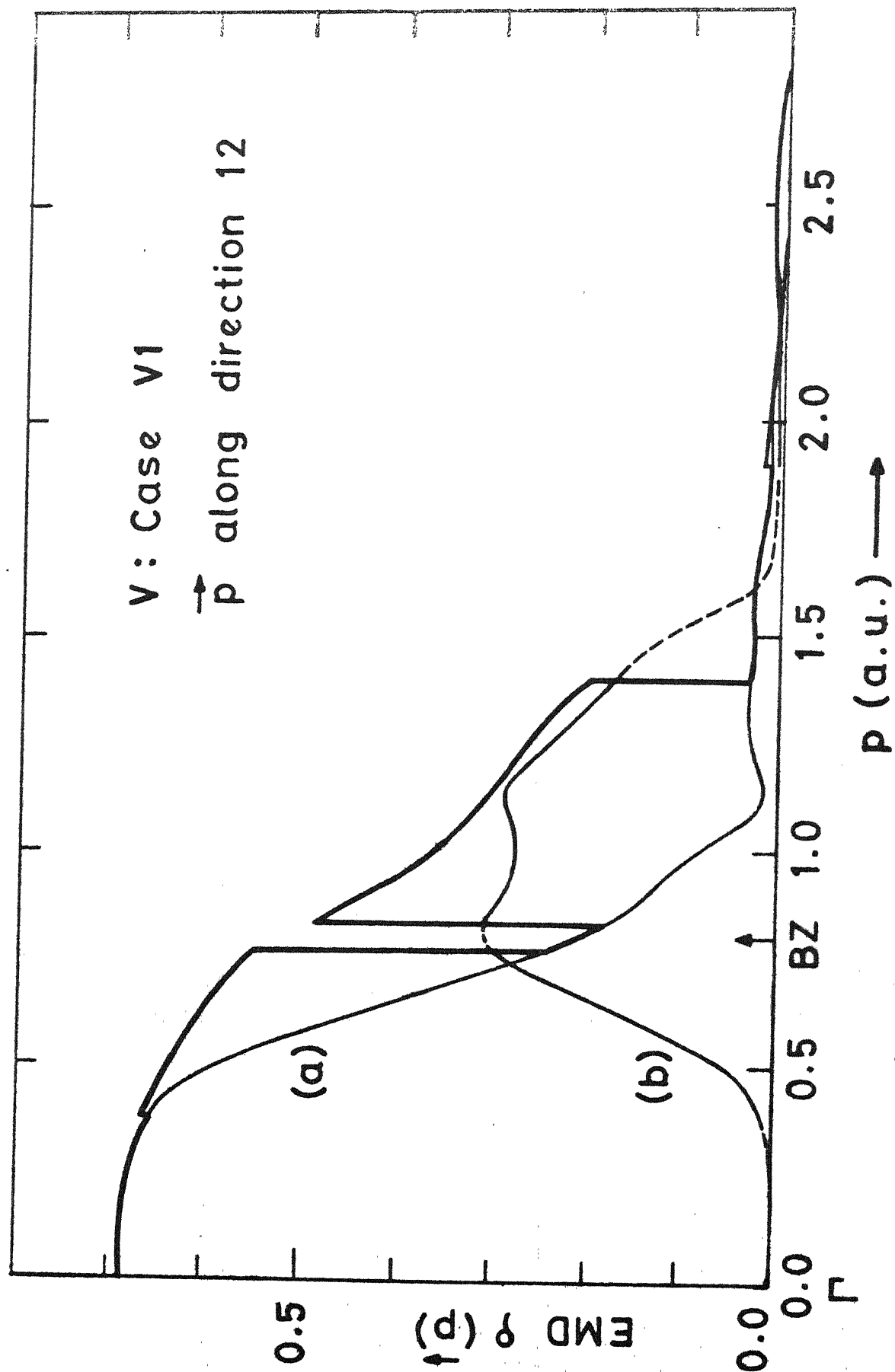


Fig. 4.33 : The EMD along  $\vec{p}$  direction 12.



in Figs. 4.10, 4.16 and 4.21. Similar plots (however without the bandstructure diagrams) for the other nine  $\vec{p}$ -directions (for the case VI) are presented in Figs. 4.25-4.33. All these results when examined together illustrate how the  $\rho(\vec{p})$  distribution changes with the direction of  $\vec{p}$  in the (100) and (110) plane and bring out the anisotropic nature of the EMD. These anisotropies can be understood in terms of the bandstructure of V, that is, in terms of two effects, (i) the Fermi surface topology and (ii) the symmetry selection rule effect which allows only the bands of the (+) symmetry to contribute along the  $(\xi, \eta, 0; \xi \neq \eta \neq 0)$  and  $(\xi, \eta, \eta; \xi \neq \eta \neq 0)$  directions. To illustrate this effect we have shown the partial EMD curves for the two (+) bands involved in Figs. 4.25 to 4.33. The vertical arrow marked by BZ in these figures indicate the boundary of the first BZ. These results can be understood and analyzed in terms of the above two (FS and selection rule) effects in a manner similar to §4.4.2 and 4.4.3.

#### 4.4.6 Isodenses of the EMD in the (100) and (110) planes in V

In order to obtain a better understanding of the EMD,  $\rho(\vec{p})$ , it is useful to plot the results in terms of constant EMD contours (or isodenses showing the curves  $\rho(\vec{p}) = \text{constant}$ ) in the (100) and (110) planes. Besides bringing out the anisotropy of the EMD, such plots of the isodenses offer the

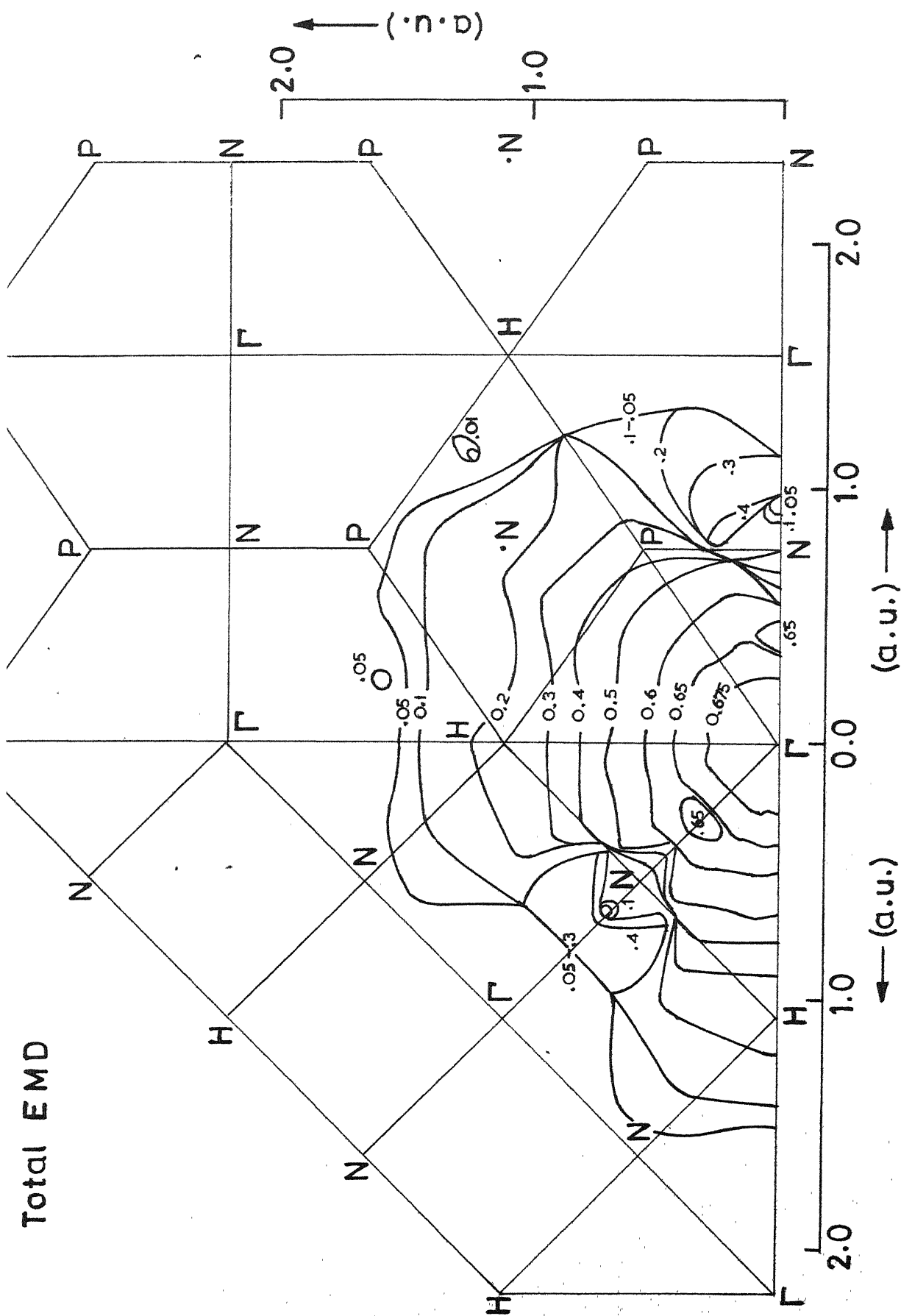


Fig. 4.34 : The total electron momentum isodense curves in the (100) and (110) planes (case VI).

v. case v2  
Total EMD

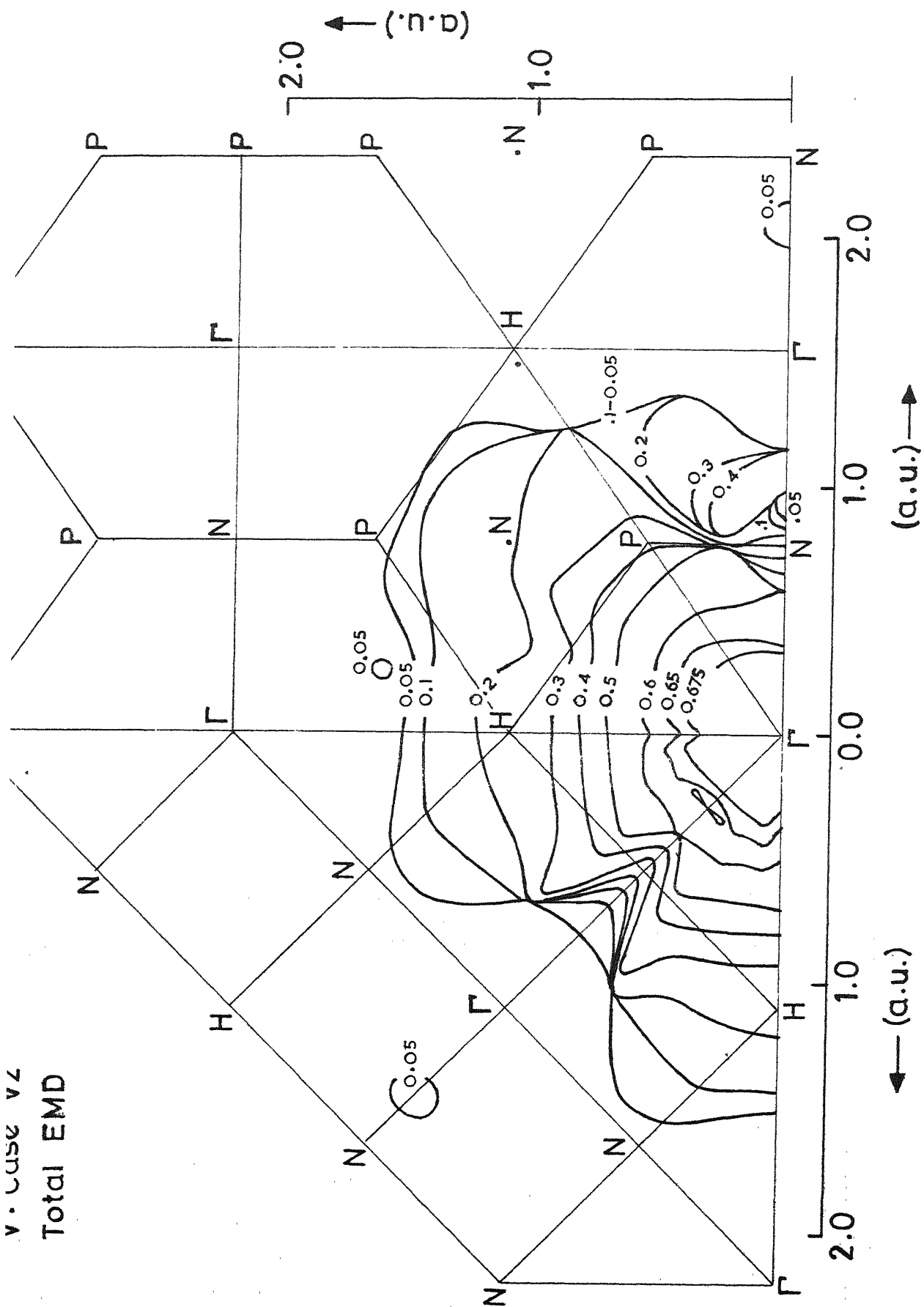


Fig. 4.35 : the total electron momentum isodensity curves in the (100) and (110) planes (case v2)

following advantages: (i) The effects of the FS topology, particularly on the high momentum components of the EMD is more clearly seen. (ii) They provide a wider basis to compare the results of the unfolding of experimental Compton profiles as these results are usually expressed in terms of such isodensities [15].

Using the present results for the EMD (for the case V1 and V2) along the twelve  $\vec{p}$ -directions (Table 4.5) isodensities for the total EMD were constructed and are shown in Figs. 4.34 and 4.35. These isodensities provide a wealth of information and it would be interesting, in future, to compare the results of Figs. 4.34-4.35 (for the total EMD) with those obtained by the unfolding procedure.

It is observed from Figs. 4.34 and 4.35 that the isodensities of the total EMD obtained from the two crystal potentials V1 and V2 are very similar except for some very minor differences. In other words, the isodensities of total EMD obtained from the unfolding of the experimental data will not be able to distinguish between the cases V1 and V2. This point would be further discussed in the next section wherein we summarise our results.

From the point of view of the bandstructure, it is equally interesting to examine the isodensities of the partial EMD contributed by the individual bands. We have plotted such

V:Case V1

Band 1 EMD

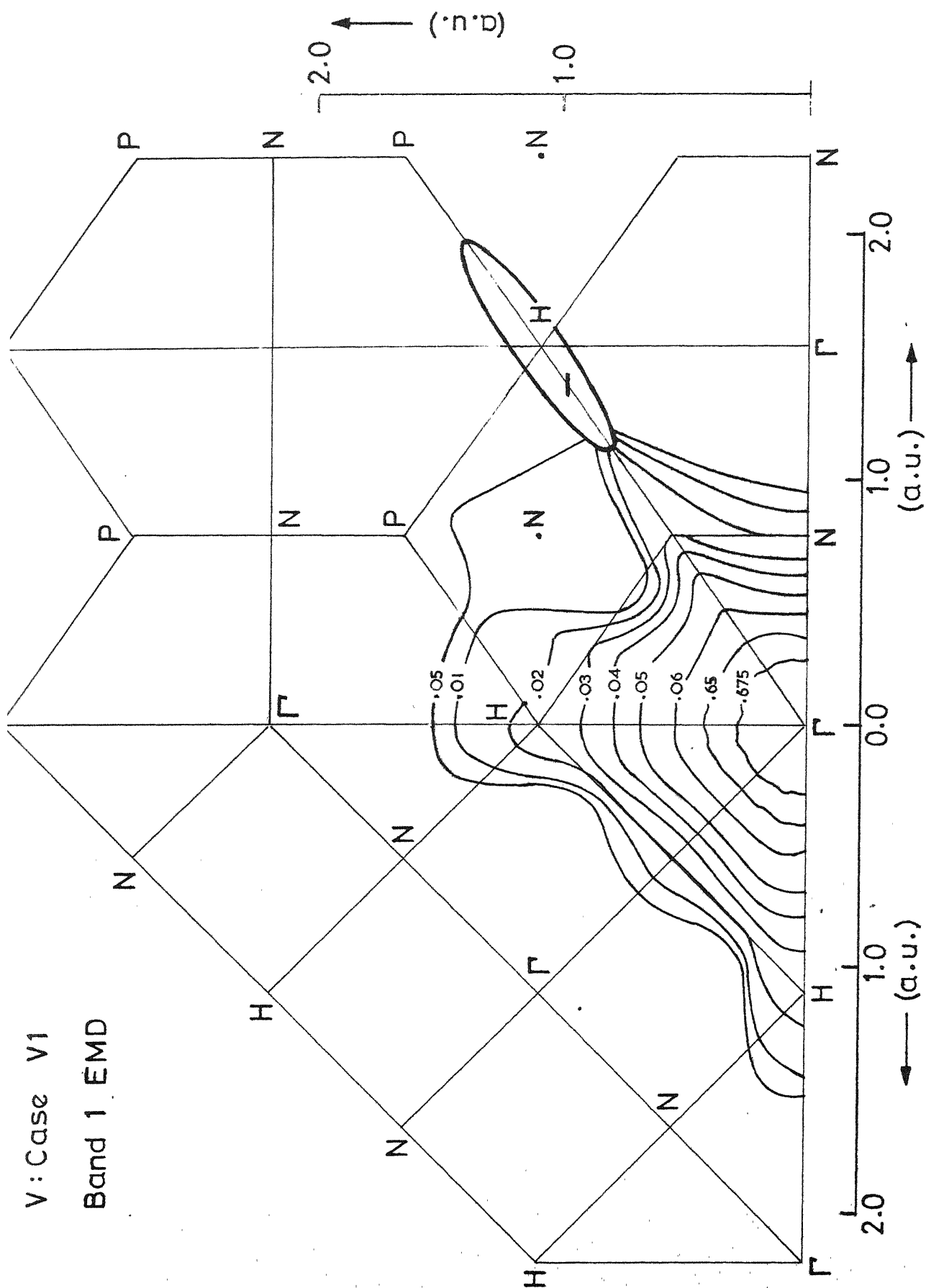


Fig. 4.36 : The electron momentum isodensity curves in the (100) and (110) planes

Fig. 4.37 : The electron momentum density curves in the (100) and (110) planes

# Band 3 EMD

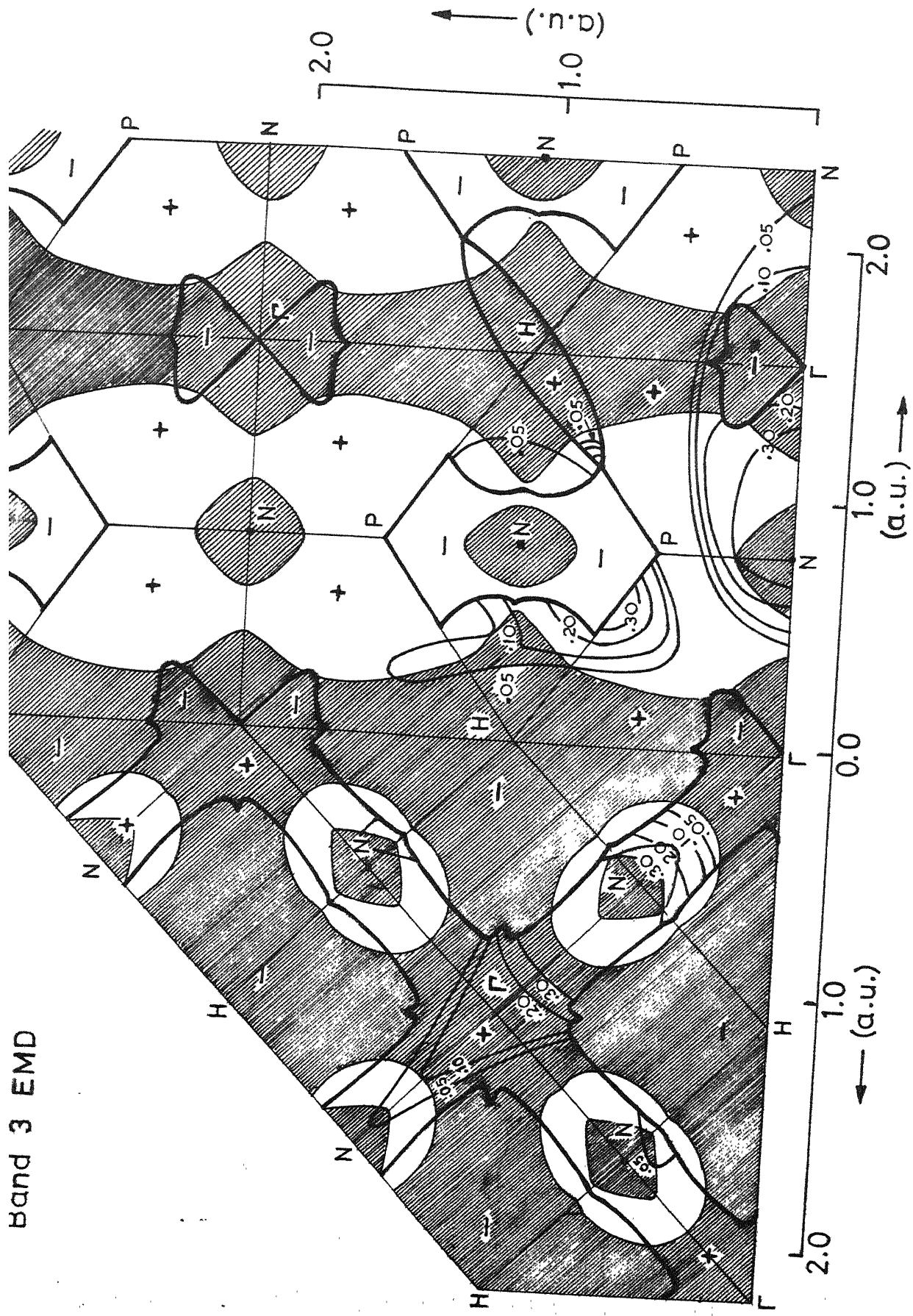


Fig. 4.38 : The electron momentum isodensity curves in the (100) and (110) planes due to the third lowest energy band (see Fig. 4.37)

isodensities for the first three (numbered according to increasing energy, i.e. lowest is termed first etc.) bands of vanadium (case VI) in the (100) and (110) planes in Figs. 4.37 and 4.38. In these figures the (+) and (-) signs indicate the symmetry of the bands in that region and the thick curves separating the (+) and (-) regions mark the lines where the adjacent bands touch or cross. There is a transfer of EMD across these boundaries as the symmetry of the bands (+/-) changes. As seen above only the bands with (+) symmetry contribute to the EMD. In Figs. 4.37 and 4.38 the Fermi surface is also marked, the shaded region denoting the unoccupied region.

The only isodensities of the EMD for V reported in the literature are those by Wakoh et al. [18] for the first band in the (100) plane. Our results (Fig. 4.36) show a good agreement with their results. These isodensities show considerable anisotropy even for the lowest band in the (110) plane. Since this band has almost no crossings with other bands and lies wholly in the occupied region below the Fermi surface, the anisotropy observed in this case arises mainly due to the intrinsic nature of the band itself, i.e., the nature of the wavefunctions which describe the band.

Figs. 4.37 and 4.38 bring out the validity of the selection rule, dependence on the FS topology and the anisotropy of the partial EMD. They also show that the sheet of th



second band FS ( $\Gamma$ -centered octahedral hole surface) is only partially observable in the (100) and (110) plane by Compton scattering. The N-centered hole ellipsoids (third band FS sheet) are observable (Fig. 4.38) only in some places in the (100) and (110) planes but with a weak intensity. Same appears to be the case with the JG-arms of the FS. Of course, these FS sheets will be more prominently observable outside the symmetry planes (100) and (110) and would therefore determine the shape of directional Compton profiles.

The results of Fig. 4.37 and 4.38 show the existence of nodal lines along the  $\langle 100 \rangle$  and  $\langle 111 \rangle$  directions. As explained by Harthoorn and Mijnders [13] this is the effect of the symmetry selection rule.

### Summary

It is well known that the bandstructure of vanadium is sensitive to small changes in the starting potential used for the calculation [2,9,19]. To study the effect of changing the potential on the bandstructure and EMD, we constructed various potentials with different 3d, 4s population and the exchange parameters  $\alpha$ . However, bandstructure calculations could not be completed for all of them because of the limitations of the Hubbard's fast approximation scheme. In particular, it was found

that the computational method worked successfully for only those potentials for which the d bandwidth was below a certain value, namely,  $\sim 0.55$  Ry.

From the results of the potentials studied the following facts seem to emerge:

- (1) There is a variation in the bandstructure when the 3d, 4s population is changed, the d bandwidth increasing with the increase in d population.
- (2) There is a variation when the exchange parameter  $\alpha$  is changed, the d bandwidth increasing when  $\alpha$  is reduced. This variation was found to be more significant than in (1). That is, when  $\alpha$  was reduced from 1 to  $2/3$ , the increase in the d bandwidth was more, than for the case where the d population was increased from  $3d^3 4s^2$  to  $3d^4 4s^1$ .
- (3) In addition to these, the bandstructure was also sensitive to whether the calculations were performed self-consistently or not.

The following potentials gave reasonably good bandstructure results when compared with the previous theoretical and experimental results:

V1 : constructed nonself-consistently with a configuration  $3d^3 4s^2$  and exchange parameter  $\alpha = 2/3$  [1].

V2 : constructed nonself-consistently with a configuration  $3d^4 4s^1$  and exchange parameter  $\alpha = 1$ .

V3 : constructed self-consistently with a configuration  $3d^3 4s^2$  and exchange parameter  $\alpha = 2/3$  [2].

The Fermi surface constructed for these potentials were found to be in agreement with those constructed by Mattheiss [10], Wakoh [7] and Papaconstantopoulos [2]. The comparison of the calculated ratios of the dimensions of the hole ellipsoid centred at the symmetry point N agreed fairly well with the experimental values reported [11].

Some of the previous calculations had reported the possibility of necks along the  $\langle 110 \rangle$  direction in the Fermi surface hole sheets connecting the JC arms along  $\langle 100 \rangle$  directions and the ellipsoids at N [10]. However, no such necks were obtained by us for any of the above three potentials.

Calculations of the EMD were performed for the above 3 potentials, detailed calculations being completed for V1 and V2. For these the EMD was calculated along 12  $\vec{p}$  directions in the (100) and (110) planes. The EMD thus obtained was found to obey the symmetry selection rules proposed by Mijnaerends [13]. The total EMD along the various  $\vec{p}$  directions could be accounted for in terms of the symmetry selection rules, Fermi surface effects and the intrinsic nature of the individual band wavefunctions. The behaviour of the EMD was brought out through isodensities in the (100) and (110) planes. It is suggested that the directional

Compton profiles from V single crystals could be experimentally measured and unfolded to obtain the EMD and then compared with the theoretical values. Because of the sensitivity of the EMD to various features of the FS (in particular the neck along the  $\langle 110 \rangle$  direction in the 3rd band hole sheet), this is especially desirable in vanadium.

Even though the bandstructure calculations are sensitive to the variations in the 3d population, the exchange parameter  $\alpha$ , and whether the calculations are self-consistent or not, some of these variations have a cancellation with each other. Thus for the potentials V1 and V2, there are no significant differences, while for V1 and V3, some differences are observed along the  $\langle 110 \rangle$  direction.

It might appear that the results of our calculations of the EMD in vanadium are not so conclusive in distinguishing between the various potentials V1, V2 and V3. It should be pointed out, once again, that in going from V1 to V2, the cancellation effect has taken place because the decrease in the d bandwidth due to the change in  $\alpha$  from  $2/3$  to 1 has almost compensated the increase in d bandwidth due to the 3d population going from 3 to 4. Similarity between the results of V1 and V2 is, therefore, not surprising. Unfortunately, our attempts to calculate the EMD for some non-self consistent potentials with the exchange parameter  $\alpha=2/3$ , e.g.,  $3d^4 4s^1$   $\alpha=2/3$  could not succeed because of the computational limitations of Hubbard's approximate scheme. This limitation can be removed by using a more accurate method like the APW method to calculate the bandstructure and EMD.

Such an APW calculation using different crystal potentials can lead to a more conclusive choice amongst the potentials when compared with experimental results. This comparison for a metal like vanadium with a significant anisotropy in the EMD would be more meaningful if it involves a number of  $\vec{k}$  directions.

In our opinion, the important conclusion brought out by the present work is as follows: For a metal like V, it is the combination of the effects of the electron configuration, exchange parameter and self-consistency (or non-self-consistency) for the different crystal potentials used that determines the total nature of the bandstructure, the FS and the EMD. It is therefore not enough to consider the effects of the electron configuration alone as was done by Paakkari et al. [6]. These authors analysed the experimental data for the Compton profiles from some 3d transition metals in the framework of the RFA model and concluded that a  $(3d)^{n-2}(4s)^2$  type of electron configuration is more appropriate for metals like Ti and V. We feel that such an analysis is somewhat incomplete and the conclusions drawn are somewhat hasty. Our results indicate that such conclusions can be drawn only after accurate bandstructure calculations employing different sets of electron configuration, exchange parameter and self-consistency are made and results carefully compared with experimental data.

# REFERENCES

1. P. E. Mijharends, 'Construction of a Muffin-Tin Potential for Metallic Vanadium', Report RCN-76-010, Reactor Centrum, Nederland, Petten (N.H.), The Netherlands, 1975 (Unpublished).
2. D. A. Papaconstantopoulos, J. R. Anderson and J. W. McCaffrey, Phys. Rev. B5, 1214 (1972).
3. S. Bhatnagar, Phys. Rev. 183, 657 (1969).
4. J. Hubbard, J. Phys. C 2, 1222 (1969).
5. D. G. Kanhere and R. M. Singru, J. Phys. F 7, 2603 (1977).
6. T. Paakkari, S. Manninen and K. -F. Berggren, Phys. Fenn. 10, 207 (1975).
7. S. Wakoh and J. Yamashita, J. Phys. Soc. Jap. 35, 1394 (1973).
8. G. A. Burdick, Phys. Rev. 129, 168 (1963).
9. L. L. Boyer, D. A. Papaconstantopoulos and B. M. Klein, Phys. Rev. B15, 3685 (1977).
10. L. F. Mattheiss, Phys. Rev. 139, A1893 (1965).
11. R. D. Parker and M. H. Halloran, Phys. Rev. B9, 4130 (1974).
12. P. E. Mijharends, Physica, 63, 235 (1973).
13. R. H. Harthoorn and P. E. Mijharends, 'The Effect of Symmetry on Electron Momentum Distribution in Solids', Report ECN-77-138, Stichting Energie-Onderzoek Centrum Nederland, Petten (N.H.), The Netherlands, 1977 (Unpublished).
14. J. F. Cornwell, Group Theory and Electronic Energy Bands in Solids, North-Holland Publishing Co., Amsterdam, 1969.
15. P. E. Mijharends in Compton Scattering, ed. B. Williams, McGraw-Hill, London, 1977; pp 323-345.
16. P. E. Mijharends, Phys. Rev. 160, 512 (1967).

17. F. M. Mueller, Phys. Rev. B15, 3059 (1977).
18. S. Wakoh and J. Yamashita, J. Phys. Soc. Jap. 35, 1406 (1973).
19. L. F. Mattheiss, Phys. Rev. 134, A970 (1964).

## Chapter 5

### DIRECTIONAL COMPTON PROFILES AND THEIR ANISOTROPIES FOR VANADIUM

#### 5.1 Introduction

In the preceding Chapter we presented our theoretical results for the EMD in V in the (100) and (110) planes and discussed these results in terms of the bandstructure and Fermi surface of V. It was pointed out that the EMD curves obtained by us for the various  $\vec{p}$ -directions could not be directly compared with the experimental results because no information about the directional EMD,  $\rho(\vec{p})$ , unfolded from the experimental Compton profiles,  $J_{hkl}(p_z)$ , has been reported in the literature. There exists another meeting ground between theory and experiment and this is through a comparison of the directional profiles  $J_{hkl}(p_z)$  and their anisotropies (or difference curves)  $\Delta J(p_z)$  defined by

$$\Delta J(p_z) = J_{h'k'l'}(p_z) - J_{hkl}(p_z) \quad (5.1)$$

It has been demonstrated, particularly in the case of transition metals [1], that as compared to the single profiles the



anisotropy curves provide perhaps a more reliable and sensitive method to compare the theory with experiment. The anisotropy curves are to be preferred because of the following two important advantages: (i) In the transition metals the core electron contribution to the profile  $J(p_z)$  is quite large (about 58% at  $p_z = 0$  for V). In a single directional profile of a transition metal the band profile is, therefore, masked by the core profile. However, the core profiles cancel out (in the approximation of the isotropic core EMD) in the  $\Delta J(p_z)$  curves and thus the anisotropy curves are more sensitive to the effects of band electrons. (ii) Secondly, the directional Compton profiles are affected by the multiple Compton scattering in the sample, the effect showing up as the reduction of the CP height,  $\Delta J(0)$ , as well as the broadening of the profile  $J(p_z)$  itself. Although corrections for multiple scattering effects can be made these corrections are always somewhat uncertain. If the sample thickness is held constant, the anisotropy curves  $\Delta J(p_z)$  should not be significantly affected by the multiple scattering corrections. In view of the above considerations we shall present in this Chapter the results of directional Compton profiles and their anisotropies  $\Delta J(p_z)$  obtained from the EMD,  $\rho(\vec{p})$ , calculated by us.

## 5.2 Method of Calculation

The calculation of the directional Compton profile  $J_{hkl}(p_z)$  from the theoretical EMD,  $\rho(\vec{p})$ , requires an evaluation of the double (or surface) integral

$$J_{hkl}(p_z) = \int_{-\infty}^{+\infty} \int \rho(\vec{p}) \, dp_x dp_y \quad (5.2)$$

The integration involved in (5.2) requires a knowledge of  $\rho(\vec{p})$  at several points throughout the momentum space. This, in turn, involves a tremendous computational effort. An alternate but approximate method, suggested by Seth and Ellis [2] consists of expanding  $\rho(\vec{p})$  as a series of lattice harmonics. The outline of this method is given below.

It was first suggested by Mijnenas [1,3] that the EMD  $\rho(\vec{p})$  can be expanded as

$$\rho(\vec{p}) = \sum_{l,v} \rho_{lv}(p) F_{lv}(\Omega_{\vec{p}}) \quad (5.3)$$

where  $F_{lv}(\Omega_{\vec{p}})$  are the lattice harmonics which form an orthonormal set of invariant linear combinations of spherical harmonics of order  $l$  while  $\Omega_{\vec{p}}$  denotes the orientation of  $\vec{p}$ . Different harmonics of the same order and symmetry type are distinguished by the label  $v$ . In the case of cubic lattices (e.g. bcc V) only the harmonics having  $l = 0, 4, 6, 8, 10, 12$  (twice), 14, ... will contribute.

Next two orthogonal coordinate systems  $R_c$  and  $R_a$  are defined. A system fixed to the crystal and denoted by

$R_c \equiv (\xi, \eta, \zeta)$  is used as the reference system for defining the lattice harmonics. Another coordinate system  $R_a = (x, y, z)$  is assumed to be fixed to the apparatus so that the z-axis is along the scattering vector. A rotation of the coordinate system  $R_c$  through the Euler angles  $\alpha, \beta$  and  $\gamma$  can make the two systems  $R_a$  and  $R_c$  coincide. The angle  $\alpha$  is a measure of the rotation of the sample around the scattering vector while the angles  $(\beta, \gamma)$  denote the polar and azimuthal angles of the z-axis (i.e. the scattering vector).

The lattice harmonics  $F_{lv}(\Omega_{\vec{p}})$  can be further expanded in terms of the spherical harmonics  $Y_{lm}(\Omega_{\vec{p}})$  through the relation [3]

$$F_{lv}(\Omega_{\vec{p}}) = \sum_m a_{lmv} Y_{lm}(\Omega_{\vec{p}}) \quad (5.4)$$

It has been shown by Mijnenas [3] that the directional Compton profile  $J_{\beta\alpha}(p_z)$  can be written as

$$J_{\beta\alpha}(p_z) = 2\pi \sum_{l,v} F_{lv}(\beta, \alpha) g_{lv}(p_z) \quad (5.5)$$

where

$$g_{lv}(p_z) = \int_{|p_z|}^{\infty} \rho_{lv}(p) P_l(p_z/p) p \, dp \quad (5.6)$$

where  $P_l$ 's are the Legendre polynomials.

In his original method Mijnenas [3] used the scheme of Eq. (5.3)-(5.6) to unfold  $\rho(\vec{p})$  from a set of experimentally measured  $J_{\beta\alpha}(p_z)$ . We followed the scheme of Seth and Ellis [2]

and Kanhere [4] to obtain  $J_{\beta\alpha}(p_z)$  from  $\rho(\vec{p})$ . This method consisted of the following steps.

- i) The starting point of our calculations was the set of  $\rho(\vec{p})$  distributions along the 12  $\vec{p}$ -directions (Fig. 4.24) obtained by us for the VI type of the crystal potential of V. These  $\rho(\vec{p})$  curves are shown in Figs. 4.11, 4.16, 4.21 and 4.25-4.33 (Chapter 4).
- ii) As a next step we used Eq. (5.3) to expand  $\rho(\vec{p})$  in terms of  $\rho_{1\nu}(\vec{p})$  and  $F_{1\nu}(\Omega_{\vec{p}})$  to obtain a set of linear equations. The expansion (5.3) was truncated at  $l = 12$ .
- iii) This set of linear equations was next solved by using a least squares fit and an inversion scheme to obtain  $\rho_{1\nu}(\vec{p})$ .
- iv) The set of  $\rho_{1\nu}(\vec{p})$  functions so obtained was next used in Eq. (5.6) to construct  $g_{1\nu}(p_z)$  functions which through Eq. (5.5) led to the construction of the directional profiles  $J_{\beta\alpha}(p_z)$ .

### 5.3 Results and Discussion

The  $g_{1\nu}$  and  $\rho_{1\nu}$  functions obtained by the above calculations are shown in Figs. 5.1, 5.2 and 5.3 for  $l = 0, 4$  and  $6$ . The function  $g_0$  describes the spherically averaged part of the Compton profile (see Eq. 5.6) while the higher

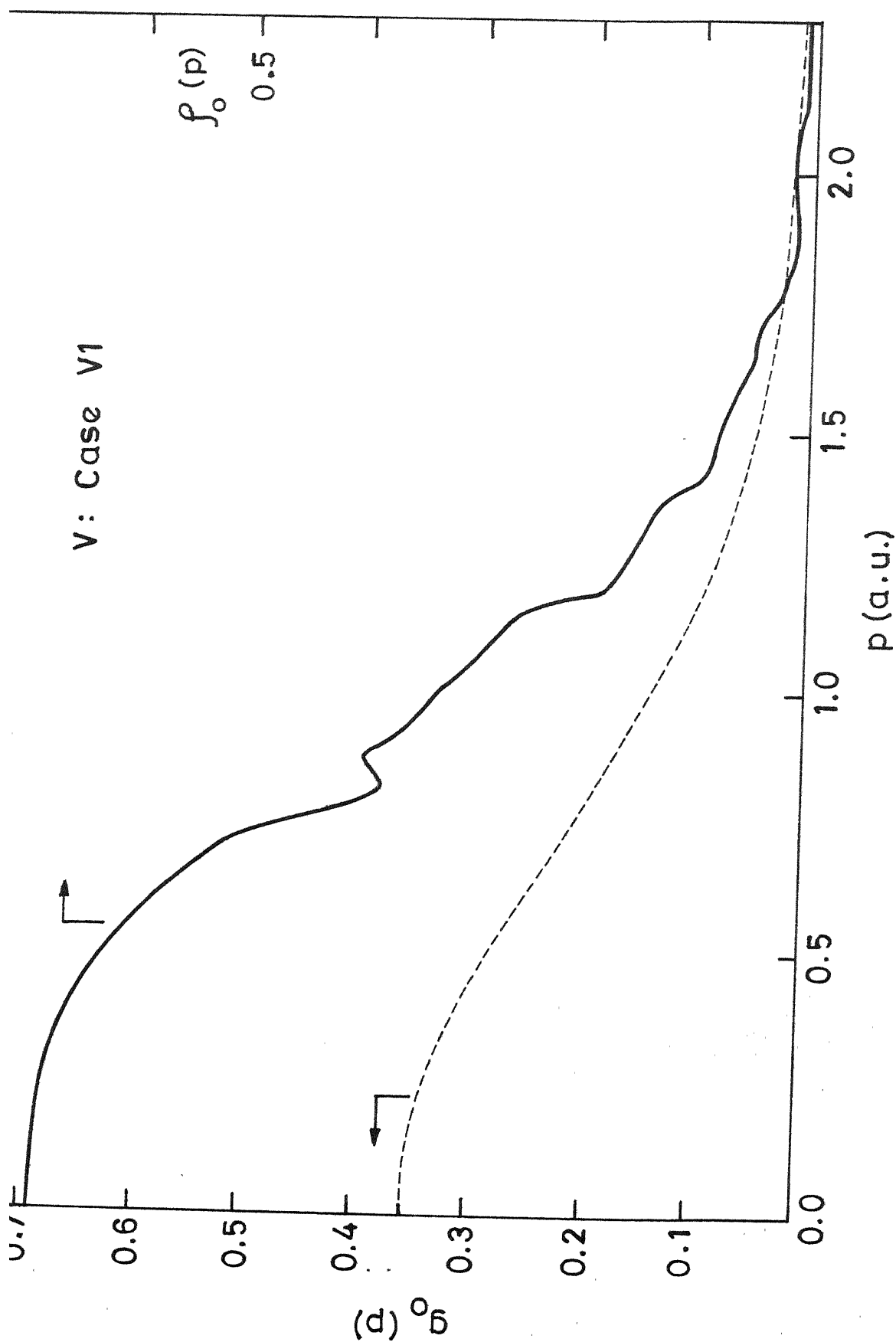


FIG. 5.1.1 : The spherically averaged Compton profile  $g_0(p)$  and the spherically averaged MD,  $f_0(p)$  (case V1).

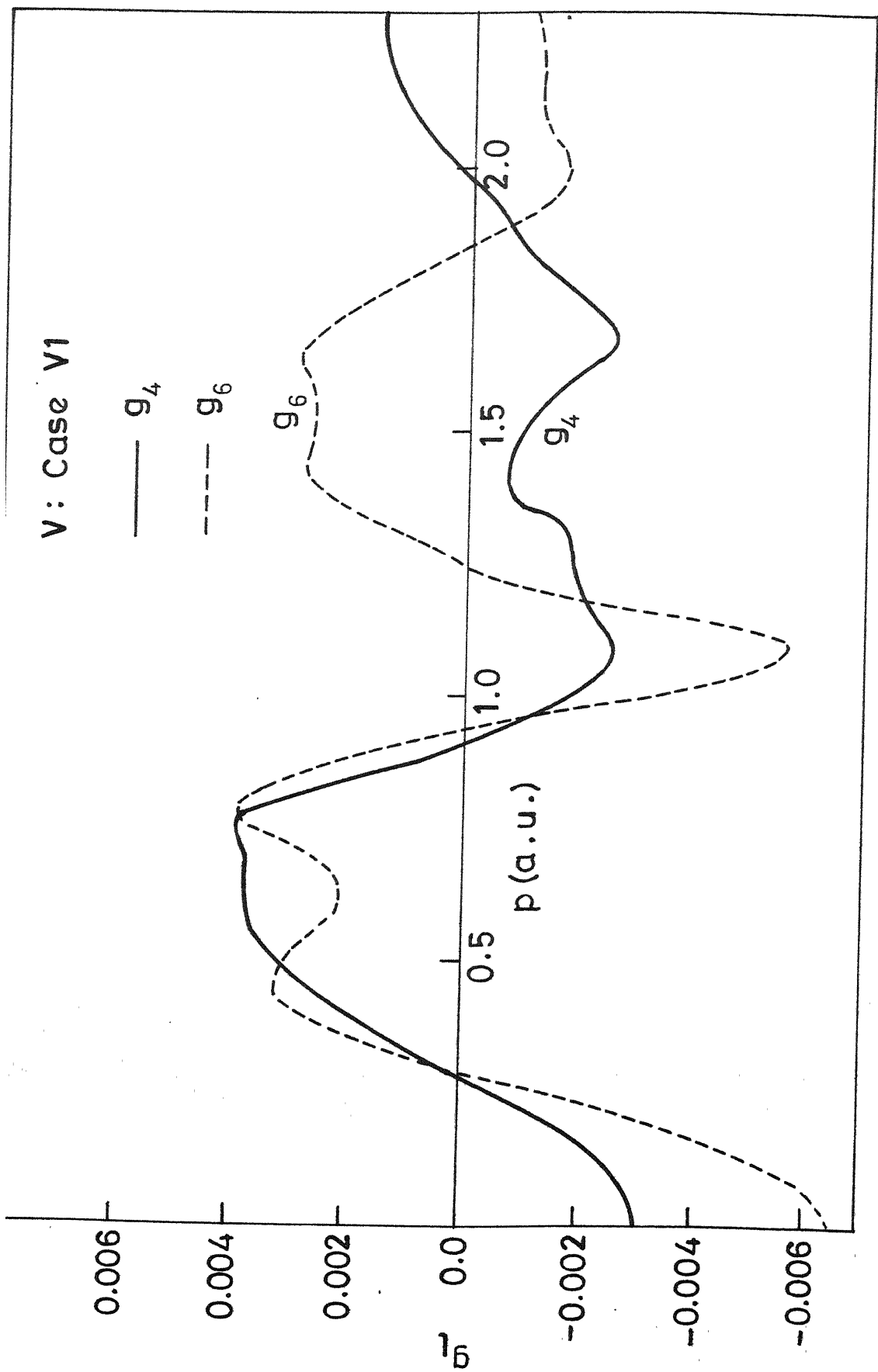


Fig. 5.2 : The Kubic harmonic components  $g_4(p)$  and  $g_6(p)$  of the Compton profiles (case V1).

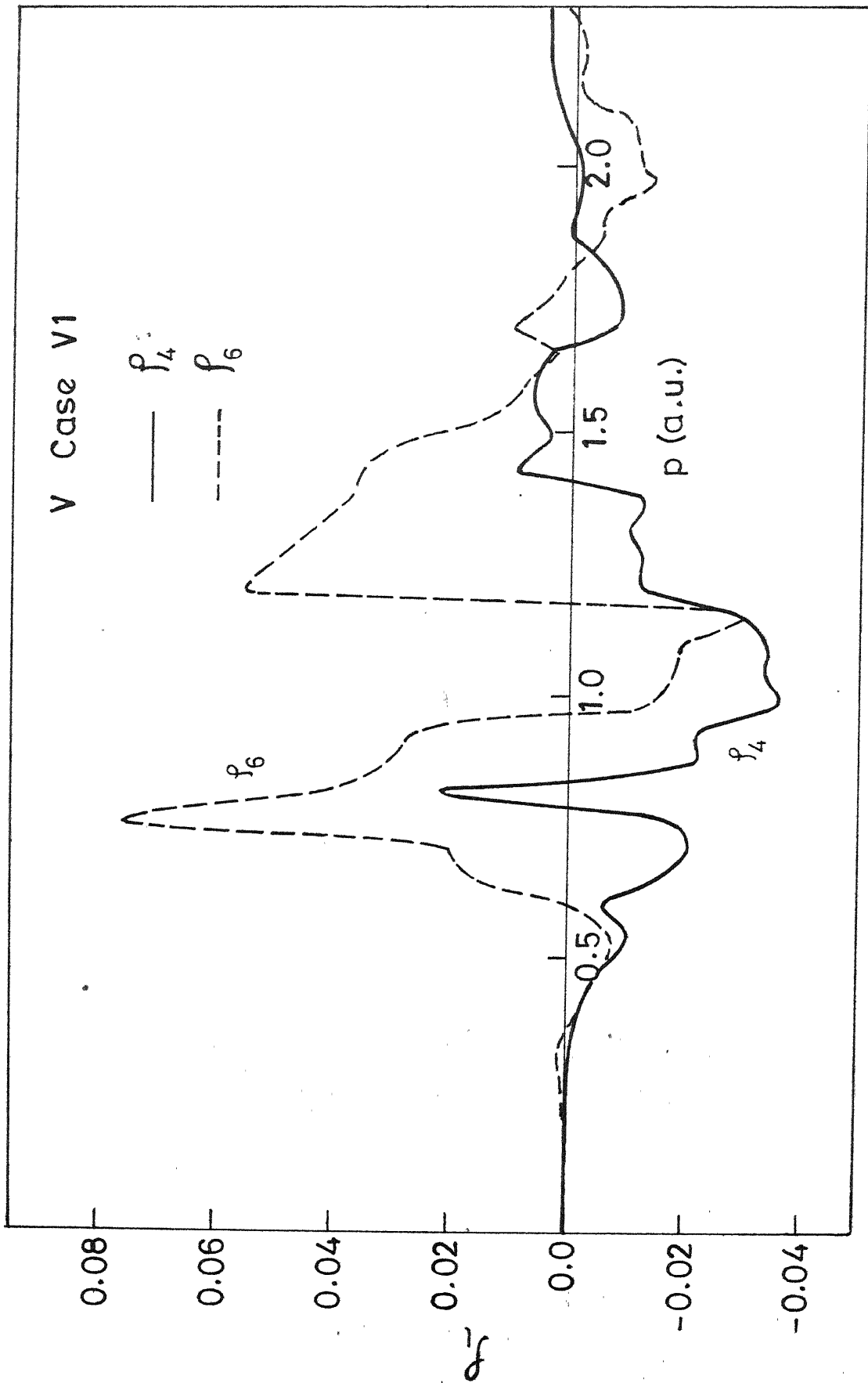


FIG. 5.3 : The cubic harmonic components  $\rho_4(p)$  and  $\rho_6(p)$  of the MHD (case V1).

( $l \geq 4$ )  $g_l$ -functions indicate the non-spherical or the anisotropic part of the Compton profile. Similarly, the  $\rho_0$  function describes the spherically averaged part of the EMD while the higher ( $l \geq 4$ )  $\rho_l$  functions describe the anisotropic part of the EMD.

Examination of Fig. 5.2 reveals that  $\rho_4$  and  $g_6$  are of comparable magnitude and they augment each other in the region  $p < 1.2$  a.u. but in the higher momentum region they cancel out. The curve for  $\rho_6$  shows more discontinuous behaviour than that for  $\rho_4$ . The structure shown by  $\rho_6$  arises from the spikes in the EMD along the  $\langle 110 \rangle$  direction and is related to the Fermi surface topology (e.g. dipping of the  $\Sigma_1$  band below the Fermi level) and its Umklapp images.

The results for  $g_l$  and  $\rho_l$  functions shown in Figs. 5.1-5.3 have one usefulness. The unfolding of the experimental Compton profiles by the lattice harmonic expansion method [1,3] also yields the plots of  $g_l$  and  $\rho_l$  curves. Examination of plots similar to those shown in Figs. 5.1-5.3 can, therefore, help design the Compton profile experiment by choosing the  $\vec{p}$ -directions (Eq. 5.5) for CP measurements.

The Compton profiles from polycrystalline samples of V has been measured by Manninen and Paakkari [5] and were later corrected for the multiple scattering effects [6]. In order to compare our theoretical profile



Table 5.1. Comparison of the spherically averaged Compton profile (present calculations) and the experimental values for polycrystalline V of Ref. [6].

$p_z$ in a.u.	$J_{\text{sph}}(p_z)$ present calc.	$J_{\text{sph}}(p_z)$ Ref. [6]
0.00	5.629	$5.405 \pm 0.08$
0.05	5.630	-
0.10	5.607	5.387
0.15	5.575	-
0.20	5.529	5.322
0.30	5.403	5.210
0.40	5.224	5.055
0.50	4.999	4.861
0.60	4.728	4.636
0.70	4.434	4.386
0.80	4.135	4.121
0.90	-	3.849
1.00	3.518	$3.576 \pm 0.07$
1.10	-	3.308
1.20	2.904	3.049
1.30	-	2.802
1.40	2.409	2.572
1.50	-	2.360
1.60	2.023	2.170
1.70	-	2.002
1.80	1.710	1.855
1.90	-	1.730
2.00	1.482	$1.623 \pm 0.05$
2.20	-	1.452
2.40	1.128	1.309

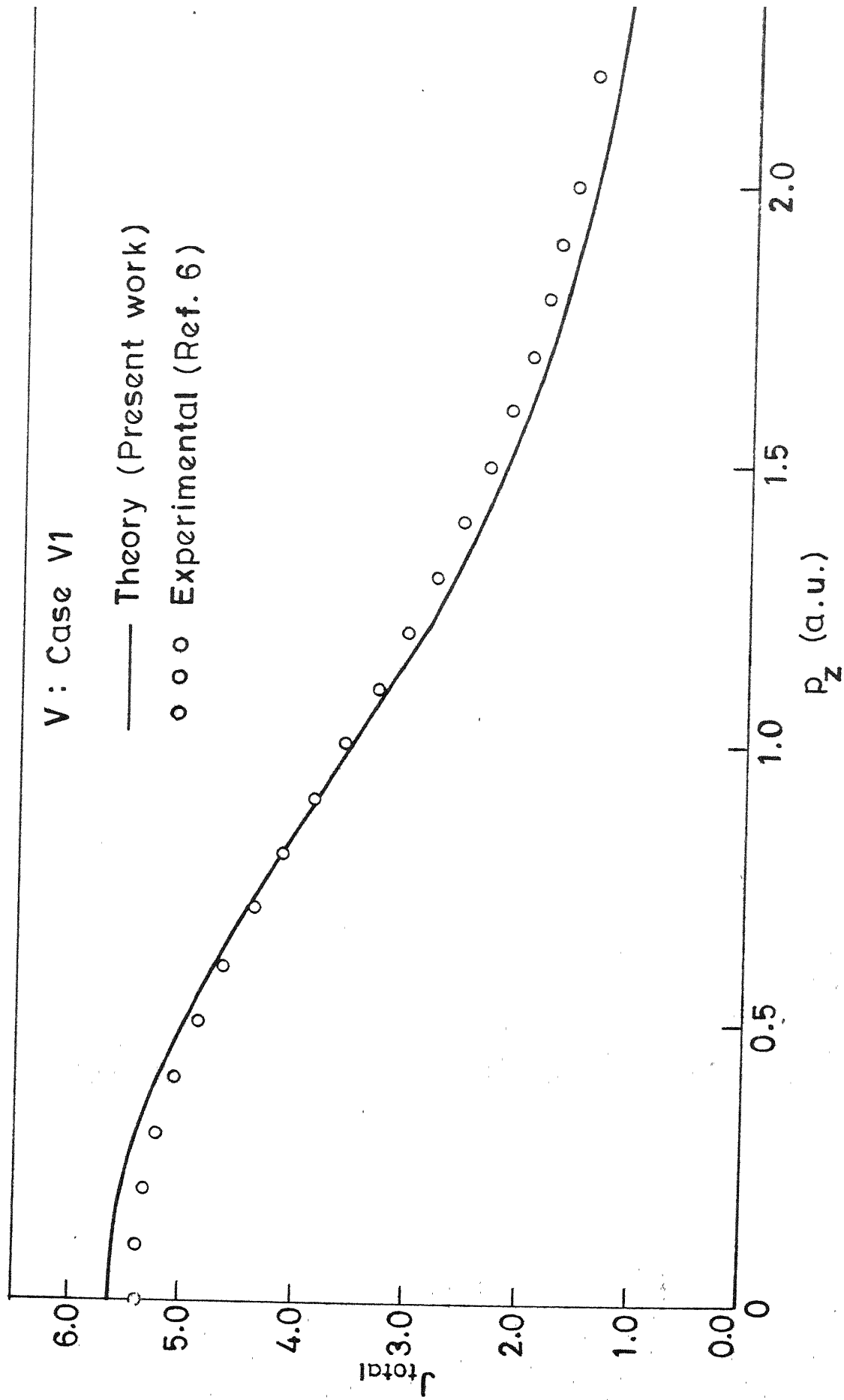


Fig. 1: The spherically averaged Compton profiles for various energies; comparison between theory and experiment.

with their results we proceeded as follows. Using the spherically averaged band profile [given by  $g_0(p_z)$  of Fig. 5.1] we first normalised it so that

$$\int_0^{2.4 \text{ a.u.}} g_0(p_z) dp_z = 2.2774 \text{ electrons}$$

where the number 2.2774 electrons was obtained by finding the area under the free-atom  $(3d)^3(4s)^2$  profile of Biggs et al. [7] between 0 and 2.4 a.u. To this normalised band profile we added the 'core' profile due to the  $(1s)^2(2s)^2(2p)^6(3s)^2(3p)^6$  electrons from the tables of Biggs et al. [7]. Such a total profile calculated for polycrystalline V is shown in Fig. 5.4 which also shows the experimental data by Paakkari et al. [6]. Both these profiles are normalised to the same area between 0 and 2.4 a.u. and are also compared in Table 5.1. The theoretical profile was convoluted with the residual instrument function of the experiment [6]. It is observed from Fig. 5.4 that our theoretical calculations slightly overestimate the contribution at low ( $p_z < 0.6$  a.u.) momenta but underestimates it at the high ( $p_z > 1.1$  a.u.) momenta. It may be pointed out that the theoretical Compton profile of V calculated by using the renormalised-free-atom model [6] also gave lower values in the momentum region  $p_z = 0.5$ - $1.5$  a.u. The slight disagreement between our calculated results and the experiment could be due to the inadequacy of the independent particle model used by us or due to some other reasons which are suggested below.

In the calculation of the spherically averaged as well as the directional profiles by the lattice harmonic expansion method we had made two approximations. Firstly the  $\rho(\vec{p})$  distributions used by us were calculated for the 12  $\vec{p}$ -directions (Fig. 4.24) all of which were lying in the symmetry planes, the (100) and the (110) planes. Thus the  $\rho(\vec{p})$  distributions along the general  $\vec{p}$ -directions (those removed from the (100) and (110) planes) were not considered while constructing the spherically averaged profile and this may lead to an incomplete spherical average. Secondly the accuracy in the calculation of the EMD by the Hubbard-Mijnarends method is limited at high momenta ( $p > 3$  a.u.) and we had therefore calculated the  $\rho(\vec{p})$  values upto  $p \sim 3$  a.u. As a result the integrations involved in Eq. (5.6) were necessarily truncated at  $p_{\max} \sim 3$  a.u. and this may lead to some error. In addition, another source of error could be the muffin-tin approximation to the crystal potential. It has been pointed out [8,9] that the non-constancy of the potential in the interstitial region ('warped muffin-tin') and the non-sphericity of the potential inside the muffin-tin sphere can affect the band structure results. Although no estimate of these effects on the EMD are available, we feel that some of the disagreement observed in Fig. 5.4 could also arise partly from these effects.

# V: Case V1

—  $J_{100}$   
.....  $J_{110}$   
---  $J_{111}$

2.5  
2.0  
1.5  
1.0  
0.5  
0

$J(p_z)$

0.5 1.0 1.5 2.0

$p_z$  (a.u.)

Fig. 5.5 : The theoretical Compton profiles [present work] along the  $\langle 100 \rangle$ ,  $\langle 110 \rangle$  and  $\langle 111 \rangle$  directions.

Wakoh and Yamashita [10] have calculated the spherically averaged Compton profile of V by a direct integration involved in Eq. (5.2) and obtained a good agreement with the earlier results of Paakkari et al. [see Ref. 10] which were perhaps not corrected for multiple scattering. It would be interesting to know whether a comparison of their theoretical profile with the revised experimental data [6] corrected for multiple scattering shows a behaviour similar to Fig. 5.4. The directional profiles obtained by us for the principal symmetry directions  $\langle 100 \rangle$ ,  $\langle 110 \rangle$  and  $\langle 111 \rangle$  are shown in Fig. 5.5 and their general features agree with the theoretical profiles calculated by Wakoh et al. [11] employing the APW method and by Callaway et al. [12] employing the LCGO method.

The most striking feature of the directional Compton profiles of V is the dip shown by the  $J_{100}(p_z)$  profile at  $p_z < 0.3$  a.u. (Fig. 5.5). To understand the origin of this dip it is not enough to examine the  $\rho(\vec{p})$  curves (Chapter 4). The directional profiles are constructed by the integration (Eq. 5.2) in the momentum space and one should therefore examine the EMD,  $\rho(\vec{p})$ , in different  $(p_x, p_y)$  planes of integration (normal to the hkl direction) for  $p_z = \text{constant}$ . However, our present results of the EMD are restricted to the (100) and (110) planes. Following Wakoh and Yamashita [10], a fair understanding can be obtained by examining the Fermi surface

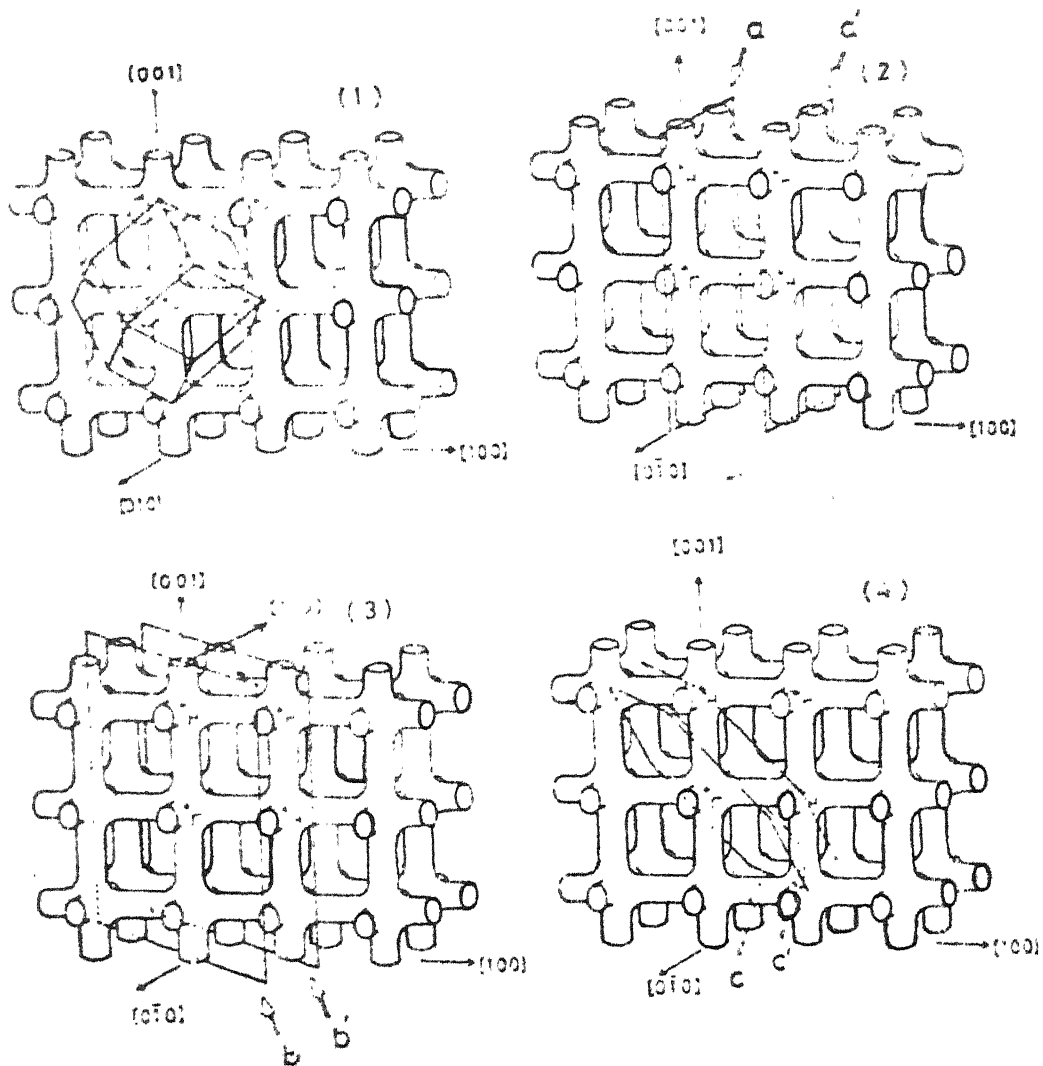


Fig. 5.6 : The schematic diagram of the F3 topology showing the various symmetry planes [10].

topology of  $V$  in the repeated zone scheme (Fig. 5.6). It must be remembered, however, that in addition to the Fermi surface topology, the effect of the symmetry selection rule (explained in § 4.4) will have to be taken into account for a complete understanding of the problem.

The concave structure (or the dip) shown by the  $J_{100}(p_z)$  profile at  $p_z \sim 0.0$  a.u. and again at  $p_z \sim 1.1$  a.u. arises primarily because of the jungle-gym structure of the Fermi surface of  $V$  (Chapter 2). In part 2 of the Fig. 5.6 are shown the planes of integration for the scattering vector along the  $[100]$  direction. Plane  $a$  passes through the point  $\Gamma(000)$  or  $p_z = 0$  while the plane  $a'$  passes through the point  $H(100)$  or  $p_z = \frac{2\pi}{a} = 1.094$  a.u. These planes  $a$  and  $a'$  contain the jungle-gym hole arms (or tubes) in two directions as well as the ellipsoidal holes around  $N$ . These unoccupied states will not contribute to the EMD in these planes. As one moves the plane of integration from  $a$  towards  $a'$ , say at  $p_z \sim 0.3$  a.u. the integration planes do not contain the jungle-gym hole arms (or the hole ellipsoids) any more. There is, therefore, a greater contribution to the EMD in this plane (as compared to  $a$ ) and as a consequence the Compton profile at  $p_z \sim 0.3$  a.u. shows a value which is higher than at  $p_z = 0.0$  a.u. This explains the concave part in the  $J_{100}(p_z)$  below  $p_z = 0.3$  a.u. The Umklapp image of this concave part occurs around  $p_z = 1.1$  a.u. as another concave curvature.



Similar considerations for the  $J_{110}(p_z)$  show that the two planes  $b$  and  $b'$  (Fig. 5.6) contain the jungle-gym hole arms in one (and not two) direction only. As a result the profile  $J_{110}(p_z)$  displays a less pronounced (or shallow) concave part at  $p_z = 0$  and again weakly at  $p_z = (2\pi/a)/\sqrt{2} = 0.774$  a.u. through the Umklapp process. Compared to the  $J_{100}$  and  $J_{110}$  profiles the  $J_{111}(p_z)$  profile shows no dips or concave structure because the planes  $c$  and  $c'$  (Fig. 5.6) normal to the  $[111]$  direction do not contain the jungle-gym hole arms.

When compared to the directional profiles (Fig. 5.7) calculated by Wakoh et al. [11] the present results (Fig. 5.5) show a qualitative agreement. However, the theoretical profiles of Wakoh et al. [11] give somewhat lower values at low momenta and slightly higher values at high momenta. Unfortunately, there are no Tables of experimentally measured directional profiles of  $V$  reported in the literature and hence a direct comparison between experimental and theoretical profiles obtained by Wakoh et al. [11] or by us is not possible. We feel that the differences between the results of Wakoh et al. [11] and the present work could be due to the different methods followed by Wakoh et al. [11] to construct the crystal potential (they have constructed the potential phenomenologically fitting state-dependent potentials to experimental FS data), to calculate the bandstructure

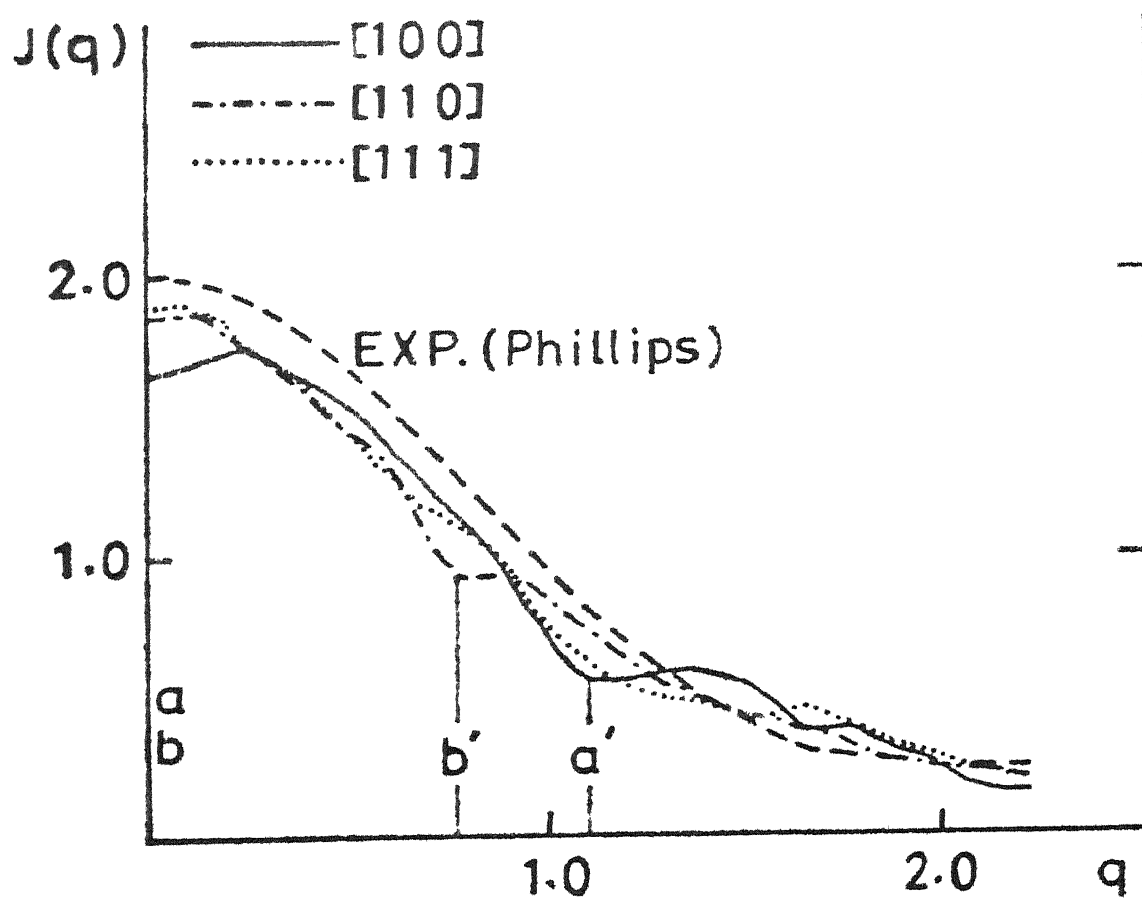


Fig. 5.7 : The directional correlation profiles calculated by Jaron et al. [11].

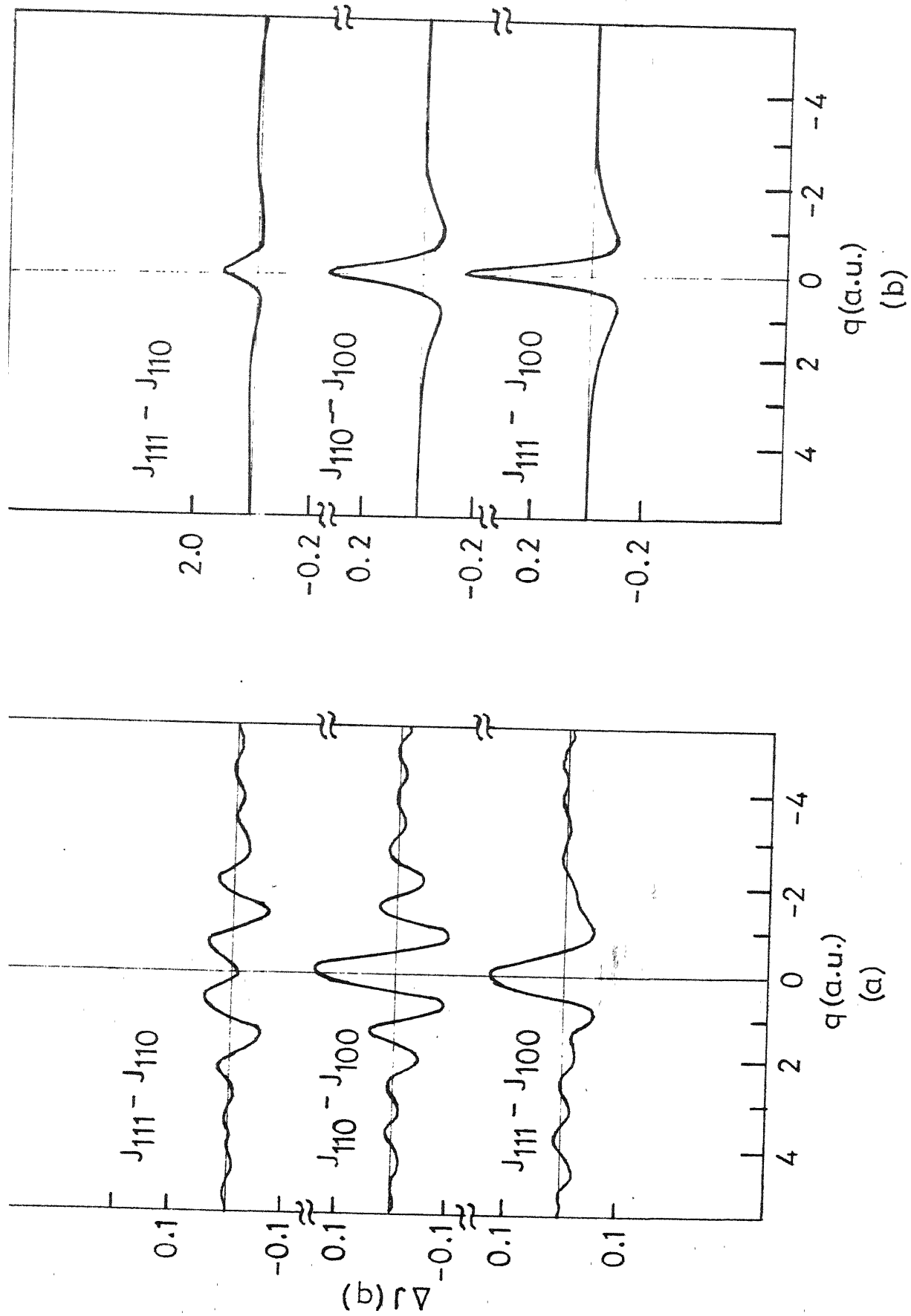


FIG. 5.8 : The Compton profile anisotropies (a) measured by Terasaki et al. [13] (b) calculated by Weiss [14].

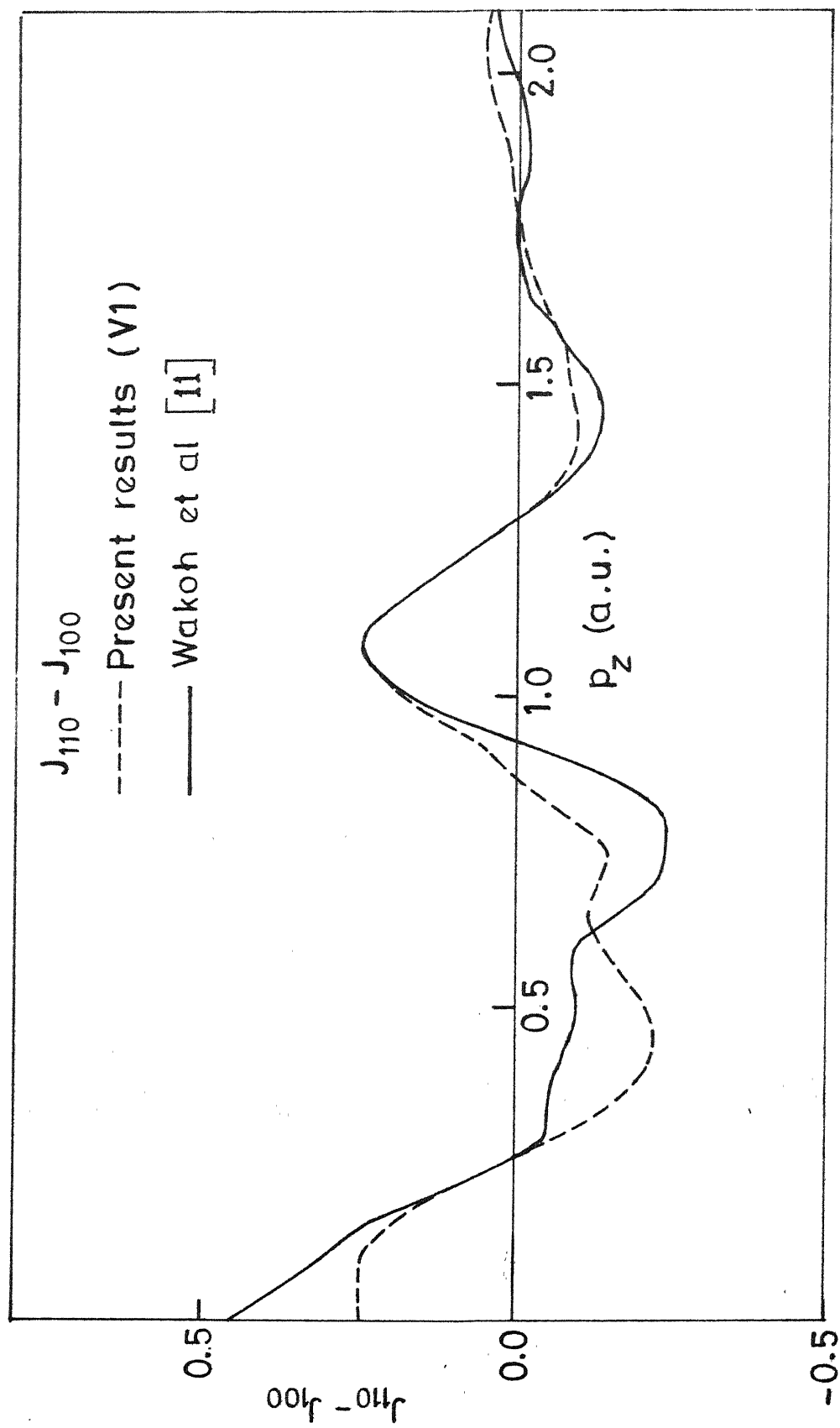


Fig. 4.9 : The theoretical Compton profile anisotropy  $J_{110} - J_{100}$ .

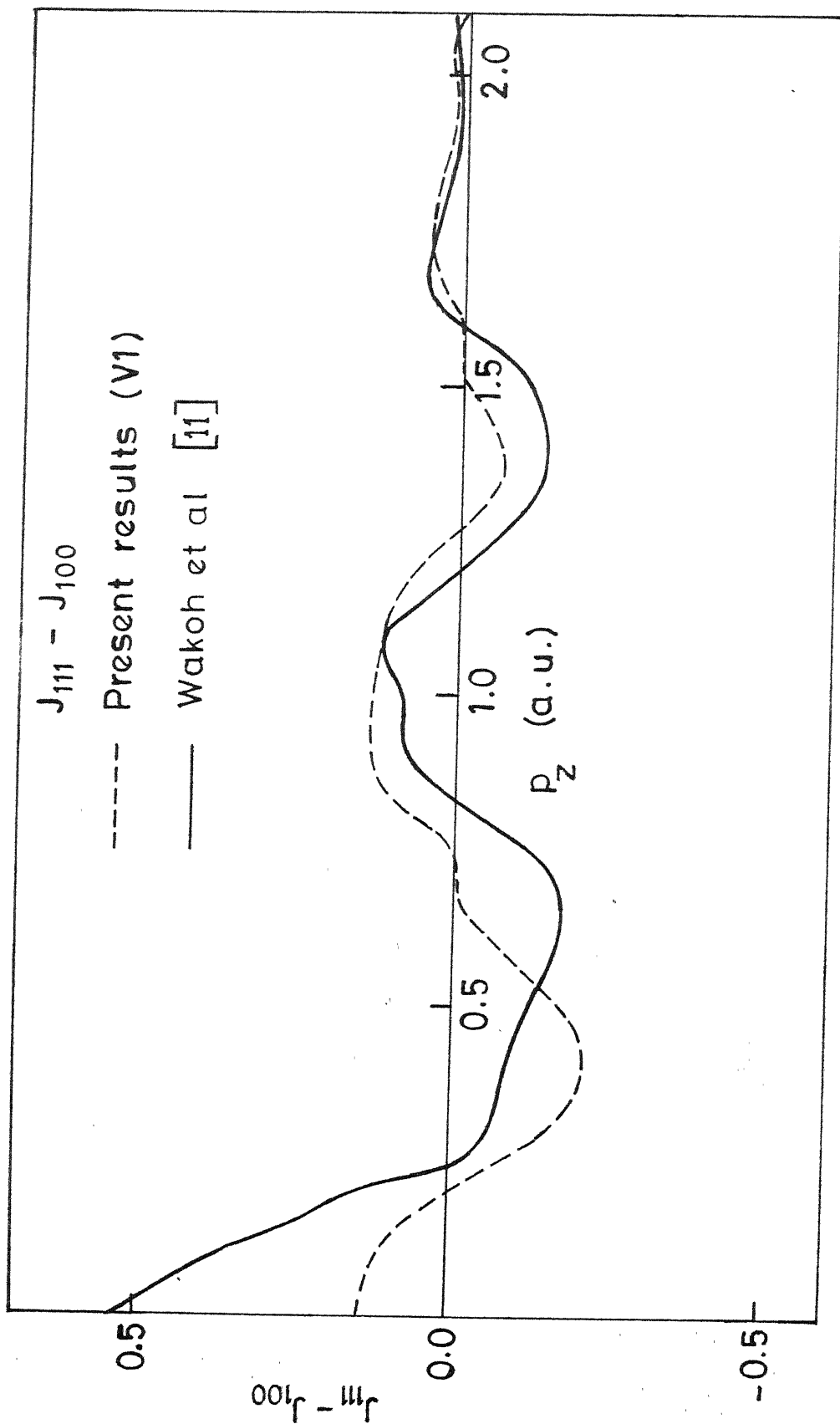


FIG. 3.10 : The theoretical Compton profile anisotropy  $J_{111} - J_{100}$ .

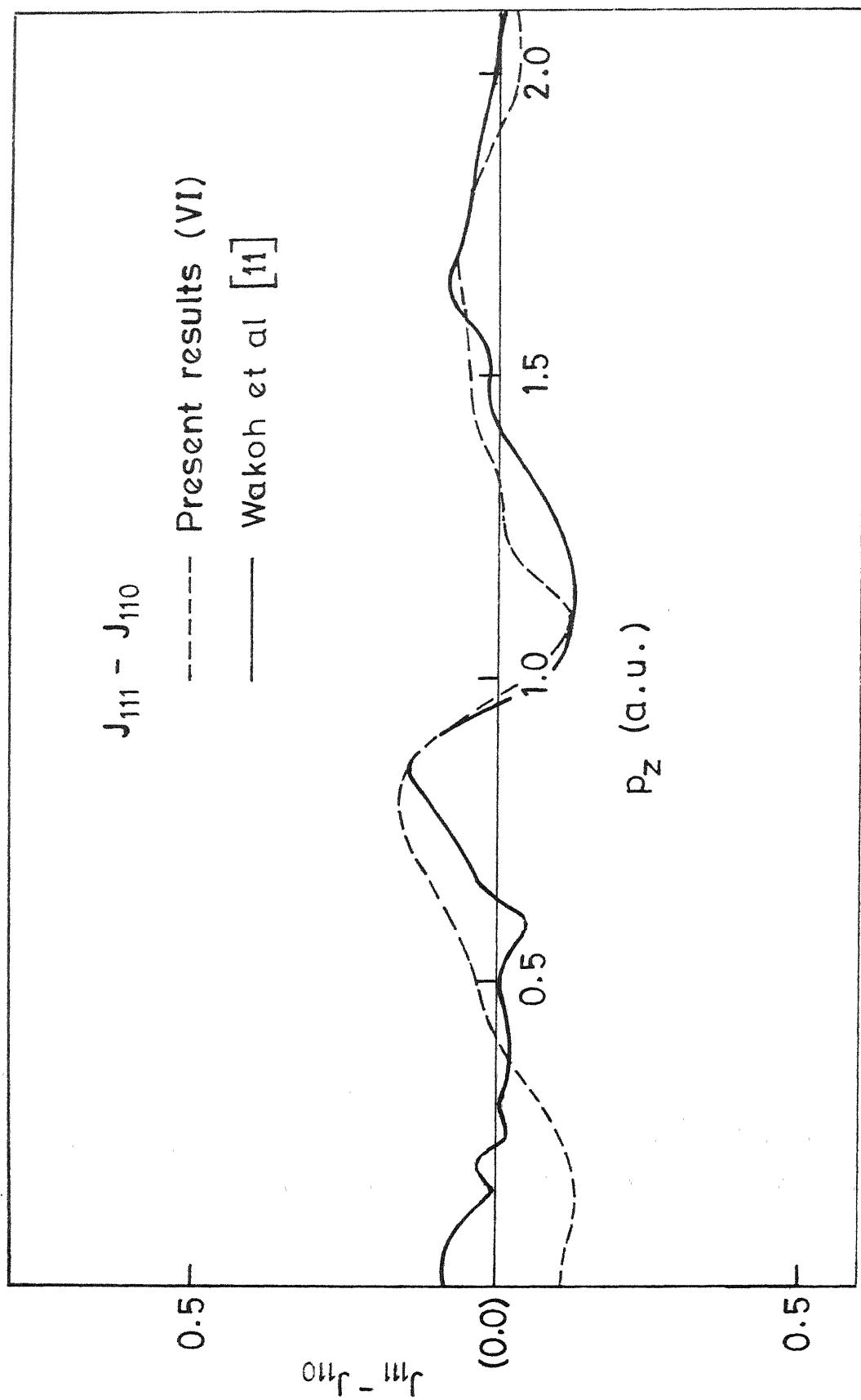


Fig. 5.11 : The theoretical Compton profile anisotropy  $J_{111} - J_{110}$ .

and EMD (they have used the APW method) and to construct  $J_{hkl}(p_z)$  from  $\rho(\vec{p})$ . The last feature could be most important because Wakoh et al. [11] have used a direct integration in the momentum space (Eq. 5.2) while we have used the approximate method of lattice harmonic expansion.

As pointed out earlier the experimental data for the directional profiles for V was reported by Terasaki et al. [13] in the form of anisotropy or difference curves and is shown in Fig. 5.8a. The corresponding anisotropy curves obtained from our directional profiles of Fig. 5.5 are shown in Figs. 5.9, 5.10 and 5.11.

A quantitative comparison between the experimental and the present theoretical anisotropy curves is not possible as Terasaki et al. [13] have not reported any numerical tables in their paper. However, a qualitative comparison of the results in Fig. 5.8a and Figs. 5.9-5.11 shows a satisfactory agreement except for the  $(J_{111}-J_{100})$  curves in the high  $(p_z > 1 \text{ a.u.})$  momentum region. The amplitudes of the sub-maxima in the experimental and theoretical anisotropy curves show a difference which could be ascribed to the effect of smoothing by the detector resolution function. The anisotropy curves calculated by us show very good agreement with the calculations of Wakoh et al. [11] except for the  $(J_{111}-J_{110})$  curves at very low momenta. The experimental  $(J_{111}-J_{110})$

curves (Fig. 5.8a) show a better agreement with our results. It may be pointed out that neither the experimental curves (Fig. 5.8a) nor the present theoretical curves (Fig. 5.9-5.11) agree with atomic model of Weiss [14] whose results (Fig. 5.8b) did not predict any submaxima and subminima in the anisotropy curves (Fig. 5.7b).



# REFERENCES

1. P. E. Mijnaarends in Compton Scattering, ed. B. Williams, McGraw-Hill, London, 1977; pp 323-345.
2. A. Seth and D. E. Ellis, Phys. Rev. A 13, 1083 (1976).
3. P. E. Mijnaarends, Phys. Rev. 160, 512 (1967).
4. D. G. Kanhere, Ph.D. Thesis, Indian Institute of Technology, Kanpur, India (Unpublished).
5. S. Manninen and T. Paakkari, Phys. Fenn. 9, 129 (1974).
6. T. Paakkari, S. Manninen and K.-F. Berggren, Phys. Fenn. 10, 207 (1975).
7. F. Biggs, L. B. Mendelsohn and J. B. Mann, Atomic Data and Nuclear Data Tables 16, 201 (1975).
8. D. D. Koelling, A. J. Freeman and F. M. Mueller, Phys. Rev. B1, 1318 (1970).
9. N. Elyashar and D. D. Koelling, Phys. Rev. B13, 5362 (1976).
10. S. Wakoh and J. Yamashita, J. Phys. Soc. Jap. 35, 1406 (1973).
11. S. Wakoh, Y. Kubo and J. Yamashita, J. Phys. Soc. Jap. 40, 1043 (1976).
12. J. Callaway, D. Laurent and C. S. Wang, Phys. Rev. (In press).
13. O. Terasaki, T. Fukamachi, S. Hosoya and D. Watanabe, Phys. Letts. 43A, 123 (1973).
14. R. J. Weiss, Philos. Mag. 14, 403 (1966).

## Chapter 6

### COMPTON PROFILES OF VANADIUM DEUTERIDE

#### 6.1 Introduction

Metal hydrides (deuterides) are solid compounds of hydrogen (deuterium) with metals. In recent years the study of metal hydrides has evoked great interest because of their possible use as storage elements of hydrogen for both fixed plant and vehicular applications [1]. In fusion reactors vanadium is considered as a construction material and severe constructional problems can arise due to the solution of hydrogen in vanadium [2]. In view of these technological applications, the physical and other properties of metal hydrides are being increasingly studied by different experimental techniques.

A fundamental and important question in these studies is the electronic structure of the metal hydrides. Although other experimental methods like photoemission studies, soft X-ray emission spectroscopy etc. are useful to investigate the electronic structure of metal hydrides, it has recently been demonstrated [3-7] that the Compton scattering method

provides a sensitive probe to study this aspect. The advantage of Compton profiles is that they are more sensitive to the electronic states of the conduction electrons but much less sensitive to the lattice distortions introduced during the process of loading hydrogen into the metals.

Two models have been proposed in the literature [8] for the electronic state assumed by hydrogen in the metal hydride. In the protonic model the hydrogen (or deuterium) atom is assumed to donate its electron to the conduction band of the host metal while in the anionic model the hydrogen is assumed to remove an electron from the conduction band to form an anion in a bound 1s state. Ab initio band-structure calculations [9-12] of palladium hydrides show that the electronic structure of metal hydrides is more complicated than either of the above two simple models.

Previous Compton profile measurements on polycrystalline  $\text{VH}_{0.45}$  [3] and on single crystalline  $\text{NbD}_{0.6}$  [4],  $\text{NbH}_{0.76}$  [5] and  $\text{NbH}_{0.29}$  [6] supported the protonic model for these hydrides. Recent studies [7] of the Compton profiles of polycrystalline  $\text{PdH}_{0.72}$ ,  $\text{VD}_{0.77}$  and  $\text{VH}_{0.71}$  support a model which takes into account the creation of metal hydrogen bonding states below the Fermi level by the introduction of hydrogen in the host lattice.

Among the transition metal hydrides, the vanadium (or niobium) hydrides are expected to show interesting

bandstructure changes because of the complicated bandstructure and Fermi surface of the host metal. The discussion in the previous Chapters has shown that the electron momentum distribution (EMD) in vanadium is very sensitive to the electron states near the Fermi level. We, therefore, thought it interesting to extend our calculations of the EMD for pure vanadium to vanadium deuteride,  $\text{VD}_{0.72}$ . No ab initio bandstructure calculations of the EMD in vanadium hydride (or deuteride) are reported in literature yet. Our present calculations can provide a theoretical basis to compare the experimental Compton profiles from the single crystalline vanadium deuteride (hydride). The present calculations are particularly applicable to vanadium deuteride  $\text{-VD}_{0.72}$  because for this system (at the room temperature) the vanadium lattice does not undergo a phase transition by deuterium loading. On the other hand, the phase diagram of  $\text{VH}_x$  is very complicated [13] and it indicates that at room temperature pure V shows the symmetry BCC ( $\alpha$ -phase) while  $\text{VH}_{0.72}$  shows a possible symmetry BCT ( $\epsilon$ -phase) [14].

## 6.2 Method of Calculation

Perhaps the most correct approach to the calculation of the Compton profile of a metal hydride is to perform an appropriate bandstructure calculation of the hydride itself

and calculate the EMD from the band wavefunctions so obtained. The Compton profiles could then be obtained from the double integration in the  $\vec{k}$ -space. However the band-structure calculations of the metal hydrides performed so far [9-12] do not report the wavefunctions or the EMD.

The basic idea behind this calculation is taken from the suggestion made by Kanhere and Singru [15]. These authors studied the systematics of the theoretical electron momentum distributions in the 3d transition metals V, Cr, Fe, Ni and Cu. They pointed out that along a particular  $\langle hkl \rangle$  direction the nature of the EMD arising out of individual bands or the  $\rho_j(\vec{p})$  curves ( $j$  being the band index) does not change much in going from one metal to the next higher metal (i.e. from V to Cr) having same (i.e. BCC or FCC) crystal structure. The total EMD,

$$\rho(\vec{p}) = \sum_{j=1}^{occ} \rho_j(\vec{p}) \quad (6.1)$$

however, shows significant changes which can be correlated with the changes in  $E_F$ . This interesting and systematic behaviour of the EMD is similar to the behaviour of the density of states,  $n(E)$ , in the 3d metals. The systematics of the  $n(E)$  curves have given rise to the so-called 'rigid band model' [16] which assumes a universal density of states,  $n(E)$ , for a given family of alloys. The Fermi energy ( $E_F$ ) of the alloy is then defined through the relation

$$N = \int_{-\infty}^{E_F} n(E) dE \quad (6.2)$$

where  $N$  is the number of conduction electrons in the alloy. We have made use of our results of the EMD for pure V to calculate the EMD and Compton profile of  $V_{D_{0.72}}$  on the basis of such a rigid band model. It is realised that an ultimate answer to the solution of this problem will have to come from the bandstructure calculation of the metal hydride system rather than an application of a rigid band approximation.

Earlier bandstructure calculations, particularly for palladium hydrides [9-12] have shown that the d-states in the host metal are almost unaffected by the hydrogen but the states possessing s-like character about the hydrogen will be modified. Thus hydrogen- (or deuterium-) vanadium bonding states are created below the Fermi level by the introduction of hydrogen (or deuterium) in the host lattice.

To examine this effect we have calculated the Compton profiles and anisotropies for  $V_{D_{0.72}}$  by two different methods with the protonic model and the rigid band approximation as the basic features of the calculations.

(a) In the first method we have assumed that in  $V_{D_{0.72}}$  the deuterium atom donates all its electrons to the conduction band of vanadium. This we shall call as the simple protonic

model (SPM). The energy bands being taken as rigid, the Fermi energy is raised from its value  $E_F$  for pure V (potential VI) to a higher value  $E'_F$  such that

$$5.0 = \int_{-\infty}^{E_F} n(E) dE \quad (6.3a)$$

$$5.72 = \int_{-\infty}^{E'_F} n(E) dE \quad (6.3b)$$

The total EMD  $\rho(\vec{p})$  was then calculated by summing Eq. (6.1) up to the new  $E'_F$  using the same  $\rho_j(\vec{p})$  values (for individual bands) that were obtained for pure vanadium (potential VI). The total EMD was thus calculated for the 12  $\vec{p}$ -directions in the (100) and (110) planes shown in Fig. 4.24.

(b) In the second method to be called as the modified protonic model (MPM) we assumed that only a fraction of the electrons of the deuterium atom are donated to the conduction bands of vanadium while the remaining fraction of electrons are accommodated in newly created deuterium-vanadium bonding states formed below the Fermi level. Switendick [9] has performed a bandstructure calculation on vanadium hydride which supports the formation of such states and shows that such vanadium-hydrogen bonding (or hybrid) states can accommodate about 0.25 electrons per H atom. Using this

data for our MPM we have assumed that  $0.25 \times 0.72$  or  $0.18$  electrons from the deuterium atom in  $VD_{0.72}$  go into the formation of vanadium-deuterium states having  $1s$  character about the deuterium site. Their wavefunctions and EMD are described by free hydrogen atom wavefunctions. The remaining  $0.75 \times 0.72$  or  $0.54$  electrons from the deuterium atom in  $VD_{0.72}$  are accommodated in the conduction band of vanadium raising its Fermi energy to a new value  $E_F''$  such that

$$5.54 = \int_{-\infty}^{E_F''} n(E) dE$$

The EMD for these 5.54 electrons is calculated by summing Eq. (6.1) up to  $E_F''$ .

In both the cases (a) and (b) the directional Compton profiles  $J_{hkl}(p_z)$  were calculated from the total EMD,  $\rho(\vec{p})$ , by following the method of Kubic harmonic expansion for the  $12\vec{p}$ -directions as described in Chapter 5. In the case (b) or MPM, the contribution to the Compton profile from the  $0.18$  electrons occupying the vanadium-deuterium bonded states was obtained by using the tables of the Compton profiles for free hydrogen atom by Biggs et al. [17].

The normalization of the area under the Compton profiles was done as follows. Firstly, the Compton profile of the free atom  $(3d)^3(4s)^2$  valence electrons was taken from the calculations of Biggs et al. [17]. The area under this



profile in the momentum region  $p = 0.0$  to  $2.4$  a.u. was found to be

$$\int_0^{2.4 \text{ a.u.}} J_{\text{free atom}}(p_z) dp_z = N_O = 2.2774 \text{ electrons.}$$

Next the Compton profiles, i.e.,  $g_O(p_z)$ ,  $J_{hkl}(p_z)$  calculated by us for pure V metal (case VI) were normalized to the same quantity  $N_O = 2.2774$  electrons as follows,

$$\int_0^{2.4 \text{ a.u.}} J_{\text{pure V}}(p_z) dp_z = N_O .$$

For  $VD_{0.72}$  the Compton profiles obtained by the simple protonic model (SPM) were normalized to a quantity  $N_a = 5.72$  ( $N_O/5.0$ ), so that

$$\int_0^{2.4 \text{ a.u.}} J_{VD_{0.72}}^{\text{SPM}}(p_z) dp_z = N_a$$

For the modified protonic model (MPM) the normalizations of the Compton profiles for  $VD_{0.72}$  corresponding to the conduction band electrons (which in this case are 5.54 as explained before) and the 0.18 electrons from the deuterium atom (which form the s-like bonding states) are done separately, as explained below.

For the 5.54 conduction or band electrons we put

$$\int_0^{2.4 \text{ a.u.}} J_{VD_{0.54}}^{\text{MPM}}(p_z) dp_z = 5.54 (N_O/5.0) = N_b .$$

To normalise the Compton profile due to the 0.18 electrons we started with the Compton profile for the hydrogen atom,  $J_H(p_z)$ , as given by Biggs et al. [17] and obtained a number  $N_c$  from

$$\int_0^{2.4 \text{ a.u.}} J_H(p_z) dp_z = N_c = 0.4933 \text{ electrons.}$$

The normalization for the 0.18 electrons of the deuterium atom which form the s-like bonding states in  $VD_{0.72}$  in the modified protonic model was then carried out as follows

$$\int_0^{2.4 \text{ a.u.}} J_{0.18D}^{MPM}(p_z) dp_z = 0.18 \times N_c$$

Finally the total profile for  $VD_{0.72}$  in the modified protonic model was obtained as

$$J_{VD_{0.72}}^{MPM}(p_z) = J_{VD_{0.54}}^{MPM}(p_z) + J_{0.18D}^{MPM}(p_z)$$

It may be pointed out that in the present calculations there is basically no difference between hydrides ( $VH_x$ ) and deuterides ( $VD_x$ ). However, our theoretical results are more directly applicable to the deuteride  $VD_{0.72}$  rather than to  $VH_{0.72}$  because of the fact that the former system does not undergo a phase transition from pure V while the latter system does.

It is also important to point out the difference between the method of present calculation and that of Lässer and

Lengeler [7]. Although these authors describe their calculations as a bandstructure calculation, the basis of their work is the Compton profile theoretically calculated by Wakoh et al. [18] for pure V using the APW bandstructure method. Lässer and Lengeler thus consider the Compton profiles as 'rigid' and adjust the Compton profile contributions according to the different models used by them. On the other hand, we feel that in a metal like V where the EMD is so sensitive to the changes in the bandstructure and Fermi energy one should treat EMD as more basic than the Compton profiles. Accordingly we have first calculated the EMD in  $\text{VD}_{0.72}$  as modified by the transfer of electrons from deuterium to the host metal. The changes in the Compton profiles in going from V to  $\text{VD}_{0.72}$  are then calculated by us from the modified EMD under the two models (i.e. SPM and MPM). Further our calculations, which start from the total EMD along various  $\vec{p}$ -directions, lead to the prediction of directional Compton profiles as well as anisotropies for the single crystals. The present calculations thus provide a wider basis for a comparison between theory and experiment and allow a more sensitive test of the two models (i.e. SPM and MPM) proposed.

### 6.3 Results and Discussion

The results of our calculations for the polycrystalline  $\text{VD}_{0.72}$  are shown in Fig. 6.1 in the form of a difference curve

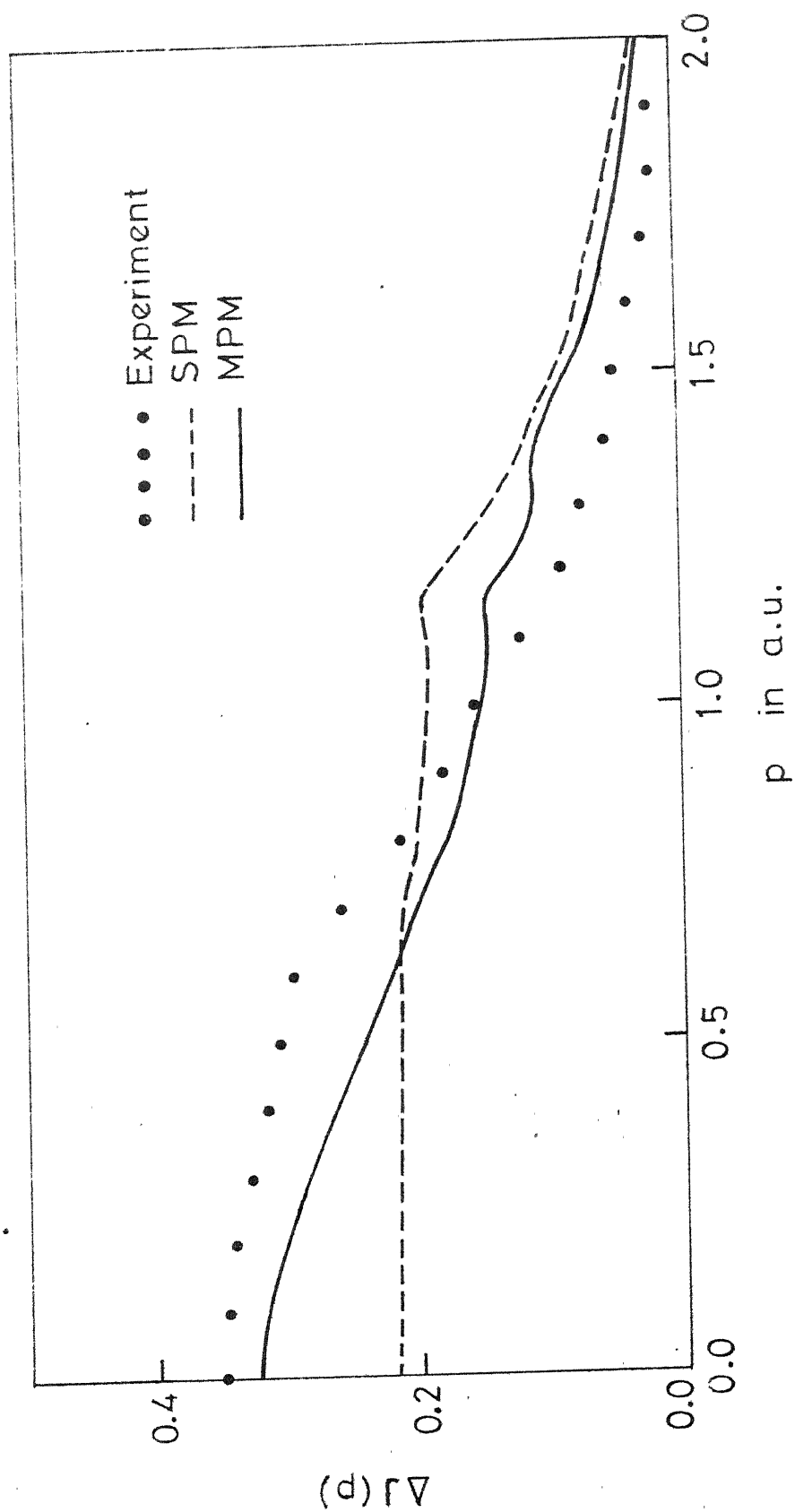


Fig. 6.1 : The theoretical (SPM and MPM) and the experimental difference curves for the spherically averaged Compton profiles from  $^{20}\text{Ne}$ .

$\Delta J(p_z) = J_{VD_{0.72}}(p_z) - J_V(p_z)$ . The isotropic profiles (corresponding to the polycrystalline  $VD_{0.72}$  or V) were obtained from the respective  $g_0$  functions (Eq. 5.6) and were normalised as explained in the previous section. The theoretical profiles have not been convoluted by the energy resolution function of the detector system. The curve marked SPM refers to the simple protonic model calculation while the other curve marked MPH describes the modified protonic model calculation. There is no experimental measurement of the Compton profile for  $VD_{0.72}$  reported in the literature. Nevertheless we have obtained the Compton profile for  $VD_{0.72}$  by using the experimental data of Lässer and Lengeler for  $VD_{0.77}$  [7] and normalising the area appropriately. The experimental data points for  $VD_{0.72}$  so obtained are shown by (.) marks in Fig. 6.1. Earlier work has already shown that neither the atomic model [7] nor the anionic model [3-7] is able to describe the Compton profiles of transition metal hydrides satisfactorily. A comparison between our theoretical curves and experimental values (Fig. 6.1) confirm the earlier finding [7] that a simple protonic model cannot correctly describe the difference curves  $\Delta J(p_z)$  in vanadium. Our present results along with those of Lässer and Lengeler [7] suggest that a modified protonic model which takes into account the formation of hydrogen-vanadium bonding states below the Fermi level is more successful in describing the

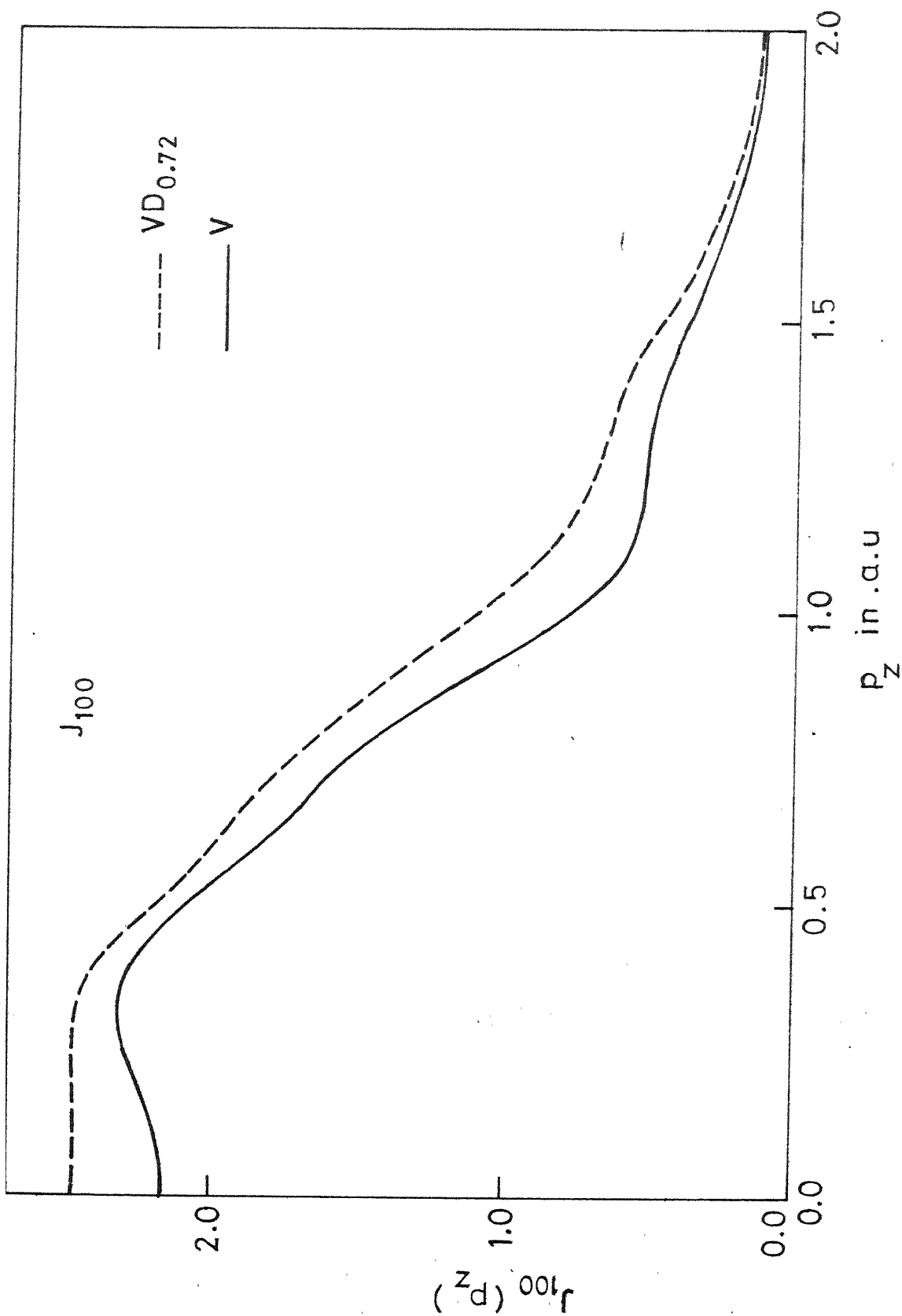


Fig. 6.2 : The theoretical Compton profiles for  $V$  and  $VD_{0.72}$  (a.u.) along the  $\langle 100 \rangle$  direction.

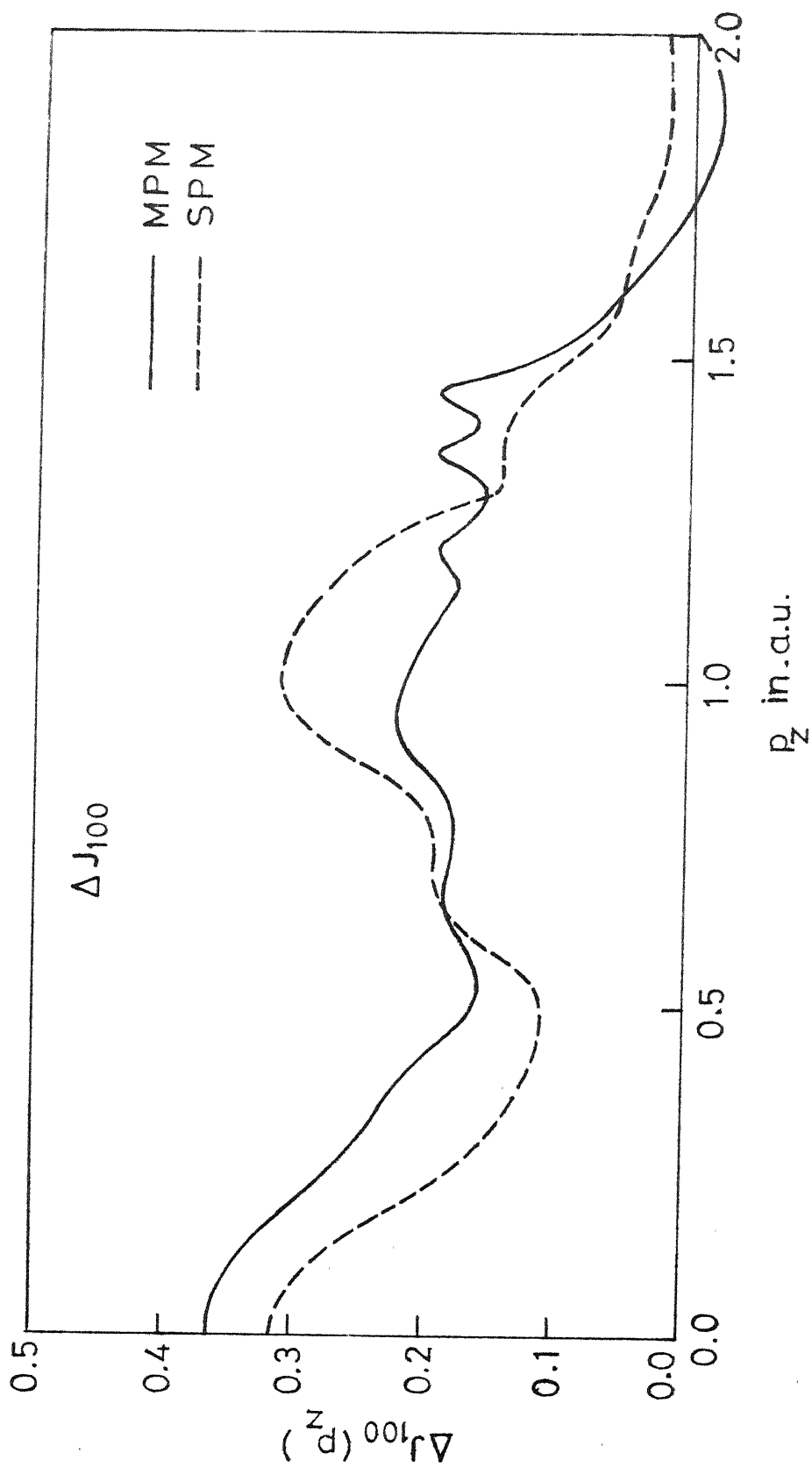


Fig. 6.3 : The difference curves  $\Delta J_{100}(p_z)$  and  $\Delta J_{100}(p_z)$  for  $V_{100}(p_z)$  (see text).

observed experimental results. The residual disagreement between the experiment and MPM values (Fig. 6.1) could be due to the approximations made by us in the MPM and those involved in deriving  $J(p_z)$  from the EMD (Chapter 5).

It was seen in Chapter 5 that in vanadium, the directional Compton profile along the  $\langle 100 \rangle$  direction reflected the complicated Fermi surface topology of vanadium -- particularly the features like the jungle-gym hole tubes along the  $\langle 100 \rangle$  directions. We have therefore compared the theoretical directional profiles  $J_{100}(p_z)$  for V and  $VD_{0.72}$  (SPM) in Fig. 6.2. It is seen that the concavity of  $J_{100}(p_z)$  in the  $p_z$  range from 0.0 to 0.5 a.u. observed in vanadium becomes more flat in  $VD_{0.72}$ . This effect is also seen in the difference profiles  $\Delta J_{100}(p_z) = J_{100}^{VD_{0.72}} - J_{100}^V$  of Fig. 6.3. This behaviour is easily understood in terms of the bandstructure and Fermi surface of vanadium.

In the construction of the Compton profile (CP)  $J_{100}(p_z)$ , the integration planes of the EMD (Eq. 5.2) are parallel to the (100) plane. For  $p_z = 0$ , the (100) integration plane passing through  $r$  contains, in the case of vanadium, four jungle-gym arms (due to the third band Fermi surface) along the  $\pm p_x$  and  $\pm p_y$  directions. The density of occupied states for this plane is relatively lower and the corresponding EMD has the features shown in Fig. 4.34. As a result, the



$J_{100}(p_z)$  curve shows a concave part in the region  $p_z=0.0-0.3$  a.u. In  $VD_{0.72}$ , however, the electrons from the deuterium atom fill up the third band considerably thus leading to a shrinkage of jungle-gym hole arms. Thus, in the (100) plane of  $VD_{0.72}$  passing through  $p_z = 0$ , there are relatively more occupied states and the contribution to the EMD is correspondingly larger. This results in a more flat behaviour of the  $J_{100}$  curve for  $VD_{0.72}$  in the region  $|p_z| < 0.3$  a.u. Similarly at the points H and the higher  $\Gamma$ -point along the  $\langle 100 \rangle$  direction, we have a more flat behaviour in the Compton profile for  $VD_{0.72}$  compared to that in vanadium. Further, the comparison of the  $J_{100}(p_z)$  profiles in Nb and  $NbH_{0.76}$  [5] show similar features which are explained by arguments same as above. This is not surprising in view of the close similarity between the Fermi surfaces (and bandstructure) of V and Nb.

The difference curves

$$\Delta J_{110}(p_z) = J_{110}^{VD_{0.72}}(p_z) - J_{110}^V(p_z)$$

and

$$\Delta J_{111}(p_z) = J_{111}^{VD_{0.72}}(p_z) - J_{111}^V(p_z)$$

are shown in Figs. 6.4 and 6.5. These results show that compared to the difference curve  $\Delta J_{111}$ , the curves  $\Delta J_{100}$  and  $\Delta J_{110}$  show more significant changes in going from the

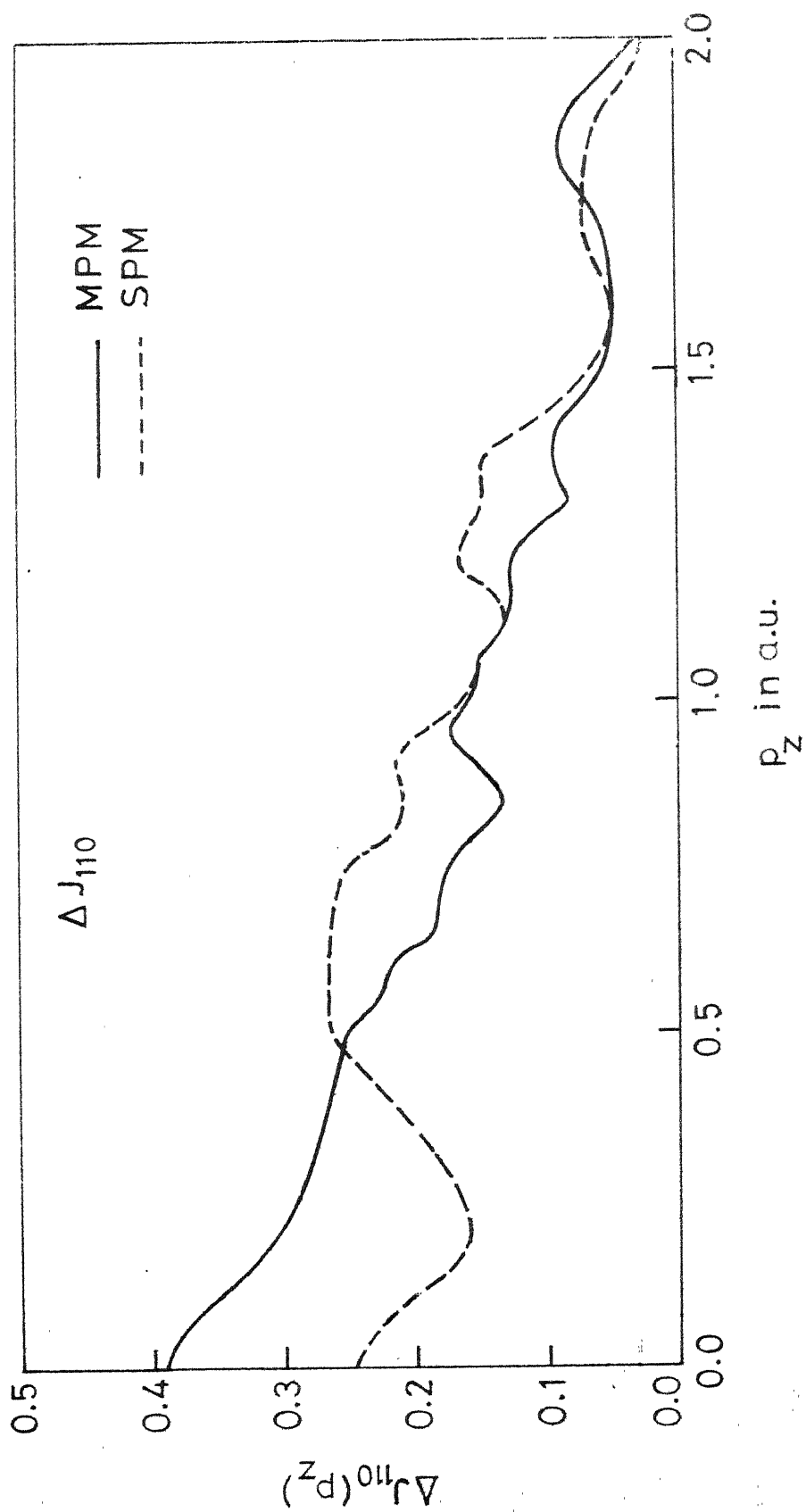


Fig. 1.4 : The difference curves  $\Delta \tilde{J}_{110}$  (SPM and MPM) for  $m_{1/2} = 1$  (see text).

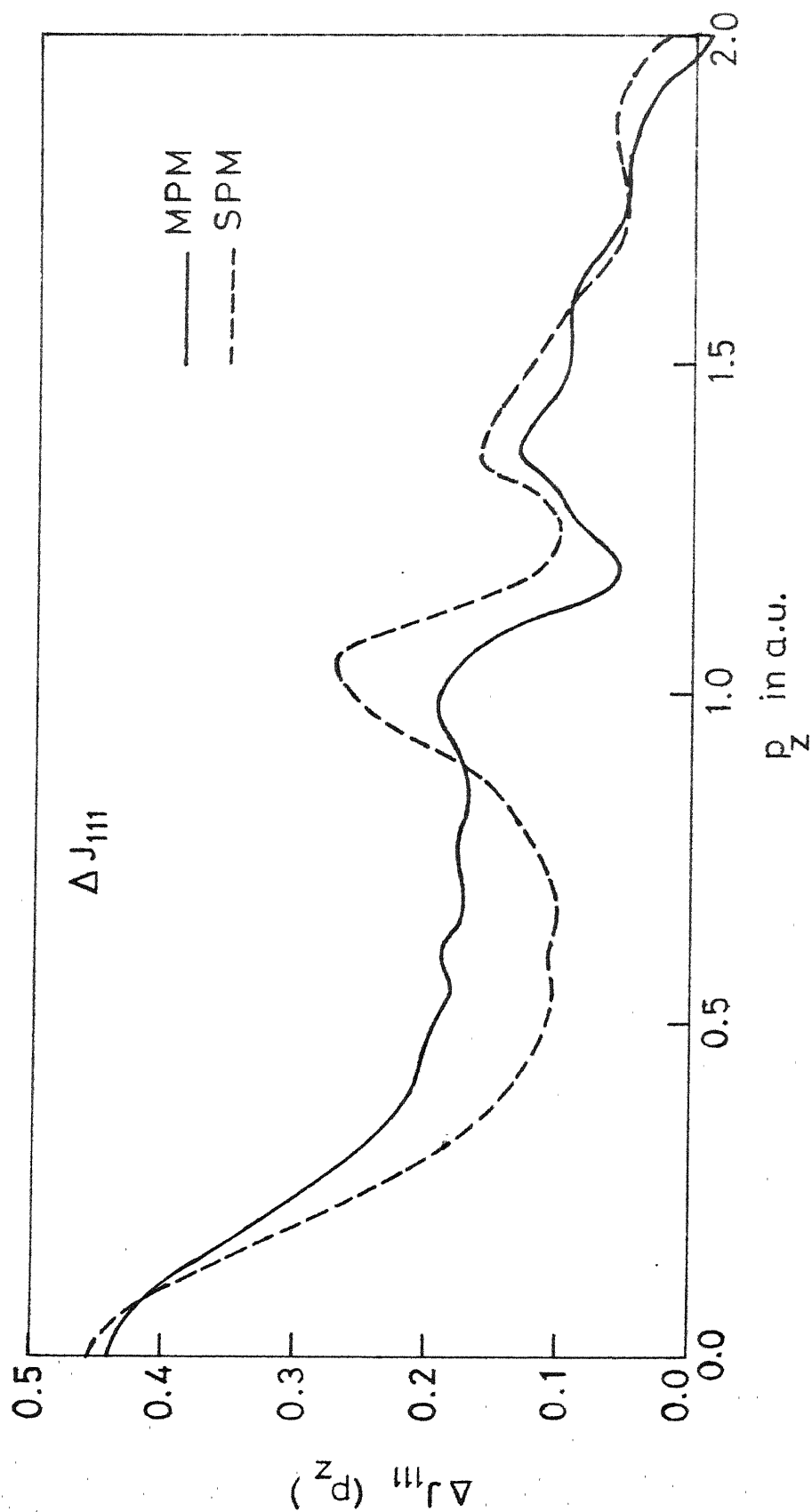


Fig. 6.5 : The difference curves  $\Delta J_{111}$  (SPM and MPM) for  $(D_{2h})_{111}$  (a.u.).

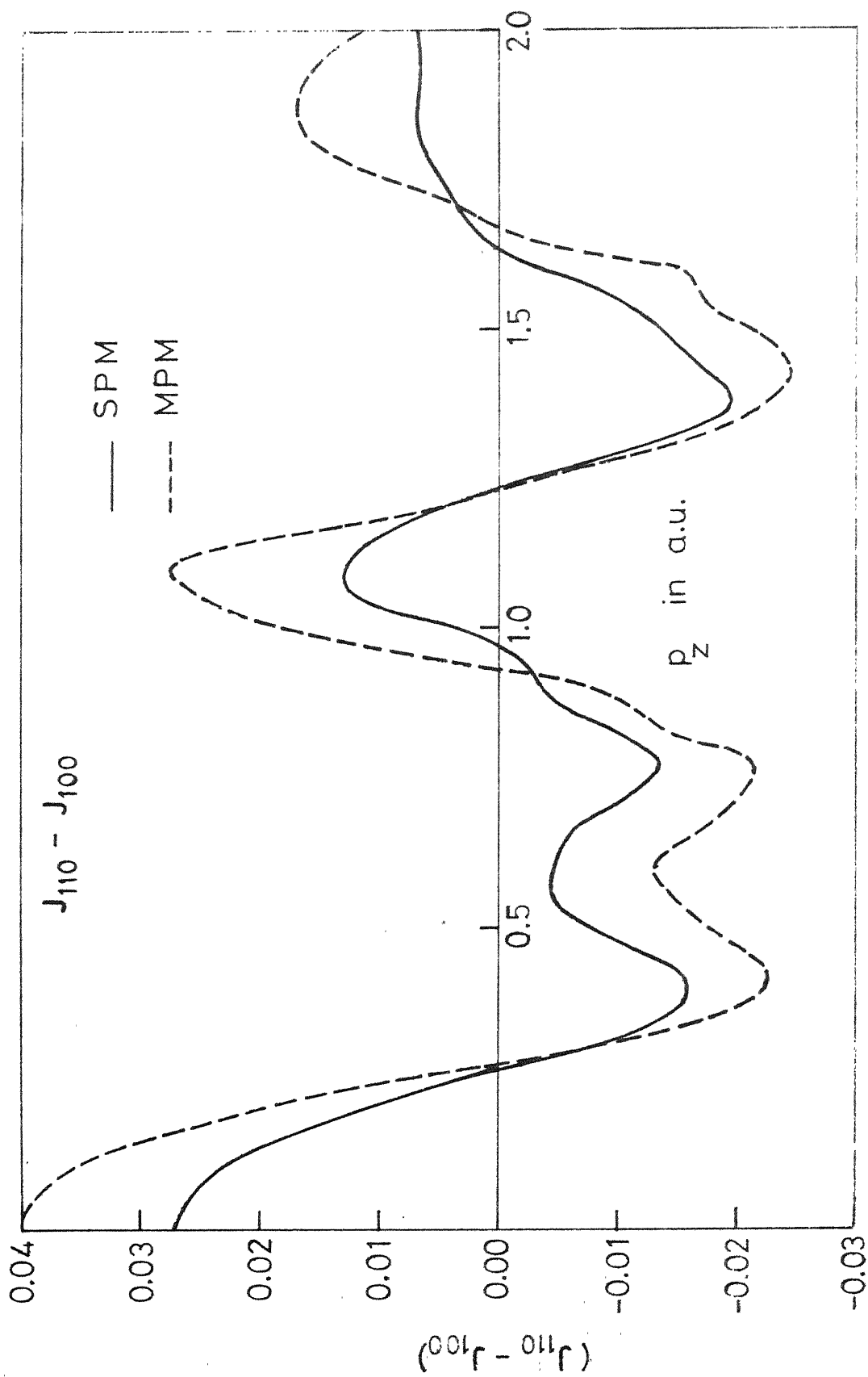


Fig. 5.11. The theoretical Compton profile anisotropy curve  $J_{110} - J_{100}$  (SPM and MPM) for  $v_L = 7$ .

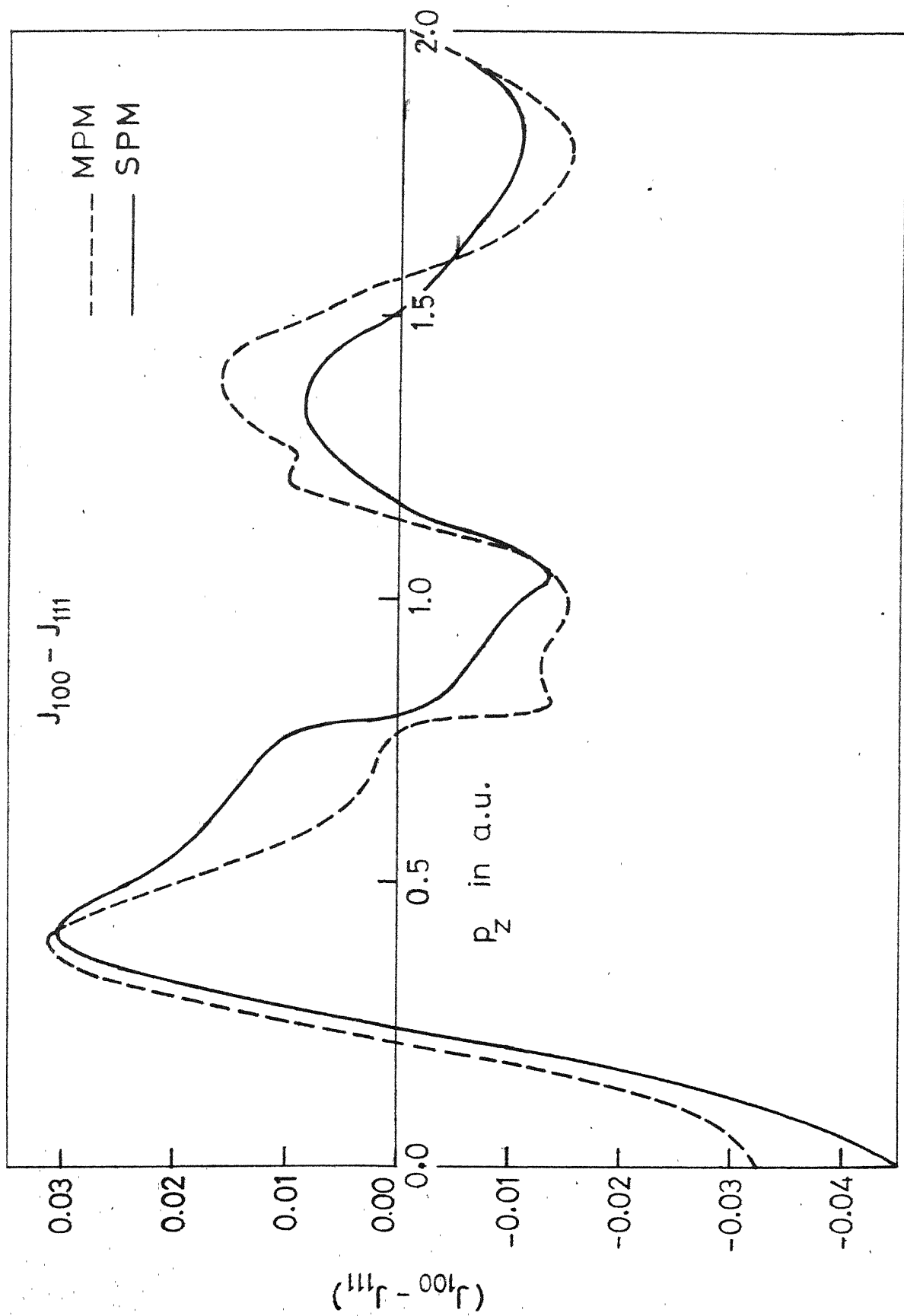


FIG. 6.7 : The theoretical Compton profile anisotropy curve  $J_{100} - J_{111}$  (SPM and MPM) for V2, etc.

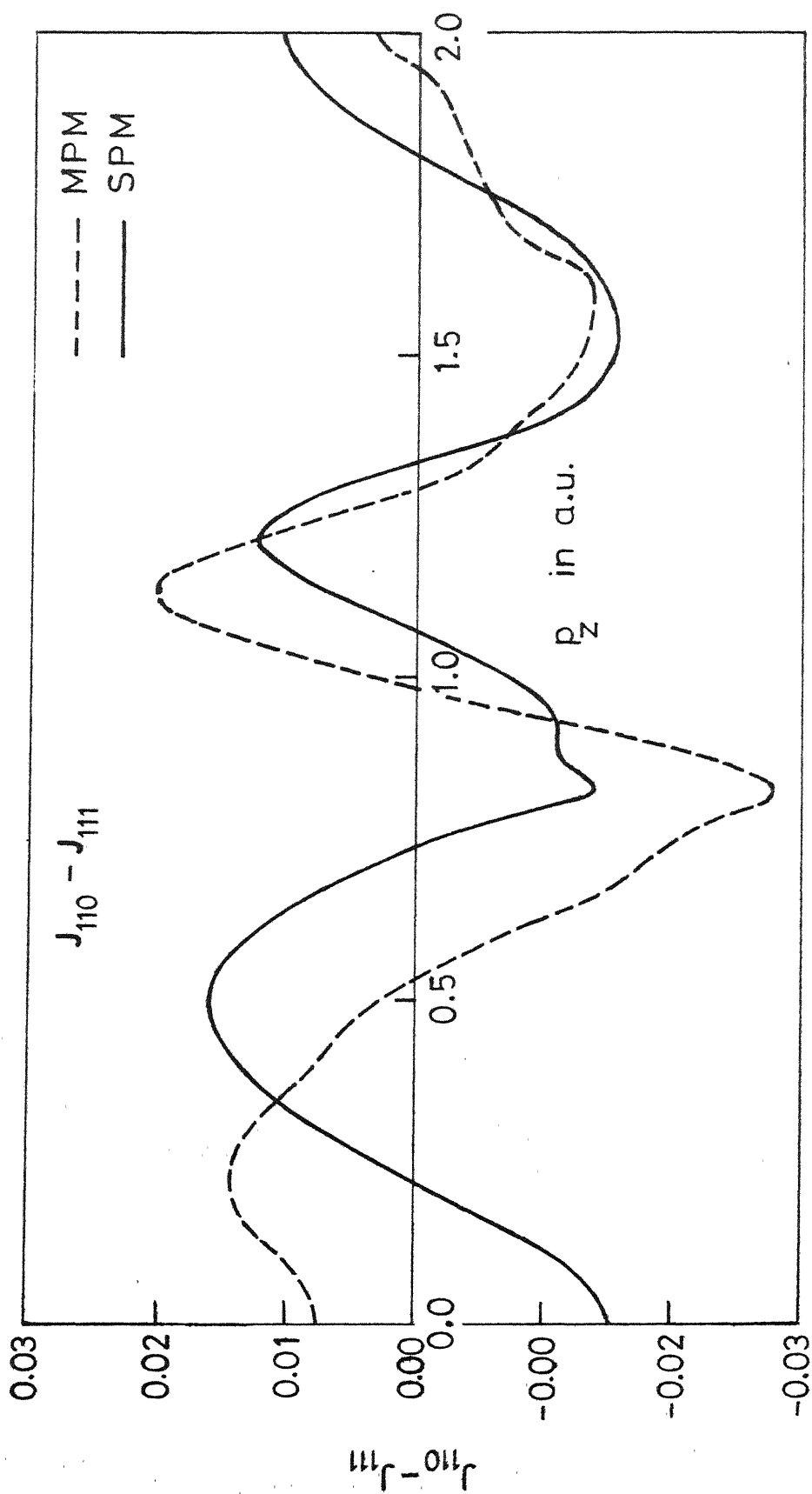


Fig. 6.8 : The theoretical Compton profile anisotropy curve  $J_{110} - J_{111}$   
(SPM and MPM) for  $VD_{0.72}$ .

simple protonic model to the modified protonic model. The anisotropy curves ( $J_{hkl} - J_{h'k'l'}$ ) for  $VD_{0.72}$  in the two different models (SPM and MPM) are given in Figs. 6.6-6.8. Here we find that the two models predict a significant difference in the anisotropy curve  $J_{110} - J_{111}$ . Thus it appears that the comparison of the theoretical results for the difference curves  $\Delta J_{100}$ ,  $\Delta J_{110}$  as well as the anisotropy curve ( $J_{110} - J_{111}$ ) with experimental values for these cases can throw more light on the relative merits of the two models.

No measurements of the directional Compton profiles of  $VD_x$  (or  $VH_x$ ) have been reported yet. Such measurements on  $NbH_x$  and  $NbD_x$  [3-6] have already added to our understanding of the electronic structure of these hydrides. We suggest that the measurement of the Compton profiles from the single crystals of  $VD_x$  and  $VH_x$  be undertaken. A comparison of these experimental results with the results of our calculations, i.e., Figs. 6.3-6.8 can then provide a basis to understand more clearly the electronic states in vanadium deuterides and hydrides.

### Summary

Compton profile measurements have been found to be a suitable probe to study the electronic structure of metal hydrides and deuterides. Even though earlier experimental studies favoured the protonic model, recent experiments [7]

have shown that this model cannot correctly explain the electronic band structure of metal hydrides. In the case of some transition metals, bandstructure calculations have shown that only a fraction of the hydrogen (or deuterium) atom electrons are transferred to the conduction band while the rest of the electrons form ls bonding states with the electrons below the Fermi surface of the host metal.

We have used our results for pure vanadium to investigate this effect. Compton profile calculations for  $\text{VD}_{0.72}$  were done by two different methods under the rigid band approximation (i.e., keeping the partial momentum densities rigid) and with the protonic model as the basis. In one, all the electrons of the deuterium atom are transferred to the conduction band (SPM) while in the other, only a fraction are transferred, the rest being assumed to form ls bonding states with the electrons below the Fermi surface of the host metal (MPM). The results of the calculation show that the MPM is more successful in explaining the experimental values obtained for polycrystalline vanadium deuteride. The difference curves  $\Delta J = J_{\text{VD}_{0.72}} - J_{\text{V}}$  as well as the anisotropies  $J_{\text{hkl}} - J_{\text{h'k'l'}}$  for the SPM and MPM show significant differences. It is suggested that comparison of these theoretical results with future experimental results on single-crystalline  $\text{VD}_{0.72}$  could throw more light on the electronic structure of hydrides and deuterides.



## REFERENCES

1. R. H. Wiswall, Jr. and J. J. Reilly, 'Metal Hyarides for Energy Storage', Proceedings of 7th Intersociety Energy Conversion Engineering Conference 1972, San Diego, California, September 25-29, 1972.
2. L. C. Ianniello, ed. 'Fusion Reactor First Wall Materials', Report WASH-1206, U.S. Atomic Energy Commission, Washington, D.C. (U.S.A.), 1972.
3. W. R. McIntire and B. W. Batterman, Phys. Status Solidi B 63, 621 (1974).
4. P. Pattison, M. Cooper and J. R. Schneider, Z. Phys. B 25, 155 (1976).
5. P. Pattison, M. Cooper, R. Holt, J. R. Schneider and N. Stump, Z. Phys. B 27, 205 (1977).
6. N. G. Alexandropoulos and W. A. Reed, Phys. Rev. B 15, 1790 (1977).
7. R. Lässer and B. Lengeler, Phys. Rev. (To be published); R. Lässer, Ph.D. Thesis, Leopold Franzens-Universität, Innsbruck (1978) Unpublished. Report Jul-1492, Kernforschungsanlage, Jülich.
8. G. G. Libowitz, The Solid State Chemistry of Binary Metal Hydrides, Benjamin, New York, 1965.
9. A. C. Switendick, in 'Hydrogen Energy', Part B, ed. T. N. Veziroglu, Plenum Publishing Corporation, New York, N.Y., U.S.A. (1977), p. 1029; also Ber. Bunsenges. Phys. Chemie 76, 555 (1972).
10. J. S. Faulkner, Phys. Rev. B 13, 2391 (1976).
11. J. Zbasnik and M. Mahnig, Z. Phys. B23, 15 (1976).
12. D. A. Papaconstantopoulos, B. M. Klein, E. N. Economou and L. L. Boyer (To be published).
13. T. Schober and A. Carl, Phys. Status Solidi A 43, 443 (1977).

14. H. Asano, Y. Abe, M. Hirabayashi, *Acta Metall.* 24, 95 (1976); also *J. Phys. Soc. Jap.* 41, 974 (1976).
15. D. G. Kanhere and R. M. Singru, *J. Phys.* F7, 2603 (1977).
16. N. F. Mott, *Adv. Phys.* 13, 525 (1964).
17. F. Biggs, L. B. Mendelsohn and J. B. Mann, *Atomic and Nuclear Data Tables* 16, 201 (1975).
18. S. Wakoh, Y. Kubo and J. Yamashita, *J. Phys. Soc. Jap.* 40, 1043 (1976).

## VITAE

The author was born in Thazhekad village in Trichur District, Kerala on 26th January 1952. He obtained his B.Sc. degree in Physics from the University College, Trivandrum (Kerala University) and the M.Sc. degree from I.I.T. Kharagpur. He joined the Ph.D. program in Physics at I.I.T. Kanpur in August 1972. He was a recipient of the National Science Talent Search Scholarship. At present he is working at I.I.T. Kanpur as a Research Scholar.

### Publications

1. Calculation of Momentum Expectation Values for 3d Transition Metals from the Electron Momentum Distribution,  
K. R. K. Gandhi and R. M. Singru,  
Presented at the Nuclear Physics and Solid State Physics Symposium (DAE), Calcutta, December, 1975.
2. Electron Momentum Distribution and Compton Profiles in Vanadium,  
K. R. K. Gandhi and R. M. Singru,  
Presented at the Nuclear Physics and Solid State Physics Symposium (DAE), Poona, December, 1977.
3. Theoretical Compton Profiles in Vanadium and Palladium Hydrides,  
K. R. K. Gandhi, R. M. Singru and D. G. Kanhere,  
Presented at the Nuclear Physics and Solid State Physics Symposium (DAE), Poona, December, 1977.
4. Anisotropy in the Compton Profiles of V and  $\text{VDO}_{0.72}$ ,  
K. R. K. Gandhi and R. M. Singru,  
Abstract in Eleventh International Congress of Crystallography, Warszawa, Poland, August 3-12, 1978.